Theoretical Studies on Organometallic Reactions and New Effective Potential for Highly Accurate Calculation

Yu-ya Ohnishi
2009

Preface

Computational chemistry is one of the important fields of recent chemistry. Especially, modern electronic structure theory such as post Hartree-Fock methods and density functional theory, which are based on the quantum chemistry, is applied to various compounds and reactions not only by theoreticians but also by experimentalists.

Organometallic compounds have attracted many researchers because of their interesting geometries, bonding natures, and reactivities, as well as complicated and flexible electronic structures. These compounds play such important roles as homogeneous catalysts, metalloenzymes, reaction intermediates, and so on. The density functional theory enables us to understand well the geometries, bonding natures, and properties of organometallic compounds and the reaction mechanisms of their catalytic reactions. However, the density functional theory involves several weak points: One of them is an underestimation of an activation barrier and another is a poor description of a dispersion interaction. Besides the density functional theory, we need highly accurate post Hartree-Fock methods. Theoretical study of organometallic compounds with post Hartree-Fock methods is, however, still difficult even in the present day because of the large size of the molecules. Since the quantitatively correct calculation of properties and energy changes is indispensable to correctly understand geometries, properties, and reactions of organometallic compounds and to design a new molecule and new reaction, we need to develop a new method that provides quantitatively correct results for large molecules.

In this thesis, I describe the theoretical studies of organometallic reactions with the electronic structure theory. Chapters 1 and 2 report theoretical studies of the hydrogenation of carbon dioxide by ruthenium complex without and with water additive, where the density functional theory and Møller-Plesset many-body perturbation theory were employed. Chapter 3 describes the comprehensive survey of theoretical methods to find what method gives quantitatively reliable results in the system bearing transition metal element. Considering the conclusions in chapter 3, I proposed new frontier orbital consistent quantum capping potential (FOC-QCP) method in chapter 4. We can apply highly sophisticated post Hartree-Fock methods to large molecule with this FOC-QCP method. In chapter 5, a theoretical study of the nickel-catalyzed carbon-carbon bond activation and carbon-carbon bond formation is reported. The highly sophisticated post Hartree-Fock method combined with the FOC-QCP method, as well as the density functional theory, is successfully applied to this reaction.

The studies presented in this thesis were carried out at the Department of Molecular Engineering, Graduate School of Engineering, Kyoto University from 2003 to 2009. I would like to express my deepest appreciation to Professor Shigeyoshi Sakaki for his helpful discussion, interesting suggestions, and encouragement. His various comments based on theoretical, physical, and inorganic chemistries were invaluable for this study. I wish to express his sincere gratitude to Associate Professor Hirofumi Sato for his shrewd and valuable suggestions. I also express gratitude to Assistant Professor Yoshihide Nakao for his technical supports. I am also grateful to Dr. Michinori Sumimoto for his many advices for organometallic reactions and computational techniques, when I started the study. I also express my sincere acknowledgement to Professor Tamejiro Hiyama and Assistant Professor Yoshiaki Nakao in the Department of Material Chemistry, Graduate School of Engineering, Kyoto University for their collaboration and kind discussion in chapter 5.

I am also grateful to Dr. Atsushi Ikeda, Dr. Daisuke Yokogawa, and Mr. Ken Saito. Scientific talks with them on various occasions were very enjoyable and fruitful to me. Acknowledgement is also made to all members of the research group of Prof.

Shigeyoshi Sakaki.

I thank Japan Society for the Promotion of Science (JSPS) for financial support (Grant-in-Aid for JSPS Fellows).

Finally, I sincerely thank my parents, Masayoshi and Naomi Ohnishi, for their understanding, encouragement, and continuous support.

Yu-ya Ohnishi

January, 2009

Contents

General Introduction

1. Interests in Organometallic Reaction

Nowadays, homogeneous catalytic processes with organometallic compounds, as well as heterogeneous catalytic processes with solid catalysts, are widely applied to syntheses of many organic compounds. Also, many industrial reactions by organometallic catalysts have been reported;[1,2] typical examples are polymerizations and hydrogenations of alkenes and alkynes, hydroformylations of alkenes, and acetic acid synthesis by carbonylation of methanol. Precise syntheses of organic compounds are also of significant importance in applied chemistry; for example, cross-coupling reactions and asymmetric syntheses are very important in synthetic chemistry.[3,4] Carbon and nitrogen fixations[5,6] by organometallic compounds have drawn a lot of interests because they promise to utilize chemically inert molecules as resources to synthesize many industrial products.

Since organometallic compounds consist of metal center(s) and several organic and/or inorganic ligands, varieties of bonding nature and electronic structures are found in them.[3,7] Due to the flexible bonding natures and electronic structures, organometallic compounds exhibit various interesting properties and reactivities. The bonding nature and electronic structure of organometallic compounds are significantly complicated due to the narrow energy gap among d orbitals, interaction between the d orbital of metal center and valence orbitals of ligands, participation of not only σ but also π orbitals of ligand, and so on. It is difficult to predict the geometry, bonding nature, and reactivity from simple consideration; in other words, organometallic compounds cannot be understood well with the traditional idea proposed by Lewis and the ligand field theory, for instance.

Several important and useful concepts have been presented for organometallic compounds so far; for example, trans effect and trans influence effect, 16- and 18-electron rules, and donation/back-donation interaction between a metal center and ligands are useful idea to discuss organometallic compounds.[7] The relations between those concepts and the quantum chemical knowledge must be elucidated. Moreover, various organometallic compounds showing unexpected geometries and properties are newly synthesized day by day. We need new concepts to understand their geometries, bonding nature, properties, and reactivities. There is no doubt that we have to present essential and fundamental knowledge of organometallic compounds based on the modern electronic structure theory.

2. Quantum Chemistry of Organometallic Reactions

Considering the above-mentioned situation, the author believes the quantum chemical method such as post Hartree-Fock methods[8] and density functional theory (DFT)[9-11] is highly desired to apply to investigation of organometallic compounds nowadays. Actually, significant advancements have been made recently in computer performance, algorithm of program, and electronic structure theory, which enable us to apply the quantum chemical methods to large and complicated molecules such as organometallic compounds. Theoretical study of organometallic reactions with the quantum chemical methods provides a lot of informative findings, which cannot be presented easily with the experimental study. For instance, we are able to easily characterize and analyze the transition state geometry with the electronic structure theory, which cannot be observed with the experimental method. Also, we are able to easily calculate the energy profile of the whole reaction and determine the rate-determining step of the reaction. Moreover, we can easily investigate new compounds by changing the metal center and/or ligands. Such investigation is valuable to understand the roles of each component such as metal center and ligands and to design a new compound and a new reaction.[12]

Though the post Hartree-Fock and DFT methods are undoubtedly powerful tool to investigate organometallic compounds and their reactions, there still remain several problems to be overcome. The largest problem is difficulty to present the accurate results with reasonable computational cost for large molecules. Generally speaking, the methods which can provide accurate results need huge computational cost. For small molecules that consist of a few atoms, the quantitatively accurate energy and properties can be provided by highly sophisticated post Hartree-Fock methods. However, it is difficult to apply such methods to organometallic compounds because they usually consist of dozens of atoms including transition metal elements. The complex electronic structures of organometallic compounds further induce another problem as follows; because organometallic compounds include many electrons in small area, the electron-electron collision, which is commonly called dynamical correlation effect, must be properly incorporated in the calculation. Also, static correlation effect must be taken into consideration in several cases because of the narrow-energy gap among d orbitals.

3. Electronic Structure Theory which can be Applied to Organometallic Compounds

Considering the complicated electronic structures of organometallic compounds, we need to carefully apply the electronic structure theory to organometallic compounds. The DFT method is widely used as a standard method to study organometallic compounds and their reactions, because the computational cost of the DFT method is relatively small and the DFT method with hybrid functionals provides considerably good geometries in general.[13,14] Actually, the mechanisms of many organometallic

Table 1. Binding Energies (kcal/mol) of $C_2H_{4-n}(CH{=}CH_2)_n$ with $Pt(PH_3)_2$ (n = 0-4)

n	CCSD(T)	MP4(SDQ)	B3LYP	B3PW91
0	22.2	22.2	14.4	21.5
1	22.6	22.5	11.3	18.4
2	21.9	22.1	6.7	13.8
3	—	22.6	4.0	11.3
4	—	21.1	-1.1	6.5

Ref. 15

reactions have been elucidated by the DFT method so far.[12] The DFT method, however, involves several problems in the evaluation of energetics of the reaction. It is well known that this method underestimates activation energies.[14] In the study of organometallic reaction, the correct activation energy is indispensable for correct understanding of the organometallic reactions. This is one of the severe defects of the DFT method. Another weak point of the DFT method is not to describe dispersion interaction, as is widely known.[11] Also, the DFT method with B3LYP and B3PW91 functionals considerably underestimates the coordination energy of π-conjugate ligand with metal center compared with post Hartree-Fock methods such as CCSD(T) and MP4(SDQ) methods, as shown in Table 1.[15] These are significantly large problems in the evaluation of energy changes because organometallic compounds often involve π-conjugate systems and the dispersion interaction is induced between bulky ligands. Thus, the current DFT method does not always present the reliable results.

Møller-Plesset (MP) many-body perturbation theory[16] has been widely applied to organometallic compounds so far because the computational cost is relatively small among the post Hartree-Fock methods. However, the reliability of the results presented by the MP method strongly depends on the quality of the Hartree-Fock wave function which is the reference.[17] The Hartree-Fock method does not present good

Table 2. Binding Energies (kJ/mol) of Acetylene, Ethylene,and Carbon Monoxide for Mononuclear Ni(0) Complexes Calculated at Different Levels of Theory.[*1]

	DFT	CCSD(T)	MP4(SDQ)	MP3	MP2
$Ni(C_2H_2)_2$ → $Ni(C_2H_2) + C_2H_2$	288	280	546	124	566
$Ni(C_2H_4)_2$ → $Ni(C_2H_4) + C_2H_4$	227	219	518	58	490
$Ni(CO)_4$ → $Ni(CO)_3 + CO$	86	104	676	−162	222
$Ni(PH_3)_2(C_2H_2)$ → $Ni(PH_3)_2 + C_2H_2$	221	262	163	240	160
$Ni(PH_3)_2(C_2H_4)$ → $Ni(PH_3)_2 + C_2H_4$	198	237	206	202	209

Ref. 19

results for many organometallic compounds because of the large electron correlation effects in the system including transition metal element. Thus, the MP method is not always a good choice for the study of organometallic compounds. For example, the MP method cannot produce the correct coordination energy of N_2 with $Ni(PH_3)_2$.[18] Hyla-Kryspin et al. also reported that the MP2-MP4(SDQ)-calculated binding energies of C_2H_2, C_2H_4, and CO with nickel(0) complexes are much different from the DFT and coupled-cluster methods, as shown in Table 2.[19]

Multi-reference perturbation theory such as complete active space (CAS) SCF[20] followed by second-order perturbation theory (CASPT2)[21] provides us more correct energy than the single-reference MP method because this method employs better reference wave function. Persson et al. reported that the CASPT2-calculated binding energies and molecular geometries of $Ni(CO)_4$, $Fe(CO)_5$, and $Cr(CO)_6$ agree very well with the experimental results.[22] However, this method cannot be applied to many organometallic reactions because it is difficult in general to employ active space in a

Table 3. Binding energy (kcal/mol) of ferrocene computed from the heterolytic dissociation $Fe(Cp)_2 \rightarrow Fe^{2+}(^1A'_1) + 2Cp^-$

	BS1[a]	BS2[a]	BS3[a]	BS4[a]
SCF	619	619	622	622
MP2	751	781	796	778
CASSCF	657	658	661	660
CASPT2	715	750	764	748
CASPT2 + BSSE[b]	680	711(712)[d]	719	717
CASPT2 + BSSE[b] + rc[c]	685	716(712)[d]	726	724
Exptl.		723±10		

Ref. 25

[a] BS1 = Fe [6s4p3d] C [3s2p1d] H [2s]
BS2 = Fe [6s4p3d1f] C [3s2p1d] H [2s]
BS3 = Fe [6s5p4d2f] C [3s2p1d] H [2s]
BS4 = Fe [6s5p4d2f] C [4s3p1d] H [2s]

[b] BSSE means basis set superposition error

[c] rc means relativistic correction

[d] Values within parentheses obtained with the ring BSSE computed in one step

consistent way throughout the reaction.

Coupled-cluster method[23] is another powerful post Hartree-Fock method. The coupled-cluster method presents correct results in many cases except for the system with large static correlation effects. Moreover, we do not need to choose the active space in the coupled-cluster method, unlike the CASSCF method. These mean the coupled-cluster method is robust compared with the methods described above. Actually, many computational results indicate the coupled-cluster method provides the correct energy changes for small molecules.[23b] However, it is considerably difficult to apply this method to large molecule due to the huge computational cost; for instance, the computational cost of coupled-cluster with single, double, and perturbative triple excitations, which is usually named CCSD(T) method,[24] increases seventh power of molecular size.

Here, it should be noted about the basis sets, which determine the space of wavefunction. Because organometallic compounds contain many electrons in relatively small area, the quality of basis sets considerably influences the accuracy of the calculation results. Pierloot et al. reported that the binding energy of ferrocene significantly depends on the basis sets, as shown in Table 3.[25] Their results indicate that the sufficiently large basis set including double-ζ f-polarization functions must be employed for Fe atom. Though the larger basis set obviously provides the better result, the use of large basis sets to organometallic compounds is usually difficult because the computational cost increases by fifth to seventh power of number of basis sets in the post Hartree-Fock methods such as MP2 to CCSD(T). It is still a big problem to compromise the accuracy and the size of basis sets in the study of organometallic compounds.

Considering the problems in the DFT method and multi-reference post Hartree-Fock methods, it is strongly desired to employ the coupled-cluster method in theoretical studies of organometallic compounds. Since the drawback of the coupled-cluster method is the computational cost, this method can be applied when the molecular size is reduced. One of the origins of large molecular size in organometallic compounds is the presence of bulky organic groups such as alkyl and aryl groups in the ligands. To reduce the molecular size, the simple replacement of such a large group with hydrogen atom is very often employed. Such a simple model, however, can reproduce neither the electronic effect nor steric effect of real substituent group, as expected. Therefore, the chemically reasonable modeling, in which both the electronic and steric effects are reproduced well, is indispensable to apply the highly sophisticated post Hartree-Fock method such as CCSD(T) to the large system including transition metal elements

4. Aims of This Thesis

In this thesis, the author wishes to report theoretical studies of organometallic reactions by modern electronic structure theory and the development of a new method which enables us to quantitatively evaluate the energy change of organometallic reactions.

In chapter 1, the author theoretically investigated the ruthenium(II)-catalyzed hydrogenation of carbon dioxide into formic acid[3,26] (eq. 1) with the DFT and MP4(SDQ) methods, where the real catalyst, *cis*-$Ru(H)_2(PMe_3)_3$, was employed in calculations and solvent effects were taken into consideration.

$$CO_2 + H_2 \xrightarrow[\text{supercritical } CO_2]{Ru(H)_2(PMe_3)_4} HCOOH \qquad (1)$$

Comparison between *cis*-$Ru(H)_2(PMe_3)_3$ and the PH_3 analogue which was previously employed as a model[27] provides us the knowledge of ligand effects in this catalytic reaction because PH_3 is considered a model of weakly electron-donating ligand such as phosphite but PMe_3 is a typical donating ligand. The purposes of chapter 1 are to present detailed knowledge of each elementary process, ligand effects, and solvent effects, and to provide theoretical answers about the rate-determining step and the pressure effects of dihydrogen molecule.

In chapter 2, the promotion effect[28] of small amount of water molecule in the ruthenium-catalyzed hydrogenation of the carbon dioxide (eq. 1) was theoretically investigated with the DFT and MP4(SDQ) methods. Though the plausible mechanism in the presence of water molecules is experimentally proposed as shown in Scheme 1,[28] the details of the mechanism is still not clear. The purposes in this chapter are to clarify the reaction mechanism in the presence of water molecules, to make comparison between the catalytic cycle in the absence of water molecules and that in the presence of

Scheme 1[28]

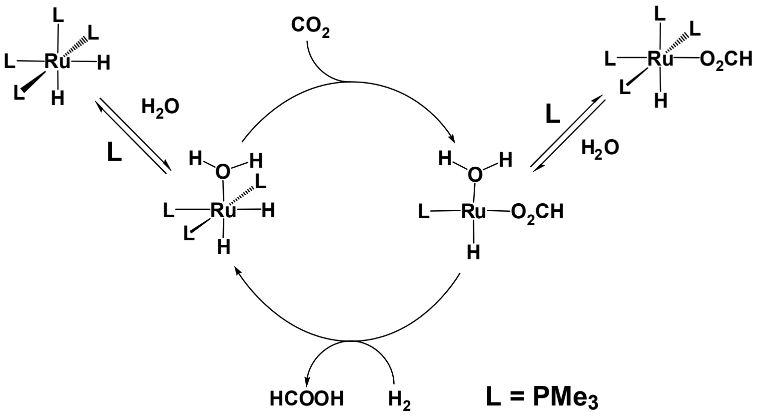

water molecules, and to provide theoretical answers to the questions how and why water molecules accelerates the reaction. Also, the author investigated if amine and alcohol accelerated this hydrogenation reaction.

In chapter 3, the H–H, CH_3–CH_3, and CH_3–CN bond activations by $Ni(PH_3)_2$ were theoretically investigated as a prototype reaction of σ-bond activation, as shown in Scheme 2. The purposes in this chapter are to clarify how much static and dynamical correlation effects are important in this type of reaction, what computational method should be applied to the reaction system including the first-row transition metal element, and what basis sets should be employed. Then, the author theoretically investigated the C–CN σ-bond activation of MeCN by $Ni(PH_3)_2$. The purposes of this part are to clarify the characteristic features of this C–CN σ-bond activation reaction and to present

Scheme 2

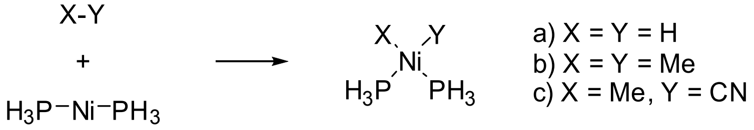

Scheme 3

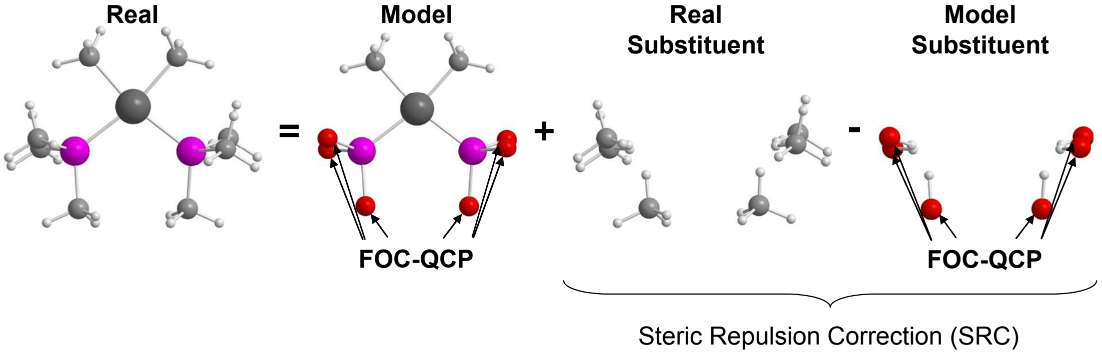

deep understanding of this reaction.

In chapter 4, a new method to construct chemically reasonable model of large organometallic compounds was presented. The author reported here the model for tertiary phosphine such as PMe_3, PEt_3, P^iPr_3, and P^tBu_3 because these phosphines are widely employed as ligands of many organometallic compounds.[29] In this method, the electronic and steric effects of bulky ligand are separately reproduced by the frontier orbital consistent quantum capping potential (FOC-QCP) method and steric repulsion correction (SRC), respectively, as shown in Scheme 3. As example, the monomerization energy of $[RhCl(P^iPr_3)_2]_2$ and the coordination energies of CO, H_2, N_2, and C_2H_4 with $[RhCl(P^iPr_3)_2]_2$ are theoretically calculated by the CCSD(T) method combined with the FOC-QCP + SRC. Those theoretical values agree well with the experimental values,[30] though the DFT-evaluated values do not always agree with the experimental ones.

In chapter 5, the author theoretically investigated the nickel(0)-catalyzed phenylcyanation of alkyne[31] (eq. 2) mainly by the DFT method and in part by the CCSD(T) method with the FOC-QCP + SRC, where PhCN and such alkynes as HC≡CH, MeC≡CH, $^iPrC\equiv CMe$, and $^tBuC\equiv CMe$ were employed as reactants. The purpose in this chapter is to elucidate the reaction mechanism, the rate-determining step, the regioselectivity of the reaction, and the determining factors of the reaction mechanism and the regioselectivity.

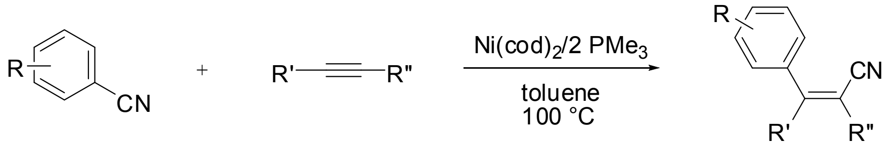

(2)

Through these studies, the author wishes to present deep understanding of organometallic reactions and construct a new computational method which can provide correct result of energetics of large organometallic systems.

References

(1) Weissermel, K.; Arpe, H. –J. *Industrial Organic Chemistry 4th Ed.*; Wiley: Weinheim, 2003.

(2) Wittcoff, H. A.; Reuben, B. G. *Industrial Organic Chemicals*; Wiley: New York, 1996.

(3) Komiya, S.; Ikariya, T. *Organometallic Chemistry - Full of Variety and Unexpectation*; Shokabo: Tokyo, 2004.

(4) Hegedus, L. S. *Transition Metals in the Synthesis of Complex Organic Molecules 2nd Ed.*; University Science Books: California, 1999.

(5) Jessop, P. G.; Ikariya, T.; Noyori, R. *Chem. Rev.* **1995**, *95*, 259-272.

(6) (a) Fryzuk, M. D.; Johnson, S. A. *Coord. Chem. Rev.* **2000**, *200-202*, 379-409. (b) Yandulov, D. V.; Shrock, R. R. *Science* **2003**, *301*, 76-78.

(7) (a) Shriver, D. F.; Atkins, P. W. *Inorganic Chemistry 3rd Ed.*; Oxford University Press: Oxford, 1999. (b) Cotton, F. A.; Wilkinson, G.; Gaus, P. L. *Basic Inorganic Chemistry 3rd Ed.*; Wiley: New York, 1995.

(8) Helgaker, T.; Jørgensen, P.; Olsen, J. *Molecular Electronic-Structure Theory*; Wiley: Chichester, 2000.

(9) Kohn, W.; Sham, L. J. *Phys. Rev.* **1965**, *140*, A 1133.

(10) Parr, R. G.; Yang, W. Density-Functional Theory of Atoms and Molecules; Oxford: New York, 1989.

(11) Koch, W.; Holthausen, M. C. *A Chemist's Guide to Density Functional Theory 2nd Ed.*; Wiley: Weinheim, 2001.

(12) Morokuma, K.; Musaev, D. J. *Computational Modeling for Homogeneous and Enzymatic Catalysis*; WILEY-VCH: Weinheim, 2008.

(13) Ziegler, T.; Autschbach, J. *Chem. Rev.* **2005**, *105*, 2695-2722.

(14) Zhao, Y.; Truhlar, D. G. *Acc. Chem. Res.* **2008**, *41*, 157-167 and references

therein.

(15) Ikeda, A.; Nakao, Y.; Sato, H.; Sakaki, S. *J. Phys. Chem. A* **2007**, *111*, 7142-7132.

(16) Møller, C.; Plesset, M. S.; *Phys. Rev.* **1934**, *46*, 618.

(17) Jensen, F. *Introduction to Computational Chemsitry, 2nd Ed.*; Wiley: Chichester, 2007.

(18) Sakaki, S.; Ohkubo, K. *J. Phys. Chem.* **1989**, *93*, 5655-5660.

(19) Hyla-Kryspin, I.; Koch, J.; Gleiter, R.; Klettke, T.; Walther, D. *Organometallics* **1998**, *17*, 4724-4733.

(20) Roos, B. O.; Taylor, P. R.; Siegbahn, P. E. M. *Chem. Phys.* **1980**, *48*, 157.

(21) Andersson, K.; Malmqvist, P. –Å.; Roos, B. O.; Sadlej, A. J.; *J. Phys. Chem.* **1990**, *94*, 5483-5488.

(22) Persson, B. J.; Roos, B. O.; Pierloot, K. *J. Chem. Phys.* **1994**, *101*, 6810-6821.

(23) (a) Crawford, T. D.; Schaefer III, H. F. *Rev. Comput. Chem.* **2000**, *14*, 33-136. (b) Bartlett, R. J.; Musial, M. *Mod. Rev. Phys.* **2007**, *79*, 291-352 and references therein.

(24) Raghavachari, K.; Trucks, G. W.; Pople, J. A.; Head-Gordin, M. *Chem. Phys. Lett.* **1987**, *157*, 479.

(25) Pierloot, K.; Persson, B. J.; Roos, B. O. *J. Phys. Chem.* **1995**, *99*, 3465-3472.

(26) (a) Jessop, P. G.; Ikariya, T.; Noyori, R. J. *Nature* **1994**, *368*, 231. (b) Jessop, P. G.; Hsiano, Y.; Ikariya, T.; Noyori, R. *J. Am. Chem. Soc.* **1994**, *116*, 8851.

(27) (a) Musashi, Y.; Sakaki, S. *J. Am. Chem. Soc.* **2000**, *122*, 3867. (b) Musashi, Y.; Sakaki, S. *J. Am. Chem. Soc.* **2002**, *124*, 7588.

(28) Jessop, P. G.; Ikariya, T.; Noyori, R. *J. Am. Chem. Soc.* **1996**, *118*, 344.

(29) Crabtree, R. H. *The Organometallic Chemistry of the Transition Metals 4th Ed.*; Wiley: New York, 2005.

(30) (a) Thorn, D. L.; Tulip, T. H.; Ibers, J. A. *J. Chem. Soc. Dalton Trans.* **1979**, 2022-2025. (b) Buesetto, C.; D'Alfonso, A.; Maspero, F.; Perego, G.; Zazzetta, A. *J. Chem. Soc. Dalton Trans.* **1977**, 1828-1834.

(31) (a) Nakao, Y.; Oda, S.; Hiyama, T. *J. Am. Chem. Soc.* **2004**, *126*, 13904. (b) Nakao, Y.; Oda, S.; Yada, A.; Hiyama, T. *Tetrahedron* **2006**, *62*, 7567.

Chapter 1

Ruthenium(II)-Catalyzed Hydrogenation of Carbon Dioxide to Formic Acid. Theoretical Study of Real Catalyst, Ligand Effects, and Solvation Effects

1.1. Introduction

Hydrogenation of carbon dioxide is one of the important and attractive subjects of research in recent transition-metal chemistry, catalytic chemistry, and organometallic chemistry.[1] This reaction was very previously carried out by Inoue and his collaborators in 1976,[2] while the turn over numbers reported were very small. In 1992 to 1994, several important studies were reported,[3-6] to our understanding. Tsai and Nicholas carried out the hydrogenation of carbon dioxide with $[Rh(NBD)(PMe_2Ph)_3]BF_4$ (NBD = norbornadiene).[3] They spectroscopically observed rhodium(III) hydride and rhodium(III) formate complexes such as $[Rh(H)_2(PMe_2Ph)_3(S)]BF_4$ (S = H_2O or THF), $[Rh(H)(PMe_2Ph)_2(\eta^2\text{-}O_2CH)]BF_4$, and $[Rh(H)(S)_n(PMe_2Ph)_{3-n}(\eta^1\text{-}O_2CH)]BF_4$ in the reaction solution. Based on their observation, they proposed that the hydrogenation reaction took place through insertion of carbon dioxide into the Rh(III)–H bond followed by reductive elimination of formic acid and oxidative addition of dihydrogen molecule to the Rh(I) center. Leitner and his collaborators succeeded the hydrogenation of carbon dioxide with a rhodium(I) hydride complex, $Rh(H)(diphos)_2$ (diphos = 1,2-bis(diphenylphosphino)ethane or 1,3-bis(diphenylphosphino)propane), as a catalyst.[4] In this reaction, a slightly different reaction mechanism was theoretically proposed by Hutschka et al.,[5] which consisted of

Scheme 1

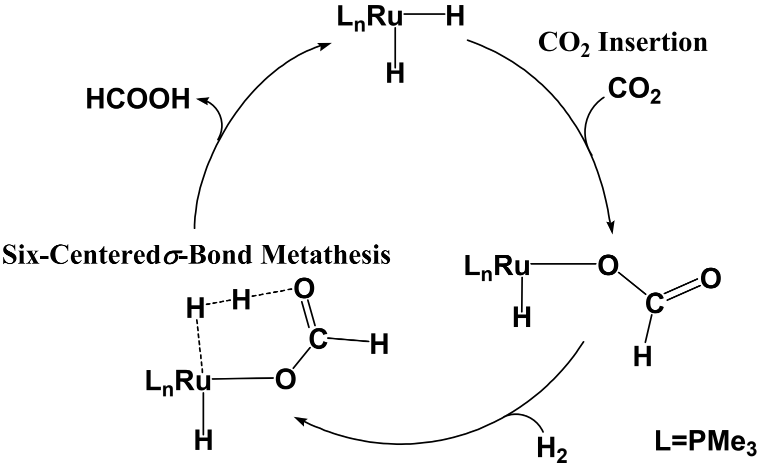

insertion of carbon dioxide into the Rh(I)–H bond followed by metathesis of the rhodium(I) η^1-formate complex with dihydrogen molecule. Jessop, Ikariya, and Noyori also succeeded in the ruthenium(II)-catalyzed hydrogenation of carbon dioxide.[6] This catalytic reaction is of particular importance because of the extremely high turnover numbers. From theoretical study, Musashi and Sakaki reported that this reaction took place through insertion of carbon dioxide into the Ru(II)–H bond and isomerization of a ruthenium(II) η^1-formate intermediate followed by metathesis of the ruthenium(II) η^1-formate intermediate with dihydrogen molecule, as shown in Scheme 1.[7] The same authors also reported that the rhodium(III)-catalyzed hydrogenation of carbon dioxide took place via the insertion of carbon dioxide into the Rh(III)–H bond followed by the reductive elimination of formic acid,[8] as experimentally proposed.[3] From these results of theoretical studies,[5,7-9] it is likely to consider that the reaction mechanism of transition-metal-catalyzed hydrogenation of carbon dioxide has been clearly elucidated. However, there remain important issues to be investigated theoretically. One of them is the rate-determining step in the ruthenium(II)-catalyzed hydrogenation of carbon dioxide. The dependence of the reaction rate on the pressure of dihydrogen molecule[6] suggests that the dihydrogen molecule participates in the rate-determining step. However, the theoretical study previously reported that the rate-determining step was the insertion of carbon dioxide into the Ru(II)–H bond.[7] This seeming discrepancy should be investigated in detail, because the difference in rate-determining step suggests the possibility that the theoretical study did not present correct results of the reaction mechanism. The next is solvent effects; although previous theoretical studies were carried out without consideration of solvent effects, the polarity of solvent is expected to influence the insertion of carbon dioxide into the metal–hydride bond and the metathesis of the metal-η^1-formate intermediate with dihydrogen molecule because their transition states are polarized. Also, not a real catalyst *cis*-$Ru(H)_2(PMe_3)_3$ but a model catalyst *cis*-$Ru(H)_2(PH_3)_3$ was employed in the previous theoretical works.[7,8] It is likely to consider that the computational results with a model system deviate from the correct features.

In this work, we theoretically investigated the ruthenium(II)-catalyzed hydrogenation of carbon dioxide into formic acid, where the real catalyst, *cis*-$Ru(H)_2(PMe_3)_3$, was employed in calculations and solvent effects were taken into consideration. Comparison between *cis*-$Ru(H)_2(PMe_3)_3$ and the PH_3 analogue provides us the knowledge of ligand effects in this catalytic reaction because PH_3 is considered a model of weakly electron-donating ligand such as phosphite but PMe_3 is a typical donating ligand. Our purposes here are to present detailed knowledge of each elementary process, ligand effects, and solvent effects, and to provide theoretical answers about the rate-determining step and the pressure effects of dihydrogen molecule. We wish to report the conclusive discussion on these issues.

1.2. Computations

Geometries were optimized with the DFT method, where the B3LYP functional was used for exchange-correlation term.[10,11] We ascertained that each optimized transition state exhibited one imaginary frequency and that the geometry changes induced by the imaginary frequency accorded with the reaction course (see Appendix Table A1 for geometries of intermediates and transition states). Energy and population changes were calculated with the DFT and MP2 to MP4(SDQ) methods. Solvation effects were evaluated with the DPCM method.[12]

Two kinds of basis set systems were used. The smaller system (BS-I) was employed in geometry optimization. In this BS-I system, core electrons of Ru (up to 3d) and P (up to 2p) were replaced with effective core potentials (ECPs), where (341/321/31) and (21/21/1) basis sets were employed for valence electrons of Ru[13] and P,[14,15] respectively. A 6-311G basis set augmented with a p-polarization function was employed for the hydride ligand, dihydrogen molecule, and the H atom of formate, where a usual 6-31G basis set was employed for the other H atoms.[16] For C and O, usual 6-31G(d) basis sets were employed.[17] The better basis set system (BS-II) was employed in evaluation of energy and population changes. In the BS-II system, a (541/541/211/1) basis set was used to represent valence electrons of Ru,[18,19] where the same ECPs as those of BS-I were employed for its core electrons. For C, O, and H, the 6-311+G(d) basis sets were used, while the usual 6-31G(d) basis sets were employed for the Me group of PMe_3. For P, the same basis set and ECPs as those of BS-I were used.

As will be shown below, the ruthenium(II) dihydride complex and ruthenium(II) η^1-formate complex form adducts with carbon dioxide and the dihydrogen molecule, respectively, in the catalytic cycle. In such processes, entropy effects should be taken into consideration. We evaluated entropy in two ways. In one way, translation, rotation, and vibration movements were considered to evaluate entropy and thermal energy, where all substrates were treated as ideal gas. The DFT/BS-I method was adopted to calculate vibration frequencies without scaling factor. In the other way, vibration movements were considered in evaluation of entropy but neither translation movements nor rotation ones were considered, since this reaction was carried out in supercritical carbon dioxide solvent in which the translation and rotation movements are considerably suppressed, compared to those in ideal gas. The free energy change estimated in this way is named ΔG_v^o hereafter. In the former estimation way, entropy significantly decreases when two molecules form an adduct, as expected. In the latter estimation way, on the other hand, entropy change is small, as will be discussed below. The former method apparently overestimates the entropy change and the thermal energy change of solution reaction, because translation and rotation movements are highly suppressed in solution. On the other hand, the latter one underestimates the entropy change and the thermal energy change because translation and rotation movements are not completely frozen in solution. A true value of free energy change would be intermediate between the ΔG^o value evaluated by the former method and the ΔG_v^o value by the latter one. Because this ambiguity remains in the estimation of entropy change and thermal energy change, we will discuss each elementary step with the usual potential energy changes and then discuss it with the free energy changes evaluated by these two ways.

Gaussian 98 program package was used for these calculations.[20] Population analysis was carried out with the method of Weinhold et al.[21] Contour map of molecular orbital was drawn with MOLEKEL program package.[22]

1.3. Results and Discussion

1.3.1. Insertion of Carbon Dioxide into the Ru(II)−H Bond

Carbon dioxide approaches the empty coordination site of *cis*-$Ru(H)_2(PMe_3)_3$ **1**, to afford a reactant complex, *cis*-$Ru(H)_2(PMe_3)_3(CO_2)$ **2**, as shown in Figure 1, in which two PMe_3 ligands exist in front of and behind the Ru center, respectively, but they are omitted for brevity in all figures. In **2**, the Ru−O and C−O distances are 2.657 and

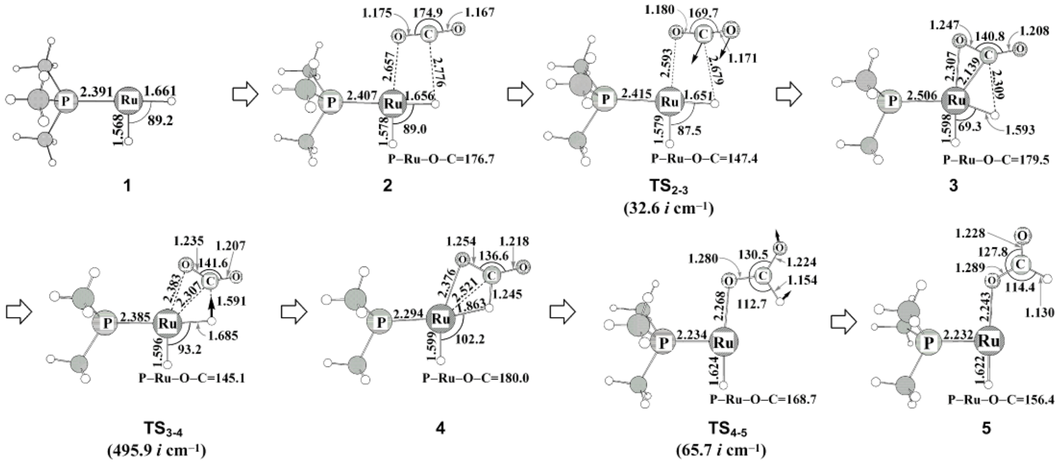

Figure 1. Geometry changes[a)] by the insertion of carbon dioxide into the Ru(II)-H bond of *cis*-$Ru(H)_2(PMe_3)_3$

Bond length in angstrom and bond angle in degree. In parenthesis is imaginary frequency of each transition state. Arrows in $\mathbf{TS_{2\text{-}3}}$ and $\mathbf{TS_{3\text{-}4}}$ represent geometry changes involved in each imaginary frequency.

a) Two PMe_3 ligands in front of and behind the Ru center are omitted in all the figures to show clearly the geometry changes by the reaction.

2.776 Å, respectively, and the OCO angle slightly decreases by about 5°. These geometrical features indicate that carbon dioxide weakly interacts with the Ru center. Starting from **2**, carbon dioxide further approaches the Ru center through the transition state $\mathbf{TS_{2\text{-}3}}$, to afford an intermediate, *cis*-$Ru(H)_2(PMe_3)_3(\eta^2\text{-}CO_2)$ **3**. Carbon dioxide has not been inserted into the Ru(II)−H bond in **3**, because the C−H distance between the H ligand and carbon dioxide is still very long (2.309 Å) in **3**. Thus, **3** is characterized as a ruthenium(II) complex of carbon dioxide. Actually, the geometrical features of **3** agree well with those of the usual transition-metal carbon dioxide complexes with a η^2-coordination structure;[23-26] for instance, the OCO angle considerably decreases to 141°, the C=O double bond that coordinates with the Ru center somewhat lengthens to 1.247 Å by 0.08 Å, and the Ru−C distance is considerably shorter than the Ru−O distance in **3**. These geometrical features are easily interpreted in terms of the charge-transfer (CT) interaction between the π* orbital of carbon dioxide

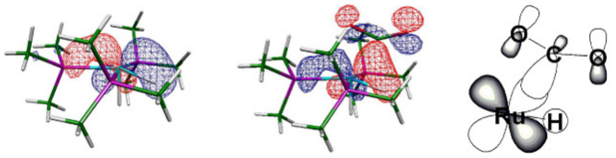

(A) HOMOs of $Ru(H)_2(PMe_3)_3$ (left) and $Ru(H)_2(PMe_3)_3(CO_2)$ (right)

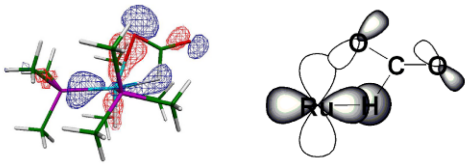

(B) Agostic interaction between the C−H bond of formate and d_σ orbital of Ru

Figure 2. Several important orbitals$^{a)}$ in *cis*-$Ru(H_2)(PMe_3)_3(CO_2)$ and $Ru(H)(\eta^1\text{-}OCOH)(PMe_3)_3$. a) The wavefunction surface with the value of 0.05e is plotted.

and the doubly occupied d_π orbital of the Ru center, as follows: Because the Ru(II) atom takes a d^6 electron configuration in **3**, the d_π orbital mainly contributes to the HOMO of *cis*-$Ru(H)_2(PMe_3)_3$, which overlaps well with the π* orbital of CO_2 in a bonding way, as shown in Figure 2A. This CT interaction increases the electron population of the π* orbital, which lengthens the C−O bond and decreases the O−C−O angle. The shorter Ru−C bond than the Ru−O bond results from the fact that the p orbital of the C atom more contributes to the π* orbital of CO_2 than does that of the O atom.

The next step is the insertion of carbon dioxide into the Ru(II)−H bond, which takes place through the transition state $\mathbf{TS_{3\text{-}4}}$ to afford a ruthenium(II) η^1-formate intermediate, $Ru(H)(\eta^1\text{-}OCOH)(PMe_3)_3$ **4**. In $\mathbf{TS_{3\text{-}4}}$, the H ligand is approaching the C atom of carbon dioxide and the C−H distance considerably shortens to 1.591 Å. The Ru−H distance moderately lengthens to 1.685 Å, while the OCO angle little changes. In **4**, the C−H bond distance (1.245 Å) of formate is somewhat longer than the usual C−H bond (1.130 Å) of formic acid by about 0.1 Å. These rather long C−H and rather short Ru−H distances suggest that a bonding interaction still exists between the Ru

Table 1. Energy changes[a)] by the interaction of carbon dioxide with the Ru center and the insertion of carbon dioxide into the Ru(II)−H bond of *cis*-$Ru(H)_2(PMe_3)_3$, the coordination of dihydrogen molecule with Ru(H)(η^1-OCOH)$(PMe_3)_3$ **5**, isomerization of the η^1-formate moiety in Ru(H)(η^1-OCOH)$(PMe_3)_3(H_2)$, and the metathesis of the η^1-formate complex with dihydrogen molecule.

	DFT	MP2	MP3	MP4(DQ)	MP4(SDQ)
Coordination of CO_2 with the Ru center					
$\Delta E(\mathbf{1}\rightarrow\mathbf{2})$	−3.2	−17.7	−12.8	−15.2	−16.5
$E_a(\mathbf{2}\rightarrow\mathbf{3})$	−0.2	−3.3	−0.9	−1.9	−2.4
$\Delta E(\mathbf{2}\rightarrow\mathbf{3})$	−7.4	−32.5	−9.7	−20.9	−21.5
Insertion of CO_2 into the Ru(II)−H bond					
$E_a(\mathbf{3}\rightarrow\mathbf{4})$	7.2	26.6	5.9	18.5	17.6
$\Delta E(\mathbf{3}\rightarrow\mathbf{4})$	4.6	32.4	0.7	18.1	17.9
Isomerization of the η^1-formate moiety					
$E_a(\mathbf{4}\rightarrow\mathbf{5})$	1.8	5.2	0.3	2.2	3.2
$\Delta E(\mathbf{4}\rightarrow\mathbf{5})$	1.4	6.1	0.4	2.5	3.8
Coordination of H_2 with the Ru center of **5**					
$\Delta E(\mathbf{5}\rightarrow\mathbf{6})$	18.3	31.7	24.1	27.7	28.0
Isomerization of the η^1-formate moiety in **6**					
$E_a(\mathbf{6}\rightarrow\mathbf{7})$	−2.6	−0.6	−2.7	−1.5	−1.3
$\Delta E(\mathbf{6}\rightarrow\mathbf{7})$	−5.8	−3.1	−5.9	−2.5	−2.6
Metathesis of the η^1-formate complex with dihydrogen molecule					
$E_a(\mathbf{7}\rightarrow\mathbf{8})$	5.5	7.9	11.3	9.5	9.0
$\Delta E(\mathbf{7}\rightarrow\mathbf{8})$	5.1	8.4	12.4	8.5	8.7

a) kcal/mol unit. The BS-II system was used for these calculations.

center and the C−H bond like the agostic interaction. Certainly, the 1s orbital of the H atom overlaps well with the unoccupied d_σ orbital of the Ru center, as shown in Figure 2B. The H atomic population is smaller than that of the usual H atom of formate, as will be discussed below. Besides **4**, there is the other isomer of the ruthenium(II) η^1-formate intermediate **5**, which is formed from **4** through the transition state $\mathbf{TS_{4\text{-}5}}$. In $\mathbf{TS_{4\text{-}5}}$, the η^1-formate moiety rotates counterclockwise, which weakens the agostic

Table 2. Comparison of computational methods in the coordination of carbon dioxide with the Ru center and the insertion of carbon dioxide into the Ru(II)−H bond of model system, *cis*-$Ru(H)_2(PH_3)_3$

	$\Delta E(\mathbf{1} \rightarrow \mathbf{3})$ (kcal/mol)	$E_a(\mathbf{3} \rightarrow \mathbf{4})$ (kcal/mol)
DFT	−1.17	5.9
MP2	−36.4	24.5
MP3	−10.6	4.5
MP4(D)	−25.7	17.2
MP4(DQ)	−22.9	16.3
MP4(SDQ)	−25.0	15.7
CCSD	−16.7	8.9
CCSD(T)	−23.4	11.6

a) $\Delta E(\mathbf{1}\rightarrow\mathbf{3})$ is the stabilization energy of **3** relative to **1**, where a negative value means that **3** is more stable than **1**. b) E_a represents the energy difference between **3** and $\mathbf{TS_{3\text{-}4}}$.

interaction between the C−H bond and the Ru center. The intermediate **5** is coordinatively unsaturated, in which the C−H bond does not interact with the Ru center and the η^1-formate moiety coordinates well with the Ru center; as a result, the Ru−O and C−H distances (2.243 and 1.130 Å, respectively) are considerably shorter than those of **4**.

Energy changes by the insertion reaction were evaluated with the DFT and MP2 to MP4(SDQ) methods, as listed in Table 1. The MP4(SDQ) method presents considerably larger stabilization energy by coordination of carbon dioxide, $\Delta E(\mathbf{1}\rightarrow\mathbf{2})$ and $\Delta E(\mathbf{2}\rightarrow\mathbf{3})$, and considerably larger activation barrier $E_a(\mathbf{3}\rightarrow\mathbf{4})$ and reaction energy $\Delta E(\mathbf{3}\rightarrow\mathbf{4})$ of the CO_2 insertion than does the DFT method, while these two methods present similar energy changes in the other elementary processes. Although these values somewhat fluctuate around MP2 and MP3 levels of theory, they less fluctuate upon going to MP4(SDQ) from MP3, and the MP4(SDQ) calculated values are intermediate between the MP2 and MP3 calculated values. To examine the reliabilities of DFT and MP4(SDQ) methods, the CCSD(T) method was applied to the insertion of carbon dioxide into the Ru(II)−H bond of the model system, *cis*-$Ru(H)_2(PH_3)_3$, because the real system is too large for us to perform the CCSD(T) calculation. The geometries of the model system were taken to be the same as those of the real system, where three PMe_3 ligands were replaced with three PH_3 ligands. As shown in Table 2, the DFT method presents much smaller reaction energy $\Delta E(\mathbf{1}\rightarrow\mathbf{3})$ and activation barrier $E_a(\mathbf{3}\rightarrow\mathbf{4})$ than does the CCSD(T) method, while the MP4(SDQ) method presents similar reaction energy $\Delta E(\mathbf{1}\rightarrow\mathbf{3})$ to that of the CCSD(T) method and moderately larger activation barrier $E_a(\mathbf{3}\rightarrow\mathbf{4})$ than that of the CCSD(T) method. These results suggest that the MP4(SDQ) method seems better than the DFT method in the present catalytic reaction. In this work, we will discuss the results based on both DFT and MP4(SDQ) methods.

The DFT and MP4(SDQ) calculated energy changes with correction of zero-point energy and free energy changes are shown in Figure 3A and B, respectively. Apparently, the activation barrier going to **3** from **2** disappears in both the DFT/BS-II and MP4(SDQ)/BS-II calculations.[27] Thus, the CO_2 complex **2** is not important and the coordination of carbon dioxide with the Ru center directly afford **3**. The free energy change ($\Delta G_v°$) with only the contribution of vibration movements is −37.1 (−9.0) kcal/mol, which is somewhat smaller than the change in ΔE, where the value without parenthesis is the MP4(SDQ) calculated one and in parentheses is the DFT calculated one, hereafter. The free energy change $\Delta G°$ in gas phase is −28.9 (−0.8) kcal/mol. This value is much smaller than the $\Delta G_v°$ value, because the adduct **3** is formed from **1** and CO_2 in this coordination process. In the CO_2 insertion into the Ru(II)−H bond, the activation barrier is 16.1 (5.6) kcal/mol, and the activation free energy changes are 16.7 (6.2) and 16.7 (6.1) kcal/mol for $\Delta G_v^{\circ\ddagger}$ and $\Delta G^{\circ\ddagger}$, respectively. These results clearly indicate that the insertion reaction takes place with moderate activation energy. However, the reverse de-insertion reaction of carbon dioxide more

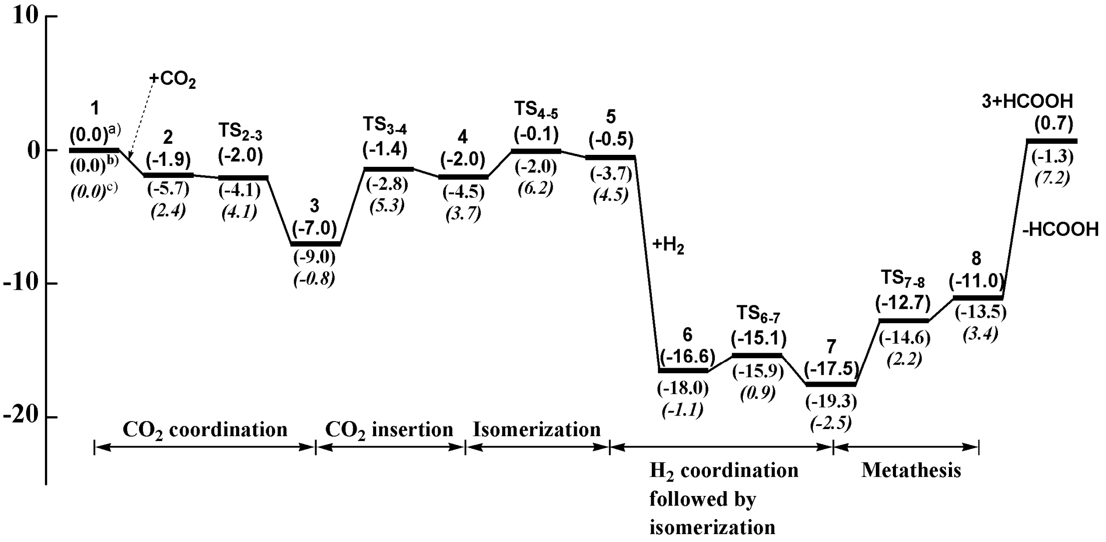

(A) DFT-calculated energy change

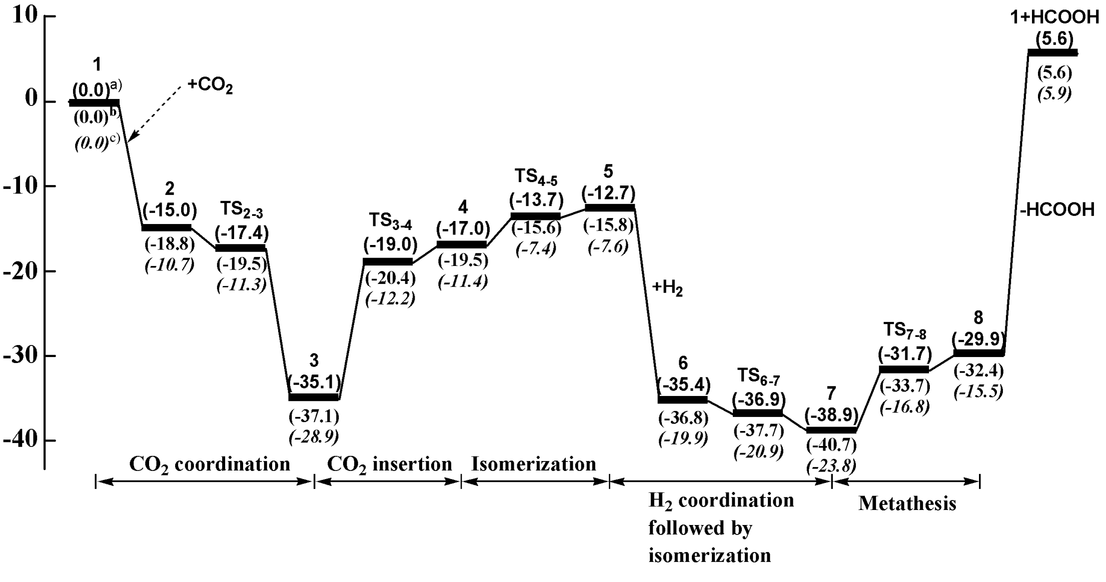

(B) MP4(SDQ)-calculated energy change

Figure 3. Potential energy change[a)] and free energy change[b,c)] (kcal/mol unit) along the catalytic cycle

a) Potential energy change with correction of zero-point energy. b) In the $\Delta G°$ value, contributions of translation, rotation, and vibration movements are considered. c) In the $\Delta G_{\mathrm{v}}°$ value, contributions of vibration movements are considered, while those of translation and rotation movements are neglected.

easily takes place with smaller activation barrier than does the insertion because the insertion is considerably endothermic. This means that the next step must proceed easily to complete the catalytic cycle; if not, the deinsertion of carbon dioxide takes place easily. The next step is the isomerization from **4** to **5**. However, this isomerization is endothermic and can not suppress the deinsertion; note that the intermediate **5** is slightly less stable than **4**. Thus, the coordination of dihydrogen molecule should occur to suppress the deinsertion of carbon dioxide, as will be discussed below in detail. Although the considerable differences in energy change are observed between the DFT and MP4(SDQ) methods, both methods clearly show that the dihydrogen molecule must coordinate with the Ru center to suppress the deinsertion, as shown in Figure 3.

It should be noted that carbon dioxide is inserted into the Ru(II)−H bond of *cis*-$Ru(H)_2(PMe_3)_3$ with moderately smaller activation barrier (7.2 kcal/mol) than that (9.5 kcal/mol) of the insertion reaction in *cis*-$Ru(H)_2(PH_3)_3$, where the activation barriers calculated with the DFT method are given without correction of zero-point energy because the DFT method was used in the previous work.[7] In other words, the donating PMe_3 ligand is more favorable for the insertion of carbon dioxide into the Ru(II)−H bond than the PH_3 ligand. The reason will be discussed below in detail.

1.3.2. Metathesis of the Ruthenium(II)-η^1-formate Intermediate, Ru(H)(η^1-OCOH)(PMe_3)$_3$ 5, with Dihydrogen Molecule

The next step is coordination of dihydrogen molecule with the Ru center of **5** followed by the metathesis of the ruthenium(II) η^1-formate intermediate with the dihydrogen molecule. Dihydrogen molecule easily coordinates with the Ru center of **5** to afford a ruthenium(II) complex of dihydrogen molecule, Ru(H)(η^1-OCOH)-$(PMe_3)_3(H_2)$ **6**, as shown in Figure 4, because **5** possesses an empty coordination site.

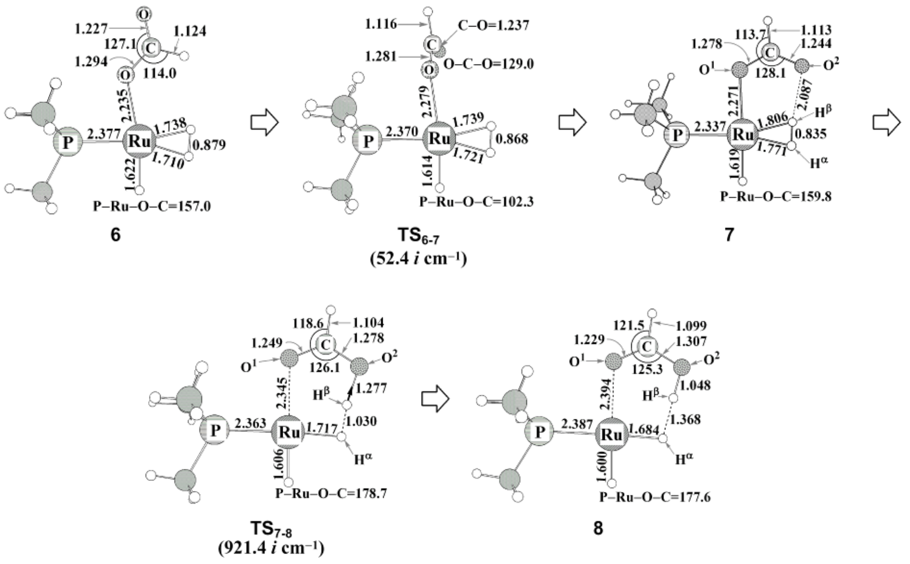

Figure 4. Geometry changes by the isomerization of the ruthenium(II)-formate complex, Ru(H)(η^1-OCOH)(PMe$_3$)$_3$, and the metathesis of Ru(H)(η^1-OCOH)(PMe$_3$)$_3$ with dihydrogen molecule[a)]

Bond length in angstrom and bond angle in degree. In parenthesis is imaginary frequency of the transition state. Arrows in **TS$_{6\text{-}7}$** and **TS$_{7\text{-}8}$** represent geometry changes involved in each imaginary frequency. a) Two PMe$_3$ ligands in front of and behind the Ru center are omitted in all the figures to show clearly the geometry changes by the reaction.

In **6**, the distances between the Ru center and two H atoms of dihydrogen molecule are 1.738 and 1.710 Å, and the H−H distance (0.879 Å) is considerably longer than the equilibrium distance (0.744 Å by the DFT/BS-I calculation). These geometrical features indicate that the dihydrogen molecule strongly coordinates with the Ru center, as will be shown below by the large stabilization energy.

However, the metathesis can not take place directly from **6**, because any hydrogen atom of the dihydrogen molecule can not approach the O atom of formate due to the unfavorable conformation of the formate moiety.[28] Thus, **6** must isomerize to **7** in which one of the oxygen atoms of formate takes a position near to the dihydrogen molecule (see Figure 4). In **TS$_{6\text{-}7}$**, the formate moiety is almost perpendicular to the

O−Ru−(H_2) plane. From **7**, the H−H bond breaking occurs through the transition state **TS_{7-8}**, to afford a ruthenium(II) complex of formic acid, $Ru(H)_2(HCOOH)(PMe_3)_3$ **8**. In **TS_{7-8}**, the H^{β} atom is moving from the H^{α} atom to the O atom of the formate moiety; see Figure 4 for H^{α} and H^{β}. The Ru−H^{α} distance considerably shortens to 1.717 Å and the position of the H^{β} atom is almost intermediate between O and H^{α} atoms. This geometry of **TS_{7-8}** is essentially the same as that of the heterolytic C−H σ-bond activation of benzene by the palladium(II)−formate complex.[29] In **8**, the O−H bond distance of formic acid is 1.048 Å, which is considerably longer than the usual O−H bond distance (0.973 Å) of free formic acid. Consistent with this long O−H bond distance, the H^{α}−H^{β} distance (1.368 Å) between formic acid and the H^{α} ligand is rather short, which indicates that some bonding interaction still exists between these two atoms, as will be discussed below. The Ru−O bond distance is 2.394 Å, which is considerably longer than that of **7**. This is interpreted in terms of the change of formate to formic acid, as follows: The formate anion in **7** possesses the C−O^1 single bond and the C=O^2 double bond in a formal sense, because the C−O^1 bond is much longer than the C−O^2 bond. Thus, the O^1 atom, which is more negatively charged than the O^2 atom, coordinates with the Ru center in **7**. In **8**, on the other hand, the C−O^1 bond becomes a double bond and the C−O^2 bond becomes a single bond because the H atom is bound with the O^2 atom. In other words, the O^1 atom possesses −1 formal charge in **7**, but it is neutral in **8** in a formal sense. As a result, the η^1-formate ligand much more strongly coordinates with the Ru center in **7** than does formic acid in **8**, which leads to the longer Ru−O^1 distance in **8** than in **7**.

Now, we wish to discuss the energy changes along these processes. As suggested from the geometry of **6**, the coordination of the dihydrogen molecule induces considerably large stabilization energy. Although significantly large differences between the DFT and MP4(SDQ) methods are not observed in energy changes of metathesis, the DFT method underestimates the stabilization energy by the coordination of dihydrogen molecule with the Ru center, compared with the MP4(SDQ) method, as listed in Table 1. The stabilization energy converges to ca. 28 kcal/mol upon going to MP4(SDQ) from MP3. Considering these results and the stabilization energy by the coordination of carbon dioxide with **1** (see above), the MP4(SDQ) method seems better than the DFT method in evaluating the stabilization energy by the coordination of dihydrogen molecule. However, both DFT and MP4(SDQ) methods lead to the same conclusion about the reaction mechanism, as will be shown below.

As shown in Figure 3, **5** undergoes the coordination of dihydrogen molecule with significantly large free energy decrease; the free energy change ($\Delta G_v°$) with only contribution of vibration movements is −21.0 (−14.3) kcal/mol and the usual free energy change ($\Delta G°$) is −12.3 (−5.6) kcal/mol. It should be noted that the $\Delta G°$ value is considerably negative even in the gas phase. As discussed above, the stabilization of **5** is necessary to suppress the deinsertion of carbon dioxide, because the deinsertion more easily occurs with a smaller activation barrier than does the insertion (vide supra). If the concentration of the dihydrogen molecule was not sufficiently large, **5** could not easily undergo the coordination of the dihydrogen molecule, and as a result, the deinsertion took place. Therefore, the catalytic reaction is suppressed when the dihydrogen molecule is not sufficiently supplied. This means that the reaction rate depends on the pressure of the dihydrogen molecule, as reported experimentally.[6b,c]

The next step is the isomerization of the ruthenium(II)-η^1-formate intermediate from **6** to **7**. The DFT/BS-II and MP2 to MP4(SDQ)/BS-II methods present negative activation barrier, probably because of some artificial error. However, it is reasonably concluded that this isomerization easily occurs with nearly no barrier. The nearly no activation barrier is not surprising because this isomerization takes place through the rotation of the formate moiety around the C−O^1 bond, as shown in Scheme 2A.

Scheme 2

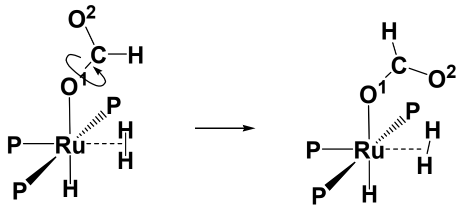

(A) Isomerization of Ru(H)(η^1-OCOH)(PMe_3)$_3$(H_2)

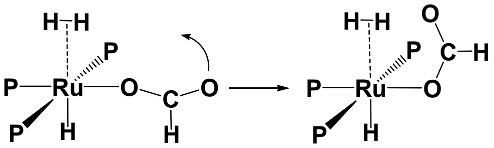

(B) Isomerization of Ru(H)(η^1-OCOH)(PH_3)$_3$(H_2)

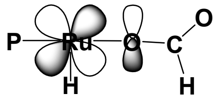

(C) Exchange repulsion between d_π orbital of Ru and lone pair orbital of η^1-formate

Finally, the H−H bond breaking takes place with the E_a value of 7.2 (4.7) kcal/mol and the $\Delta G^{\circ\ddagger}$ and $\Delta G_v^{\circ\ddagger}$ values of 7.0 (4.7) kcal/mol. Because these E_a and $\Delta G^{\circ\ddagger}$ values are smaller than those of the insertion reaction in both DFT and MP4(SDQ) calculations, it should be concluded that the insertion of carbon dioxide into the Ru(II)−H bond is the rate-determining step.

1.3.3. Energy Changes along Whole Catalytic Cycle and Solvent Effects

Here, we wish to summarize the energy changes along the catalytic cycle. Apparently, the MP4(SDQ) method provides the substantially larger stabilization energy by the coordination of carbon dioxide (**1** → **3**) and dihydrogen molecule (**5** → **6**) and the substantially larger activation barrier and endothermicity of the CO_2 insertion (**3** → **5**) than does the DFT method, while the energy changes in the other elementary steps

Table 3. Solvation effects on the free energy changes[a)] of important elementary steps

	Gas phase		*n*-heptane		THF	
	$\Delta G_v^{\circ\ddagger}$	$\Delta G_v^{0\circ}$	$\Delta G_v^{\circ\ddagger}$	ΔG_v°	$\Delta G_v^{\circ\ddagger}$	ΔG_v°
CO_2 Coordination						
2 → 3	1.6	−3.3	−1.8	−9.8	1.5	−10.7
CO_2 insertion						
3 → 4	6.2	4.5	5.4	3.4	5.3	2.5
Isomerization of formate in $Ru(H)(\eta^1\text{-}OCOH)(PMe_3)_2$						
4 → 5	2.5	0.8	1.0	0.7	0.4	0.2
Coordination of dihydrogen molecule						
5 → 6		−14.3		−12.0		−16.4
Isomerization of formate in $Ru(H)(\eta^1\text{-}OCOH)(PMe_3)_2(H_2)$						
6 → 7	2.1	−1.3	−1.9	−4.9	0.2	−3.3
Metathesis with heterolytic H−H bond activation						
7 → 8	4.7	5.8	6.3	8.5	7.4	10.0

a) ΔG_v° values (in kcal/mol) are provided here. In parentheses are ΔG° value (in kcal/mol). The DFT/BS-II method was employed to evaluate the electronic energy.

are not different very much. Despite the above mentioned differences, both methods show common features in energy changes; (1) the coordination of carbon dioxide with the Ru center is exothermic, (2) the insertion of carbon dioxide into the Ru(II)−H bond followed by the isomerization of the η^1-formate is endothermic, (3) the rate-determining step is the insertion of carbon dioxide into the Ru(II)−H bond, and (4) the coordination of dihydrogen molecule is considerably exothermic enough to suppress the deinsertion.

Solvent effects were evaluated with the DPCM method,[12] where *n*-heptane was selected because super critical carbon dioxide is considered to be similar to normal alkane. Also, solvent effects by THF were investigated to present some information about the use of polar solvent. Interestingly, the activation barrier of the metathesis considerably increases in the order gas phase < *n*-heptane < THF, as shown in Table 3, while the activation barrier and the reaction energy of the CO_2 insertion moderately

Scheme 3

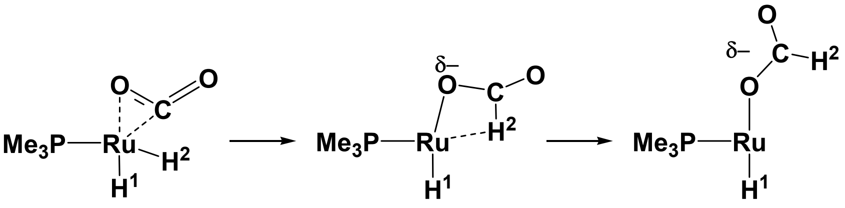

	3	**$TS_{3\text{-}4}$**	**4**	**$TS_{4\text{-}5}$**	**5**
Dipole moment	6.47 D	6.27 D	7.52 D	8.24 D	8.10 D
Natural charge	H^1 = 0.004 H^2 = 0.023 $CO_2 + H^2$ = -0.417		H^1 = -0.062 H^2 = 0.014 $OCOH^2$ = -0.588		H^1 = -0.128 H^2 = 0.019 $OCOH^2$ = -0.794

decrease in the order gas phase > *n*-heptane > THF.[30]

It is worthy of investigation to clarify the reason that the metathesis (**7→8**) becomes difficult in polar solvent. This is easily interpreted in terms that **7** consists of the anionic formate and the positively charged Ru moieties but **8** consists of neutral formic acid and the neutral Ru moieties in a formal sense; in other words, the highly polar species converts to the less polar species in the metathesis. Thus, the polar solvent is not favorable for the metathesis. It is also interesting that the activation barrier of the CO_2 insertion into the Ru(II)−H bond moderately decreases in the order gas phase > *n*-heptane > THF, while the reaction energies ΔE(**3→4**) and ΔE(**4→5**) decrease in the order gas phase > *n*-heptane > THF to a greater extent than does E_a(**3→4**). This is interpreted in terms that the transition state $\mathbf{TS_{3\text{-}4}}$ is similar to the intermediate **3**; actually, the dipole moments of **3** and $\mathbf{TS_{3\text{-}4}}$ are 6.47 and 6.27 D, as shown in Scheme 3. In other words, the ruthenium(II) η^2-carbon dioxide complex **3** contains the considerably strong CT interaction between the π* orbital of CO_2 and the d_π orbital of Ru, the strength of which is similar to that of the polarized $\mathbf{TS_{3\text{-}4}}$.[31] Upon going to **4** from $\mathbf{TS_{3\text{-}4}}$, dipole moment considerably increases, because the charge transfer becomes considerably strong in **4**. As a result, polar solvent such as THF

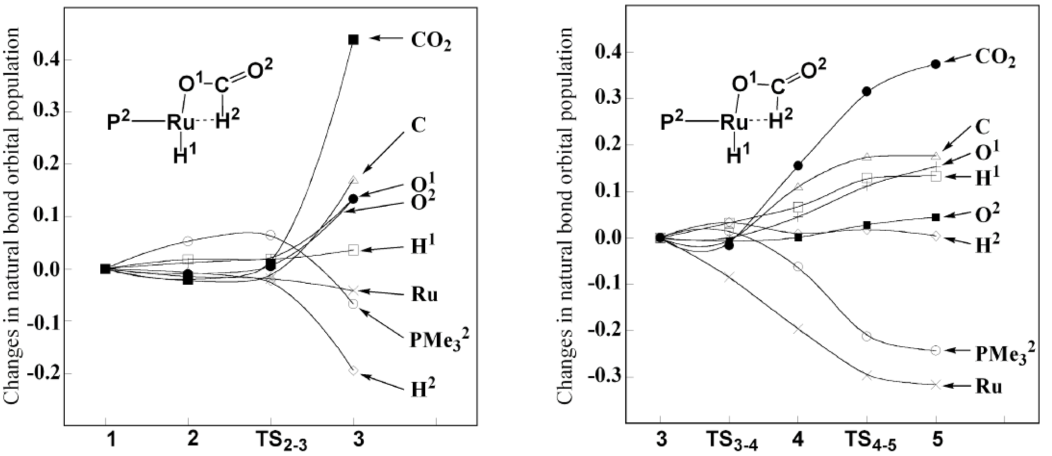

(A) Coordination of CO_2 (B) CO_2 insertion into the Ru(II)-H bond

Figure 5. Population changes[a)] in the coordination of carbon dioxide with the Ru center and the insertion reaction of carbon dioxide into the Ru(II)−H bond
a) NBO populations are shown here. The positive value represents the increase in electron population, and vice versa.

decreases the reaction energy Δ*E*(**3**→**4**) to a greater extent than E_a(**3**→**4**) (see Table 3). Upon going to **5** from **4**, the dipole moment further increases, and therefore, polar solvent decreases E_a(**4**→**5**) and Δ*E*(**4**→**5**). This is because the anionic η^1-formate takes a position more distant from the positively charged Ru center in **5** than in **4**. Considering these solvent effects, the polar solvent facilitates the CO_2 insertion reaction.

1.3.4. Population Changes and Electronic Process in the Insertion Reaction and Their Differences between the PMe_3 Complex and the PH_3 Analogue

Although significant differences in reaction behavior between PMe_3 and PH_3 have not been reported in the transition-metal complexes of dihydrogen molecule[32] and the oxidative addition of dihydrogen molecule to $Pt(PR_3)_2$,[33] it is worthwhile to discuss here the differences in the CO_2 insertion reaction between the PMe_3 and PH_3 complexes. The differences are summarized, as follows. (1) The ruthenium(II) complex of carbon dioxide **3** exists as an intermediate in the PMe_3 system, while it did not exist in the PH_3 system.[7] (2) The η^1-OCOH moiety takes a position trans to PH_3 in $Ru(H)(\eta^1\text{-OCOH})(PH_3)_3$, while it is at a position trans to the H(hydride) ligand in $Ru(H)(\eta^1\text{-OCOH})(PMe_3)_3$. And, (3) the insertion reaction takes place with the moderately smaller activation barrier in the PMe_3 system than in the PH_3 system.

Electron populations are useful to find reasons of these differences. The electron population of carbon dioxide considerably increases upon going to **3** from **1**, as shown in Figure 5A. The increase in electron population of carbon dioxide is in general observed in the coordination of carbon dioxide with the transition-metal complex, because the charge-transfer from the metal center to carbon dioxide mainly contributes to the coordinate bond of carbon dioxide with the metal center.[26] In **3**, the π^* orbital of carbon dioxide overlaps well with the d_π orbital of the Ru center, as discussed above and in Figure 2A. This π-back donation is stronger in *cis*-$Ru(H)_2(PMe_3)_3(CO_2)$ than in the PH_3 analogue, because PMe_3 is more donating than PH_3, as shown by their lone pair orbital energies; the lone pair orbital of PMe_3 is at −8.91 (−6.00) eV and that of PH_3 is at −10.54 (−7.57) eV, where the values without parentheses are Hartree−Fock orbital energies and in parentheses are Kohn−Sham orbital energies. As a result, *cis*-$Ru(H)_2(PMe_3)_3(CO_2)$ exists as a stable intermediate but the PH_3 analogue does not. However, the Ru atomic population little decreases in **3**, unexpectedly, while the electron populations of the H and $PMe_3{}^2$ ligands decrease in **3**. Because the C−H distance is very long, the direct interaction between the H ligand and carbon dioxide is not formed. It is likely to consider that the charge-transfer from the Ru center to carbon dioxide occurs and the Ru center is supplied electron density by the H and $PMe_3{}^2$ ligands.

In the insertion reaction, the electron population of carbon dioxide further increases, while the electron populations of the Ru center and $PMe_3{}^2$ decrease, as shown in Figure 5B. These population changes clearly show that the charge-transfer from $Ru(H)_2(PMe_3)_3$ to carbon dioxide significantly occurs in the insertion reaction, as reported previously.[34] Because PMe_3 possesses its lone pair orbital at a higher energy than that of PH_3 (see above), the PMe_3 complex is more favorable for this charge-transfer than the PH_3 complex, as follows: (1) The H^2 atomic population is 1.172e in *cis*-$Ru(H)_2(PMe_3)_3$ and 1.115e in *cis*-$Ru(H)_2(PMe_3)_3$. (2) The molecular orbital $\varphi(H_{1s})$, that mainly consists of the 1s orbital of the H ligand, participates in the charge transfer to carbon dioxide. This $\varphi(H_{1s})$ orbital is at a −8.61 (−5.82) eV in *cis*-$Ru(H)_2(PMe_3)_3$ but at −9.44 (−6.76) eV in *cis*-$Ru(H)_2(PH_3)_3$, where the values without parentheses are Hartree−Fock orbital energies (HF/BS-II) and those in parentheses are Kohn−Sham orbital energies (DFT/BS-II). And, (3) the Ru(II)−H bond is weaker in *cis*-$Ru(H)_2(PMe_3)_3$ than in *cis*-$Ru(H)_2(PH_3)_3$, because of the stronger trans influence of PMe_3 than that of PH_3; actually, the Ru(II)−H bond (1.661Å) is considerably longer in *cis*-$Ru(H)_2(PMe_3)_3$ than that (1.641Å) in *cis*-$Ru(H)_2(PH_3)_3$. From all these factors, carbon dioxide is more easily inserted into the Ru(II)−H bond in *cis*-$Ru(H)_2(PMe_3)_3$ than in *cis*-$Ru(H)_2(PH_3)_3$. We wish to mention here that the H^2 atomic population little changes upon going to **4** from **3**, unexpectedly, despite the charge transfer from $Ru(H)_2(PMe_3)_3$ to carbon dioxide. This result is interpreted in terms that the H^2 ligand is supplied electron density by the Ru center and $PMe_3{}^2$.

The difference in geometry between $Ru(H)(\eta^1\text{-OCOH})(PMe_3)_3$ and the PH_3 analogue is also understood in terms of the trans-influence of PMe_3 and PH_3. Because the H ligand exhibits much stronger trans influence than PH_3, the η^1-OCOH moiety tends to avoid the position trans to the H ligand. As a result, the η^1-OCOH moiety takes a position trans to PH_3 in $Ru(H)(\eta^1\text{-OCOH})(PH_3)_3$ $\mathbf{5_Hb}$ (see Figure 6A). This

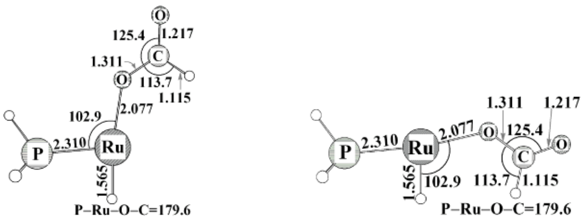

$\mathbf{5_H}$ (+18.4)a,b) $\mathbf{5_Hb}$ (0.0)a)

(A) Two isomers of Ru(H)(η^1-OCOH)(PH_3)$_3$

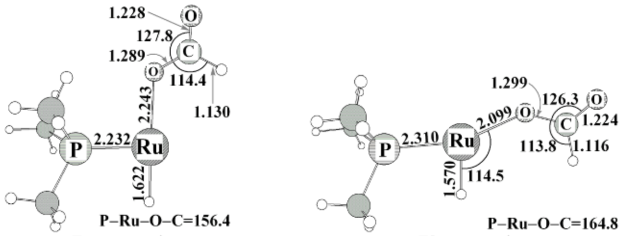

5 (+5.6)a) **5b** (0.0)a)

(B) Two isomers of Ru(H)(η^1-OCOH)(PMe_3)$_3$

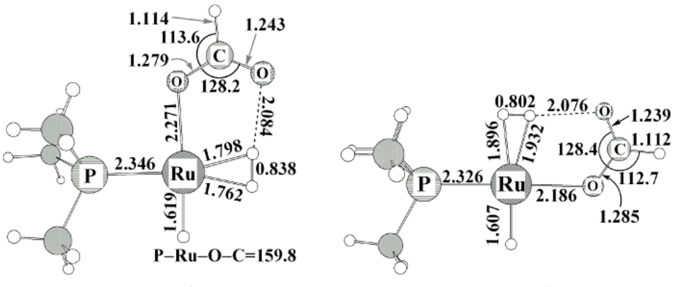

7 (-1.1)a) **7'** (0.0)a)

(C) Two isomers of Ru(H)(η^1-OCOH)(PMe_3)$_3$(H_2)

Figure 6. Geometries of two isomers of Ru(H)(η^1-OCOH)(PH_3)$_3$, Ru(H)-(η^1-OCOH)(PMe_3)$_3$, and Ru(H)(η^1-OCOH)(PH_3)$_3$(H_2)c)

Bond length in angstrom and bond angle in degree. a) In parentheses are the relative energy (in kcal/mol) calculated with the DFT/BS-II method. b) $\mathbf{5_H}$ converts to $\mathbf{5_Hb}$ during the geometry optimization. This is an assumed structure in which the PRuO angle was taken to be 90.0°. c) Two PMe_3 ligands in front of and behind the Ru center are omitted in all the figures to show clearly the geometry changes by the reaction.

structure is considerably more stable than the other one $\mathbf{5_H}$ by 18.4 kcal/mol in which the η^1-OCOH moiety is at a position trans to the H ligand (Figure 6A). Because $\mathbf{5_H}$ is much less stable than $\mathbf{5_Hb}$, not $\mathbf{5_H}$ but $\mathbf{5_Hb}$ is easily formed by the insertion reaction in the PH_3 system unlike that in the PMe_3 system, as reported previously.[7] On the other hand, Ru(H)(η^1-OCOH)(PMe_3)$_3$ **5** is moderately less stable than the other structure **5b**, where the η^1-OCOH moiety is at a position trans to the H(hydride) ligand in **5** and at a position trans to PMe_3 in **5b** (see Figure 6B). This is because PMe_3 exhibits much stronger trans influence than PH_3 and the trans influence is not different very much between hydride and PMe_3 ligands. As a result, the insertion reaction of carbon dioxide yields **5**; note that the position change of carbon dioxide must necessarily occur to afford **5b**, which needs additional activation barrier because carbon dioxide must move across the doubly occupied d_π orbital of Ru to afford **5b**. Moreover, the intermediate **5b** does not easily undergo the metathesis with the dihydrogen molecule, as will be discussed below, whereas **5b** is slightly more stable than **5**. Thus, **5b** is not important in the catalytic cycle.

At the end of this section, we wish to discuss the bonding interaction between formate and the Ru center in **4** which was mentioned above. The H atomic population of free formate is 1.105e but decreases to 0.986e in **4** (see Appendix Figure A1). This small H atomic population in **4** indicates that the 1s orbital of the H atom interacts with the unoccupied d_σ orbital of the Ru center.

1.3.5. Population Changes by Coordination of Dihydrogen Molecule with the Ru Center and Their Differences between PMe_3 and PH_3 Systems

Although the ruthenium(II) η^1-formate intermediate **5** possesses an empty coordination site at a position trans to PMe_3, the PH_3 analogue possesses such an empty

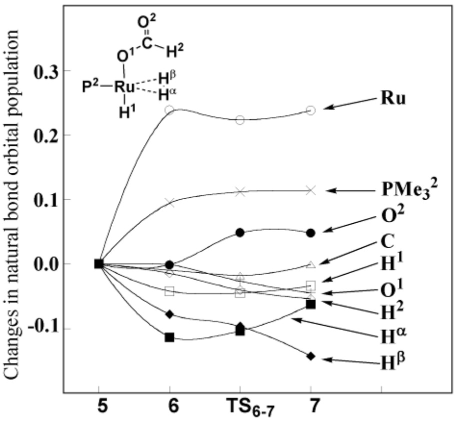

Figure 7. Population changes$^{a)}$ by the coordination of dihydrogen molecule with the Ru center followed by the isomerization of the ruthenium(II)-η^1-formate complex Ru(H)(η^1-OCOH)$(PMe_3)_3$

a) The positive value represents the increase in electron population, and vice versa.

coordination site at a position trans to the H ligand. Thus, the ruthenium complex of dihydrogen molecule takes a different geometry between PMe_3 and PH_3 systems; in the PMe_3 system, the dihydrogen molecule is at a position trans to PMe_3, while it is at a position trans to the H ligand in the PH_3 system. As a result, the new H ligand is formed at a position trans to PMe_3 in the PMe_3 system, while it is formed at a position trans to the H ligand in the PH_3 system. The difference in geometry of ruthenium(II) η^1-formate intermediate leads to differences in the coordination of dihydrogen molecule and the metathesis between PMe_3 and PH_3 systems, as will be discussed below.

As shown in Figure 7, the electron population of dihydrogen molecule decreases and those of Ru and $PMe_3{}^2$ increase in the coordination of dihydrogen molecule with the Ru center, where $PMe_3{}^2$ is at a position trans to dihydrogen molecule. These results indicate that dihydrogen molecule induces the charge-transfer from dihydrogen molecule to the Ru center, to suppress the charge-transfer from $PMe_3{}^2$ to the Ru center. The stabilization energy by the coordination of dihydrogen molecule is 16.1 kcal/mol in the PMe_3 system, which is much larger than that (7.6 kcal/mol) of the PH_3 system, where these energies were evaluated with the DFT/BS-II method and the zero-point energy was not added. This is because dihydrogen molecule takes a position trans to the H ligand in the PH_3 system but at a position trans to PMe_3 in the PMe_3 system. Because the deinsertion is suppressed by coordination of dihydrogen molecule with the Ru center, the PMe_3 system is more favorable for the suppression of the deinsertion than the PH_3 system. This means that the PMe_3 system is better than the PH_3 system for this catalytic reaction.

1.3.6. Population Changes and Electronic Process in the Isomerization of the Ruthenium(II) η^1-Formate Intermediate Followed by the Metathesis with Dihydrogen Molecule, and Their Differences between the PMe_3 Complex and the PH_3 Analogue

Interesting differences between the PMe_3 and PH_3 systems are observed in the isomerization of the ruthenium(II) η^1-formate intermediate and the metathesis with dihydrogen molecule, as follows: (1) The isomerization of the ruthenium(II) η^1-formate more easily occurs in the PMe_3 system than in the PH_3 system. (2) The geometry changes in the metathesis are different between these two systems. And, (3) the metathesis takes place with a smaller activation barrier in the PMe_3 system than in the PH_3 system.

As mentioned above, the isomerization of the ruthenium(II) η^1-formate intermediate occurs with considerably large activation barrier (8.5 kcal/mol) in the PH_3 system but with nearly no barrier (−2.6 kcal/mol) in the PMe_3 system, where the activation barrier in parentheses are calculated with the DFT/BS-II method. This is because the isomerization occurs in a different manner between PMe_3 and PH_3 systems. In the PMe_3 system, the isomerization of **6** occurs via the rotation of the formate moiety about the $C-O^1$ bond (Scheme 2A). Such isomerization does not need a large

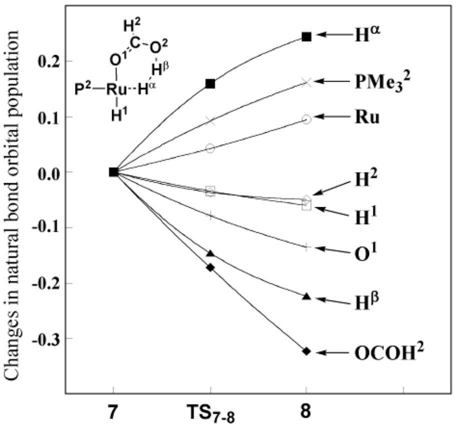

Figure 8. Population changes[a)] by the metathesis of the ruthenium(II)−formate complex, Ru(H)(η^1-OCOH)(PMe_3)$_3$, with dihydrogen molecule

a) The positive value represents the increase in electron population, and vice versa.

activation barrier, because the Ru−η^1-OCOH bond is little weakened by the rotation. On the other hand, the isomerization of the PH_3 system occurs in a different way, as shown in Scheme 2B. In the transition state, the lone pair orbital of the η^1-formate anion deviates from the direction toward the Ru center. Thus, this geometry gives rise to the Ru−O bond weakening and the exchange repulsion between the doubly occupied d_π orbital of Ru and the lone pair orbital of formate, as shown in Scheme 2C. As a result, the activation barrier of the isomerization becomes large in the PH_3 system.

In the metathesis, the H^β atomic population considerably decreases, while the H^α atomic population considerably increases, as shown in Figure 8. These population changes clearly show that the metathesis occurs via the heterolytic H−H bond breaking in which the H^β atom becomes proton and the H^α atom becomes hydride. Also, the O^1 atomic population considerably decreases, because the formate anion changes into formic acid and the O^1 atom becomes neutral in formic acid in a formal sense. The electron population of Ru increases upon going to **8** from **7**, probably because the H^α (hydride) ligand, which is formed at a position trans to PMe_3, supplies electron density to the Ru center. This H^α ligand suppresses the electron donation of PMe_3 to the Ru center, which leads to increase in the electron population of PMe_3. In **8**, the H^α and H^β atomic populations are 1.182e and 0.534e, respectively. This result indicates that the electrostatic stabilization interaction exists between the positively charged H^β atom and the negatively charged H^α atom. The H^β atomic population is somewhat larger than that of free formic acid. This electron population suggests that the charge-transfer occurs from the H^α ligand to the LUMO of formic acid in **8**; actually, the LUMO of formic acid mainly consists of the 1s orbital of H^β and extends toward H^α (see Appendix Figure A3).

The metathesis of $Ru(H)(\eta^1\text{-}OCOH)(PMe_3)_3$ **7** with dihydrogen molecule occurs with a smaller activation barrier in the PMe_3 system than that (E_a = 8.2 kcal/mol) in the PH_3 system. This is interpreted in terms of the trans-influence of the H and PMe_3 ligands, as follows: In the metathesis of the PH_3 system, the H(hydride) ligand is formed at a position trans to the H(hydride) ligand. This structure is unfavorable because two hydride ligands are at positions trans to each other; remember that the hydride ligand exhibits strong trans-influence. In the metathesis of the PMe_3 system, on the other hand, it is formed at a position trans to PMe_3. Thus, the metathesis of the PMe_3 system more easily occurs than that of the PH_3 system.

It should be investigated here whether or not the metathesis takes place in the PMe_3 system when it starts from **5b**, because **5b** is moderately more stable than **5** and the metathesis takes place from the similar intermediate **5_Hb** in the PH_3 system (see Figure 6 for **5**, **5b**, **5_H**, and **5_Hb**). First, two isomers (**7** and **7'**) of $Ru(H)(\eta^1\text{-}OCOH)(PMe_3)_3(H_2)$ were optimized, as shown in Figure 6C, where dihydrogen molecule is at a position trans to PMe_3 in **7** but at a position trans to the H ligand in **7'** (see Figures 6 and 9 for **7** and **7'**). These two isomers are in similar energy to each other (see Figure 9). Then, we tried to optimize *trans*-$Ru(H)(PMe_3)_2(HCOOH)$ **8'**, in which formic acid is at a position trans to PMe_3. This is the product of

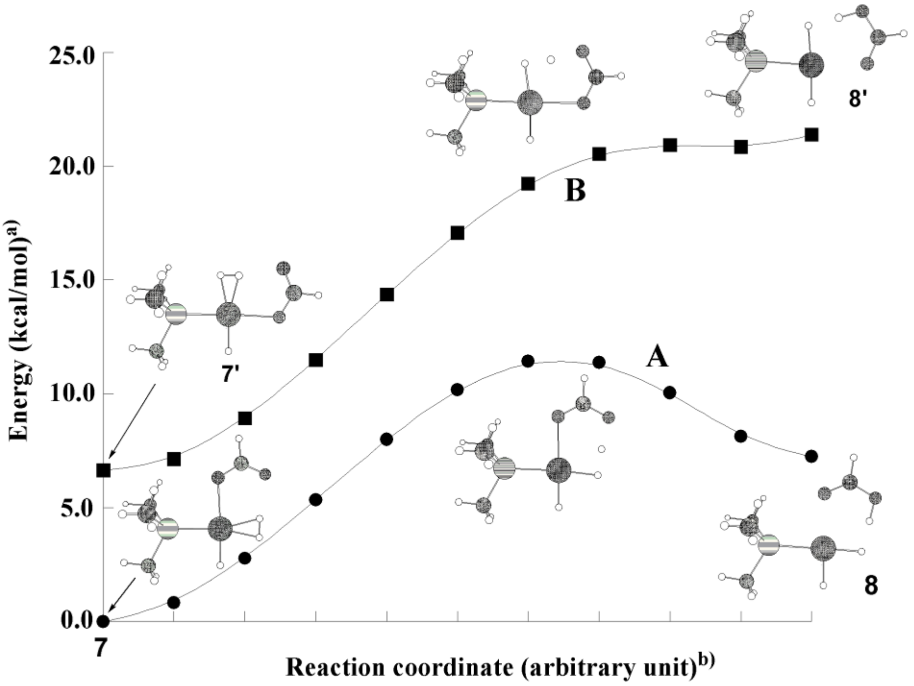

Figure 9. Potential energy changes$^{a)}$ by the IRC calculation of metathesis starting from **7**$^{b)}$ to **8** and the assumed geometry changes$^{c)}$ of the metathesis starting from **7'** to **8'** $^{c)}$

a) The DFT/BS-II calculation (in kcal/mol). b) See Figure 6 for **7**, **8**, **7'**, and **8'**. c) The positions of H_2 and η^1-formate moiety are exchanged to each other in the IRC calculation of the metathesis from **7** to **8**. c) Two PMe_3 ligands in front of and behind the Ru center are omitted in all the figures to show clearly the geometry changes by the reaction.

metathesis starting from **7'**. However, **8'** returns to **7'** during the geometry optimization of **8'**. Thus, we performed IRC calculation of the metathesis starting from **7** to **8**, as shown in Figure 9 (line A), and then calculated the energy changes along the geometry changes in which the positions of H_2 and η^1-OCOH are exchanged to each other, as shown in Figure 9 (line B). The latter geometry changes are considered the reasonable model of the metathesis starting from **7'** to **8'**. Apparently, the metathesis starting from **7'** is considerably endothermic (see the line B of Figure 9). More important is that the reverse reaction (**8'→7'**) occurs with nearly no barrier. On the other hand, the metathesis easily proceeds from **7** to **8** with a moderate activation barrier

Scheme 4

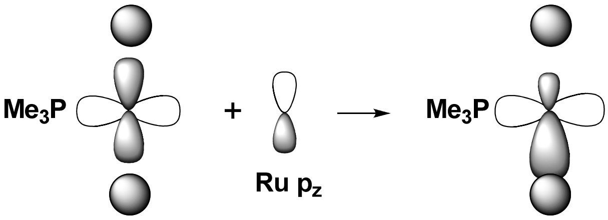

(see the line A of Figure 9). These results clearly indicate that the metathesis can occur only when dihydrogen molecule is at a position trans to PMe_3. In the PH_3 system, on the other hand, the metathesis can take place even when dihydrogen molecule is at a position trans to the H ligand like **7’**, as reported previously.[7] This difference between PMe_3 and PH_3 systems is interpreted as follows: Because the lone pair orbital of PMe_3 is at higher energy than that of PH_3, PMe_3 pushes up the d_σ orbital of Ru in energy to a greater extent than does PH_3. As a result, the d_σ–p_σ mixing takes place in the PMe_3 system to a greater extent than in the PH_3 system. This d_σ–p_σ mixing strengthens one Ru–H bond but weakens the other Ru–H bond, as shown in Scheme 4. Consequently, one H ligand tends to dissociate from the Ru center in **8’** to form dihydrogen molecule; in other words, **8’** easily returns to **7’**. In the PH_3 system, such d_σ–p_σ mixing does not take place effectively because the d_σ orbital of Ru is at considerably low energy in the PH_3 system. Thus, **8’** is not stable and the metathesis can not take place from **7’** to **8’** in the PMe_3 system unlike the metathesis in the PH_3 system.

From these results, it is concluded that **5b** and **7’** are not important in the catalytic cycle of the PMe_3 system but **5** is an important intermediate which undergoes easily the coordination of dihydrogen molecule to afford **6** and that the isomerization of the η^1-formate moiety followed by the metathesis easily takes place starting from **6** through **7** in the PMe_3 system.

1.4. Conclusions

Reaction mechanism of hydrogenation of carbon dioxide to formic acid catalyzed by *cis*-$Ru(H)_2(PMe_3)_3$ was theoretically investigated with the DFT and MP4(SDQ) methods. This reaction takes place through the insertion of carbon dioxide into the Ru(II)−H bond, the coordination of dihydrogen molecule to the ruthenium(II) η^1-formate intermediate, the isomerization of the ruthenium(II) η^1-formate intermediate, and the metathesis of the ruthenium(II) η^1-formate intermediate with dihydrogen molecule. The rate-determining step is the insertion of carbon dioxide into the Ru(II)−H bond. Although this is not consistent with the experimental results seemingly, the coordination of dihydrogen molecule with the ruthenium(II) η^1-formate intermediate **5** necessarily takes place after the insertion reaction, to suppress the deinsertion. Thus, the reaction rate increases with increase in the pressure of dihydrogen molecule, which is consistent with the experimental results.

In the PMe_3 system, the ruthenium(II) η^2-carbon dioxide complex exists as an intermediate, unlike the PH_3 system. Also, the ruthenium(II) η^1-formate intermediate takes a different geometry between PMe_3 and PH_3 systems; in the former system, the η^1-formate takes a position trans to the H ligand, while it takes a position trans to PH_3 in the latter one. The insertion of carbon dioxide into the Ru(II)−H bond occurs with somewhat smaller activation barrier in the PMe_3 system than in the PH_3 system. These results are clearly interpreted in terms of the much stronger donation ability and trans influence of PMe_3 than those of PH_3.

The isomerization of the ruthenium(II) η^1-formate intermediate takes place with a much smaller activation barrier in the PMe_3 system than in the PH_3 system. This is because the η^1-formate intermediate of the PMe_3 system takes a different geometry from that of the PH_3 system due to the stronger trans influence of PMe_3 than that of PH_3. Also, the metathesis more easily proceeds in the PMe_3 system than in the PH_3 system, because of the different geometries of the ruthenium(II) η^1-formate intermediate. Thus, it is concluded that the use of donating ligand is recommended for this catalytic reaction because the donating ligand facilitates the insertion of carbon dioxide into the Ru(II)−H bond, the coordination of dihydrogen molecule with the Ru center, the isomerization of the ruthenium(II) η^1-formate intermediate, and the metathesis.

Solvent effects were also investigated with the DPCM method. Interestingly, non-polar solvent facilitates the metathesis, while polar solvent facilitates the insertion of carbon dioxide into the Ru(II)−H bond. Thus, the use of polar solvent is recommended for this catalytic reaction because the insertion reaction is the rate-determining step.

In conclusion, the experimental results are reasonably interpreted theoretically and the conclusive discussion of the reaction mechanism and each elementary step is presented here. We wish to present the prediction that the strongly donating ligand and the polar solvent would improve the efficiency of this catalytic reaction. Of course, the present study does not explain all the experimental results of ruthenium-catalyzed hydrogenation of carbon dioxide; for instance, interesting experimental results of the effects of bidentate phosphine ligand[35] and the acceleration by water and alcohol[6b,c,36] have not been theoretically investigated here. In particular, the effects of additives such as water and alcohol are of considerable importance, because of the possibilities that these additives lower the activation barrier of the conversion of carbon dioxide to formate, as experimentally[37] and theoretically suggested.[38] These issues should be theoretically investigated in near future.

1.5. Appendix

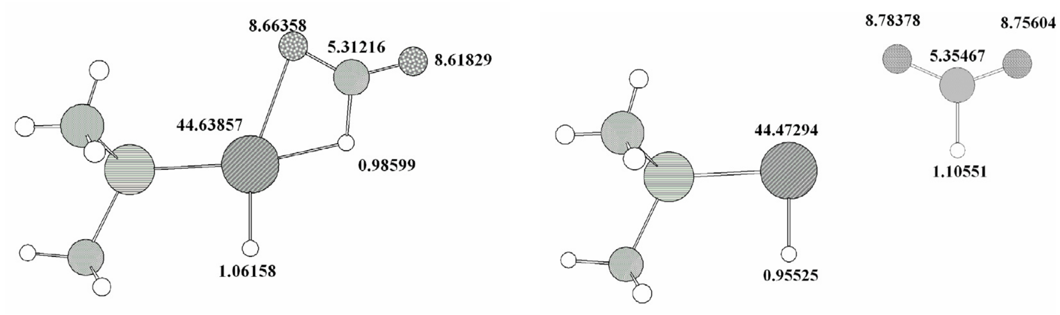

(A) RuH(η^1-OCOH)(PMe$_3$)$_3$ **4** (B) [RuH (PMe$_3$)$_3$]$^+$ + OCOH$^-$

Figure A1. Electron population of RuH(η^1-OCOH)(PMe$_3$)$_3$ **4**[a)] and its fragments[a)]. a) Two PMe$_3$ ligands which are in front and behind of this sheet are omitted for brevity.

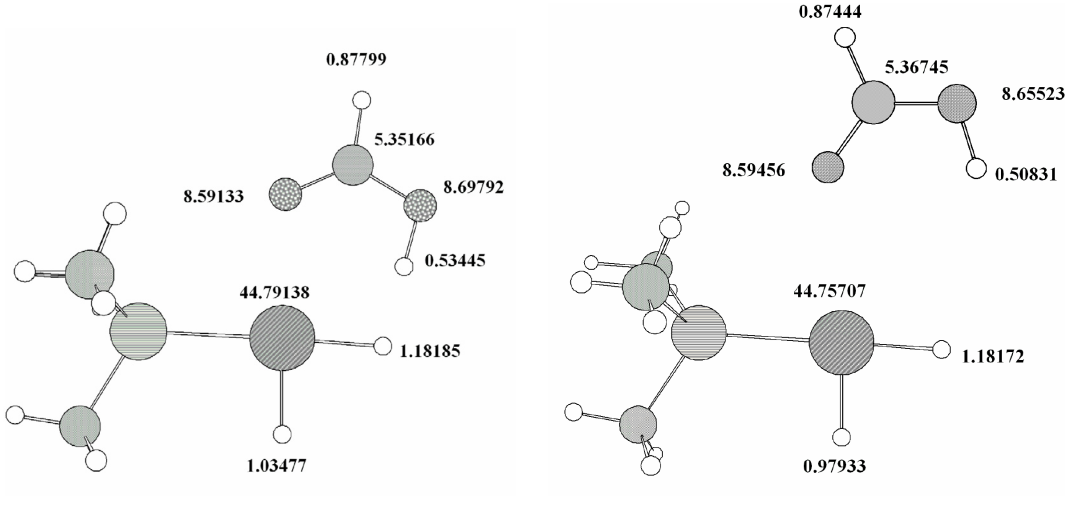

(A) Ru(H)$_2$(HCCOH)(PMe$_3$)$_3$ **8** (B) Ru(H)$_2$(PMe$_3$)$_3$ + HCOOH

Figure A2. Electron population of Ru(H)$_2$(HCCOH)(PMe$_3$)$_3$ **8**[a)] and its fragments[a)]. a) Two PMe$_3$ ligands which are in front and behind of this sheet are omitted for brevity.

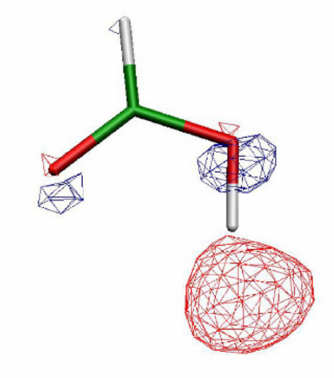

Orbital energy = 1.906 eV (RHF/BS-II)

Figure A3. The LUMO of formic acid. Contour value is 0.05e.

References

1) (a) Braunstein, P.; Matt, D.; Nobel, D. *Chem. Rev.* **1988**, *88*, 747. (b) Behr, A. *Angew. Chem., Int. Ed. Engl.* **1988**, *27*, 661. (c) Jessop, P. G.; Ikariya, T.; Noyori, R. *Chem. Rev*. **1995**, *95*, 259. (d) Darensbourg, D. J.; Holtcamp, M. W. *Coord. Chem. Rev.* **1996**, *153*, 155. (e) Walther, D.; Rubens, M.; Rau, S. *Coord. Chem. Rev.* **1999**, *182*, 67.

2) Inoue, Y.; Izumida, H. Sasaki, S.; Hashimoto, H. *Chem. Lett.* **1976**, 863. Sasaki, S.; Inoue, Y.; Hashimoto, H. *J. Chem. Soc., Chem. Commun.* **1976**, 605.

3) Tsai, J. C.; Nicholas, K. H. *J. Am. Chem. Soc.* **1992**, *114*, 5117.

4) (a) Graf, E.; Leitner, W. *J. Chem. Soc., Chem. Commun.* **1992**, 623. (b) Burgemeister, T.; Kasmer, F.; Leitner, W. *Angew. Chem., Int. Ed. Engl.* **1993**, *32*, 739. (c) Gassner, F.; Leitner, W. *J. Chem. Soc., Chem. Commun.* **1993**, 1465.

5) (a) Hutschka, F.; Dedieu, A.; Eichberger, M.; Fornika, R.; Reitner, W. *J. Am. Chem. Soc.* **1997**, *119*, 4432. (b) Hutschka, F.; Dedieu, A. *J. Chem. Soc., Dalton Trans.* **1997**, 1899.

6) (a) Jessop, P. G.; Ikariya, T.; Noyori, R. J. *Nature* **1994**, *368*, 231. (b) Jessop, P. G.; Hsiano, Y.; Ikariya, T.; Noyori, R. *J. Am. Chem. Soc.* **1994**, *116*, 8851. (c) Jessop, P. G.; Ikariya, T.; Noyori, R. *J. Am. Chem. Soc.* **1996**, *118*, 344.

7) Musashi, Y.; Sakaki, S. *J. Am. Chem. Soc.* **2000**, *122*, 3867.

8) Musashi, Y.; Sakaki, S. *J. Am. Chem. Soc.* **2002**, *124*, 7588.

9) Sakaki, S.; Musashi, Y. in *Catalysis by Metal Complexes Vo. 25, Computational Modeling of Homogeneous Catalysis*, Ed. by Maseras, F.; Lledos, A. Kluwer Acad. Publ., Dordrecht, 2002, 79.

10) (a) Becke, A. D. *Phys. Rev. A*, **1988**, *38*, 3098. (b) Becke, A. D. *J. Chem. Phys.* **1983**, *98*, 5648.

11) Lee, C.; Yang, W.; Parr, R. G.. *Phys. Rev. B*, **1988**, *37*, 785.

12) (a) Miertus, S.; Scrocco, E.; Tomasi, J. *Chem. Phys.* **1981**, *55*, 117. (b) Pascual-Ahuir, J. L.; Silla, E.; Tomasi, J.; Bonaccorsi, R. *J. Comput. Chem.* **1987**, *8*, 778. (c) Floris, F.; Tomasi, J. *J. Comput. Chem.* **1989**, *10*, 616. (d) Tomasi, J.; Persico, M. *Chem. Rev.* **1994**, *94*, 2027.

13) Hay, P. J.; Wadt, W. R. *J. Chem. Phys.* **1985**, *82*, 299.

14) Wadt, W. R.; Hay, P. J. *J. Chem. Phys.* **1985**, *82*, 284.

15) Höllwarth, A.; Böhme, M.; Dapprich, S.; Ehlers, A. W.; Gobbi, A.; Jonas, V.; Köhler, K. F.; Stegmann, R.; Veldkamp, A.; Frenking, G. *Chem. Phys. Lett.*, **1993**, *208*, 237.

16) Krishnan, R.; Binkley, J. S.; Seeger, R.; Pople, J. A. *J. Chem. Phys.* **1980**, *72*, 650.

17) Hehre, W. J.; R. Ditchfield, R.; Pople, J. A. *J. Chem. Phys.* **1972**, *56*, 2257.

18) Couty, M.; Hall, M. B. *J. Comput. Chem.* **1996**, *17*, 1359.

19) Ehlers, A. W.; Böhme, M.; Dapprich, S.; Gobbi, A.; Höllwarth, A.; Jonas, V.; Köhler, K. F.; Stegmann, P.; Veldkamp, A.; Frenking, G. *Chem. Phys. Lett.* **1993**, *208*, 111.

20) Frisch, M. J.; Trucks, G. W.; Schlegel, H. B.; Scuseria, G. E.; Robb, M. A..; Cheeseman, J. R.; Zakrzewski, V. G.; Montgomery, J. A.; Stratmann, R. E.; Burant, J. C.; Dapprich, S.; Millam, J. M.; Daniels, A. D.; Kudin, K. N.; Strain, M. C.; Farkas, O.; Tomasi, J.; Barone, V.; Cossi, M.; Cammi, R.; Mennucci, B.; Pomelli, C.; Adamo, C.; Cliford, S.; Ochterski, J.; Petersson, G. A.; Ayala, P. Y.; Cui, Q.; Morokuma, K.; Malick, D. K.; Rabuck, A. D.; Raghavachari, K.; Foresman, J. B.; Cioslowski, J.; Ortiz, J. V.; Stefanov, B. B.; Liu, G.; Liashenko, A.; Piskorz, P.; Komaromi, I.; Gomperts, R.; Martin, R. L.; Fox, D. J.; Keith, T.; Al-Laham, M. A.; Peng, C. Y.; Nanayakkara, A.; Gonzalez, C.; Challacombe,

M.; Gill, P. M. W.; Johnson, B. G.; Chen, W.; Wong, M. W.; Andres, J. L.; Head-Gordon, M.; Replogle, E. S.; Pople, J. A. *Gaussian 98*, Gaussian Inc., Pittsburgh PA, **1998**.

21) Reed, A. E.; Curtis, L.A.; Weinhold, F. *Chem. Rev.* **1988**, *88*, 849, and references therein.

22) Flükiger, P.; Lüthi, H. P.; Portann, S.; Weber, J. *MOLEKEL v.4.3* for Scientific Computing , Manno, Switzerland, 2002-2002. Portman, S.; Lüthi, H. P., *CHIMIA*, **2000**, *54*, 766.

23) Aresta, M.; Nobile, F.; Albano, V. G.; Formni, E.; Manassero, M. *J. Chem. Soc., Chem. Commun.* **1975**, 636.

24) Bristow, G. S.; Hitchcock, P. B.; Lappert, M. F. *J. Chem. Soc., Chem. Commun.* **1981**, 1145.

25) Alvarez, R.; Carmona, E.; Marin, J. M.; Poveda, M. L.; Gutierrez-Puebla, E.; Monge, A. *J. Am. Chem. Soc.*, **1986**, *108*, 2286.

26) (a) Sakaki, S. in *Stereochemistry of Organometallic and Inorganic Compounds, Vol. 4, Stereochemical Control, Bonding and Steric Rearrangements,* Ed. by Bernal, I. Elsevier, Amsterdam, 1990, p.95. (b) Sakaki, S.; Kitaura, K.; Morokuma, K. *Inorg. Chem.* **1982**, *21*, 760.

27) Although the geometry optimization by the DFT/BS-I method yielded the weak CO_2 complex **2**, the DFT/BS-I calculation indicated that **2** easily converts to **3** with nearly no barrier. The small discrepancy between the DFT/BS-I and DFT/BS-II calculations is not important.

28) From **6**, the metathesis with dihydrogen molecule can take place through the four-center transition state. However, our previous theoretical study indicated that the six-center transition state is much lower in energy than the four-center transition state in the metathesis of the ruthenium(II)-η^1-formate complex with

the dihydrogen molecule.[7] Thus, it is likely to consider that the metathesis takes place through the six-center transition state if the isomerization of **6** easily takes place with moderate activation barrier.

29) Biswas, B.; Sugimoto, M.; Sakaki, S. *Organometallics*, **2000**, *19*, 3895.

30) The energy changes by the DFT method indicate that the rate-determining step becomes the metathesis in n-heptane and THF, while those by the MP4(SDQ) method indicate that the rate-determining step is the CO_2 insertion in *n*-heptane and THF.

31) Electron populations little change upon going from **3** to $\mathbf{TS_{3\text{-}4}}$, as shown in Figure 5. Thus, no factor that slightly decreases the dipole moment in $\mathbf{TS_{3\text{-}4}}$ is found in electron population changes.

32) Eckert, J.; Kubas, G. J.; Hall, J. H.; Hay, J.; Boyle, C. M. *J. Am. Chem. Soc.* **1990**, *112*, 2324.

33) Matsubara, T.; Maseras, F.; Koga, N.; Morokuma, K. *J. Phys. Chem.* **1996**, *100*, 2503.

34) (a) Sakaki, S.; Ohkubo, Y. *Inorg. Chem.* **1989**, *28*, 2583. (b) Sakaki, S.; Ohkubo, Y. *Inorg. Chem.* **1987**, *27*, 2020. (c) Sakaki, S.; Ohkubo, Y. *Organometallics* **1989**, *8*, 2970. (d) Sakaki, S.; Musashi, Y. *J. Chem. Soc., Dalton Trans.* **1994**, 3047. (e) Sakaki, S.; Musashi, Y. *Inorg. Chem.* **1995**, *34*, 1914. (f) Sakaki, S.; Musashi, Y. *Int. J. Quant. Chem.* **1996**, *57*, 481. (g) Musashi, Y.; Sakaki, S. *J. Chem. Soc., Dalton Trans.* **1998**, 577.

35) Kröcher, O.; Köppel, R. A.; Baiker, A. *Chem. Commun.* **1997**, 453.

36) Munshi, P.; Main, A. D.; Linehan, J. C.; Tai, C. –C.; Jessop, P. G. *J. Am. Chem. Soc.* **2002**, *124*, 7963.

37) Koike, T.; Ikariya, T. *Adv. Synth. Catal.* **2004**, *346*, 37.

38) (a) Matsubara, T. *Organometallics* **2001**, *20*, 19. (b) Matsubara, T.; Hirao, K.

Organometallics **2001**, *20*, 5769.

Chapter 2

Ruthenium(II)-Catalyzed Hydrogenation of Carbon Dioxide to Formic Acid. Theoretical Study of Significant Acceleration by Water Molecule

2.1. Introduction

Catalytic hydrogenation of carbon dioxide by transition-metal complexes is one of the most important and the most interesting subjects of research in recent transition-metal chemistry, catalytic chemistry, and organometallic chemistry.[1] The first report was presented by Inoue and his collaborators in 1976.[2] They successfully carried out this hydrogenation reaction with M(diphos) (M = Ni or Pd), $Pd(PPh_3)_4$, $RhCl(PPh_3)_3$, $RuH_2(PPh_3)_4$, and $IrH_3(PPh_3)_3$ in the presence of amine. However, the turnover numbers reported were small. Since this first report, a lot of works have been carried out on the hydrogenation of carbon dioxide. For instance, Darensbourg and his collaborators performed the hydrogenation of carbon dioxide with $[MH(CO)_6]^-$ (M = Cr, Mo, or W) in 1984.[3] In 1989, Taqui Kahn and his collaborators applied $[Ru(edtaH)Cl]^-$ to the hydrogenation and reported somewhat large turn over numbers of about 180.[4] In 1992, Tsai and his collaborator[5] and Leitner and his collaborator[6] successfully carried out Rh(III)- and Rh(I)-catalyzed hydrogenation of carbon dioxide, respectively. In 1994, Jessop, Ikariya, and Noyori succeeded extremely efficient hydrogenation of carbon dioxide with $RuX(Y)(PMe_3)_4$ (X, Y = H, Cl, or O_2CMe).[7] This report draws a lot of attentions because of the extremely high turn over numbers.

Scheme 1

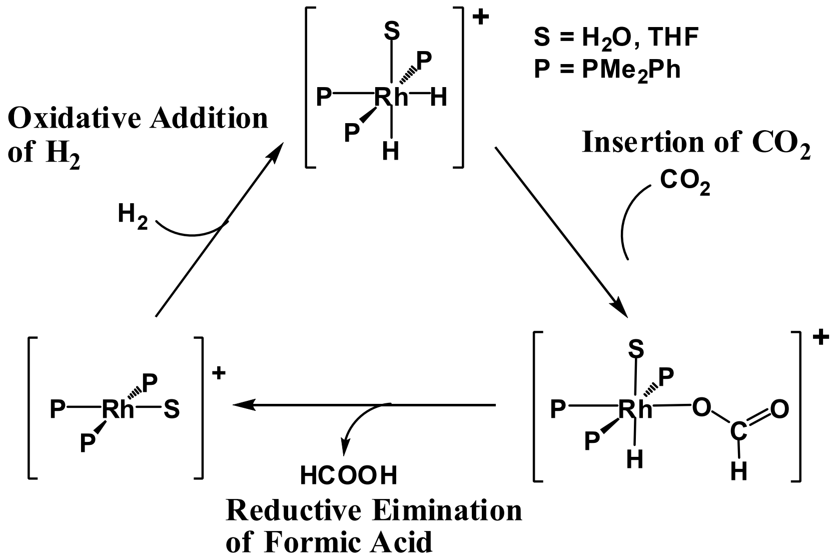

The other interesting result reported is that small amount of water significantly enhances the catalytic efficiency. Later, a similar promotion effect of water in the Ru-catalyzed hydrogenation was reported by a different group, where a ruthenium complex, $TpRuH(PPh_3)(CH_3CN)$ (Tp = hydrotris(pyrazolyl)borate), was employed as a catalyst.[8] Also, not only water but also various alcohols accelerate hydrogenation of carbon dioxide catalyzed by $RuX(Y)(PMe_3)_4$.[9] Although the mechanism of acceleration by water and alcohols were discussed experimentally[9] and theoretically,[8] details of whole catalytic cycle are still ambiguous, to our knowledge.

Reaction mechanisms of transition-metal-catalyzed hydrogenation of carbon dioxide have been experimentally and theoretically discussed in the absence of water molecule. For instance, Tsai and his collaborator spectroscopically observed $[RhH(\eta^2\text{-}O_2CH)(PMe_2Ph)_3(S)]^+$ and $[RhH(\eta^1\text{-}O_2CH)(PMe_2Ph)_{3,2}(S)_{1,2}]^+$ (S = solvent such as H_2O or THF) in the catalytic reaction solution and proposed that the hydrogenation of carbon dioxide took place through the insertion of carbon dioxide into the Rh(III)−H bond followed by the reductive elimination of formic acid and the oxidative addition of dihydrogen molecule to the Rh(I) center to reproduce active

Scheme 2

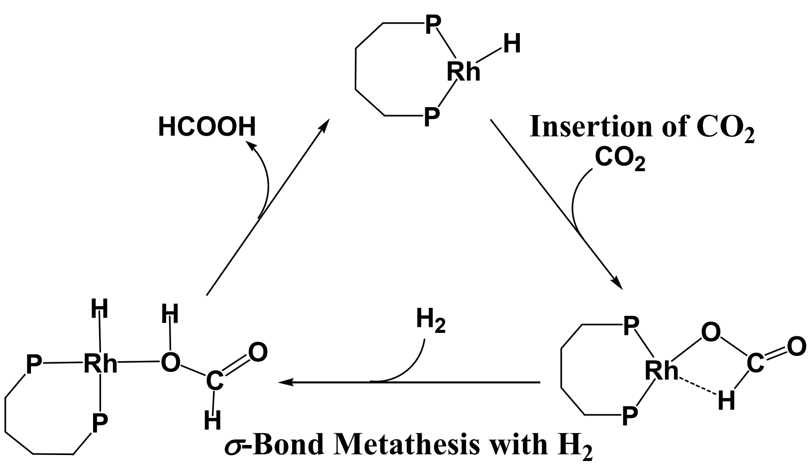

species (see Scheme 1). Our theoretical study presented clear evidence to support this reaction mechanism.[10] Hutschka and his collaborators also theoretically investigated the reaction mechanism of Rh(I)-catalyzed hydrogenation of carbon dioxide and proposed that the hydrogenation took place through the insertion of carbon dioxide into the Rh(I)−H bond followed by the metathesis of the Rh(I) η^1-formate complex with dihydrogen molecule (Scheme 2).[11] We also theoretically investigated Ru(II)-catalyzed hydrogenation of carbon dioxide and clearly showed that this reaction took place through the insertion of carbon dioxide into the Ru(II)−H bond and the isomerization of ruthenium(II) η^1-formate intermediate followed by the metathesis of the ruthenium(II) η^1-formate intermediate with a dihydrogen molecule, as shown in Scheme 3.[12] Although the reaction mechanism of transition-metal-catalyzed hydrogenation of carbon dioxide has been theoretically investigated well as described above, all those works devoted attentions to the hydrogenation in the absence of water molecule.

The catalytic cycle of the hydrogenation of carbon dioxide in the presence of water molecule has not been investigated yet, except for only a few theoretical works of related elementary step.[13,14] One theoretical work with the DFT method reported

Scheme 3

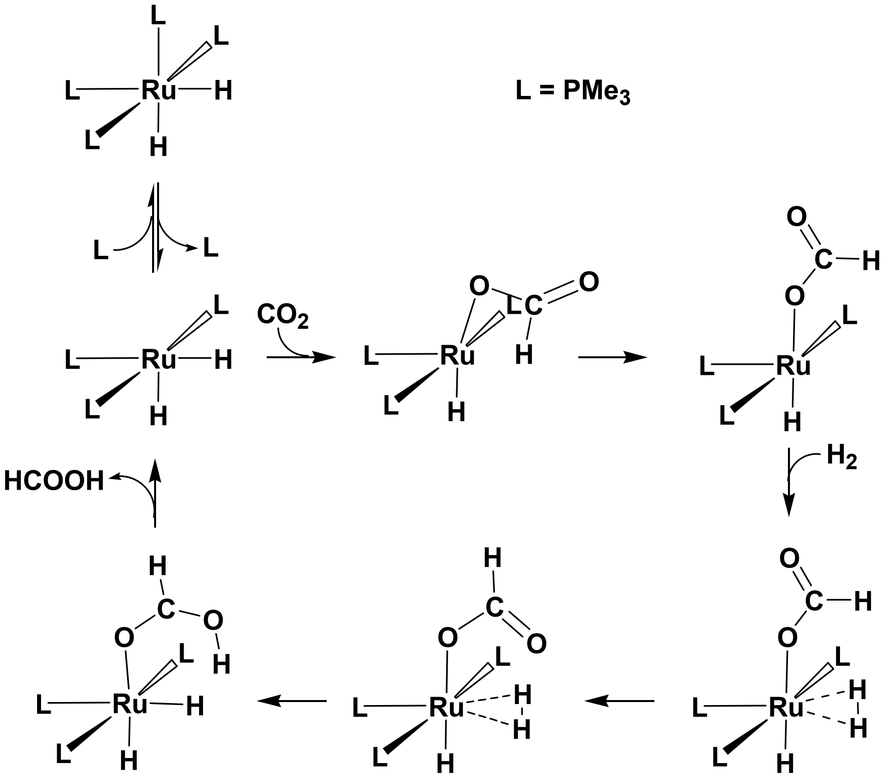

that water molecule accelerated the insertion of carbon dioxide into the Ru(II)−H bond of TpRuH(PPh_3)(CH_3CN).[13] The reaction of carbon dioxide with (Cp-$CH_2CH_2NH_2$)Ru(H)(diphos) was also theoretically investigated with the DFT method.[14] This work reported that not the insertion of carbon dioxide into the Ru(II)−H bond but the H attack to carbon dioxide easily took place because the amine chain accelerated the reaction through hydrogen bonding interaction between the H atom of the amine chain and the O atom of carbon dioxide. However, the whole catalytic cycle was not investigated in these works. To clarify the roles of water molecule, the whole catalytic cycle must be theoretically investigated and each elementary step must be compared with each other.

In this work, we theoretically investigated the Ru(II)-catalyzed hydrogenation of carbon dioxide into formic acid in the presence of water molecule, where the real catalyst, *cis*-Ru(H)$_2$(PMe$_3$)$_3$, was employed for calculation. Our purposes here are to clarify the reaction mechanism in the presence of water molecule, to make a comparison between the catalytic cycle in the absence of water molecule and that in the presence of water molecule, and to provide theoretical answers to questions how and why water molecule accelerates the reaction. Also, we investigated if amine and alcohol accelerated this hydrogenation reaction.

2.2. Computational Details

Geometries were optimized with the DFT method, where the B3LYP hybrid functional[15,16] was used for exchange−correlation term. We ascertained that each optimized transition state exhibited one imaginary frequency and that geometry changes induced by the imaginary frequency were consistent with the reaction course. Energy and population changes were calculated with the DFT and MP2-MP4(SDQ) methods. Solvation effects were evaluated with the DPCM method.[17] The CCSD(T) method was also employed in the most important elementary step to check the reliability of the DFT and MP4(SDQ) methods.

Two kinds of basis set systems were used. In geometry optimization, the following basis set system (BS-I) was employed: Core electrons of P (up to 2p) and Ru (up to 3d) were replaced with Los Alamos effective core potentials (ECPs),[18] and the valence electrons were represented with (21/21/1) and (341/321/31) basis sets,[19] respectively. For carbon dioxide and the methyl group of trimethylphosphine, 6-31G(d) basis sets were used.[19] For the hydride ligand, dihydrogen molecule, and water molecule, 6-311G(d,p) basis sets[20] were used. Energy changes were calculated with a better basis set system (BS-II), using geometries optimized by the DFT(B3LYP)/BS-I method. In BS-II, a (541/541/211/1) basis set[18a,21,22] was employed for Ru with the same ECPs as those of BS-I. For the hydride ligand, dihydrogen molecule, water molecule, carbon dioxide, and formate anion, cc-pVDZ basis sets were employed,[23] where a d-polarization function was added to each atom and a diffuse function was added to the O atom (aug-cc-pVDZ). For P, the same basis set and ECPs as those of BS-I were used. For the methyl group of trimethylphosphine, 6-31G basis sets were used in order to reduce the computational cost of the MP4(SDQ) calculations.

We evaluated the free energy change in two ways like our previous works.[12b,24] In one way, translation, rotation, and vibration movements were considered to evaluate entropy and thermal energy, where all substrates were treated as ideal gas. We evaluated the entropy effects under the typical reaction conditions, where the pressures of H_2 and CO_2 were 80 and 120 atm, respectively, and the temperature was 323.15 K. The DFT/BS-I method was used to calculate vibration frequencies without a scaling factor. In the other way, vibration movements were considered in evaluation of entropy but neither translation movements nor rotation ones were considered, since this reaction was carried out in supercritical carbon dioxide solvent, in which the translation and rotation movements are considerably suppressed, unlike those in ideal gas. The free energy change estimated in this way is named ΔG_v hereafter. In the former estimation way, entropy significantly decreases when two molecules form an adduct, as expected. In the latter estimation method, on the other hand, entropy change is small, as will be discussed below. The former method apparently overestimates entropy and thermal energy changes of solution reaction, because translation and rotation movements are considerably suppressed in solution. On the other hand, the latter one underestimates entropy and thermal energy changes because translation and rotation movements are not completely frozen in solution. A true value of free energy change would be intermediate between the ΔG value evaluated by the former method and the ΔG_v value by the latter one. Because this ambiguity

Scheme 4

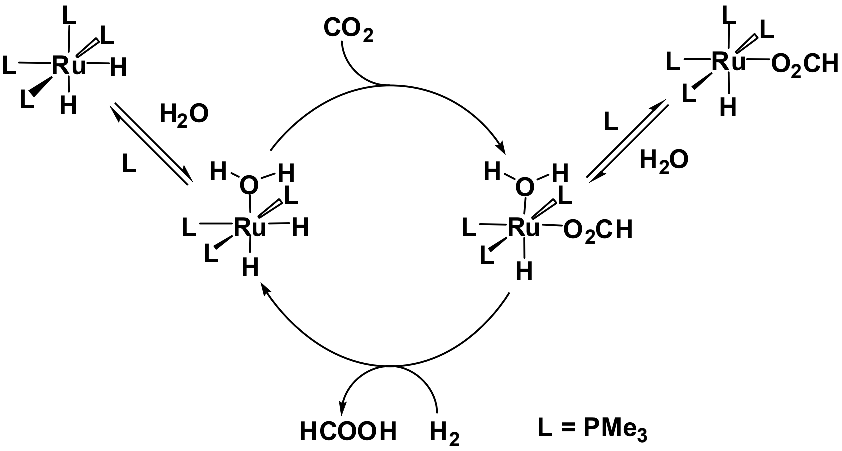

remains in the estimation of entropy and thermal energy changes, we will discuss each elementary step with the usual potential energy changes and then discuss it with the free energy changes evaluated in these two ways.

Gaussian 98 program package was used for these calculations.[25] Population analysis was carried out with the method of Weinhold et al.[26] Molecular orbitals were drawn with the MOLEKEL program package.[27]

2.3. Results and Discussion

2.3.1. Hydride Migration from Ru(II) Center to CO_2

cis-$RuH_2(PMe_3)_3(H_2O)$ was experimentally proposed to be formed from *cis*-$RuH_2(PMe_3)_4$ as an active species in the presence of water molecules,[7c] as shown in Scheme 4. Because *cis*-$RuH_2(PMe_3)_4$ is a six-coordinate complex, it is likely that associative substitution of PMe_3 for H_2O does not occur easily. In dissociative substitution, *cis*-$RuH_2(PMe_3)_3$ is formed first, in which a vacant site is at a position trans to H because of the strong trans influence of the H(hydride) ligand. Then, H_2O approaches the Ru center at the vacant site to form $Ru(H)_2(PMe_3)_3(H_2O)$ **1**. In **1**, the H_2O moiety tilts toward the H^1 ligand, as shown in Figure 1, because the H^3 atom of

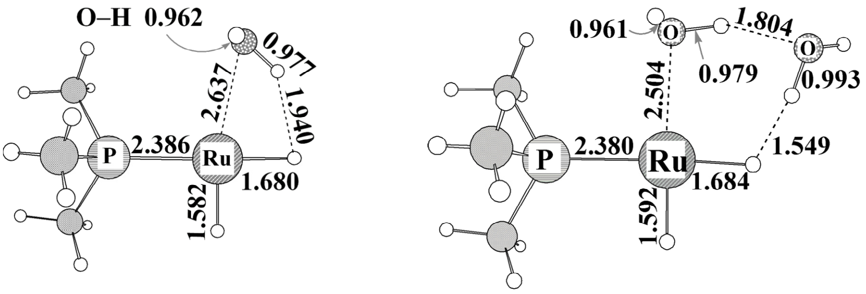

1 **2**

Figure 1. Geometries[a)] of *cis*-Ru(H)$_2$(PMe$_3$)$_3$(H$_2$O) and *cis*-Ru(H)$_2$(PMe$_3$)$_3$(H$_2$O)$_2$ Bond length in angstrom and bond angle in degree.
a) Two PMe$_3$ ligands above and below the Ru center are omitted in all the figures to show clearly the geometry changes by the reaction.

Scheme 5

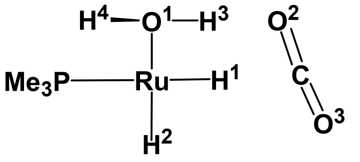

H$_2$O is drawn to the H^1 ligand by the proton−hydride (H^3−H^1) electrostatic interaction, where H^1, H^2 etc are defined in Scheme 5; the NBO net charge is −0.205*e* for H^1 and +0.511*e* for H^3. This distorted Ru−OH$_2$ coordinate bond is weaker than the usual Ru−OH$_2$ coordinate bond with normal coordination structure, because the overlap between the lone pair orbital of H$_2$O and the empty d_σ orbital of Ru is smaller in this geometry than that in the normal coordinate structure. Since it is likely that water molecules form a cluster in hydrophobic super critical carbon dioxide, we investigated the possibility that a cluster of two water molecules binds with the Ru complex to afford Ru(H)$_2$(PMe$_3$)$_3$(H$_2$O)$_2$ **2**. In **2**, the six-membered ring structure that consists of Ru and two H$_2$O molecules distorts little, as shown in Figure 1; one H$_2$O interacts with the H^1 ligand, keeping hydrogen bond with the H$_2$O ligand that coordinates with the

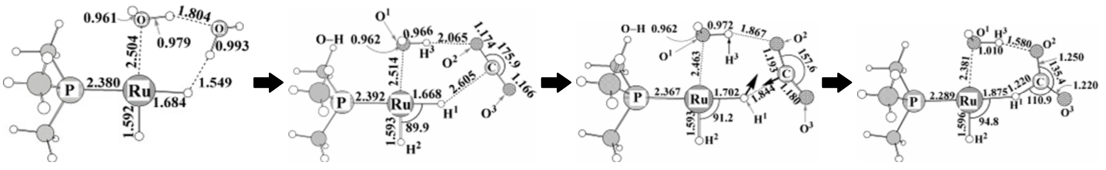

2 **3** **$TS_{3\text{-}4}$** **4**

(269.1 *i* cm^{-1})

Figure 2. Geometry changes by the nucleophilic attack of the hydride ligand to the C center of carbon dioxide in *cis*-$Ru(H)_2(PMe_3)_3(H_2O)(CO_2)$
Bond length is in angstrom and bond angle in degree. In parenthesis is imaginary frequency. Arrows in **$TS_{3\text{-}4}$** represent important movements of nuclei in the transition state.

Ru center in a normal coordination structure. Formation of **2** yields larger stabilization energy than formation of **1**, as shown in eqs 1a and 1b, where the stabilization energy was evaluated with the MP4(SDQ)/BS-II method.

$Ru(H)_2(PMe_3)_3 + H_2O \rightarrow Ru(H)_2(PMe_3)_3(H_2O)$ **1** $\Delta E = -13.6$ kcal/mol (1a)

$Ru(H)_2(PMe_3)_3 + (H_2O)_2 \rightarrow Ru(H)_2(PMe_3)_3(H_2O)_2$ **2** $\Delta E = -24.5$ kcal/mol (1b)

In the next step, CO_2 approaches **2** to form a precursor complex, *cis*-$Ru(H)_2(PMe_3)_3(H_2O)(CO_2)$ **3**, through substitution of H_2O for CO_2, as shown in Figure 2. In **3**, the six-membered ring that consists of Ru, H_2O, and CO_2 distorts little like **2**. It is noted that the $H^3{-}O^2$ distance (2.065 Å) is much shorter than the $H^1{-}C$ distance (2.605 Å). This short $H^3{-}O^2$ distance suggests that **3** is mainly formed by the $H^3{-}O^2$ hydrogen-bonding interaction. The OCO bond angle is 175.9° and the $C{-}O^2$ and $C{-}O^3$ bond distances are 1.174 Å and 1.166 Å, respectively, which are almost the same as those of free CO_2. These geometrical parameters are consistent with the small binding energy of CO_2 with the Ru complex, as will be discussed below.

Starting from **3**, CO_2 approaches the H^1 ligand to afford a formate adduct, $Ru(H)(HCO_2)(H_2O)(PMe_3)_3$ **4** through the transition state **$TS_{3\text{-}4}$**. In **$TS_{3\text{-}4}$**, the OCO bond angle decreases to 157.6°, and $C{-}O^2$ and $C{-}O^3$ distances increase to 1.193 and

1.180 Å, respectively. The H^2−C distance shortens to 1.844 Å, and the Ru−H^1 bond lengthens to 1.702 Å. In the imaginary frequency, the H^1 ligand is approaching the C center of CO_2 and the C center is also approaching the H^1 ligand, as shown by arrows in **$TS_{3\text{-}4}$** of Figure 2. These geometrical features suggest that the hydride (H^1) ligand attacks the C center of CO_2. In **4**, the H^1−C distance is 1.220 Å, which is considerably longer than the usual C−H bond (1.160 Å) of the formate anion. This indicates that the C−H bond of formate forms an agostic interaction with the Ru center, because the H atom of formate is negatively charged and the empty d_σ orbital expands toward the H atom of formate. Interestingly, the rather short distance (1.580 Å) between the H^3 atom of H_2O and the O^2 atom of formate clearly shows that the hydrogen bond between these two atoms becomes stronger in **4** than in **3**. The hydrogen bond and the agostic interaction will be discussed below in more detail. It should be noted here that this reaction from **3** to **4** is quite different from the usual CO_2 insertion into the metal−hydride bond, as follows: The C and O atoms of CO_2 do not coordinate with the Ru center in the reactant **3** and the O atom of formate does not interact with the Ru center in the product **4**; remember that in the absence of water molecule CO_2 coordinates with the Ru center and the CO_2 insertion into the Ru−H bond takes place to afford the Ru-(η^1-OCOH) intermediate in which the O atom of formate coordinates with the Ru center.[12b]

Energy changes of the reaction from **2** to **4** are calculated with various methods, as shown in Table 1. Both the DFT and MP2 to MP4(SDQ) calculations indicate that the substitution of H_2O for CO_2 is moderately endothermic, which means that the interaction between CO_2 and $Ru(H)_2(PMe_3)_3(H_2O)$ is not sufficiently strong. A similar activation barrier (E_a) is calculated with all these computational methods. Although the reaction energy considerably fluctuates at the MP2 and MP3 levels, it converges upon going from MP3 to MP4(SDQ) and the DFT-calculated reaction

Table 1. Energy change $(\Delta E_1)^a$ of the adduct formation of carbon dioxide with *cis*-$Ru(H)_2(PR_3)_3(H_2O)_2$, the activation barrier $(E_a)^a$, and the reaction energy $(\Delta E_2)^a$ of the nucleophilic attack of hydride to carbon dioxide in *cis*-$Ru(H)_2(PR_3)_3(H_2O)(CO_2)$.

	R = Me			R = H[b]		
Method	ΔE_1	E_a	ΔE_2	ΔE_1	E_a	ΔE_2
MP2	7.6	10.8	6.8	8.0	13.6	19.0
MP3	8.2	10.9	−1.5	8.4	13.6	10.3
MP4(D)	7.6	10.9	2.9	7.9	13.6	14.7
MP4(DQ)	7.2	11.4	3.9	7.5	14.1	15.7
MP4(SDQ)	7.3	10.6	3.3	7.7	13.4	15.0
CCSD	−	−	−	7.9	13.4	12.3
CCSD(T)	−	−	−	8.3	12.6	12.2
DFT(B3LYP)	9.0	11.0	3.6	8.8	13.8	13.0
PCM(*n*-heptane)[c]	9.8	11.1	−1.2			
PCM(THF)[c]	9.2	10.8	−5.7			

[a] ΔE_1, E_a and ΔE_2 represent the relative energy of **3** to **2**, that of $\mathbf{TS_{3\text{-}4}}$ to **2**, and that of **4** to **2**, respectively. These values were calculated by MP2–MP4(SDQ), CCSD, CCSD(T) and DFT(B3LYP)/BS-II methods (kcal/mol).

[b] In the single point calculation of R = H, the geometry was taken to be the same as that of R = Me, where the P−H bond length was fixed to 1.430 Å which is optimized value of free PH_3.

[c] The PCM calculations were carried out with the DFT(B3LYP)/BS-II method.

energy is almost the same as the MP4(SDQ)-calculated value. Also, we applied the CCSD(T) method to this reaction, where PMe_3 was replaced with PH_3 because $Ru(H)_2(PMe_3)_3(H_2O)(CO_2)$ was too large to perform the CCSD(T) calculation. As shown in Table 1, the DFT, MP2 to MP4(SDQ), and CCSD(T) methods present similar activation barriers, and the DFT-calculated reaction energy is almost the same as the CCSD(T)-calculated value. Although the MP4(SDQ)-calculated reaction energy is moderately larger than the CCSD(T)- and DFT-calculated values, the difference between them is not large. These results indicate that the DFT and MP4(SDQ) methods present reliable energy changes here. The endothermicity of this reaction is evaluated to be 3.3 and 3.6 kcal/mol with the MP4(SDQ) and DFT methods, respectively.[28] Interestingly, the activation barrier of the hydride attack is considerably smaller than that (16.1 kcal/mol) of the usual CO_2 insertion reaction into the Ru−H bond; in other words, this hydride attack much more easily occurs than the usual CO_2 insertion into the Ru−H bond. Also, it should be noted that the former is slightly endothermic (ΔE = 3.3 kcal/mol) but the latter is considerably endothermic (ΔE = 18.1 kcal/mol). These results directly relate to the acceleration by water molecule, as will be discussed below in more detail.

Solvent effects were investigated with the DPCM method, where we employed parameters of *n*-heptane to mimic hydrophobic atmosphere of supercritical carbon dioxide, as in our previous work,[12b] and those of THF to make a comparison between nonpolar and polar solvents. The activation barrier is little different in the gas phase, *n*-heptane, and THF, while the reaction energy considerably changes; although the nucleophilic attack is endothermic in the gas phase, it becomes slightly exothermic in *n*-heptane and moderately exothermic in THF. The small solvent effect on the activation barrier is interpreted in terms of the reactant-like transition state. The increase in exothermicity by a polar solvent is easily understood by considering that the product **4** is more polar than the reactant **2**. Thus, it is concluded that the polar solvent accelerates this nucleophilic attack and that this nucleophilic attack becomes exothermic (much less endothermic, at least) in super critical carbon dioxide.

2.3.2. Isomerization of Formate Moiety in Ru(H)(OCOH)(H_2O)-(PMe_3)$_3$ Followed by Coordination of a Dihydrogen Molecule

In **4**, the O and H atoms of formate interact with the aqua ligand through the hydrogen bond and with the Ru center through an agostic interaction, respectively,

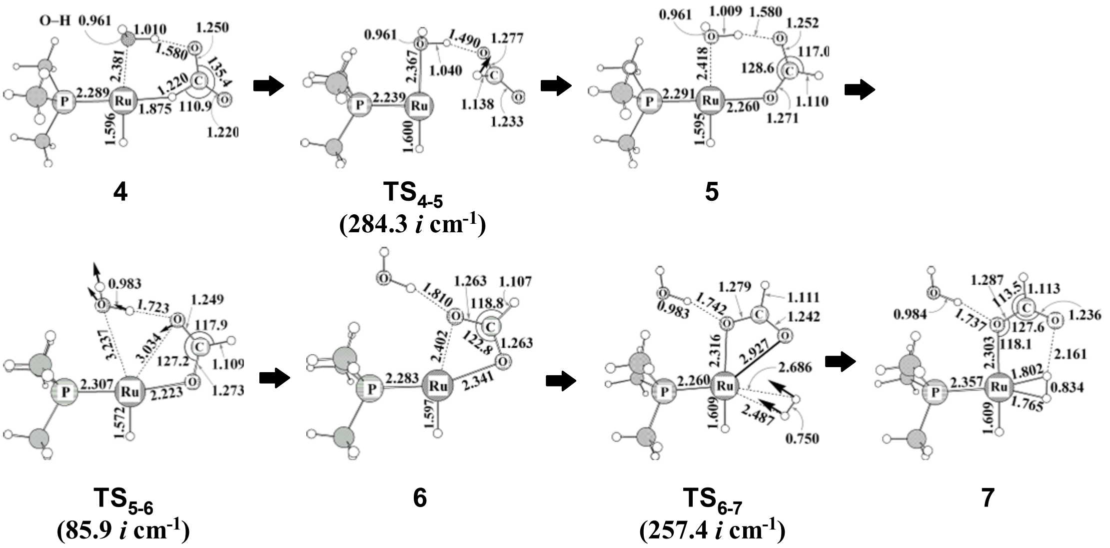

4 **TS$_{4\text{-}5}$** (284.3 *i* cm^{-1}) **5**

TS$_{5\text{-}6}$ (85.9 *i* cm^{-1}) **6** **TS$_{6\text{-}7}$** (257.4 *i* cm^{-1}) **7**

Figure 3. Geometry changes by the isomerization of the formate moiety in *cis*-Ru(H)(PMe$_3$)$_3$(OCOH)(H_2O) followed by coordination of dihydrogen molecule to the Ru center[a)]

Bond length is in angstrom and bond angle in degree. a) In parentheses are imaginary frequency. Arrows in **TS$_{4\text{-}5}$**, **TS$_{5\text{-}6}$** and **TS$_{6\text{-}7}$** represent important movements of nuclei in these transition states.

whereas the formate anion usually coordinates with the metal center through the negatively charged O atom. Thus, **4** is not very stable and the rotational isomerization of the formate anion easily takes place around the C−O bond to afford the usual η^1-formate complex, Ru(H)(η^1-OCOH)(H_2O)(PMe$_3$)$_3$ **5**, through **TS$_{4\text{-}5}$**, as shown in Figure 3. The activation barrier is moderate; it is 6.7 and 6.4 kcal/mol by the DFT and MP4(SDQ) calculations, respectively, as shown in Table 2A. It is noted that this rotational isomerization is considerably exothermic; 17.1 and 22.8 kcal/mol by the DFT and MP4(SDQ) calculations, respectively. In **5**, it is also noted that the H^3−O^2 distance between the aqua and the formate ligands changes little from that of **4**, which clearly shows that the hydrogen bond between the aqua and the formate ligands in **5** is as strong as that in **4**. Thus, the small activation barrier and the large exothermicity mainly come from the formation of the strong Ru−(η^1-OCOH) bond and

Table 2. Activation barriers and reaction energies[a] of the isomerization reaction from $Ru(H)(\eta^1\text{-}HCOO)(H_2O)(PMe_3)_3$ **4** to $Ru(H)(\eta^1\text{-}OCOH)(H_2O)(PMe_3)_3$ **5** and that from **5** to $Ru(H)(\eta^2\text{-}O_2CH)(PMe_3)_3(H_2O)$ **6**

(A) Reaction from **4** to **5**

Method	E_a	ΔE
MP2	6.7 (6.8)[b]	−21.3(−20.0)[b]
MP3	3.7 (3.8)	−25.2 (−23.8)
MP4(D)	5.5 (5.6)	−23.4 (−22.1)
MP4(DQ)	5.4 (5.5)	−23.7 (−22.3)
MP4(SDQ)	6.4 (6.5)	−22.8 (−21.4)
DFT(B3LYP)	6.7 (6.8)	−17.1 (−16.7)
PCM(*n*-heptane)[c]	7.3	−15.8
PCM(THF)[c]	8.8	−14.7

(B) Reaction from **5** to **6**

Method	E_a	ΔE
MP2	7.5 (6.7)[b]	0.4 (−0.5)[b]
MP3	6.8 (6.0)	1.6 (0.7)
MP4(D)	7.1 (6.3)	1.0 (0.1)
MP4(DQ)	6.8 (6.0)	0.7 (−0.2)
MP4(SDQ)	7.2 (6.4)	0.5 (−0.5)
DFT(B3LYP)	4.5 (3.7)	0.0 (−1.0)
PCM(*n*-heptane)[c]	6.3	2.3
PCM(THF)[c]	9.2	5.5

[a] These values are calculated by MP2–MP4(SDQ) and DFT(B3LYP)/BS-II methods (kcal/mol).

[b] With correction of zero-point energy.

[c] The PCM calculations were carried out with the DFT(B3LYP)/BS-II method.

the breaking of the weak agostic interaction between the C−H bond and the Ru center. The solvent effects are not significantly large, as shown in Table 2A; the activation barrier moderately increases in the order gas phase < *n*-heptane < THF, and the exothermicity moderately decreases in the order gas phase > *n*-heptane > THF. This is easily interpreted as follows: two negatively charged O atoms take positions distant from the Ru center in **4**, but one of them coordinates with the Ru center in **5**; in other words, the polarity decreases upon going to **5** from **4**.

Because the formate anion usually coordinates with the metal center as a bidentate ligand, we optimized the Ru-(η^2-formate) complex **6**, in which one water molecule was added to **6** to balance with **5**. The water molecule interacts with the O atom of η^2-formate through a hydrogen-bonding interaction. Intermediate **5** converts to **6** through the transition state $\mathbf{TS_{5\text{-}6}}$ with a moderate activation barrier of 4.5 and 7.2 kcal/mol from the DFT and MP4(SDQ) calculations, respectively, as shown in Table 2B. Interestingly, **6** is as stable as **5**, whereas the η^2-formate ligand more strongly coordinates with the Ru center in **6** than does the η^1-formate ligand. This is interpreted as follows: The Ru−O bond of the Ru-(η^1-formate) complex is stronger than the Ru−O bond of the Ru-(η^2-formate) complex, as clearly shown by the Ru−O^3 bond of **5** being shorter than that of **6** by 0.08 Å. Thus, the Ru−OH_2 bond and one strong Ru−O bond of **5** compensate well two Ru−O bonds of **6**. As a result, **6** is as stable as **5**. Solvent effects are somewhat large here. The activation barrier and endothermicity considerably increase in the order gas phase < *n*-heptane < THF. This is because one negatively charged O atom coordinates with the Ru center in **5**, but two negatively charged O atoms coordinate with the Ru center in **6**; in other words, the polarity of the reaction system decreases upon going to **6** from **5**.

The next step is the coordination of a dihydrogen molecule with **6**. The dihydrogen molecule approaches the Ru center from the right-hand side in Figure 3, to afford the dihydrogen complex, Ru(H)(η^1-OCOH)(H_2)(PMe_3)$_3$(H_2O), **7**, through the transition state **$TS_{6\text{-}7}$**. The geometry of **7** is essentially the same as that of the previously reported dihydrogen complex Ru(H)(η^1-OCOH)(H_2)(PH_3)$_3$;[12b] the distances between the Ru center and the H atom are 1.802 and 1.765 Å, and the H−H distance (0.834 Å) is much longer than the equilibrium distance (0.744 Å by the DFT/BS-I calculation). These geometrical features indicate that the dihydrogen molecule strongly coordinates with the Ru center. This **6** → **7** reaction requires a somewhat large activation barrier because the Ru−O^3 bond should be broken in this reaction; the barrier is calculated to be 7.3 kcal/mol with the DFT method and 8.1 kcal/mol with the MP4(SDQ) method, as shown in Table 3A. The energy of the reaction is −6.6 kcal/mol in the DFT calculation and −7.6 kcal/mol in the MP4(SDQ) calculation. The reaction energy moderately fluctuates at the MP2 and MP3 levels but converges upon going to MP4(SDQ) from MP3, suggesting that the MP4(SDQ) method presents a reliable binding energy of the dihydrogen molecule. Solvation effects are moderate in this process. The activation barrier slightly decreases in the order gas phase > *n*-heptane > THF, and the exothermicity moderately increases in the order gas phase < *n*-heptane < THF. This is because the η^2-formate moiety changes to the η^1-formate moiety upon going to **7** from **6**; in other words, this is reverse of the conversion of **5** to **6**.

Because two molecules participate in this elementary step to form one adduct, the entropy effect should be considered. The $\Delta G^\ddagger$ and $\Delta G_v^\ddagger$ values are estimated to be 16.0 and 10.9 kcal/mol based on DFT-calculated potential energy changes and 16.8 and 11.7 kcal/mol based on the MP4(SDQ)-calculated potential energy changes. If we adopt the $\Delta G^\ddagger$ value in gas phase, this step becomes rate-determining. If we adopt $\Delta G_v^\ddagger$ value without contribution from translation and rotation movements, the metathesis becomes the rate-determining step. These issues will be discussed below

Table 3. Activation barriers and reaction energies[a] of the coordination of dihydrogen molecule to the ruthenium center (**6** → **7**) and the metathesis reaction (**7** → **8**)

(A) Reaction from **6** to **7**

Method	E_a	ΔE
MP2	8.7 (11.9)[b]	−9.8 (−4.7)[b]
MP3	6.9 (10.1)	−7.3 (−2.1)
MP4(D)	7.8 (10.9)	−8.1 (−3.0)
MP4(DQ)	7.8 (11.0)	−8.1 (−3.0)
MP4(SDQ)	8.1 (11.2)	−7.6 (−2.4)
DFT(B3LYP)	7.3 (10.4)	−6.6 (−1.5)
PCM(*n*-heptane)[c]	6.6	−8.0
PCM(THF)[c]	6.0	−8.8

(B) Reaction from **7** to **8**

Method	E_a	ΔE
MP2	12.4 (10.6)[b]	12.9 (12.8)[b]
MP3	16.1 (14.3)	17.0 (16.8)
MP4(D)	13.7 (11.9)	13.8 (13.7)
MP4(DQ)	13.5 (11.8)	13.2 (13.0)
MP4(SDQ)	13.2 (11.4)	13.2 (13.0)
DFT(B3LYP)	9.0 (7.3)	9.3 (9.2)
PCM(*n*-heptane)[c]	10.2	10.3
PCM(THF)[c]	11.2	10.3

[a] These values are calculated by MP2–MP4(SDQ) and DFT(B3LYP)/BS-II methods (kcal/mol).

[b] With correction of zero-point energy.

[c] The PCM calculations were carried out with the DFT(B3LYP)/BS-II method.

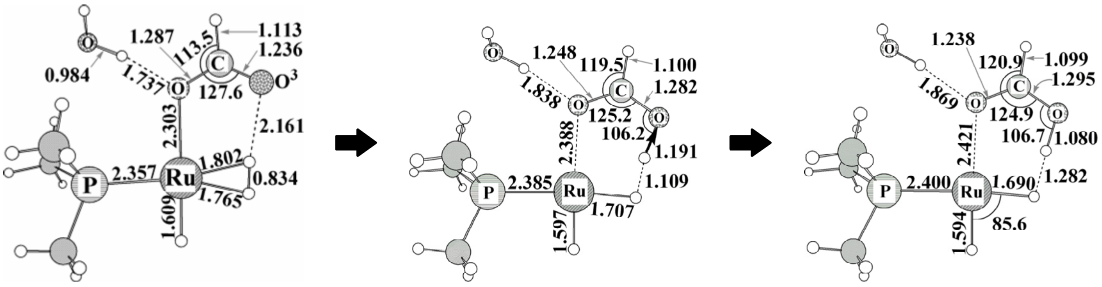

7 **$TS_{7\text{-}8}$** **8**

($761.5\, i$ cm^{-1})

Figure 4. Geometry changes by the metathesis of *cis*-$Ru(H)(PMe_3)_3(\eta^1\text{-}OCOH)$-$(H_2O)$[a)]
In parenthesis is imaginary frequency. a) Arrow in **$TS_{7\text{-}8}$** represents important movements of nuclei in these transition states.

in detail.

Of course, we must consider the possibility that the dihydrogen coordination with the Ru center occurs in **5** without conversion to **6**. This reaction course does not participate in the catalytic cycle, as will be discussed below (Scheme 9).

2.3.3. Metathesis of Dihydrogen Molecule with the Ru-(η^1-OCOH) Complex

Starting from **7**, the metathesis of the Ru-(η^1-OCOH) moiety with a dihydrogen molecule proceeds through **$TS_{7\text{-}8}$**,[30] to form $Ru(H)_2(PMe_3)_3(HCOOH)$ **8**, in which the formic acid coordinates with the Ru center, as shown in Figure 4. The geometry changes by the metathesis are essentially the same as those of the metathesis in the absence of water molecule,[12b] except for the presence of water molecule interacting with formic acid through a hydrogen-bonding interaction. As the metathesis proceeds, the O−H distance between water and formic acid becomes longer, which indicates that the hydrogen bond becomes weaker in the reaction. This is because the O^3 atom of **7** is negatively charged in a formal sense, but it becomes neutral in **8**. As a result, the activation barrier of the metathesis is moderately larger in the presence of water molecule than that in the absence of water molecule, as shown in Table 3B; it is calculated to be 9.0 and 13.2 kcal/mol with the DFT and the MP4(SDQ) methods, respectively, in the presence of water molecule and 4.9 and 9.0 kcal/mol with the DFT and the MP4(SDQ) methods, respectively, in the absence of water molecule. In this step, somewhat large differences between the DFT and MP4(SDQ) methods are observed in the activation barrier and reaction energy. Both activation barrier and reaction energy considerably fluctuate at the MP2 and MP3 levels, but they converge upon going to MP4(SDQ) from MP3. Here, we adopted MP4(SDQ)-calculated energy changes.

The activation barrier and the endothermicity moderately increase in the order gas phase < *n*-heptane < THF. The discussion is omitted here because it was discussed in our previous work.[12b]

2.3.5. Energy Changes along the Whole Catalytic Cycle

Energy changes along whole catalytic cycle are shown in Figure 5, where the correction of zero-point energy is made in Figure 5; note that the values in Figure 5 are different from those of Tables 1−3 because the correction of zero-point energy was not made in those tables. In the absence of water molecule, the Ru-(η^1-OCOH) intermediate is produced by the usual CO_2 insertion into the Ru−H bond, which occurs with a considerably large activation barrier of 17.6 kcal/mol and endothermicity of 21.7 kcal/mol,[12b] where the MP4(SDQ)-calculated values are given.[28] On the other hand, when water molecule is present, the H attack to CO_2 easily takes place with a very small activation barrier of 3.4 (2.1) kcal/mol and exothermicity of 1.6 (2.9) kcal/mol to afford **4**, where the MP4(SDQ)- and DFT-calculated values are given without parentheses and in parentheses, respectively, hereafter. If we take **2** as a

(A) DFT-calculated energy change

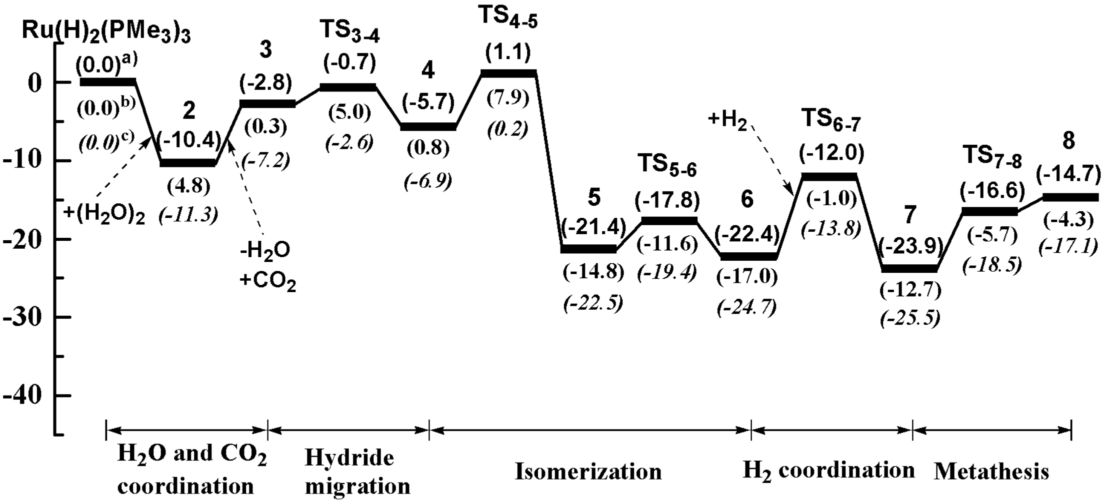

(B) MP4(SDQ)-calculated energy change

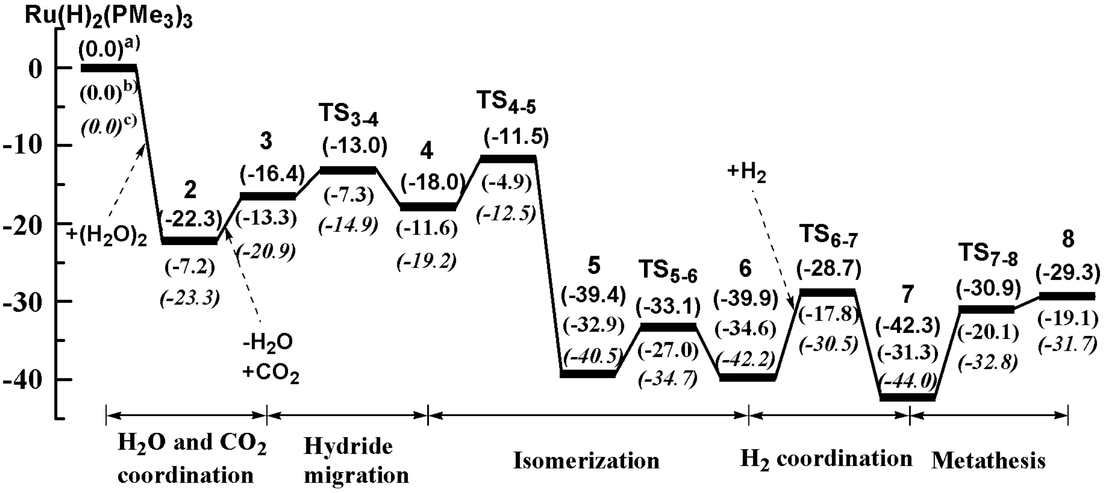

Figure 5. Potential energy change[a)] and free energy change[b,c)] (kcal/mol unit) along the catalytic cycle

a) Potential energy change with correction of zero-point energy. b) In the ΔG value, contributions of translation, rotation, and vibration movements are considered. c) In the ΔG_V value, contributions of vibration movements are considered, while those of translation and rotation movements are neglected.

standard (because **3** is less stable than **2**), then the activation barrier and the endothermicity increase to 9.3 (9.7) kcal/mol and 4.3 (4.7) kcal/mol, respectively. It should be noted that the isomerization of the OCOH moiety easily takes place in **4** with an activation barrier of 6.5 (6.8) kcal/mol and the considerably large exothermicity of 21.4 (15.7) kcal/mol to afford the stable intermediate $Ru(H)(\eta^1\text{-OCOH})(H_2O)(PMe_3)_3$, **5**. Because this intermediate is very stable, the back reaction does not occur. In the absence of water molecule, on the other hand, the coordination of a dihydrogen molecule with $Ru(H)(\eta^1\text{-OCOH})(PMe_3)_3$ must occur to suppress the back reaction because the CO_2 insertion into the Ru−H bond is considerably endothermic;[12b] in other words, the deinsertion of CO_2 more easily occurs with a smaller activation barrier than the CO_2 insertion if the dihydrogen molecule does not coordinate with the Ru center. However, the coordination of the dihydrogen molecule is a bimolecular process, but the isomerization of **4** is a unimolecular process. Moreover, the concentration of dihydrogen molecule is not sufficiently large under the reaction conditions; remember that the yield of formic acid increases with an increase in the dihydrogen pressure.[7b] Thus, the isomerization of **4** more easily takes place than the coordination of a dihydrogen molecule with $Ru(H)(\eta^1\text{-OCOH})(PMe_3)_3$. These results are summarized as follows: (1) A water molecule suppresses the usual CO_2 insertion, which is considerably endothermic. (2) The nucleophilic attack of the H ligand to CO_2 easily takes place to afford the ruthenium(II) hydride η^1-formate intermediate **5**, the reason for which will be discussed below in detail. (3) The thus-formed **5** is extremely stable, and therefore, the back reaction from **5** to **2** does not occur easily.

The next step is the isomerization of the η^1-formate intermediate **5** to the η^2-formate intermediate **6**, the activation barrier of which is calculated to be 6.3 (3.6) kcal/mol. The coordination of a dihydrogen molecule with **6** needs a moderate activation barrier of 11.2 (10.4) kcal/mol. The final step is the metathesis, the activation barrier of which is 11.4 (7.3) kcal/mol. From these results, the rate-determining step is either the metathesis or the coordination of the dihydrogen molecule. Both activation barriers are smaller than that (17.6 kcal/mol) of the CO_2 insertion into the Ru−H bond, which is the rate-determinig step in the absence of a water molecule. Thus, the presence of a water molecule changes the rate-determining step and considerably decreases the activation barrier of the rate-determining step; in other words, the hydrogenation of carbon dioxide is accelerated very much by the presence of water molecules.

We wish to mention here the ΔG surface. The activation free energy change $\Delta G^{\ddagger}$ is little different from the potential energy change in the H attack to CO_2 and the metathesis of **7**, because these two steps are unimolecular process. However, the $\Delta G^{\ddagger}$ value for the coordination of the dihydrogen molecule is 16.8 (16.0) kcal/mol, being much larger than the potential energy change because the coordination of a dihydrogen molecule is a bimolecular process. This value is similar to the $\Delta G^{\ddagger}$ value of the CO_2 insertion, which is the rate-determining step in the absence of water molecule. However, we must remember that the translation and rotation movements are considerably suppressed in supercritical carbon dioxide compared to those in an ideal gas. This means that the decrease in entropy by the coordination of a dihydrogen molecule is overestimated here. If we assumed that translation and rotation movements are completely suppressed, the activation free energy change was given by the $\Delta G_{\mathrm{v}}^{\ddagger}$ value. This value is almost the same as the potential energy change and much smaller than the $\Delta G^{\ddagger}$ value. The true value of the free energy change is between these two values. Summarizing these results, the conclusions are presented as follows: (1) The activation free energy change of the dihydrogen coordination step (**6** → **7**) is smaller than 16.8 (16.0) kcal/mol (see above and Figure 5), i.e., smaller than that of the CO_2 insertion. (2) The activation free energy change of this step (**6** → **7**) could be larger than 11.7 (10.9) kcal/mol, which is almost the same as the $\Delta G^{\ddagger}$ value of the metathesis (**7** → **8**), 11.2 (7.0) kcal/mol (see above and Figure 5). (3) Thus, the dihydrogen coordination step (**6** → **7**) is rate-determining in the presence of water molecules. (4) Because its activation free energy change is smaller than that of the CO_2 insertion, the reaction is accelerated by the presence of water molecules in the free energy surface, too.

At the end of this section, we wish to mention the solvent effects on the whole catalytic cycle. The activation barrier of the dihydrogen coordination step moderately decreases in the order gas phase > *n*-heptane > THF, while the activation barrier of the metathesis increases in the order gas phase < *n*-heptane < THF. Thus, the use of a moderately polar solvent is recommended.

2.3.6. The Reason Water Molecule Accelerates the Hydride Attack to Carbon Dioxide

It is of considerable interest to clarify the reason for the very low activation barrier of the hydride attack. As shown in Figure 6, not only the C atomic population but also the O atomic population considerably increases and the H^1 atomic population considerably decreases in this step. The Ru atomic population considerably decreases, also. This is because the donating hydride ligand is removed from the Ru center to carbon dioxide, which weakens the charge transfer from the hydride ligand to the Ru center. These population changes are consistent with our understanding that the nucleophilic attack of the hydride ligand to carbon dioxide takes place in this step. To understand well these population changes, we investigated the nucleophilic attack of bare hydride to carbon dioxide, as shown in Figure 7, where the geometry of the H---CO_2 moiety was taken to be the same as that of the full reaction system, $Ru(H)_2(PMe_3)_3(H_2O)(CO_2)$. Interestingly, not only the C atom but also the O atom

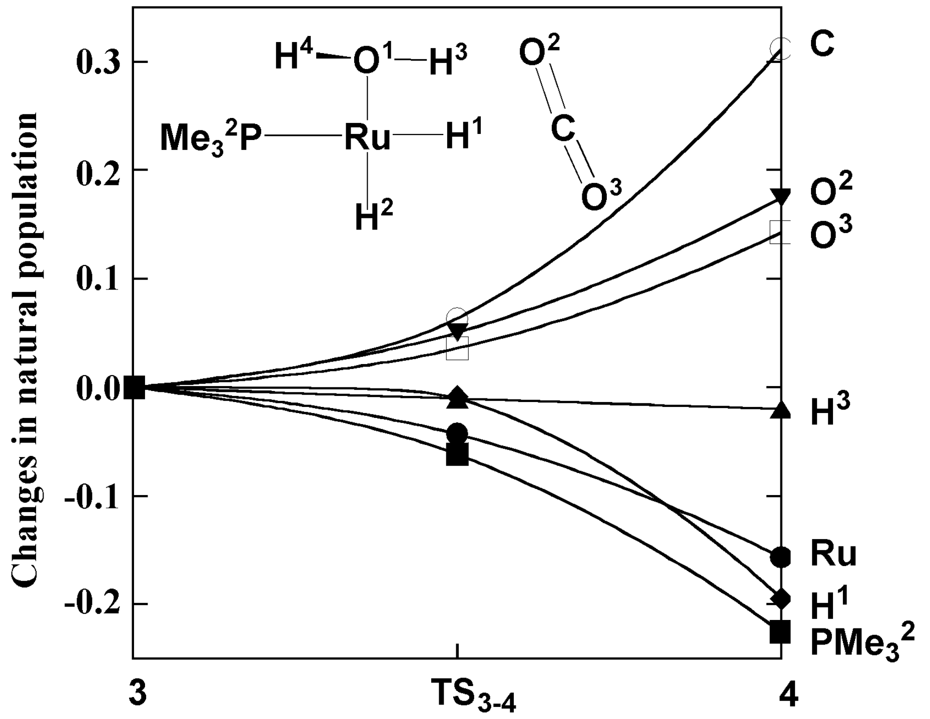

Figure 6. Population changes[a] by the nucleophilic attack of the hydride ligand to carbon dioxide in *cis*-Ru(H_2)(PMe_3)$_3$(H_2O)(CO_2)

a) Positive value represents an increase in population and vice versa

Scheme 6

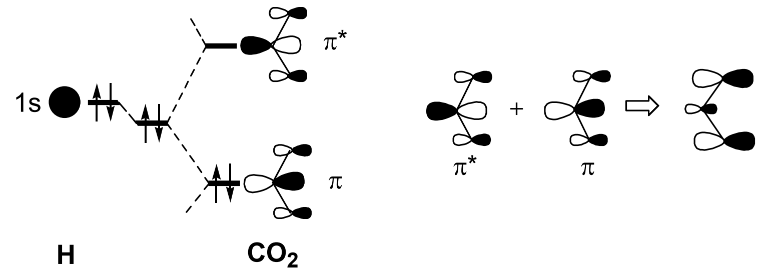

becomes more negatively charged in the model reaction, as was observed in Figure 6. This is because the hydride 1s orbital overlaps with the π* orbital of carbon dioxide in a bonding way, into which the π orbital of carbon dioxide mixes in an antibonding way because the π orbital is at lower energy than the hydride 1s orbital, as schematically shown in Scheme 6.[29] Actually, a similar molecular orbital is observed in the real reaction system; as shown in Figure 8A, the H 1s orbital, which is localized on the H

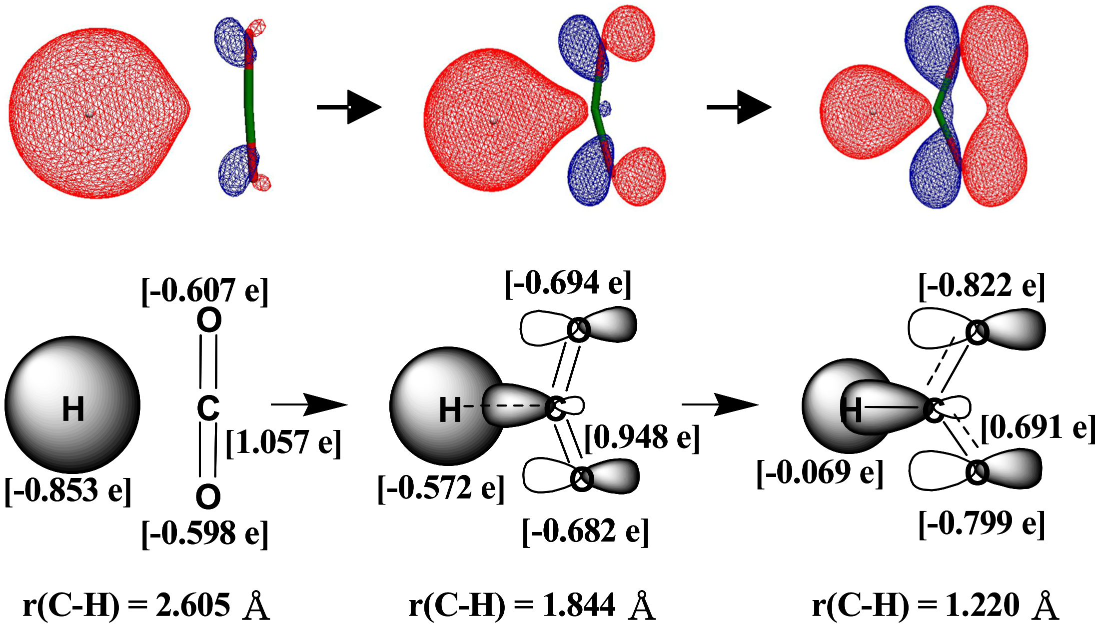

Figure 7. Population changes by the nucleophilic attack of hydride (H$^-$) to free carbon dioxide$^{a)}$

a) NBO populations are given. Geometry of this model system was taken to be the same as that of the nucleophilic attack in *cis*-Ru$(H_2)(PMe_3)_3(H_2O)(CO_2)$

ligand in **3**, starts to overlap with the π^* orbital of carbon dioxide in **TS$_{3\text{-}4}$** and then the p orbital of the O atom becomes considerably large in **4**. This orbital mixing considerably increases the negative charge on the O atoms. As a result, the hydrogen bond between the O atom of CO_2 and the H atom of the water molecule becomes stronger, as the reaction proceeds. Actually, the H---O distance between the aqua ligand and CO_2 becomes shorter, as the nucleophilic attack proceeds. Also, the bonding overlap between the H atom of a water molecule and the O atom of CO_2 becomes large, as shown in Figure 8B, as the reaction proceeds. This hydrogen bond contributes to the stabilization of the transition state and the product. It is of considerable interest to show how much the hydrogen bond contributes to the stabilization energy. The strength of the hydrogen bond is evaluated as follows: In

(A) Molecular orbitals mainly consists of the H 1s orbital

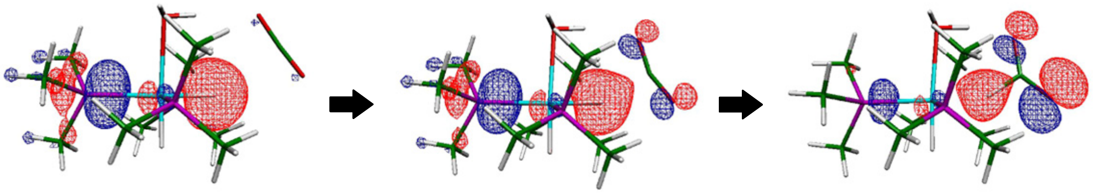

-5.84 eV　-6.23 eV　-6.58 eV

3　TS$_{3\text{-}4}$　4

(B) Molecular orbitals involving the interaction between the H atom of water and the O atom of carbon dioxide

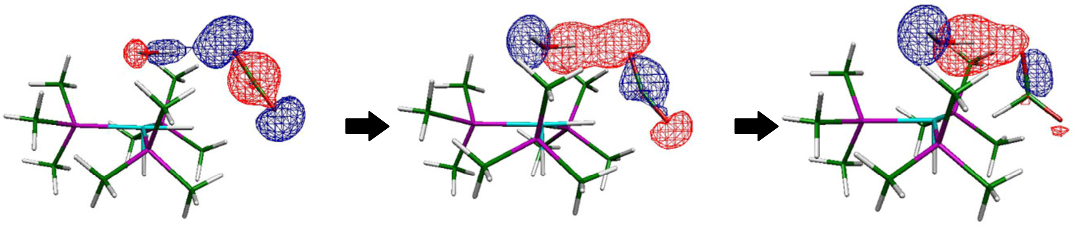

-15.75 eV　-15.22 eV　-14.61 eV

3　TS$_{3\text{-}4}$　4

Figure 8. Changes of Kohn-Sham orbital by the nucleophilic attack of the hydride ligand to carbon dioxide in *cis*-Ru(H)$_2$(PMe$_3$)$_3$(H$_2$O)(CO$_2$)

Scheme 7

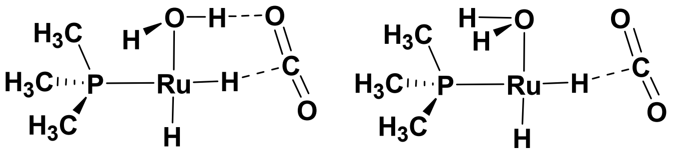

(A) H$_2$O rotation in Ru(H)$_2$(PMe$_3$)$_3$(H$_2$O)(CO$_2$)

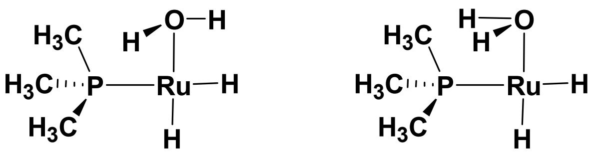

(B) H$_2$O rotation in Ru(H)$_2$(PMe$_3$)$_3$(H$_2$O)

3 and **4**, the orientation of H_2O is rotated by 90° so as to place the H atom at a position distant from CO_2, in which the hydrogen bond is not formed, as shown in Scheme 7A. This orientation change induces the steric repulsion between PMe_3 and H_2O. The increase in the steric repulsion is estimated by calculating the assumed geometry of $Ru(H)_2(PMe_3)_3(H_2O)$ in which the orientation of H_2O is rotated by 90°, as shown in Scheme 7B. The energy difference between the system with the hydrogen bond and that without the hydrogen bond increases from 6.0 kcal/mol in **3** to 11.6 kcal/mol in **TS$_{3\text{-}4}$** and 22.8 kcal/mol in **4**. The steric repulsion is estimated to be 3.3 kcal/mol in **3**, 3.7 kcal/mol in **TS$_{3\text{-}4}$**, and 5.3 kcal/mol in **4**. Thus, the stabilization energy by the hydrogen bond is 2.7 kcal/mol in **3**, but increases to 5.9 kcal/mol in **TS$_{3\text{-}4}$** and 17.5 kcal/mol in **4**. From these results, it is clearly concluded that the transition state and the product are considerably stabilized by the hydrogen bond between CO_2 and the aqua ligand.

Also, the other interesting feature is observed in the C−H bonding region between the H ligand and CO_2, as shown in Figure 8A. In the product **4**, the H 1s orbital interacts with the empty d_σ orbital of the Ru center to form an agostic interaction. This typical agostic interaction between the C−H bond of formate and the empty d orbital of the Ru center also contributes to the stabilization of **4**.

In conclusion, the H attack to carbon dioxide easily takes place in the presence of water molecules by the hydrogen bond and the agostic interaction of the C−H bond with the Ru center.

2.3.7. Nucleophilic Attack of Hydride in the Presence of Alcohol and Amine

From the above discussion, we can expect that the hydride attack to carbon dioxide is accelerated by the molecule that has a lone pair orbital utilized for

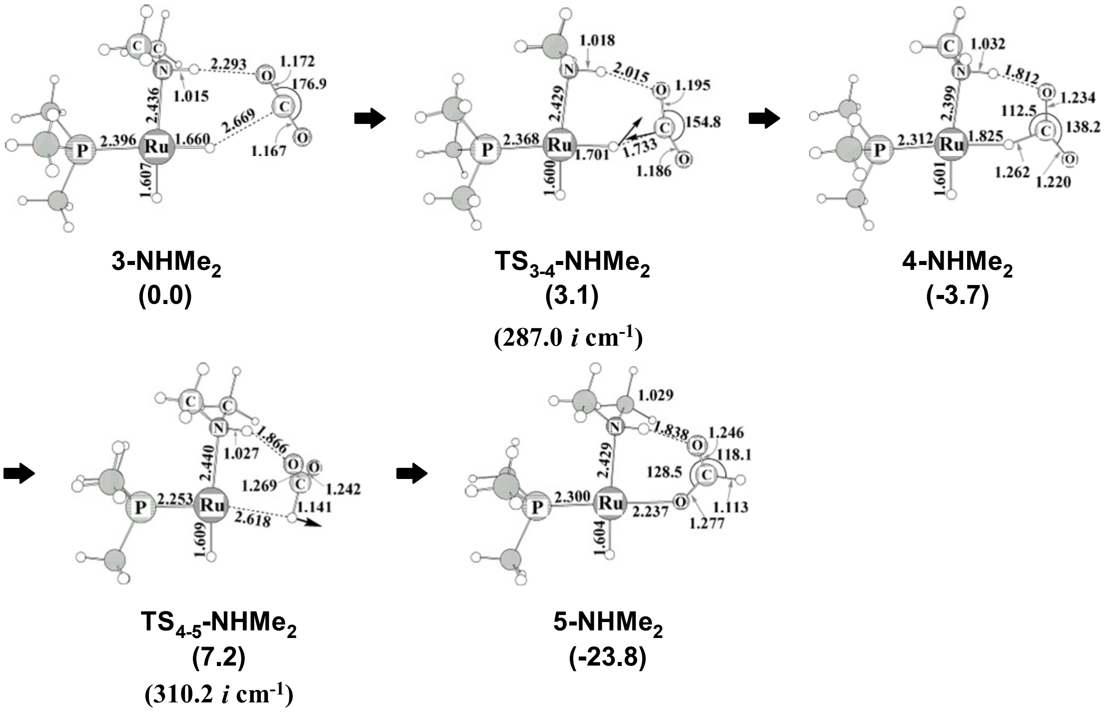

Figure 9. Geometry changes by the nucleophilic attack of the hydride ligand to the C center of carbon dioxide in *cis*-Ru(H)$_2$(PMe$_3$)$_3$(NHMe$_2$)(CO$_2$)
In parenthesis is imaginary frequency. Arrows in **TS$_{3\text{-}4}$-NHMe$_2$** represent important movements of nuclei in the transition state.

coordination with the Ru center and a proton-like hydrogen atom utilized for hydrogen bond with the O atom of CO$_2$. Methanol and dimethylamine are good candidates for such a molecule. Here, we investigated the hydride attack in the presence of methanol, ammonia, and dimethylamine. As shown in Figure 9, the H−N distance between dimethylamine and CO$_2$ becomes shorter as the H attack proceeds. This geometry change is essentially the same as that of the reaction in the presence of water molecules. Almost the same geometry changes are observed in the NH$_3$ and methanol complexes (see Appendix Figures A2 and A3). The activation barrier was evaluated to be 2.1, 2.1, 2.9, and 3.1 kcal/mol for water, methanol, ammonia, and dimethylamine complexes, respectively, with the DFT method. These activation barriers are similar to or slightly larger than that of the reaction of the aqua complex.

Although the reaction of the methanol complex is as exothermic as that of the aqua complex, that of the dimethylamine complex is more exothermic but that of the ammonia complex is less exothermic than that of the aqua complex; the reaction energy is −2.9, −2.6, +0.6, and −3.7 kcal/mol for aqua, methanol, ammonia, and dimethylamine complexes, respectively, where the DFT-calculated values are given. Thus, it is clearly concluded that not only a water molecule but also Lewis base possessing a proton-like H atom are useful to accelerate the hydride attack to CO_2.

2.3.8. Possibilities That the Other Elementary Processes Participate in the Catalytic Cycle

We also examined whether the other elementary process participates in the catalytic cycle. One of such candidates is the possibility that the CO_2 insertion into the Ru−H bond is accelerated by the presence of water molecules. One water molecule interacts with the O atom of CO_2, which coordinates with the Ru center, as shown in Figure 10, because this O atom is less congested than the other O atom of CO_2. The similar interaction of water with CO_2 was previously proposed.[13] The O−H distance between H_2O and CO_2 is 1.87Å in the reactant and becomes somewhat shorter as the CO_2 insertion proceeds. This geometry change suggests that the hydrogen bonding interaction between H_2O and CO_2 becomes stronger in the CO_2 insertion to stabilize the transition state and the product. The activation barrier is evaluated to be 5.4 and 14.7 kcal/mol with the DFT and MP4(SDQ) methods, respectively. These values are moderately smaller than the CO_2 insertion in the absence of water molecule but considerably larger than the hydride attack to carbon dioxide. Moreover, the reaction is considerably endothermic like that in the absence of water molecules; in other words, the deinsertion of carbon dioxide more easily takes place than the insertion. This means that the dihydrogen coordination necessarily

Scheme 8

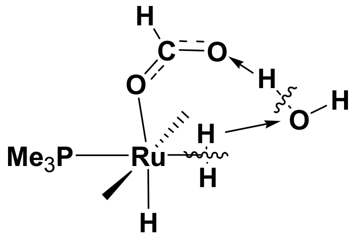

Scheme 9

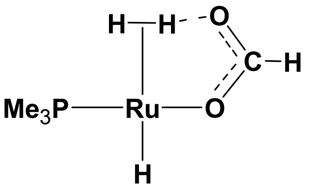

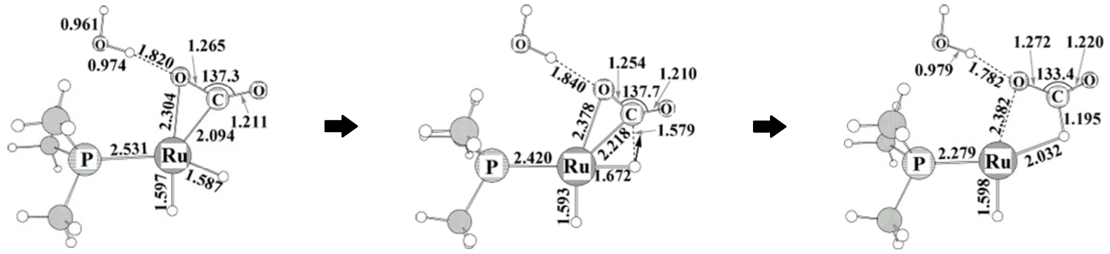

3b
(0.0/*0.0*)

TS$_{3b\text{-}4b}$
(5.4/*14.7*)
(538.8 *i* cm^{-1})

4b
(4.7/*17.4*)

Figure 10. Geometry changes by the insertion of carbon dioxide into the Ru–H bond of *cis*-Ru(H)$_2$(PMe$_3$)$_3$(CO$_2$) in the presence of water molecule[a)]

a) In parenthesis is imaginary frequency. Arrows in **TS$_{3b\text{-}4b}$** represent important movements of nuclei in the transition state. In parentheses are energy changes; normal letter represents the DFT-calculated energy change and italic letter represents the MP4(SDQ)-calculated energy change (kcal/mol unit).

occurs to complete the hydrogenation reaction. Thus, it is concluded that the CO$_2$ insertion is less favorable than the H attack in the presence of water molecules.

The other possible role of the water molecule is to participate in the formation of formic acid by adding a proton to formate and taking a proton from the dihydrogen molecule, as shown in Scheme 8.[8,31] We investigated this water-assisted proton relay reaction, as shown in Figure 11. However, the activation barrier was evaluated to be 13.3 kcal/mol with the DFT method, which is much larger than that (7.3 kcal/mol) of the simple metathesis by 6.0 kcal/mol. From these results, it is concluded that the usual metathesis more favorably occurs than this water-assisted proton relay and that this process is not responsible for acceleration by water molecules.

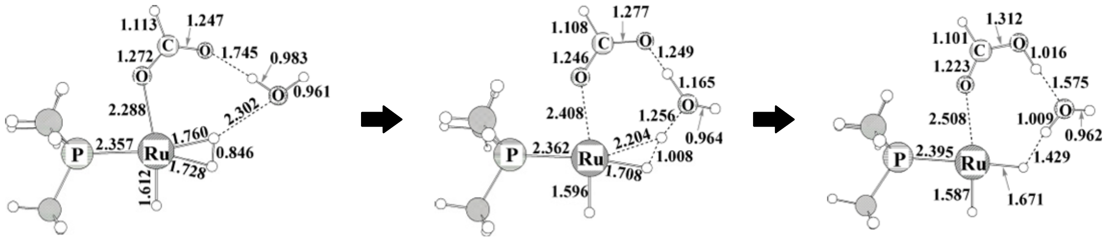

7' **$TS_{7'\text{-}8'}$** **8'**

(1191.9 *i* cm^{-1})

Figure 11. Geometry changes by the water-assisted proton relay reaction of Ru(H)(η^1-OCOH)(PMe$_3$)$_3$ with dihydrogen molecule
Bond length in angstrom and bond angle in degree. In parenthesis is imaginary frequency of the transition state.

We must consider the other possible isomer of the dihydrogen complex in which dihydrogen molecule takes a position trans to hydride, as shown in Scheme 9. This complex is expected to be easily formed through substitution of a water molecule for a dihydrogen molecule in **4**. However, the metathesis does not take place starting from this dihydrogen complex, as was reported previously.[12b] The reason was easily interpreted in terms of the trans influence of the hydride ligand; the product of such metathesis is not stable because two hydride ligands take positions trans to each other.

2.4. Conclusions

Ru-catalyzed hydrogenation of carbon dioxide to formic acid was theoretically investigated with DFT and MP2 to MP4(SDQ) methods, to clarify the reaction mechanism in the absence of water molecules and the reasons that a small quantity of water significantly accelerated this hydrogenation reaction. Several interesting differences are observed between the reactions in the presence and the absence of water molecules, as follows: The active species is *cis*-Ru(H)$_2$(PMe$_3$)$_3$ in the absence of water molecule but *cis*-Ru(H)$_2$(PMe$_3$)$_3$(H$_2$O)$_2$ in the presence of water molecule. The CO$_2$ adduct is also different; in the presence of water molecules, CO$_2$ cannot directly interact with the Ru center but interacts with the hydride and aqua ligands, while carbon dioxide directly coordinates with the Ru center to afford $Ru(H)_2(\eta^2-CO_2)(PMe_3)_3$ in the absence of water molecules. As a result, the Ru-(η^1-formate) intermediate is produced through CO_2 insertion in the absence of water molecules but through nucleophilic attack of the H ligand to CO_2 in the presence of water molecules. The nucleophilic attack easily takes place with a small activation barrier and much less endothermicity (or small exothermicity in super critical carbon dioxide). The rearrangement of the formate moiety to afford RuH(η^1-OCOH)-$(PMe_3)_3(H_2O)$ also easily takes place with a small activation barrier and an extremely large exothermicity. This process stabilizes the reaction system very much; in other words, the back reaction is suppressed by this unimolecular process. After this rearrangement, the dihydrogen molecule coordinates with the Ru center, which needs a moderate activation barrier. The final step is metathesis, which occurs in essentially the same manner as that of the reaction in the absence of water molecules. In the potential energy surface, the metathesis is the rate-determining step. Its activation barrier is much smaller than that of the CO_2 insertion into the Ru−H bond, which is the rate-determining step in the absence of water molecules. In the free energy surface, on the other hand, the coordination of dihydrogen molecule with the Ru center is rate-determining. Although its activation free energy change in the gas phase is estimated to be similar to that of the CO_2 insertion, the real value of the free energy change should be smaller than that of CO_2 insertion because the entropy decreases much less here than in the gas phase.[32] Thus, it should be clearly concluded that the presence of water molecules accelerates the hydrogenation in either potential energy changes or free energy changes.

The acceleration by water molecule arises from the fact that the Ru-(η^1-formate) intermediate is easily formed through nucleophilic attack of the H ligand to CO_2 in the presence of water molecules. This is because the hydrogen-bonding interaction between the H atom of water and the O atom of carbon dioxide becomes stronger in the nucleophilic attack to decrease the activation barrier and the endothermicity. The other reason for the acceleration is that the back reaction from Ru(H)(HCO_2)-(PMe_3)$_3$(H_2O) to the Ru(H)$_2$(PMe_3)$_3$(H_2O)(CO_2) is suppressed by the isomerization of the formate moiety in the presence of the water molecule. In the absence of water molecules, the coordination of the dihydrogen molecule with the Ru center must occur to suppress the deinsertion of CO_2. This coordination process is much exothermic, but this process occurs less easily than the isomerization of the formate moiety because the concentration of dihydrogen molecule is not sufficiently large in the reaction solution and also this is bimolecular process, which occurs less easily than the unimolecular process, such as the isomerization of the Ru-(formate) moiety. Not only water molecules but also alcohols and amines can accelerate the nucleophilic attack in the same manner.

2.5. Appendix

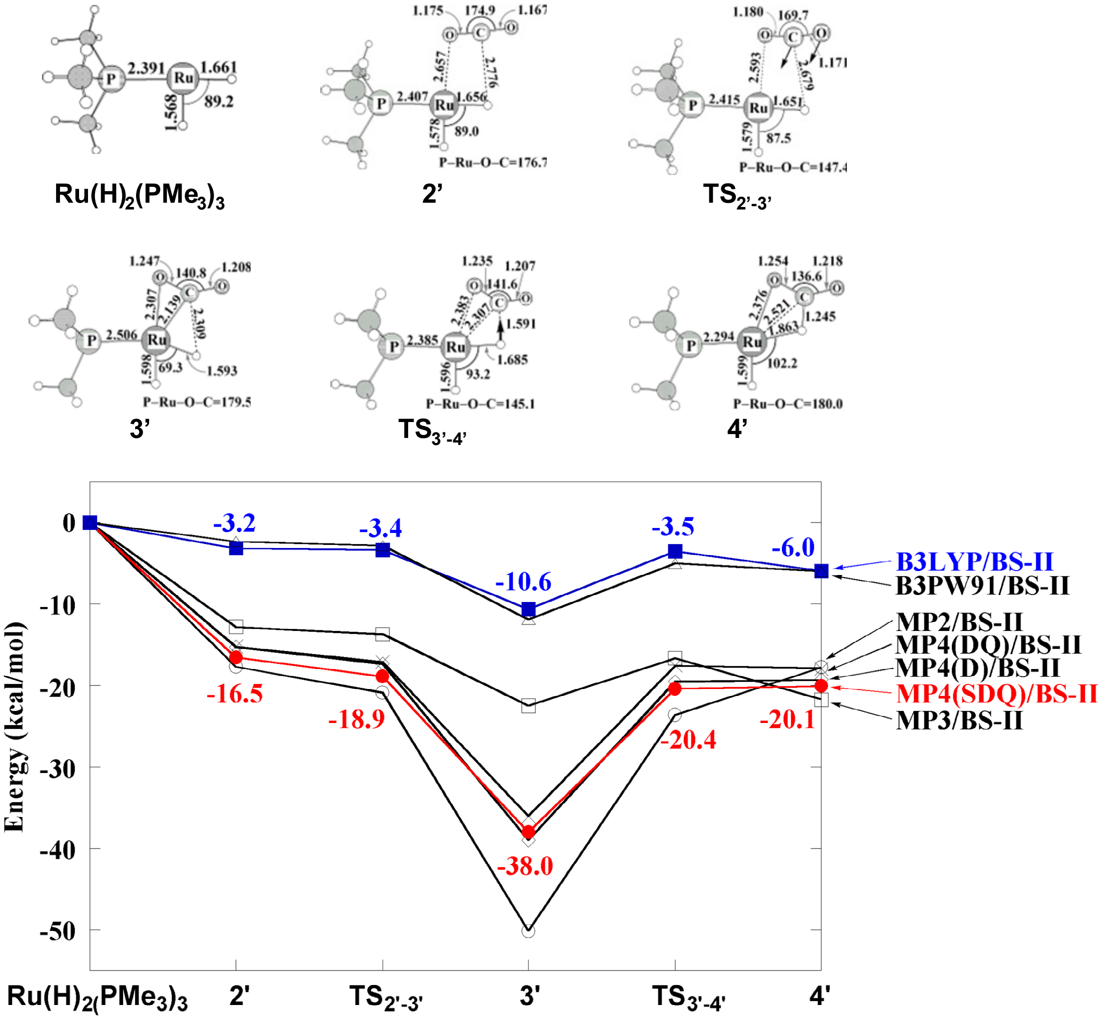

Figure A1. Energy changes of the insertion of carbon dioxide into the Ru–H bond of *cis*-$Ru(H)_2(PMe_3)_3(CO_2)$

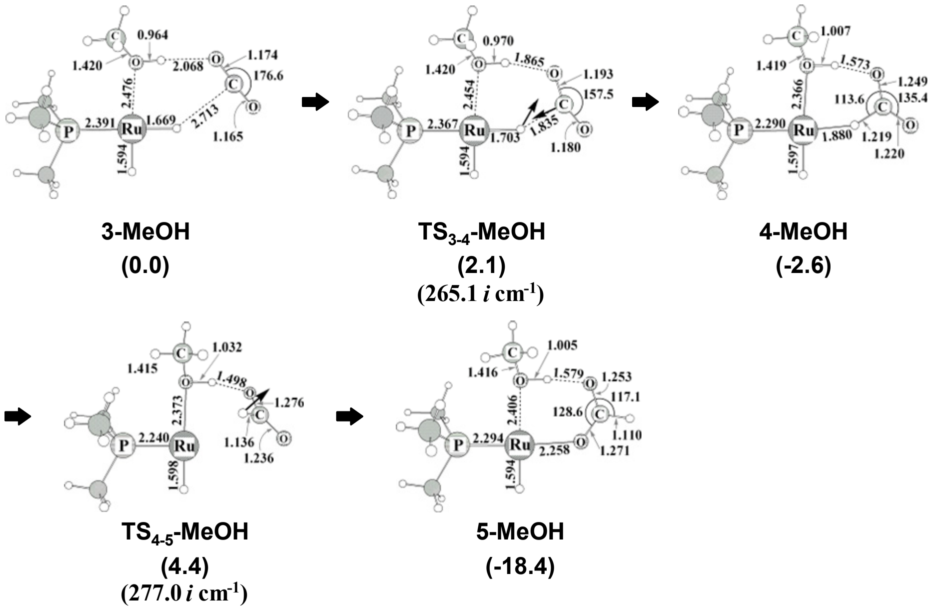

Figure A2. Geometry changes by the nucleophilic attack of the hydride ligand to the C center of carbon dioxide in *cis*-Ru(H)$_2$(PMe$_3$)$_3$(CH$_3$OH)(CO$_2$)

In parenthesis is imaginary frequency. Arrows in **TS$_{3\text{-}4}$-MeOH** represent important movements of nuclei in the transition state.

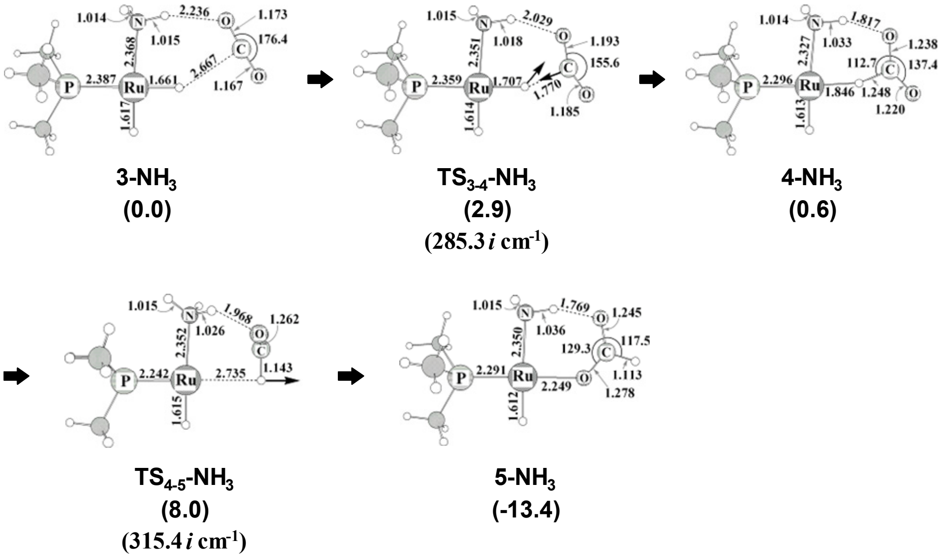

Figure A3. Geometry changes by the nucleophilic attack of the hydride ligand to the C center of carbon dioxide in *cis*-Ru(H)$_2$(PMe$_3$)$_3$(NH$_3$)(CO$_2$)

In parenthesis is imaginary frequency. Arrows in **TS$_{3\text{-}4}$-NH$_3$** represent important movements of nuclei in the transition state.

References

1) (a) Braunstein, P.; Matt, D.; Nobel, D. *Chem. Rev.* **1988**, *88*, 747. (b) Behr, A. *Angew. Chem., Int. Ed. Engl.* **1988**, *27*, 661. (c) Jessop, P. G.; Ikariya, T.; Noyori, R. *Chem. Rev.* **1995**, *95*, 259. (d) Darensbourg, D. J.; Holtcamp, M. W. *Coord. Chem. Rev.* **1996**, *153*, 155. (e) Walther, D.; Rubens, M.; Rau, S. *Coord. Chem. Rev.* **1999**, *182*, 67.

2) Inoue, Y.; Izumida, H. Sasaki, S.; Hashimoto, H. *Chem. Lett.* **1976**, 863. Sasaki, S.; Inoue, Y.; Hashimoto, H. *J. Chem. Soc., Chem. Commun.* **1976**, 605.

3) (a) Darensbourg, D. J.; Ovalles, C. O. *J. Am. Chem. Soc.* **1984,** *106,* 3750. (b) Darensbourg, D. J.; Ovalles, C. O. *J. Am. Chem. Soc.* **1987,** *109,* 3330.

4) Taqui Khan, M. M.; Halligudi, S. B.; Shukla, S. *J. Mol. Catal.* **1989,** *57,* 47.

5) Tsai, J. C.; Nicholas, K. H. *J. Am. Chem. Soc.* **1992**, *114*, 5117.

6) (a) Hutschka, F.; Dedieu, A.; Eichberger, M.; Fornika, R.; Leitner, W. *J. Am. Chem. Soc.* **1997**, *119*, 4432. (b) Hutschka, F.; Dedieu, A. *J. Chem. Soc., Dalton Trans.* **1997**, 1899.

7) (a) Jessop, P. G.; Ikariya, T.; Noyori, R. J. *Nature* **1994**, *368*, 231. (b) Jessop, P. G.; Hsiano, Y.; Ikariya, T.; Noyori, R. *J. Am. Chem. Soc.* **1994**, *116*, 8851. (c) Jessop, P. G.; Ikariya, T.; Noyori, R. *J. Am. Chem. Soc.* **1996**, *118*, 344.

8) Yin, C.; Xu, Z.; Yang, S. -Y.; Ng, S. M.; Wong, K. Y.; Lin, Z.; Lau, C. P. *Organometallics* **2001,** *20,* 1216.

9) Munshi, P.; Main, A. D.; Linehan, J. C.; Tai, C. -C.; Jessop, P. G. *J. Am. Chem. Soc.* **2002,** *124,* 7963.

10) Musashi, Y.; Sakaki, S. *J. Am. Chem. Soc.* **2002**, *124*, 7588.

11) Hutschka, F.; Dedieu, A.; Eichberger, M.; Fornika, R.; Leitner, W. *J. Am. Chem. Soc.* **1997**, *119*, 4432. (b) Hutschka, F.; Dedie, A. *J. Chem. Soc.,*

Dlaton Trans. **1997**, 1899.

12) (a) Musashi, Y.; Sakaki, S. *J. Am. Chem. Soc.* **2000**, *122*, 3867. (b) Ohnishi, Y.; Matsunaga, T.; Nakao, Y.; Sato, H.; Sakaki, S. *J. Am. Chem. Soc.* **2005**, *127*, 4021.

13) Yin, C.; Xu, A.; Yang, S. –Y.; Ng, S. M.; Wong, K. Y.; Lin, Z.; Lau, C. P. *Organometallics* **2001**, *20*, 1216.

14) Matsubara, T. *Organometallics* **2000,** *20,* 19.

15) (a) Becke, A. D. *Phys. Rev. A*, **1988**, *38*, 3098. (b) Becke, A. D. *J. Chem. Phys.* **1993**, *98*, 5648.

16) Lee, C.; Yang, W.; Parr, R. G.. *Phys. Rev. B*, **1988**, *37*, 785.

17) (a) Miertus, S.; Scrocco, E.; Tomasi, J. *Chem. Phys.* **1981**, *55*, 117. (b) Pascual-Ahuir, J. L.; Silla, E.; Tomasi, J.; Bonaccorsi, R. *J. Comput. Chem.* **1987**, *8*, 778. (c) Floris, F.; Tomasi, J. *J. Comput. Chem.* **1989**, *10*, 616. (d) Tomasi, J.; Persico, M. *Chem. Rev.* **1994**, *94*, 2027.

18) (a) Hay, P. J.; Wadt, W. R. *J. Chem. Phys.* **1985**, *82*, 299. (b) Wadt, W. R.; Hay, P. J. *J. Chem. Phys.* **1985**, *82*, 284. (c) Höllwarth, A.; Böhme, M.; Dapprich, S.; Ehlers, A. W.; Gobbi, A.; Jonas, V.; Köhler, K. F.; Stegmann, R.; Veldkamp, A.; Frenking, G. *Chem. Phys. Lett.*, **1993**, *208*, 237.

19) Hehre, W. J.; R. Ditchfield, R.; Pople, J. A. *J. Chem. Phys.* **1972**, *56*, 2257.

20) Krishnan, R.; Binkley, J. S.; Seeger, R.; Pople, J. A. *J. Chem. Phys.* **1980**, *72*, 650.

21) Couty, M.; Hall, M. B. *J. Comput. Chem.* **1996**, *17*, 1359.

22) Ehlers, A. W.; Böhme, M.; Dapprich, S.; Gobbi, A.; Höllwarth, A.; Jonas, V.; Köhler, K. F.; Stegmann, P.; Veldkamp, A.; Frenking, G. *Chem. Phys. Lett.* **1993**, *208*, 111.

23) Dunning, T. H., Jr. *J. Chem. Phys.* **1989,** *90,* 1007.

24) (a) Tamura, H.; Yamazaki, H.; Sato, H.; Sakaki, S. *J. Am. Chem. Soc.* **2003**, *125*, 16114. (b) Sakaki S.; Takayama, T.; Sumimoto, M.; Sugimoto, M. *J. Am. Chem. Soc.* **2004**, *126*, 3332. (c) Sumimoto, M.; Iwane, N.; Takayama, T.; Sakaki, S. *J. Am. Chem. Soc.* **2004**, *126*, 10457.

25) Pople, J. A. et al. *Gaussian 98*, *version A.11.3* Gaussian Inc., Pittsburgh PA, **1998**.

26) Reed, A. E.; Curtis, L.A.; Weinhold, F. *Chem. Rev.* **1988**, *88*, 849, and references therein.

27) Flükiger, P.; Lüthi, H. P.; Portann, S.; Weber, J. *MOLEKEL v.4.3* for Scientific Computing, Manno, Switzerland, 2000-2002. Portman, S.; Lüthi, H. P., *CHIMIA*, **2000**, *54*, 766.

28) (a) The DFT method presented much smaller activation barrier (5.6 kcal/mol) and endothermicity (6.5 kcal/mol) than does the MP4(SDQ) method. The activation barrier considerably fluctuates at MP2 and MP3 levels but seems converge upon going to MP4(SDQ) from MP3 (see ref. 12b and Appendix Figure A1). The small activation barrier by the DFT calculation results from the underestimation of the stabilization energy of the CO_2 complex, $Ru(H)_2(PMe_3)_3(CO_2)$. Our recent theoretical work[28b] clearly shows that the binding energy of π-conjugate system with the transition metal complex is underestimated by the DFT method. Thus, we employed here the MP4(SDQ)-evaluated energy change for the CO_2 insertion step. (b) Kameno, Y.; Ikeda, A.; Nakao, Y.; Sato, H.; Sakaki, S. *J. Phys. Chem. A* **2005,** *109,* 8055.

29) (a) Similar orbital mixing was reported previously.[29b] (b) Sakaki, S.; Aizawa, T.; Koga, N.; Morokuma, K.; Ohkubo, K. *Inorg. Chem.* **1989**, *28*, 103. Sakaki, S.; Ohkubo, K. *Inorg. Chem.* **1989**, *28*, 2583. Sakaki, S. *J. Am.*

Chem. Soc. **1992**, *114*, 2055.

30) The product **8** is calculated to be slightly more stable than the transition state **TS$_{7\text{-}8}$** by 0.3 kcal/mol with the DFT/BS-I method, while **8** is calculated to be in almost the same energy as **TS$_{7\text{-}8}$** with the MP4(SDQ)/BS-II method. However, the correction of zero-point energy more destabilizes **8** in energy than **TS$_{7\text{-}8}$**, and as a result, **8** becomes less stable than **TS$_{7\text{-}8}$**, as shown in Figure 5, though the energy difference is very small. The smaller zero-point energy of **TS$_{7\text{-}8}$** than that of **8** arises from the fact that the O–H stretching of the formate moiety contributes to the zero-point energy of **8** but little to that of **TS$_{7\text{-}8}$** because the O–H stretching is mainly involved in the imaginary frequency. **TS$_{7\text{-}8}$** is considered reasonable from the geometry and the geometry changes in imaginary frequency. Though **8** is in almost the same energy as **TS$_{7\text{-}8}$**, amine was added to the solution in excess under real experimental conditions, to stabilize the product by formation of adduct with formic acid. Thus, the similar stabilities of **8** and **TS$_{7\text{-}8}$** are not unreasonable.

31) Casey, C. P.; Johnson, J. B.; Singer, S. W.; Cui, Q. *J. Am. Chem. Soc.* **2005**, *127*, 3100.

32) The entropy considerably decreases when adduct is formed in gas phase because partition functions of the translation and rotation movements considerably decrease. On the other hand, those movements are highly suppressed in the solution. This means that the entropy decrease in gas phase is much larger than that in solution, in general.

Chapter 3

Theoretical Study of Oxidative Additions of H_2 and MeCN to Nickel(0) Complex: Significantly Large Correlation Effects and Characteristic Features of the Reaction

3.1. Introduction

Activation of the C-CN σ-bond of nitrile by low-valent transition-metal complex is one of the challenging reactions in organometallic chemistry because it is not easy to activate the strong C-CN σ-bond with transition-metal complexes and the C-CN σ-bond activation can be utilized for organic synthesis. As a result of various attempts, several examples of stoichiometric C-CN σ-bond activation reaction by transition-metal complex have been reported, so far: Very previously, σ-bond activation of benzonitrile (PhCN) was succeeded with platinum(0),[1,2] palladium(0),[2] and nickel(0)[2] complexes. Also, C-CN σ-bond activation with nickel(0)[3,4] and molybdenum(0) complexes[5] has been reported. Recently, the C-CN σ-bond activation by nickel(0) complexes was comprehensively investigated by Jones and his collaborators.[6] Though these C-CN σ-bond activation reactions take place through the oxidative addition, different type of C-CN σ-bond activation was performed with help of silyl group in rhodium(III)[7] and iron(II) complexes.[8] Besides these stoichiometric reactions, the C-CN σ-bond activation is included as key elementary step in interesting catalytic reactions, Ni(0)-catalyzed biaryl synthesis[9] and Ni(0)-catalyzed carbocyanation of alkyne.[10]

Considering that nickel(0) complexes have been often used in these stoichiometric and catalytic reactions, it is worth investigating theoretically the C-CN σ-bond activation by nickel(0) complexes. However, no theoretical study has been reported about the C-CN σ-bond activation and no detailed knowledge has been presented about it; for instance, knowledge of transition state structure and electronic process has not been reported yet, though it is necessary to understand well the C-CN σ-bond activation and catalytic reaction via the C-CN σ-bond activation.

As well known, non-dynamical (static) and dynamical electron correlation effects[11] must be carefully considered in theoretical study of nickel complexes. Actually, an outer (second) 3d' shell, which has one nodal plane in radial part like 4d shell, must be included in the active space of the CASPT2 calculation of Ni to present correct energy differences among various electronic states,[12] and incorporation of 3p-3d intershell correlation is necessary for evaluation of energy differences among various electronic states in the first-row transition-metal atoms.[13] These results suggest us to employ properly active space in the multi-reference calculation. Also, many theoretical works have been carried out to evaluate binding energies of nickel(0) complexes with post Hartree-Fock[12-28] and DFT[29-32] methods. However, no organometallic reaction of nickel complex has been theoretically investigated with multi-reference method such as CASPT2 and MRMP2 methods, except for a few limited works;[33] in these pioneering works, the reaction of H_2 with bare Ni atom was theoretically investigated with the CASSCF method, while the active space employed did not include the outer 3d' shell. The lack of multi-reference calculation of chemical reaction is easily understood, as follows: Though active space should be adequately selected to incorporate well non-dynamical correlation effects, such selection cannot be easily made in the case of reaction because orbital energy and orbital nature significantly change in the reaction in general.

Because of the above-mentioned difficulties in theoretical study of nickel complexes, it is necessary to clarify what type of computational method should be applied to organometallic reactions of nickel complexes. In this work, we theoretically investigated oxidative addition of H_2 to $Ni(PH_3)_2$. We selected this reaction as a prototype of Ni(0)-promoted σ-bond activation. Our purposes here are to clarify how much non-dynamic and dynamic correlation effects are important in this type of reaction, what computational method should be applied, and what basis sets should be employed. Then, we theoretically investigated the C-CN σ-bond activation of MeCN by $Ni(PH_3)_2$ with the computational method that provides reliable results about the oxidative addition of H_2 to $Ni(PH_3)_2$. Our purposes of this part are to clarify the characteristic features of this C-CN σ-bond activation reaction and to present detailed understanding of this reaction.

3.2. Computational Method

In the oxidative addition reaction of H_2 with $Ni(PH_3)_2$, reactant, transition state, and product were optimized by the DFT method with B3LYP functional,[34,35] where Wachters basis set (14s9p5d1f)/[9s5p3d1f][36] augmented with an f polarization function,[37] which is called Wa-TZ(f) hereafter, was used for Ni and 6-31G(d,p) basis sets[38] were employed for the other atoms. In all the stationary points, frequency calculations were performed to confirm if it was equilibrium structure or transition state. We also carried out IRC calculation to ascertain if the transition state was connected with the reactant and the product.

Potential energy curves (PECs) were calculated by various methods and various basis sets, as follows: In CASSCF and CASPT2 calculations, (21s15p10d6f)/[6s5p4d2f] basis set,[39] which is called ANO hereafter, was employed for Ni. In CCSD(T), broken-symmetry (Bs) MP2 to MP4(SDTQ),[40] and DFT calculations, ANO, cc-pVTZ,[41] Wa-TZ(f),[36,37] 6-31G(f),[42] and m6-31G(f)[43] were employed for Ni, where one g-polarization function was omitted in cc-pVTZ basis set. These all-electron basis sets are constructed for non-relativistic calculations. Besides, (311111/22111/411/1) basis set[44] was employed for valence electrons of Ni and energy-consistent effective core potentials (ECPs) of the Stuttgart-Dresden-Bonn group were employed to replace its core electrons (up to 2p). This basis set is called SDB. Also, (761/681/51/1) and (7511/6711/411/1) basis sets[45] were employed for valence electrons of Ni and the shape-consistent ECPs of Christiansen, Ermler, and coworkers[45] were employed to replace its core electrons. These basis sets are called CE-DZ and CE-TZ, respectively. These basis sets with ECPs includes relativistic effect in their potentials. BLYP,[34,35] B1LYP,[46] B3PW91,[47] PBE1PBE,[48] and mPW1PW91[49] functionals were employed in DFT calculations. Bs-MP2 to Bs-MP4 methods were also used,[40] where cc-pVTZ basis set was employed for Ni. In all these calculations, cc-pVDZ basis sets were employed for the other atoms. In several CCSD(T) calculations, we used cc-pVTZ basis sets[50] for ligand atoms to examine how much basis sets of ligand moiety influence computational results.

In the CASSCF calculations, three kinds of active space, (4e 4a), (10e 10a), and (12e 12a), were employed, where (*m*e *n*a) represents that the active space consists of *m* electrons and *n* orbitals. These active spaces will be discussed below in detail.

In the oxidative addition reaction of MeCN, all geometries were optimized by the DFT method with either B3LYP or B3PW91 functional, where Wa-TZ(f), SDB, and cc-pVTZ basis sets were employed for Ni and 6-31G(d,p) basis sets for the other atoms. In all the stationary points, frequency calculations were performed to confirm if it was equilibrium structure or transition state. To estimate energy change, the CCSD(T) and DFT methods were employed where Wa-TZ(f), SDB, and cc-pVTZ basis sets were used for Ni and cc-pVDZ basis sets for the other atoms.

We used Gaussian 03 program package[51] for DFT, Bs-MP2 to MP4(SDTQ), and CCSD(T) calculations and MOLCAS (version 5.4) program package[52] for CASSCF and

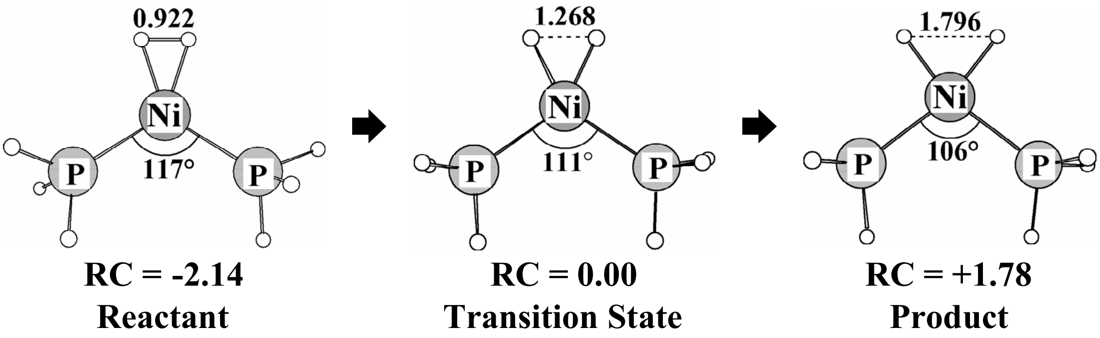

Figure 1. Geometry change in the oxidative addition of H_2 to $Ni(PH_3)_2$ optimized by the DFT(B3LYP) method.[a)] Bond lengths are in angstrom and bond angles are in degree. RC means reaction coordinate obtained by IRC calculation.
a) The Wa-TZ(f) and 6-31G(d,p) basis set was employed for Ni and the other atoms, respectively. All geometries have C_2 symmetry.

CASPT2 calculations. Molecular orbitals were drawn with MOLEKEL program.[53] Population analysis was carried out with the method of Weinhold et al.[54]

3.3. Results and Discussion

3.3.1. Geometry Changes by Oxidative Additions of H_2 and MeCN to $Ni(PH_3)_2$

Geometry changes in the oxidative addition of H_2 to $Ni(PH_3)_2$ are shown in Figure 1, where RC represents reaction coordinate evaluated by IRC calculation with the DFT(B3LYP) method. Although the product, *cis*-$Ni(H)_2(PH_3)_2$, could be optimized by the DFT(B3LYP)/Wa-TZ(f) method, the product became less stable than the transition state when better basis set was employed, as will be discussed below in detail.

In the oxidative addition of MeCN, we investigated the basis set effects on geometries, where we concentrated on transition state because the transition state structure significantly depends on the basis set in the oxidative addition of H_2 to

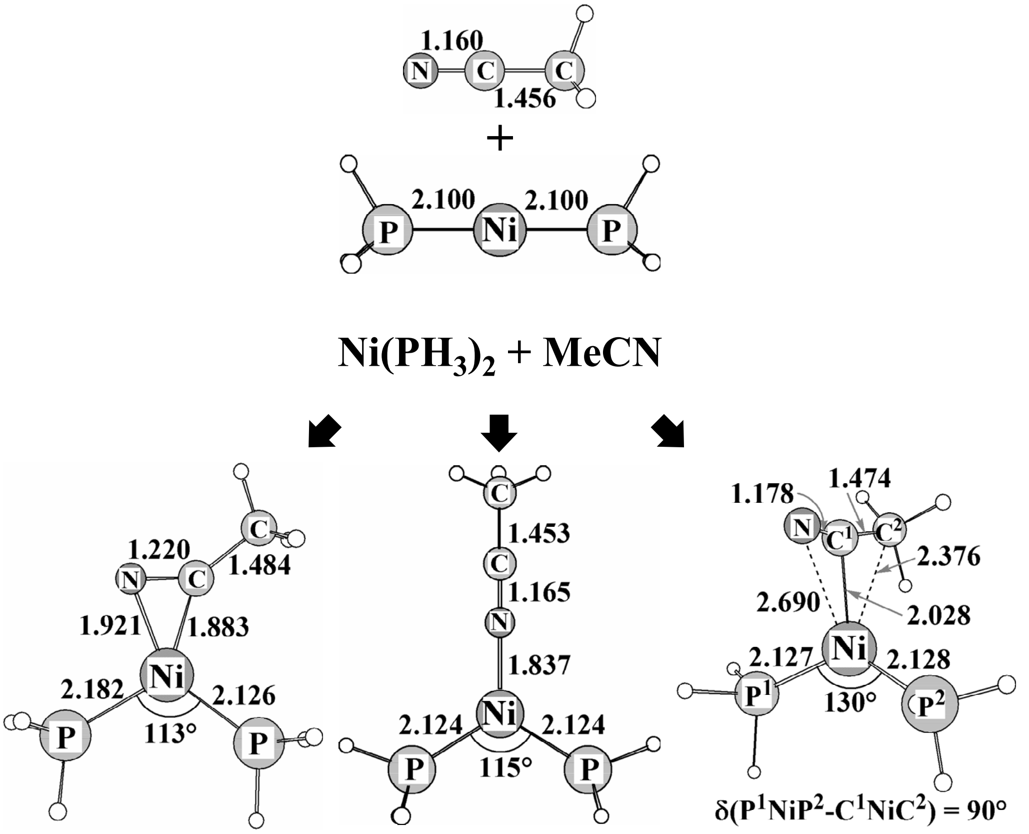

1a **1b** **1c**

Figure 2. Three possible geometries of Ni(PH$_3$)$_2$(MeCN) optimized by the DFT(B3PW91) method.[a] Bond lengths are in angstrom and bond angles are in degree.

a) SDB and 6-31G(d,p) basis sets were employed for Ni and the other atoms, respectively.

Ni(PH$_3$)$_2$. We employed here Wa-TZ(f), cc-pVDZ, and SDB basis sets on Ni and 6-31G(d) on the other atoms; we will show the quality of the cc-pVTZ is enough to present reliable energy changes below. The DFT(B3LYP)/Wa-TZ(f)-optimized transition state structure is considerably different from the DFT(B3LYP)/cc-pVTZ- and DFT(B3LYP)/SDB-optimized ones; for example, the C-CN bond length is calculated to be 1.754 Å by the DFT(B3LYP)/Wa-TZ(f) method but 1.818 Å by the DFT(B3LYP)/cc-pVTZ method (see Appendix Figure A1). On the other hand, the

DFT(B3LYP)/SDB method provides almost the same transition state structure as the DFT(B3LYP)/cc-pVTZ-optimized one. These results indicate that Wa-TZ(f) cannot be used for Ni. Considering that the large size of cc-pVTZ, we employed the SDB basis set for Ni in geometry optimization of the oxidative addition of MeCN to $Ni(PH_3)_2$ hereafter.

Then we optimized geometries of reactant complex $Ni(PH_3)_2(MeCN)$ **1a-1c**, transition state $\mathbf{TS_{1\text{-}2}}$, and product *cis*-$Ni(CN)(Me)(PH_3)_2$ **2** with the DFT(B3LYP) and DFT(B3PW91) methods, as shown in Figure 2. Though both of these two methods yield similar geometries of reactant, transition state, and product, the DFT(B3LYP) method failed to optimize one of the reactant complexes **1c** in which the C atom of CN group interacts with the Ni center (see Appendix Figure A2 for the DFT(B3LYP)-optimized geometry changes). This is easily understood in terms of the fact that the C atom of CN weakly interacts with $Ni(PH_3)_2$ in **1c** and B3LYP functional is not useful very much for such a weak interaction; note that B3PW91 functional is better than B3LYP functional for van der Waals interaction.[55] It is concluded here the DFT(B3PW91)/SDB method should be used for geometry optimization.

3.3.2. Energy Changes by Oxidative Additions of H_2 and MeCN to $Ni(PH_3)_2$

To investigate what computational method and basis sets present reliable potential energy curve (PEC), we evaluated the energy changes by the oxidative addition of H_2 to $Ni(PH_3)_2$ with such computational methods as CASSCF, CASPT2, CCSD(T), Bs-MP2 to Bs-MP4(SDTQ), and DFT methods and various basis sets for Ni, where the DFT(B3LYP)/Wa-TZ(f)-optimized geometries were employed (see Figure 1). The CASSCF(4e 4a) method presents the downhill PEC, as shown in Figure 3. The (4e 4a) active space consists of occupied Ni(d), Ni(d) + H(1s), unoccupied Ni(d), and Ni(d) −

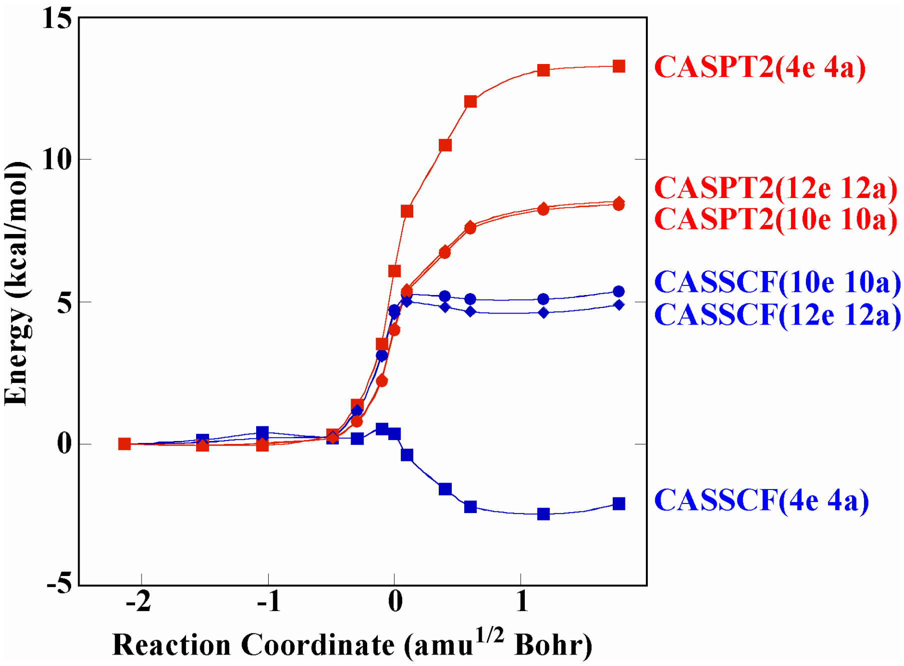

Figure 3. Potential energy curves of the oxidative addition of H_2 to $Ni(PH_3)_2$ calculated by the CASSCF and CASPT2 methods with the various active spaces[a)]
a) ANO and cc-pVDZ basis sets were employed for Ni and the other atoms, respectively.

H(1s) orbitals, as shown in Figure 4, where "+" and "–" represent bonding and antibonding combinations, respectively. The $Ni(d_\sigma) + H_2(\sigma)$ combination is observed in canonical orbital, as shown in Figure 4. Although we included this orbital in the (4e 4a) active space, it changed to Ni(d) orbital during CASSCF calculation. This change suggests that intra 3d-shell correlation is important. It is noted that CASPT2 calculation with the same active space presents completely uphill PEC, which is totally different from the CASSCF(4e 4a) calculation. CASSCF(10e 10a) and CASSCF(12e 12a) calculations present uphill PEC, too, where the active space (10e 10a) consists of five occupied 3d orbitals and five second 3d' (outer 3d) orbitals, as shown in Figure 4. The active space (12e 12a) contains occupied $3p_z$ and unoccupied $4p_z$ orbitals in addition to 10 electrons and 10 orbitals of the (10e 10a) active space. We added these

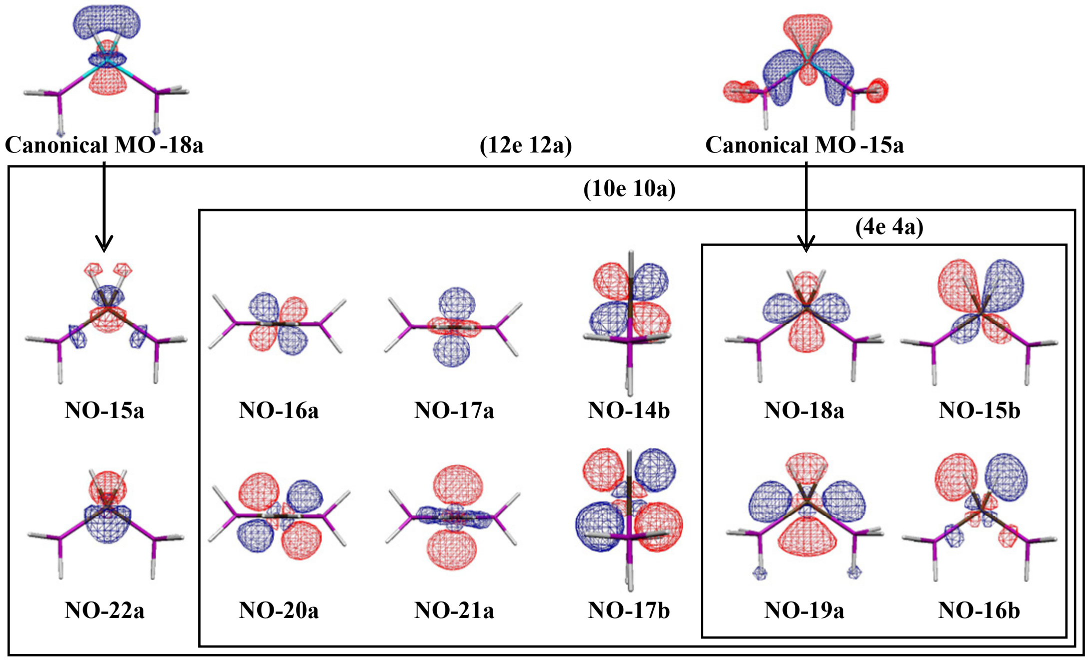

Figure 4. Pseudonatural orbitals (NOs) in the CASSCF calculations.

occupied $3p_z$ and unoccupied $4p_z$ orbitals to the active space, because the importance of 3p-3d correlation was reported previously.[13] In this CASSCF(12e 12a) calculation, we included canonical MO-18a shown in Figure 4. However, this orbital changed to NO-15a during the CASSCF calculation. This means that the 3p-3d correlation is more important than the correlation arising from the dihydrogen σ orbital. The CASPT2(10e 10a) and CASPT2(12e 12a) calculations present more uphill PECs than those by CASSCF calculations with the same active spaces, indicating that dynamical correlation plays important role in this reaction. Also, it is noted that (10e 10a) and (12e 12a) active spaces present almost the same PECs in both CASSCF and CASPT2 calculations. From these results, it should be concluded that (10e 10a) is necessary to incorporate well non-dynamic correlation effects in this reaction but (4e 4a) is too small, the dynamical correlation plays important role in this oxidative addition, and the CASPT2(10e 10a) method provides the reliable energy change of this oxidative addition reaction.

Then, we carried out CCSD(T), Bs-MP4, and DFT calculations, where the DFT(B3LYP)/Wa-TZ(f)-optimized geometries were employed (Figure 1). As shown in Figure 5, the endothermicity is calculated to be 7 kcal/mol by the CCSD(T)/ANO method. This is slightly smaller than the CASPT2(10e 10a)/ANO-calculated value by about 1.5 kcal/mol. To investigate basis set effects, cc-pVTZ, SDB, CE-TZ, CE-DZ, Wa-TZ(f), 6-31G(f), and m6-31G(f) were employed for Ni, where cc-pVDZ basis sets were employed for the other atoms. It is noted that the CCSD(T)/cc-pVTZ method presents almost the same PEC as that of the CCSD(T)/ANO method. When the other basis sets are employed for Ni, however, CCSD(T)-calculated PEC becomes completely different from the CASPT2(10e 10a)/ANO- and CCSD(T)/ANO-calculated ones. On the other hand, the CCSD(T)-calculated endothermicity little depends on the basis sets of ligand moiety; it is calculated to be 6.9 and 6.7 kcal/mol with cc-pVDZ and cc-pVTZ basis sets, respectively, where cc-pVTZ basis set was employed for Ni. Here, we wish to mention the relativistic effect on the PEC. The Douglas-Kroll-Hess second order scalar relativistic effect moderately decreases the endothermicity to 4.8 kcal/mol by about 2 kcal/mol in CCSD(T) calculation (see Appendix Figure A3). Also, it should be noted that the shape of PEC is still uphill and essentially the same that by non-relativistic calculations and completely different from the PECs by the CCSD(T)/SDB and CE-TZ. This result indicates that the relativistic effect is not large in this system. We will present discussion based on non-relativistic calculations.

In Bs-MP2 to Bs-MP4(SDTQ) calculations, PEC considerably fluctuates, as shown in Figure 6; actually, the reaction is calculated to be exothermic by Bs-HF, Bs-MP2, Bs-MP3, Bs-MP4(D), and Bs-MP4(DQ) methods but endothermic by Bs-MP4(SDQ) and Bs-MP4(SDTQ) methods. The Bs-MP4(SDTQ) method yields almost the same endothermicity as that of the CASPT2(10e 10a)/ANO method.

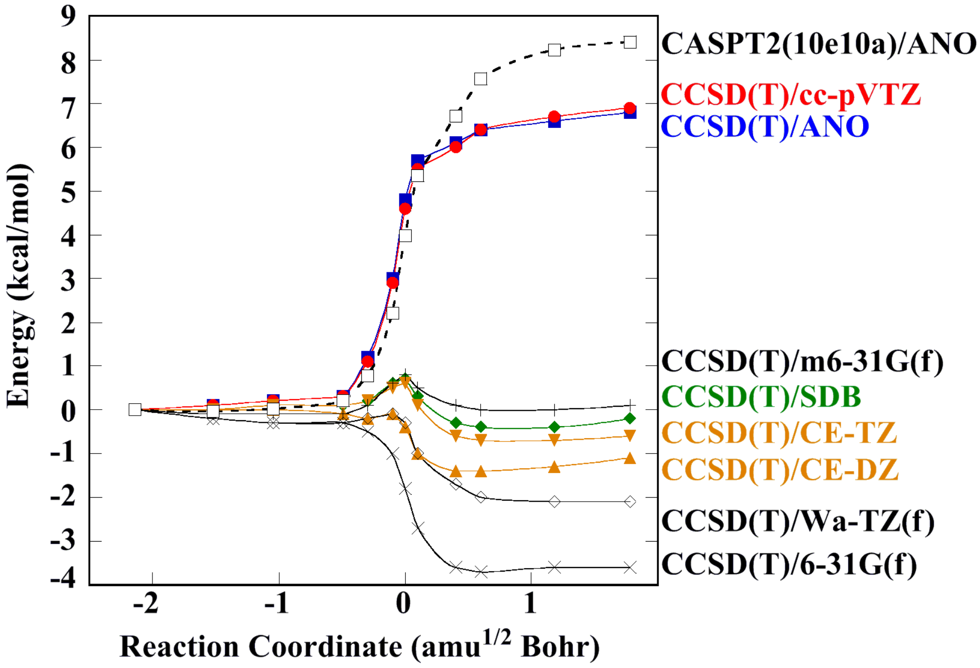

Figure 5. Potential energy curves of the oxidative addition of H_2 to $Ni(PH_3)_2$ calculated by the CCSD(T) method[a)]

a) The various basis sets were employed for Ni and cc-pVDZ basis sets were employed for the other atoms.

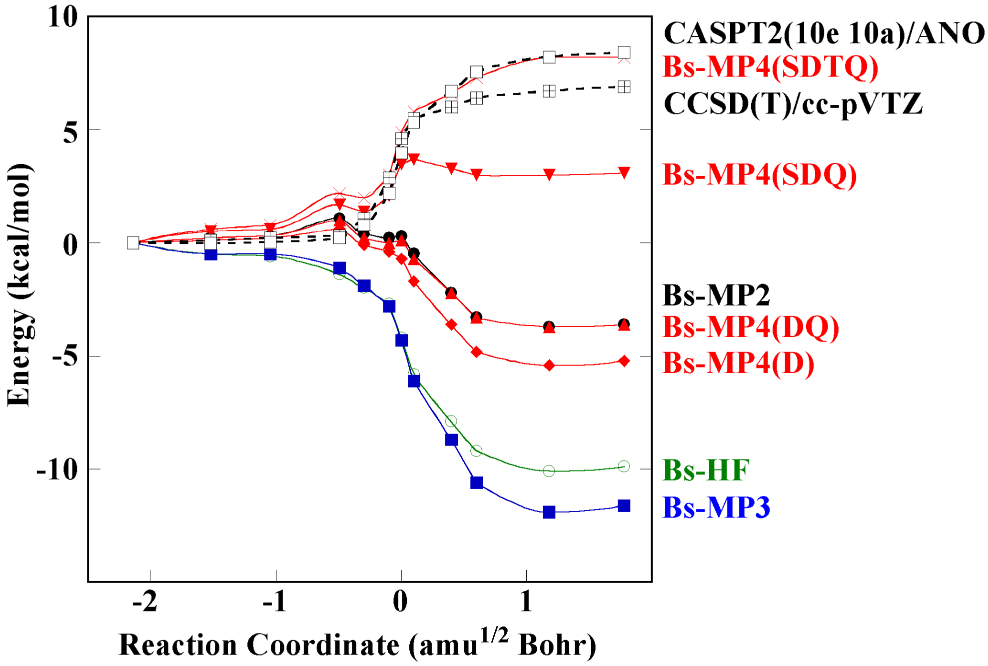

Figure 6. Potential energy curves of the oxidative addition of H_2 to $Ni(PH_3)_2$ calculated by the broken symmetry (Bs) MP2 to MP4(SDTQ) methods. [a)]

a) The cc-pVTZ and cc-pVDZ basis sets were employed for Ni and the other atoms, respectively.

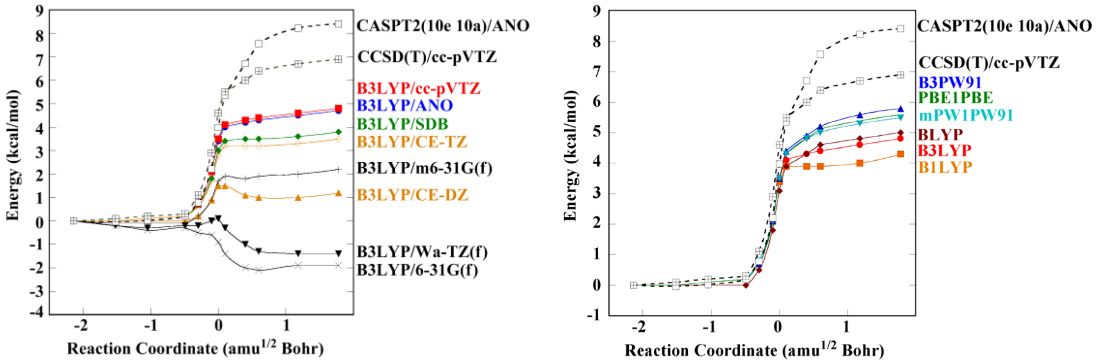

(A) Basis set effects[a)]   (B) Dependence on functional[b)]

Figure 7. Potential energy curves of the oxidative addition of H_2 to $Ni(PH_3)_2$ calculated by the DFT method

a) The various basis sets were employed for Ni and cc-pVDZ basis sets were employed for the other atoms. b) The cc-pVTZ and cc-pVDZ basis sets were employed for Ni and the other atoms, respectively.

However, the Bs-MP4(SDTQ)-calculated PEC is not smooth around TS, though the fluctuation is small, being less than 0.5 kcal/mol. This non-smooth PEC is interpreted in terms of fluctuation of singlet biradical nature; the $\langle S^2 \rangle$ value of Bs-HF wavefunction slightly increases from 0.5943 to 0.6064 upon going from RC = −2.14 to RC = −0.49 but then considerably decreases from 0.6064 to 0.3207 upon going from RC = −0.49 to RC = +1.78 (see Appendix Table A1). This change of $\langle S^2 \rangle$ value indicates that the singlet biradical nature slightly increases upon going from RC = −2.14 to RC = −0.49 but starts to decrease considerably after RC = −0.49.[40] From these results, it is concluded that Bs-MP4(SDTQ) method should be applied carefully to this oxidative addition reaction, in particular, around TS.

In DFT calculations, basis set effects were first examined with B3LYP functional, as shown in Figure 7(A). The DFT/ANO and DFT/cc-pVTZ methods yield uphill PEC like the CCSD(T)/ANO and CASPT2(10e 10a)/ANO methods, while the endothermicity is somewhat smaller than the CASPT2(10e 10a)/ANO- and

CCSD(T)/ANO-calculated values. The DFT/SDB and DFT/CE-TZ methods present further smaller endothermicity than the DFT/ANO and DFT/cc-pVTZ methods, though the difference is small. DFT/m6-31G(f)- and DFT/CE-DZ-calculated PECs are still uphill but considerably different from CCSD(T)/cc-pVTZ- and DFT(B3LYP)/cc-pVTZ-calculated PECs. Both DFT/Wa-TZ(f) and DFT/6-31G(f) methods give completely different PECs from those of the CCSD(T)/ANO and CASPT2(10e 10a)/ANO methods. It is concluded that though basis set effects are not large in DFT calculation in general, basis sets better than triple-zeta quality should be employed for Ni in this type of reaction.

Energy changes also somewhat depend on functional, as shown in Figure 7(B). B3PW91, PBE1PBE, and mPW1PW91 present almost the same endothermicity, which is still smaller than those of the CCSD(T)/ANO and CASPT2(10e 10a)/ANO methods but moderately larger than those of B3LYP, BLYP, and B1LYP. Moreover, PECs calculated with B3PW91, PBE1PBE, and mPW1PW91 functionals are smooth, while those calculated with B3LYP, B1LYP, and BLYP are not.

We evaluated the energy changes of the oxidative addition of MeCN to $Ni(PH_3)_2$ with the CCSD(T)/cc-pVTZ method, because this method presents reliable energy changes in the oxidative addition of H_2 to $Ni(PH_3)_2$, where the DFT(B3PW91)/SDB-optimized geometries were employed. The activation barrier (E_a) is defined as an energy difference between $\mathbf{TS_{1\text{-}2}}$ and **1a** because **1a** is the most stable reactant complex. The reaction energy is defined as either an energy difference (ΔE_1) between the product **2** and the sum of reactant or the energy difference (ΔE_2) between **2** and the most stable reactant complex **1a**. As shown in Table 1, the E_a value is about 35 kcal/mol. This large E_a value indicates that this oxidative addition occurs with difficulty. The ΔE_1 value is -15.8 kcal/mol, but the ΔE_2 value is 14.7 kcal/mol; in other words, the product **2** is more stable than the sum of reactants but less stable than

Table 1. Energy changes (kcal/mol) by the oxidative addition of MeCN to $Ni(PH_3)_2$

Basis set for Ni	Method	**1a**a)	**1b**a)	**1c**a)	$\mathbf{TS_{1\text{-}2}}$ (E_a)b)	**2**	
						ΔE_1c)	ΔE_2d)
cc-pVTZ	CCSD(T)	-30.5	-20.3	-7.1	5.4 (36.9)	-15.8	14.7
	DFT(B3PW91)	-26.4	-18.7	-3.0	10.7 (37.1)	-7.7	18.7
	DFT(B3LYP)	-22.0	-16.3	0.7	14.9 (36.9)	-5.7	16.3
SDB	CCSD(T)	-33.9	-18.9	-5.5	1.2 (35.1)	-25.5	8.4
	DFT(B3PW91)	-25.5	-17.6	-2.4	11.3 (36.8)	-7.6	17.9
	DFT(B3LYP)	-21.6	-15.4	1.4	15.1 (36.7)	-6.5	15.1
Wa-TZ(f)	CCSD(T)	-48.2	-27.7	-15.6	-16.5 (31.7)	-45.8	2.4
	DFT(B3PW91)	-43.0	-28.6	-13.8	-8.5 (34.5)	-32.1	10.9
	DFT(B3LYP)	-38.7	-26.2	-10.5	-4.4 (34.3)	-30.3	8.4

a) The energy difference between $Ni(PH_3)_2(MeCN)$ and the sum of $Ni(PH_3)_2$ and MeCN. b) The energy difference between $\mathbf{TS_{1\text{-}2}}$ and **1a**. c) The energy difference between **2** and the sum of $Ni(PH_3)_2$ and MeCN. d) The energy difference between **2** and **1a.**

1a. These results indicate that the difficulty of this oxidative addition arises from the presence of too stable reactant complex **1a**.

Also, we evaluated the energy changes with the CCSD(T), DFT(B3PW91), and DFT(B3LYP) methods with three basis sets for Ni to examine if the DFT method is useful or not in this reaction; note that it is important information how much the DFT-calculated energy deviates from that of the CCSD(T)/cc-pVTZ method because the CCSD(T)/cc-pVTZ method can not be applied to the large system but the DFT/cc-pVTZ method can be applied. When cc-pVTZ and SDB are employed for Ni, the similar activation barrier (E_a) is evaluated by CCSD(T), DFT(B3PW91), and DFT(B3LYP) methods, while the DFT method moderately underestimates the stability of **2**. When Wa-TZ(f) basis set is employed for Ni, all methods present considerably different energetics from the CCSD(T)/cc-pVTZ-calculated one; for example, the DFT(B3LYP)/Wa-TZ(f) and DFT(B3PW91)/Wa-TZ(f) methods give moderately different E_a value and considerably different ΔE_1 and ΔE_2 values from those of the

CCSD(T)/cc-pVTZ method. These results show that Wa-TZ(f) cannot be used for these oxidative addition reactions of Ni(0) complex, as observed in the oxidative addition of H_2 to $Ni(PH_3)_2$.

These results lead to several important conclusions, as follows: (1) Either ANO or cc-pVTZ basis set should be used for Ni in the CCSD(T) calculation but SDB, CE-TZ, CE-DZ, Wa-TZ(f), 6-31G(f), and m6-31G(f) basis sets cannot be used. (2) The reliable energy changes are calculated with CASPT2(10e 10a)/ANO, CCSD(T)/ANO, and CCSD(T)/cc-pVTZ methods. (3) The Bs-MP4(SDTQ)/cc-pVTZ method should be used carefully around transition state. (4) In DFT calculation, ANO, cc-pVTZ, SDB, and CE-TZ should be used, while CE-DZ, m6-31G(f), Wa-TZ(f), and 6-31G(f) basis sets cannot be used. (5) The DFT methods are useful to evaluate activation barrier. (6) We must be careful about the tendency of the DFT method to underestimate moderately the binding energy and the reaction energy.

3.3.3. Origin of Electron Correlation Effects

It is worth discussing the origin of the significantly large electron correlation effects in the oxidative addition of H_2 to $Ni(PH_3)_2$. We inspected the electron population of natural orbitals (NOs) evaluated by the CASSCF(10e 10a) method. As shown in Figure 8(A), the populations of NO-15b, NO-16b, NO-18a, and NO-19a considerably change while the remains little change. This means that these four orbitals play key role in the reaction. Consistent with these population changes, the weight of configuration 2 suddenly increases around TS but that of configuration 3 decreases around TS, as shown in Figure 8(B). The configuration 2 consists of two-electron excitation from NO-15b to NO-16b, where NO-15b and NO-16b mainly include Ni(d) + H(1s) bonding interaction and its antibonding counterpart, respectively. Thus, the configuration 2 becomes important, when Ni-H bond is formed. The

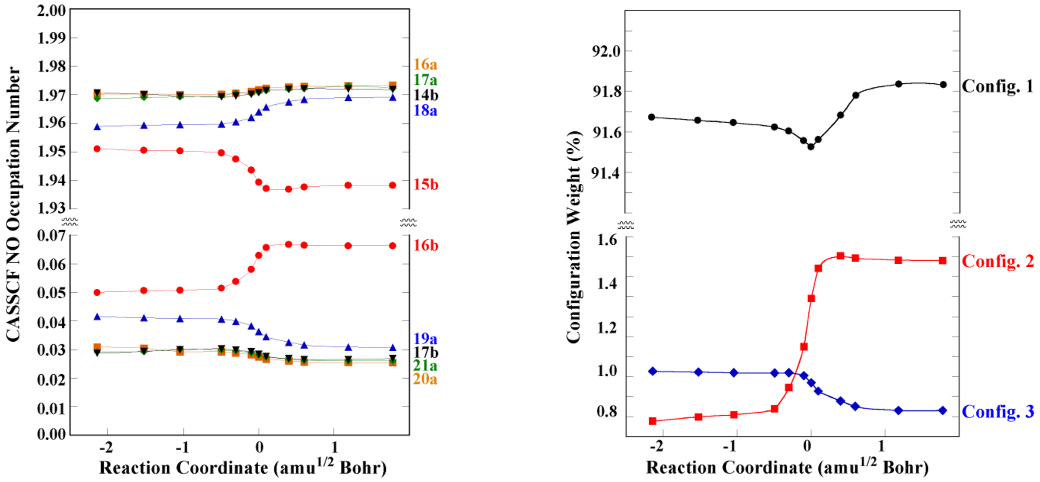

(A) Changes of NO occupation numbers (B) Changes of configurationn weights

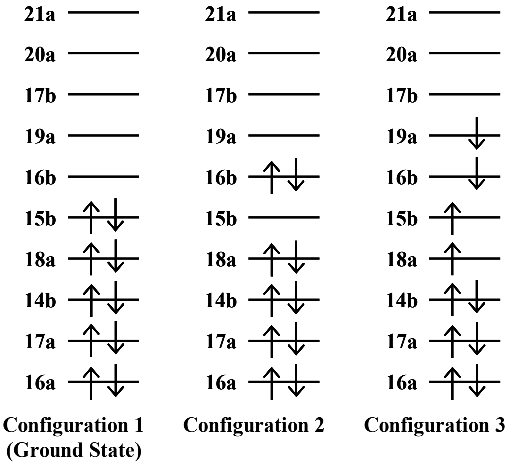

(C) Schematic representation of configurations

Figure 8. Occupation numbers of pseudonatural orbitals (NOs) and configuration weights in the oxidative addition of H_2 to $Ni(PH_3)_2$.

configuration 3 mainly consists of one-electron excitation from NO-18a to NO-19a and that from NO-15b to NO-16b, where NO-18a and NO-19a mainly involve 3d and the outer (second) 3d' orbitals, respectively. Because the Ni-H bond is little formed before TS, this configuration corresponds not to the correlation effect of the Ni-H bond but to intra 3d-shell correlation. In the CASSCF(4e 4a) calculation, these four orbitals are involved in the active space. However, the CASSCF(4e 4a)- and CASPT2(4e 4a)-calculated PECs are considerably different from the CASSCF(10e 10a)- and CASPT2(10e 10a)-calculated PECs, as discussed above. This significantly large difference indicates that the other type of electron correlation plays important roles. The (10e 10a) active space includes five doubly-occupied 3d and the five outer (second) 3d' orbitals which have one nodal plane in radial part like 4d-shell, as shown in Figure 4. The distributions and energies of 3d electrons significantly change in the oxidative addition reaction because the oxidation state of the metal center increases by 2 in a formal sense. It is noted that the 3d' orbital with nodal plane is necessary to describe well the electron re-distributions and energy changes of 3d electrons by this reaction. This type of electron correlation effect is understood as "in-out" correlation.[12] In the first-row transition-metal complexes, this type of correlation is in particular important, because the 3d orbitals are directly influenced by change of metal oxidation state due to the absence of inner d shell.[56]

3.3.4. Characteristic Feature of Oxidative Addition of MeCN to Ni(0) Complex

Here, we will discuss the characteristic features of the oxidative addition reaction of MeCN to $Ni(PH_3)_2$. In the reactant complex, three possible isomers were optimized, as already shown in Figure 2. In **1a**, the CN triple bond directly interacts with Ni. This η^2-CN side-on coordination form is the most stable. The η^1-end-on coordination

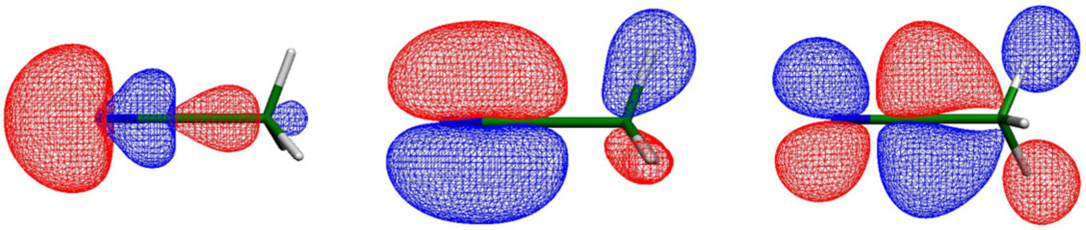

Lone pair
-9.87 eV

CN π
-9.01 eV

CN π*
0.90 eV

Figure 9. Three important molecular orbitals[a] of MeCN
a) Kohn-Sham orbital. Surface value is 0.05 a.u.

form **1b** is the next and the η^1-C interacting form **1c** is the least stable. In **1a**, the C-N bond considerably lengthens to 1.220 Å. This is because MeCN coordinates to Ni mainly through the charge transfer from the Ni d_π orbital to the CN π* orbital; in other words, π-back-donation plays important role. This π-back-donation is also responsible to the longer Ni-N distance than the Ni-C distance, as follows: The C p_π orbital more contributes to the CN π* orbital than the N p_π orbital, as shown in Figure 9, which leads to larger overlap between Ni d_π and C p_π orbitals than that between Ni d_π and N p_π orbitals, as shown in Scheme 1A. In **1b**, the CN bond length (1.165 Å) is almost the same as that of free MeCN (1.160 Å). In this form, the π-back donation somewhat participates in the coordinate bond, while its contribution is smaller than that in **1a** because the CN π* orbital less overlaps with the Ni d_π orbital than does the C p_π orbital due to the smaller contribution of N p_π orbital than that of C p_π orbital in the CN π* orbital, as shown in Scheme 1B. The N lone pair orbital also participates in the coordinate bond through σ-donation (see also Scheme 1B). The π-back donation leads to lengthening of the CN bond, while the σ-donation leads to shortening of the CN bond.[57] As a result, the CN bond length little changes by the coordination. In **1c**, the C atom of CN mainly interacts with Ni; actually, the Ni-N distance is considerably longer than the Ni-C distance. The CN (1.178 Å) bond is moderately longer than that

Scheme 1. Bonding interaction between Ni(PH_3)$_2$ and MeCN

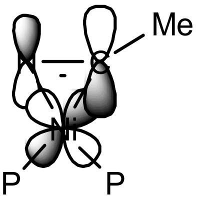

(A) η^2-side on coordination form (**1a**)

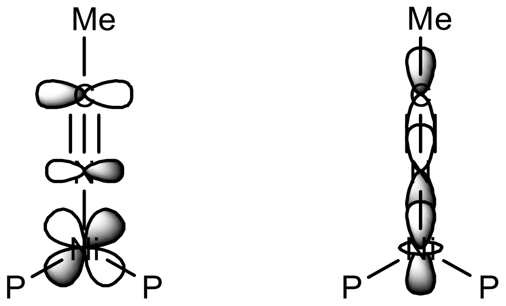

(B) η^1-end on coordination form (**1b**)

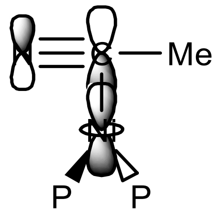

(C) η^1-C coordination form (**1c**)

Table 2. Population changes[a)] by coordination of MeCN with $Ni(PH_3)_2$

	1a	**1b**	**1c**
Ni	-0.4528	-0.3236	-0.2519
Ni(3d)	-0.2853	-0.1550	-0.0608
$PH_3{}^1$	0.0137	0.1273	0.0565
$PH_3{}^2$	0.0150	0.1273	0.0565
MeCN	0.4241	0.0691	0.1389

a) Positive value means increase in electron population and vice versa.

of free MeCN. This is easily interpreted in terms of the back-donation from the Ni d_σ to the CN π^* orbital, as shown in Scheme 1C. This back-donation in **1c** is weaker than in **1a**, as follows: the Ni d_σ orbital interacts with the CN π^* orbital more weakly than does the Ni d_π orbital, because the d_π orbital is HOMO and at higher energy than the d_σ orbital.[58,59] The strength of back-donation can be als uonderstood from the population changes of MeCN, as shown in Table 2. In **1a**, the population of MeCN considerably increases by the coordination, indicating that the considerably strong π-back donation is formed between Ni and MeCN, as discussed above. The electron population of MeCN moderately increases in **1c** and the least in **1b**. These population changes are consistent with the above discussion that the π-back donation mainly participates in the coordinate bond of **1c** but both of the σ-donation and π-back donation participate in the coordinate bond of **1b** in a similar extent.

In transition state $\mathbf{TS_{1\text{-}2}}$, the C-CN bond considerably lengthens to 1.808 Å and the Ni-CN distance shortens to 1.803 Å, as shown in Figure 10, which is moderately shorter than that in the product, interestingly. It is also noted that the $Ni\text{-}CH_3$ distance is considerably longer than the Ni-CN distance. These geometrical features suggest that the Ni-CN bonding interaction induces the C-CN bond cleavage, which will be discussed below. It is also noted that the C-CN bond is not coplanar to the PNiP plane but the dihedral angle between PNiP and CNiC planes is 143°. This type of non-planar

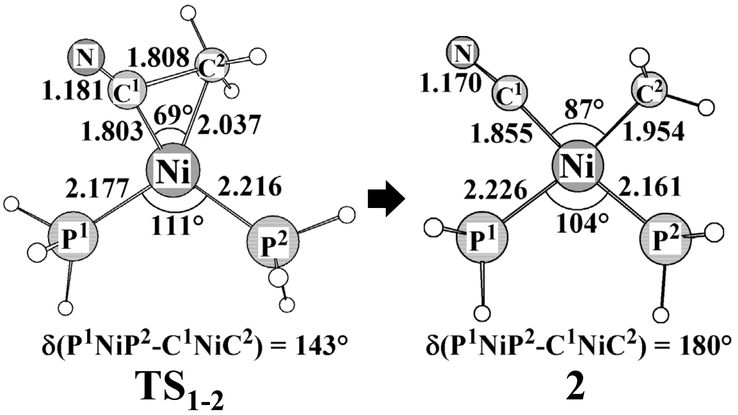

Figure 10. Geometry change in oxidative addition of MeCN to $Ni(PH_3)_2$ optimized by the DFT(B3PW91) method, where SDB and 6-31G(d,p) basis sets were employed for Ni and the other atoms, respectively. Bond lengths are in angstrom and bond angles are in degree.

transition state structure was reported previously and analyzed in the oxidative additions of CH_3-CH_3 and CH_3-SiH_3 to $Pt(PH_3)_2$.[60] We omit the discussion of the non-planar transition state structure here because detailed discussion was presented previously.[60]

The product **2** is completely square planar. The Ni-P^1 bond is longer than the Ni-P^2 bond, indicating that the *trans*–influence effect of CH_3 is stronger than that of CN. This is because the Me group is electron-donating and the CN group is electron-withdrawing. We investigated oxidative addition of ethane, C_2H_6, to $Ni(PH_3)_2$ to clarify characteristic features of oxidative addition of MeCN to Ni(0) by making comparison between C_2H_6 and MeCN. In this reaction, the reactant complex could not be optimized.[61] In the transition state $\mathbf{TS_{3\text{-}4}}$, the Ni-C distance is 1.942 Å, being moderately shorter than that of $\mathbf{TS_{1\text{-}2}}$ but somewhat longer than the Ni-CN distance of $\mathbf{TS_{1\text{-}2}}$, as shown in Figure 11. The Ni-P distance is slightly longer than the Ni-P^1 distance of $\mathbf{TS_{1\text{-}2}}$ and moderately shorter than the Ni-P^2 distance of $\mathbf{TS_{1\text{-}2}}$. This transition state is non-planar, too, in which the dihedral angle is 114°. The product,

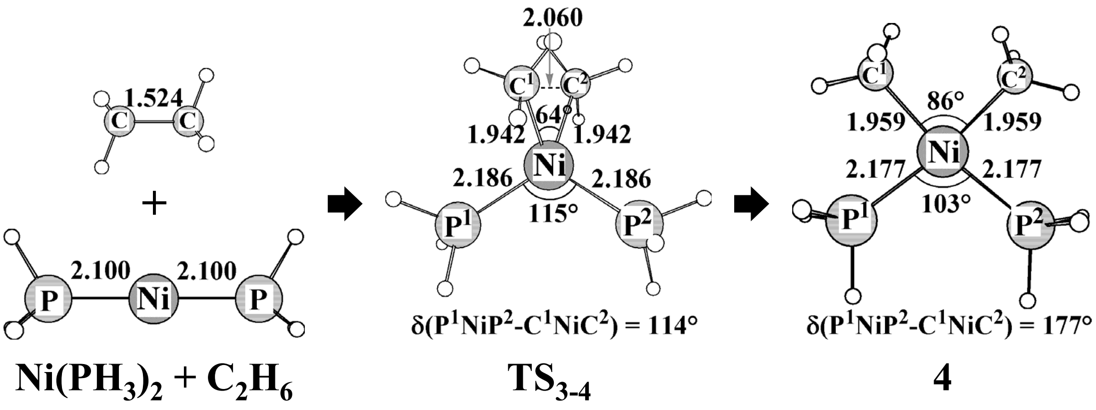

Figure 11. Geometry change in oxidative addition of ethane to $Ni(PH_3)_2$ optimized by the DFT(B3PW91) method, where SDB and 6-31G(d,p) basis sets were employed for Ni and the other atoms, respectively. Bond lengths are in angstrom and bond angles are in degree.

cis-$Ni(Me)_2(PH_3)_2$ **4**, is a typical four-coordinate planar complex. The Ni-CH_3 distance is almost the same as that of **2**.

In the oxidative addition of C_2H_6 to $Ni(PH_3)_2$, **TS$_{3\text{-}4}$** and **4** are 25.2 (31.5) and 6.5 (13.8) kcal/mol less stable than the sum of reactants $Ni(PH_3)_2$ + C_2H_6, as shown in Figure 12, where the values without and with parentheses are CCSD(T)- and DFT(B3PW91)-calculated values, respectively, hereafter. This activation barrier is much smaller than that of the oxidative addition of MeCN to $Ni(PH_3)_2$. However, **TS$_{3\text{-}4}$** is much less stable than **TS$_{1\text{-}2}$**, if they are compared to the sum of reactants (see Figure 12). Thus, it is calculated that the smaller activation barrier of this oxidative addition arises from the absence of the stable reactant complex.

In these oxidative addition reactions, charge-transfer (CT) interaction between doubly-occupied d_π orbital of Ni and empty σ^*-antibonding orbital of MeCN and C_2H_6 plays important roles to break the C-C and C-CN σ-bond and to form M-Me and M-CN bonds.[62] Such σ^* orbitals of MeCN and C_2H_6 are shown in Figure 13, where geometries are taken from the IRC calculations of oxidative additions of MeCN and

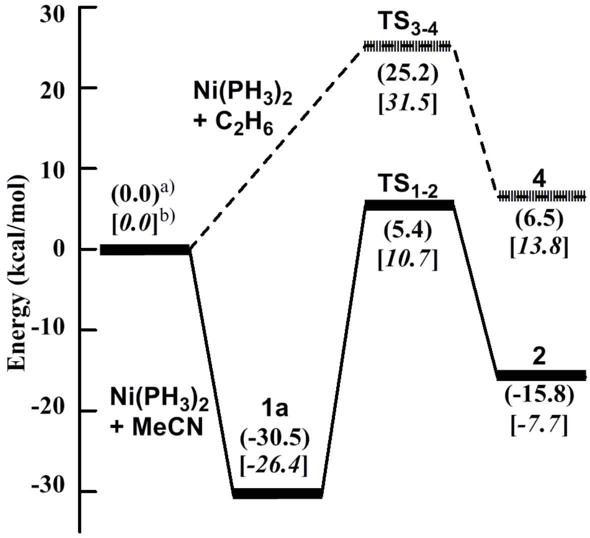

Figure 12. Energy changes (kcal/mol) in the oxidative addition of MeCN (solid line) and C_2H_6 (dashed line) to $Ni(PH_3)_2$.

a) In parentheses are the CCSD(T)-calculated energy changes, where cc-pVTZ and cc-pVDZ basis sets were employed for Ni and the others, respectively.

b) In brackets are the DFT(B3PW91)-calculated energy changes, where the same basis sets were employed as these of the CCSD(T)-calculation.

Scheme 2. Orbital mixing in the CN π^* orbital

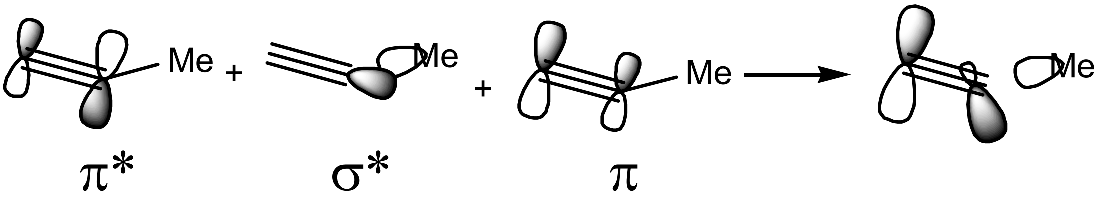

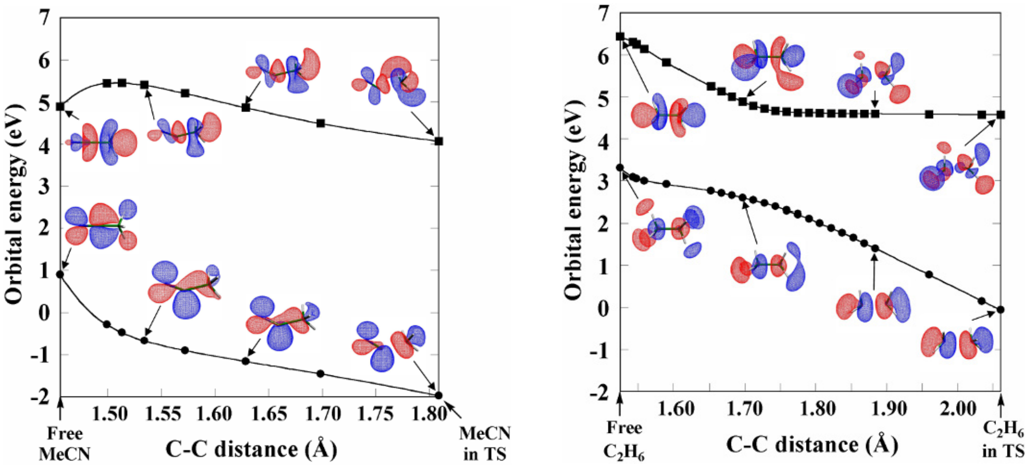

(A) MeCN fragment (B) C_2H_6 fragment

Figure 13. Two important unoccupied molecular orbitals[a)] in (A) MeCN and (B) C_2H_6 fragments. Geometries of MeCN and C_2H_6 are taken from IRC calculations of the oxidative additions of MeCN and C_2H_6 to $Ni(PH_3)_2$.

a) Kohn-Sham orbital

C_2H_6. Apparently, LUMO is C-CN and C-C σ*-antibonding orbitals in MeCN and C_2H_6, respectively, when the geometries of MeCN and C_2H_6 are taken to be the same as those of transition states. However, LUMO of free MeCN is π* orbital and that of free C_2H_6 is C-H σ* orbital. As shown in Scheme 2, the distortion of Me-CN induces the π*-σ* mixing, into which the π-bonding orbital mixes in an anti-bonding way with the σ*-antibonding orbital because the π orbital is at lower energy than the σ* orbital. These orbital mixings lead to the LUMO of distorted MeCN (Figure 13(A)). The distortion of C_2H_6 lowers the energy of the C-C σ*-antibonding orbital because the antibonding overlap of orbitals decreases by the distortion, while the energy of the C-H σ*-antibonding orbital little changes by the distortion. As a result, the C-C σ*-antibonding orbital becomes LUMO in the distorted C_2H_6 and the C-H σ* orbital becomes next LUMO. It is noted that the LUMO of the distorted MeCN is at much lower energy than that of the distorted C_2H_6 (Figure 13). This is because the LUMO of MeCN mainly consists of the CN π* orbital, which is at much lower energy than the

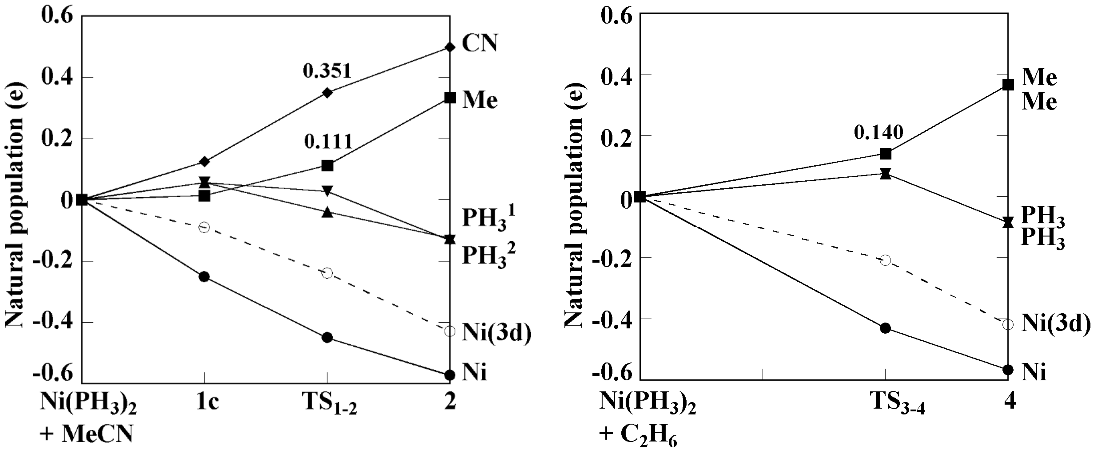

(A) MeCN (B) Ethane

Figure 14. Changes of natural populations[a)] by oxidative additions of (A) MeCN and (B) ethane to Ni(PH$_3$)$_2$.

a) The DFT(B3PW91) method was employed, where cc-pVTZ and cc-pVDZ basis sets were employed for Ni and the other atoms, respectively.

C-CN σ^* orbital, and the Me sp^3 orbital overlaps with the CN π^* orbital in a bonding way in the LUMO of distorted MeCN. As a result, the transition state of the C-CN σ-bond activation of MeCN is at lower energy than that of C_2H_6.

Differences in the electronic structure between the oxidative additions of MeCN and C_2H_6 to Ni(PH$_3$)$_2$ are found in the population changes, as shown in Figure 14. The electron populations of Me and CN groups considerably increase and the Ni atomic population and the Ni d orbital population considerably decrease, as expected. These changes are consistent with our understanding that this is oxidative addition reaction. It is noted that the sum of electron population of Me and CN groups more increases in the oxidative addition of MeCN than the sum of electron population of two Me groups in the oxidative addition of C_2H_6. The Ni atomic population more decreases in the oxidative addition of MeCN than in the oxidative addition of C_2H_6. The significant difference is also observed in the population change of PH$_3$ group: The population of PH$_3$ more decreases in the oxidative addition of MeCN than in the oxidative addition of

C_2H_6. All these results arise from the facts that the LUMO of MeCN is at a lower energy than that of C_2H_6, the CN group is electron-withdrawing but the Me group is electron-donating.

Also, it is noted that **2** is more stable but **4** is less stable than the sum of reactants. To investigate these differences between MeCN and C_2H_6, we evaluated the Ni-Me and Ni-CN bond energies, considering the following reactions:

$Ni(PH_3)_2 + CH_3CH_3 \rightarrow Ni(Me)_2(PH_3)_2$ ΔE = 6.5 (13.8) kcal/mol (1)

$Ni(PH_3)_2 + MeCN \rightarrow Ni(CN)(Me)(PH_3)_2$ ΔE = -15.8 (-7.7) kcal/mol (2)

$CH_3CH_3 \rightarrow 2\ \cdot Me$ ΔE = 94.4 (95.8) kcal/mol (3)

$MeCN \rightarrow \cdot Me + \cdot CN$ ΔE = 122.3 (128.9) kcal/mol (4)

The difference in reaction energy between eq(1) and eq(3) corresponds to twice of Ni-Me bond energy and the reaction energy difference between eq(2) and eq(4) corresponds to the sum of Ni-Me and Ni-CN bond energies. Thus, the Ni-Me and Ni-CN bond energies are evaluated to be 44.0 (41.0) and 94.1 (95.7) kcal/mol, respectively. Though the C-CN bond of MeCN is considerably stronger than the C-C bond of C_2H_6 by 27.9 (33.1) kcal/mol, the Ni-CN bond is much stronger that the Ni-Me bond by 50.1 (54.7) kcal/mol. This is the reason why the oxidative addition of MeCN to $Ni(PH_3)_2$ is more exothermic than that of C_2H_6.

3.4. Conclusions

Oxidative addition of H_2 to $Ni(PH_3)_2$ was theoretically studied because this is considered as a prototype of nickel-promoted σ-bond activation reaction. We employed here CASSCF, CASPT2, CCSD(T), broken symmetry (Bs) MP2 to MP4(SDTQ), and DFT methods to investigate what methods present reliable results. In CASSCF and CASPT2 calculations, the active space should consist of 10 electrons and 10 orbitals which includes 3d and five outer 3d' orbitals. The CCSD(T) method presents almost the same result as the CASPT2 method with active space of 10 electrons and 10 orbitals, when either ANO or cc-pVTZ basis set is used for Ni. However, the CCSD(T) method presents significantly different energy changes, when smaller basis sets than these twos were employed for Ni. The Bs-MP4(SDTQ) method presents similar energy changes to those of the CCSD(T)/ANO, CCSD(T)/cc-pVTZ, and CASPT2/ANO methods, while the potential energy curve (PEC) is not smooth around the transition state. The DFT(B3LYP)-calculated reaction energy is somewhat smaller than the CASPT2- and CCSD(T)-calculated values, though the difference is not very large. ANO, cc-pVTZ, and triple-zeta quality basis sets with Stuttgart-Dresden-Bonn ECPs present much better results than Wa-TZ(f) and 6-31G(f) basis sets in the DFT calculations. B3PW91 and mPW1PW91 present moderately better energy changes than BLYP, B1LYP, and B3LYP.

Oxidative addition of MeCN to $Ni(PH_3)_2$ was investigated by the DFT(B3PW91) and CCSD(T) methods. These two methods present almost the same activation barrier, when cc-pVTZ is employed for Ni. However, the DFT method moderately underestimates the binding energy of the reactant complex and the reaction energy compared to the CCSD(T) method.

This oxidative addition exhibits interesting characteristic features, as follows: The barrier height is lower and the product is more stable relative to infinite separation than those of the oxidative addition of C_2H_6. The lower barrier arises from the lower energy of the C-CN σ*-orbital of the distorted MeCN than that of the distorted C_2H_6. The larger exothermicity of the C-CN σ-bond activation arises from the stronger Ni-CN bond than the Ni-Me bond.

3.5. Appendix

Table A1. <S^2> values of broken symmetry Hartree Fock wavefunction.

RC	-2.14	-1.52	-1.04	-0.49	-0.30	-0.10
<S^2>	0.5943	0.5981	0.5998	0.6064	0.5919	0.5704

RC	0	+0.10	+0.40	+0.60	+1.19	+1.78
<S^2>	0.5435	0.5034	0.4333	0.3720	0.3243	0.3207

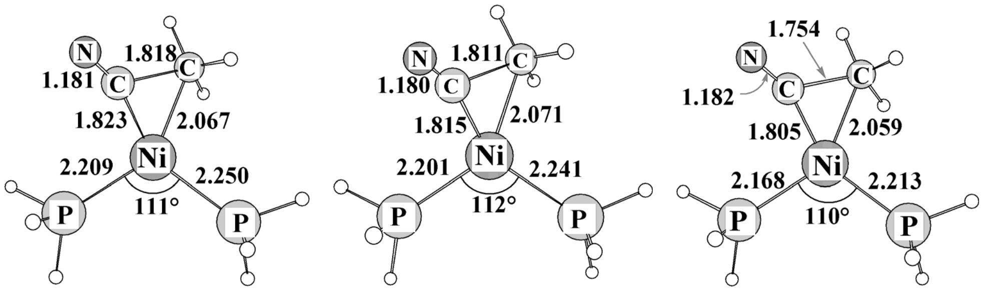

Ni : cc-pVTZ
Others : 6-31G(d,p)

Ni : SDB
Others : 6-31G(d,p)

Ni : Wa-TZ(f)
Others : 6-31G(d,p)

Figure A1. The transition state geometries of oxidative addition of MeCN to Ni(PH_3)$_2$ optimized by the DFT(B3LYP)method, where cc-pVTZ, SDB, and Wa-TZ(f) basis sets were employed for Ni and 6-31G(d,p) basis sets were employed for the other atoms. Bond lengths are in angstrom and bond angles are in degree.

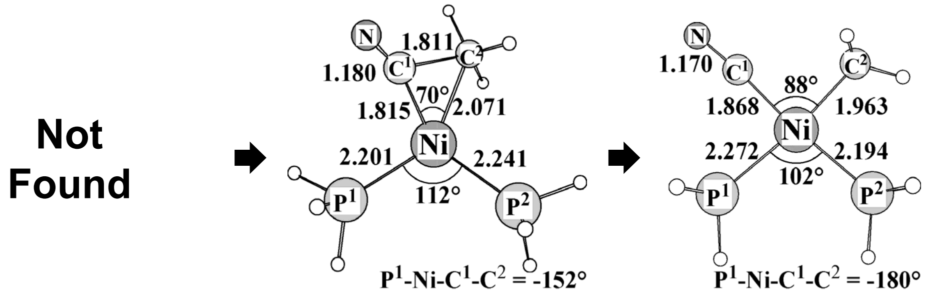

1c **TS_{1-2}** **2**

Figure A2. Geometry change in oxidative addition of MeCN to $Ni(PH_3)_2$ optimized by the DFT(B3LYP) method, where SDB and 6-31G(d,p) basis sets were employed for Ni and the other atoms, respectively. Bond lengths are in angstrom and bond angles are in degree.

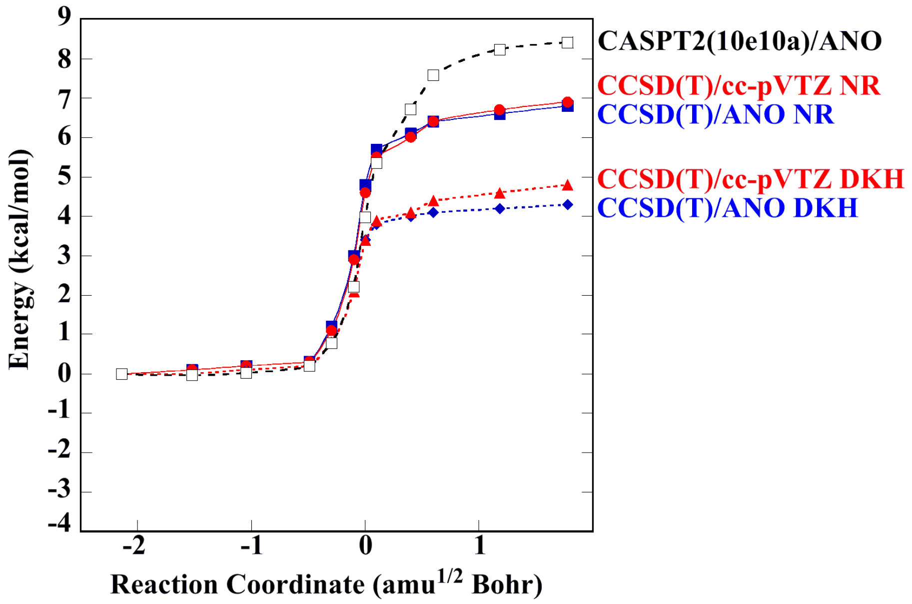

Figure A3. Potential energy curves of the oxidative addition of H_2 to $Ni(PH_3)_2$ calculated by the non-relativistic (NR) and relativistic (DKH) CCSD(T) methods[a)]

a) In the relativistic calculations, the ANO-RCC[b)] and cc-pVTZ-DK[c)] basis sets were employed for Ni. b) Roos, B. O.; Lindh, R.; Malmqvist, P.–Å.; Veryazov, V.; Widmark, P.-O. *J. Phys. Chem. A* **2005,** *109,* 6575-6579. c) Balabanov, N. B.; Peterson, K. A. *J. Chem. Phys.* **2005,** *123,* 064107.

References

1) Gerlach, D. H.; Kane, A. R.; Parshall, G. W.; Jesson, J. P.; Muetterties, E. L. *J. Am. Chem. Soc.* **1971,** *93,* 3543.

2) Parshall, G. W. *J. Am. Chem. Soc.* **1974,** *96,* 2360.

3) (a) Morvillo, A.; Turco, A. *J. Organometal. Chem.* **1981,** *208,* 103. (b) Favero, G.; Morvillo, A.; Turco, A. *ibid.* **1983,** *241,* 251.

4) Abla, M.; Yamamoto, T. *J. Organometal. Chem.* **1997,** *532,* 267.

5) Churchill, D.; Shin, J. H.; Hascall, T.; Hahn, J. M.; Bridgewater, B. M.; Parkin, G. *Organometallics* **1999,** *18,* 2403.

6) (a) Garcia, J. J.; Jones, W. D. *Organometallics* **2000,** *19,* 5544. (b) Garcia, J. J.; Brunkan, N. M.; Jones, W. D. *J. Am. Chem. Soc.* **2002,** *124,* 9547. (c) Brunkan, N. M.; Brestensky, D. M.; Jones, W. D. *J. Am. Chem. Soc.* **2004,** *126,* 3627.

7) (a) Taw, F. L.; White, P. S.; Bergman, R. G.; Brookhart, M. *J. Am. Chem. Soc.* **2002,** *124,* 4192. (b) Taw, F. L.; Mueller, A. H.; Bergman, R. G.; Brookhart, M. *J. Am. Chem. Soc.* **2003,** *125,* 9808.

8) (a) Nakazawa, H.; Kawasaki, T.; Miyoshi, K.; Suresh, C. H.; Koga, N. *Organometallics* **2004,** *23,* 117. (b) Nakazawa, H.; Kamata, K.; Itazaki, M. *Chem. Commun.* **2005,** 4004.

9) Miller, J. A. *Tetrahedron Lett.* **2001,** *42,* 6991.

10) (a) Nakao, Y.; Oda, S.; Hiyama, T. *J. Am. Chem. Soc.* **2004** *126, 13904.* (b) Nakao, Y.; Oda, S.; Yada, A.; Hiyama, T. *Tetrahedron* **2006,** *62,* 7567.

11) The non-dynamical (static) correlation is understood in terms of the electron correlation effect that is incorporated by use of multi-configurational wave function as the reference state; in other words, the incorporation of this type electron correlation effect is necessary when many electronic states are in

similar energy to the ground state. The dynamical correlation is understood in terms of the electron correlation effects induced by collisions of two or more electrons. Helgaker, T.; Jørgensen, P.; Olsen, J. *Molecular Electronic-Structure Theory*; John Wiley: New York, 2000

12) Andersson, K.; Roos, B. O. *Chem. Phys. Lett.* **1992,** *191,* 507.

13) Pieloot, K.; Tsokos, E.; Roos, B. O. *Chem. Phys. Lett.* **1993,** *214,* 583.

14) Bagus, P. S.; Roos, B. O. *J. Chem. Phys.* **1981,** *75,* 5961.

15) (a) Walch, S. P.; Bauschlicher, C. W., Jr. *J. Chem. Phys.* **1983,** *78,* 4597. (b) Bauschlicher, C. W., Jr. *J. Chem. Phys.* **1986,** *84,* 260.

16) Blomberg, M. R. A.; Brandemark, U. B.; Siegbahn, P. E. M.; Mathisen, K. B.; Karlström, G. *J. Phys. Chem.* **1985,** *89,* 2171.

17) Widmark, P. –O.; Roos, B. O.; Siegbahn, P. E. M. *J. Phys. Chem.* **1985,** *89,* 2180.

18) Bauschlicher, C. W., Jr.; Bagus, P. S.; Nelin, C. J.; Roos, B. O. *J. Chem. Phys.* **1986,** *85,* 354.

19) Blomberg, M. R. A.; Brandemark, U. B.; Siegbahn, P. E. M.; Wennerberg, J.; Bauschlicher, C. W. Jr. *J. Am. Chem. Soc.* **2004,** *126,* 3627.

20) Blomberg, M. R. A.; Brandemark, U. B.; Johansson, J.; Siegbahn, P.; Wennerberg, J. *J. Chem. Phys.* **1988,** *88,* 4324.

21) Blomberg, M. R. A.; Siegbahn, P. E. M.; Lee, T. J.; Rendell, A. P.; Rice, J. E. *J. Chem. Phys.* **1991,** *95,* 5898.

22) Sodupe, M.; Bauschlicher, C. W., Jr.; Lee, T. J. *Chem. Phys. Lett.* **1992,** *189,* 266.

23) Pou-Amérigo, R.; Merchan, M.; Nebot-Gil, I.; Malmqvist, P-. A.; Roos, B. O. *J. Chem. Phys.* **1994,** *101,* 4893.

24) Persson, B. J.; Roos, B. O.; Pierloot, K. *J. Chem. Phys.* **1994,** *101,* 6810.

25) Pierloot, K.; Persson, B. J.; Roos, B. O. *J. Phys. Chem.* **1995,** *99,* 3465.

26) Dapprich, S.; Ehlers, A. W.; Frenking, G. *Chem. Phys. Lett.* **1995,** *242,* 521.

27) Bernardi, F.; Bottoni, A.; Calcinari, M.; Rossi, I.; Robb, M. A. *J. Phys. Chem. A* **1997,** *101,* 6310.

28) Xu, X.; Lü, X.; Wang, N.; Zhang, Q.; Ehara, M.; Nakatsuji, H. *Int. J. Quant. Chem.* **1999,** *72,* 221.

29) Jonas, V.; Thiel, W. *J. Chem. Phys.* **1995,** *102,* 8474.

30) Adamo, C.; Lelj, F. *J. Chem. Phys.* **1995,** *103,* 10605.

31) van Wüllen, C. *J. Chem. Phys.* **1996,** *105,* 5485.

32) Hyla-Krypsin, I.; Koch, J.; Gleiter, R.; Klettke, T.; Walther, D. *Organometallics* **1998,** *17,* 4724.

33) (a) Blomberg, M. R. A.; Siegbahn, P. E. M. *J. Chem. Phys.* **1983,** *78,* 986. (b) Blomberg, M. R. A.; Siegbahn, P. E. M. *ibid.* **1983,** *78,* 5682.

34) (a) Becke, A. D. *Phys. Rev. A* **1988,** *38,* 3098. (b) Becke, A. D. *J. Chem. Phys.* **1993,** *98,* 5648.

35) Lee, C.; Yang, W.; Parr, R. G. *Phys. Rev. B* **1988,** *37,* 785.

36) Wachters, A. J. H. *J. Chem. Phys.* **1970,** *52,* 1033.

37) Raghavachari, K.; Trucks, G. W. *J. Chem. Phys.* **1989,** *91,* 1062.

38) (a) Hariharan, P. C.; Pople, J. A. *Theor. Chim. Acta.* **1973,** *28,* 213. (b) Francl, M. M.; Petro, W. J.; Hehre, W. J.; Binkley, J. S.; Gordon, M. S.; DeFrees, D. J.; Pople, J. A. *J. Chem. Phys.* **1982,** *77,* 3654.

39) Pou-Amérigo, R.; Merchán, M.; Nebot-Gil, I.; Widmark, P. –O.; Roos, B. O. *Theor. Chim. Acta.* **1995,** *91,* 149.

40) (a) Čížek, J.; Paldus, J. *J. Chem. Phys.* **1967,** *47,* 3976. (b) Yamaguchi, K.; Fueno, T.; Fukutome, H. Chem. Phys. Lett. **1973,** *22,* 460. (c) Seeger, R.; Pople, J. A. *J. Chem. Phys.* **1977,** *66,* 3045. (d) Crawford, T. D.; Kraka, E.;

Stanton, J. F.; Cremer, D. *J. Chem. Phys.* **2001,** *114,* 10638, and references therein.

41) Balabanov, N. B.; Peterson, K. A. *J. Chem. Phys.* **2005,** *123,* 064107.

42) Rassolov, V. A.; Pople, J. A.; Ratner, M. A.; Windus, T. L. *J. Chem. Phys.* **1998,** *109,* 1223.

43) Mitin, A. V.; Baker, J.; Pulay, P. *J. Chem. Phys.* **2003,** *118,* 7775.

44) Dolg, M.; Stoll, W. H.; Preuss, H. *J. Chem. Phys.* **1987,** *86,* 866.

45) (a) Hurley, M. M.; Fernandez Pacios, L.; Christiansen, P. A.; Ross, R. B.; Ermler, W. C. *J. Chem. Phys.* **1986,** *84,* 6840. (b) Couty, M.; Hall, M. B. *J. Comput. Chem.* **1996,** *17,* 1359. (c) Ehlers, A. W.; Böhme, M.; Dapprich, S.; Gobbi, A.; Höllwarth, A.; Jonas, V.; Köhler, K. F.; Stegmann, R.; Veldkamp, A.; Frenking, G. *Chem. Phys. Lett.* **1993,** *208,* 111.

46) Adamo, C.; Barone, V. *Chem. Phys. Lett.* **1997,** *274,* 242.

47) Perdew, J. P.; Wang, Y. *Phys. Rev. B* **1992,** *45,* 13244.

48) Perdew, J. P.; Burke, K.; Ernzerhof, M. *Phys. Rev. Lett.* **1997,** *78,* 1396.

49) Adamo, C.; Barone, J. *J. Chem. Phys.* **1998,** *108,* 664.

50) Dunning, T. H. Jr. *J. Chem. Phys.* **1989,** *90,* 1007.

51) Pople, J. A. et al. *Gaussian03*, Revision C.02 Gaussian, Inc., Wallingford CT, **2004**.

52) Widmark, P.-O. et al. *MOLCAS Version 5.4*; Lund University: Lund, Sweden, **2002**.

53) Flükiger, P.; Lüthi, H. P.; Portann, S.; Weber, J. *MOLEKEL v.4.3* for Scientific Computing, Manno, Switzerland, 2002-2002. Portman, S.; Lüthi, H. P., *CHIMIA*, **2000**, *54*, 766.

54) Reed, A. E.; Curtis, L. A.; Weinhold, F. *Chem. Rev.* **1988**, *88*, 849, and references therein.

55) Tsuzuki, S.; Lüthi, H. P. *J. Chem. Phys.* **2001,** *114,* 3949.

56) Frenking, G.; Fröhlich, N. *Chem. Rev.* **2000,** *100,* 717.

57) The C-N distances of MeCN becomes shorter by interaction of MeCN with proton; R(CN) = 1.147 Å in MeCN···H$^+$ and 1.160 Å in free MeCN, where the DFT(B3PW91)/6-31G(d,p) method was used.

58) (a) Albright, T. A.; Hoffmann, R.; Thibeault, J. C.; Thorn, D. L. *J. Am. Chem. Soc.* **1979,** *101,* 3801. (b) Sakaki, S.; Tsuru, N.; Ohkubo. K. *J. Phys. Chem.* **1980,** *84,* 3390.

59) Similar differences in back-donation was reported in the η^2-side on and the η^1-C coordination CO_2 complexes of $Ni(PH_3)_2$

60) Sakaki, S.; Mizoe, N.; Musashi, Y.; Biswas, B.; Sugimoto, M. *J. Phys. Chem. A* **1998,** *102,* 8027.

61) In the previous theoretical work with the MP2 method,[58] the reactant complex could be optimized. However, the stabilization energy is very small, indicating that the complex was in a very shallow minimum even if it was. Thus, the E_a value is little influence by the presence of the reactant complex.

62) Sakaki, S. *Topics Organomet. Chem.* **2005,** *12,* 31, and references therein.

Chapter 4

Frontier Orbital Consistent Quantum Capping Potential (FOC-QCP) for Bulky Ligand of Transition Metal Complexes

4.1. Introduction

In many computational studies of transition metal complexes, the DFT method is widely used nowadays. However, the DFT method tends to underestimate the binding energies of late-transition metal complexes with large π-conjugate systems.[1] Also, the DFT method does not describe correctly the dispersion interaction[2] which plays important role in the interaction between bulky ligand and bulky substrate. In such cases, post-Hartree-Fock (HF) methods should be employed. Møller-Plesset (MP) perturbation theory, the least expensive post-HF method, is usually applied to large system since its computational cost is reasonable. The MP method, however, often fails to describe the electronic structure of the first-row transition metal complex[3,4] since the electron correlation effect is considerably large and the HF wave function, which is used as a reference wave function of the MP method, is much different from exact wave function in the first-row transition metal complex. On the other hand, *ab initio* methods such as CCSD(T) (coupled cluster singles and doubles with non-iterative evaluation of triples), CCSDT, and CASPT2 (complete active space with second-order perturbation theory) methods can present reliable results in most of the first row transition metal complexes such as nickel[4] and chromium[5] complexes. However, they need considerably large computational cost.

Because of the large computational cost, various quantum mechanical/molecular mechanical (QM/MM) methods are widely used for the theoretical studies of large systems.[6] In the QM/MM method, a whole system is spatially divided into the chemically active region and the environment region.[7-9] The QM/MM method is becoming the standard technique to investigate proteins nowadays.[10] This method is also used to study the solid catalysts[11] and transition metal complexes.[12,13]

However, the QM/MM method involves problems. Boundary problem is one of the major problems in the QM/MM methods, as well known, which is how to treat the connection between the QM and the MM regions. The simple answer is so-called link atom (LA) approach,[7-9,14-18] in which the dangling bond in the QM region is usually capped by the hydrogen atom. Though the free valence of dangling bond is covered by the H-link atom, this H-link atom leads to neglect of the electronic effect of the real substituent which is eliminated from the QM region and treated in the MM region.[19-21] As a result, this simple H-link atom method gives rise to considerable error in the study of transition metal complexes because the electronic structure of metal center is sensitive to the ligands, as will be discussed in this paper.

Another approach to solve boundary problem is the localized self-consistent field (LSCF) method by Rivail et al.[22] In the LSCF method, the frozen localized orbital is employed to fix the free valence. Since this method does not introduce the extra atom in the QM region, the electronic structure near the boundary is kept as it is in the real system. However, it is difficult to change the direction of the frozen orbital which should be orthogonalized to the other orbitals in the QM region, when the geometry changes occur in reaction or dynamics, for example.[22d] Gao et al. proposed another strategy called generalized hybrid orbital (GHO) method to solve the orthogonalization problem.[23] In the GHO method, four orbitals are placed on the boundary atom to represent sp^3 hybrids and one of them is the active orbital which is included in the QM calculation and the other three orbitals are treated as auxiliary

Scheme 1

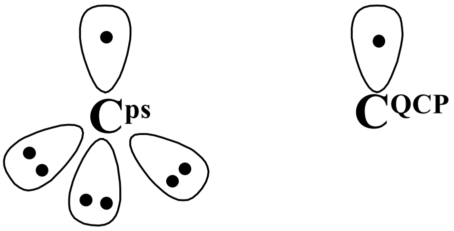

(a) Pseudobond approach **(b) QCP**

frozen orbitals which are necessary to satisfy the orthogonal condition. The GHO method is now employed in many studies of dynamics of proteins.[24]

The alternative approach to large molecules is the ONIOM method developed by Morokuma and his co-workers.[13,25] In the ONIOM method, a whole system is separated into an important region (model) and the other region; for example, in the 2-layer ONIOM (ONIOM2) method, the energy of total system is represented by the sum of the high level (expensive) calculation of model and the difference between low level (inexpensive) calculations of model and real systems, as shown below,

$$E_{\mathrm{ONIOM2}} = E_{\mathrm{low,real}} - E_{\mathrm{low,model}} + E_{\mathrm{high,model}}, \tag{1}$$

where the terms of "low" and "high" in subscript mean the computational level to be applied. In the model system, extra atoms must be introduced to cap dangling bonds, when the real system is one molecule. Thus, the ONIOM method has the same problem of electronic structure deviation like the LA approach.

Several approaches have been tried to solve this boundary problem in the LA approach. Antes and Thiel used the specially parameterized link atom called adjusted connection atom.[16] This method improves the electronic structures near the boundary but it has been implemented only for the semi-empirical method. For the *ab initio* and DFT methods, Zhang et al. proposed pseudobond approach,[26] in which the boundary atom has seven electrons like halogen atom, as shown in Scheme 1, and the electronic property of real system (usually sp^3 carbon atom) is reproduced with the effective core potential (ECP). This strategy is simple but reproduces well the charge and geometrical features. DiLabio et al. proposed similar scheme called quantum capping potential (QCP) method[27] for the *ab initio* and DFT methods. In the QCP method, the electronic properties are also reproduced with the parameterized ECP but the boundary atom has only one electron like hydrogen atom. The conventional ECP format is employed in these methods and thus these methods can be easily applied to various systems. Yasuda and Yamaki reported the similar method, which is called minimum principle.[28] In this method, the effective potential was placed not only on the boundary atom but also on the atom attached to the boundary atom. Recently, Slaviček and Martínez proposed multicentered valence electron effective potential (MC-VEEP) method[29] based on QCP. They introduced the effective potentials to the hydrogen atom of methyl group to reproduce the exchange repulsion, while the hydrogen atom has no basis set. Poteau and co-workers recently developed effective group potential (EGP) method[30] to replace functional group such as SiH_3, PH_3, NH_3, CO, or Cp (cyclopentadienyl) by an imaginary system bearing bonding electrons and effective potential without nucleus. In the EGP method, the effective potential includes generalized projection operator unlike the pseudobond approach and the QCP method. This leads to the generality of the theory. They succeeded to calculate the large transition metal complexes with *ab initio* method such as CASPT2 method[30c] by reducing the number of electrons explicitly treated. However, it is not easy to use this method in practice because the EGP method does not use the conventional ECP format.

In many transition metal complexes, the tertiary phosphine (PR_3) is used as ligand. Because the large tertiary phosphine considerably increases the size of the transition metal complex, the CASPT2 and CCSD(T) methods cannot be applied to the transition metal complexes with such large phosphine. Thus, it is worthy representing large alkyl group of tertiary phosphine with the QCP method. The lone pair orbital of tertiary phosphine plays important roles in the coordinate bond of tertiary phosphine. This means that the parameters of the QCP should be determined so as to reproduce the lone pair orbital energy of PR_3. The same idea was very previously proposed by Koga and Morokuma with the different shift operator.[31] In their method, Coulomb integral of a chosen orbital of a model system is shifted to reproduce the lone pair orbital energy of the real system.

In this paper, first, we wish to report how to construct the QCP method to reproduce the lone pair orbital energy of PR_3, where R is alkyl group such as Me (methyl), Et (ethyl), ^{i}Pr (isopropyl), and ^{t}Bu (*tert*-butyl). Because the lone pair orbital of PR_3 is HOMO and plays important roles as frontier orbital, such parameterized QCP method is called frontier orbital consistent QCP (FOC-QCP), hereafter. Then, we will examine the performance of this method in the reductive elimination reaction of ethane from $M(Me)_2(PR_3)_2$ [M = Ni, Pd, Pt. R = Me, Et] which is one of the typical organometallic reactions. The next is to propose new procedure to incorporate the steric effects of the real group into the model system with the post-HF method. This procedure is very effective; note that the steric repulsion has not been corrected well in the most QM/MM methods but the correction of steric repulsion is necessary to present reliable result, as will be shown in this work. Also, we will evaluate the coordination energies of small molecules (CO, H_2, N_2, and C_2H_4) with $[RhCl(P^iPr_3)_2]_2$, using the combination of the CCSD(T), FOC-QCP, and SRC methods, to compare the theoretically evaluated binding energies with the experimental values.[32]

4.2. Theory; The FOC-QCP Method and Parameterization

First, we wish to mention the outline of the QCP method and how to determine the effective potentials for the tertiary phosphine. As described above, the QCP method employs the conventional ECP format;

$$U^{EP} = U_L(r) + \sum_{l=0}^{L-1} \sum_{m=-l}^{l} \{U_l(r) - U_L(r)\} |l,m\rangle\langle l,m| \tag{2}$$

where the U_l is the effective potential which comes from the individual Fock equation (eq. 3) and the L is the maximum quantum number of angular momentum of projection operator.

$$\left(-1/2\nabla^2 - Z_v/r + U_l + W_l\right)\chi_l = \varepsilon_l \chi_l \tag{3}$$

The χ_l is the shape-consistent pseudo-orbital constructed by all-electron atomic valence orbitals and the ε_l is the corresponding orbital energy. The Z_v is the effective nuclear charge, which is usually taken to be equal to the number of valence electrons. The W_l includes Coulomb and exchange integrals between the valence electrons. The U_l effectively replaces the core-valence Coulomb and core-valence exchange terms of the all-electron operator. In the conventional codes, the individual U_l is represented by Gaussian expansion, eq. 4;

$$U_l(r) = r^{-2} \sum_i C_{li} r^{n_{li}} \exp\left(-\zeta_{li} r^2\right), \tag{4}$$

where n_{li} is integer of 0, 1, or 2.

The first step is to set the conventional ECP and the valence basis set of carbon atom. Usually, the ECP of carbon atom is used to replace two 1*s* electrons, while four electrons of 2s and 2p orbitals are explicitly treated as valence electrons. In this case, the effective nuclear charge Z_v is four. In the QCP method, on the other hand, three valence electrons are further replaced by ECP, and therefore, the effective nuclear charge becomes one (Z_v = 1). Consistent with this nuclear charge, the Coulomb term in Fock operator must be decreased from $-4/r$ to $-1/r$. To consider this Coulomb term, the $-3/r$ term is added to the usual ECP for carbon. The ECP should decay as the distance becomes larger, because of the screening by the electrons in valence shell. Thus, the additional exponential term ($\exp(-\zeta r^2)$) is added to decrease the ECP as the distance increases. As a result, the eq. 5 is employed here, in which the power of r ($n-2$) is taken to be -1.

$$U_l(r)_{\mathrm{QCP}} = U_l(r) + Cr^{n-2}\exp\left(-\zeta r^2\right), \tag{5}$$

where $U_l(r)$ means conventional ECP for carbon.

In the original QCP method, the exponent ζ value is fixed to be 1.29 and the coefficient is optimized so as to reproduce the geometrical features and Mulliken populations of ethane in which one of methyl groups is replaced with the QCP carbon atom ($\mathrm{C}^{\mathrm{QCP}}$). In the MC-VEEP method, on the other hand, the sum of coefficients is fixed to be -3.

In eq. 5, we need to optimize the coefficient C and the exponent ζ of the additional term. Preliminarily, we investigated the dependency of the computational results on the coefficient, in which the FOC-QCP method was applied to the reductive elimination of ethane from Pt(II) complex. The coefficient was arbitrarily assumed to be -2.8, -2.9, -3.0, -3.1, and -3.2. Then, the ζ value was numerically optimized for each coefficient value, so as to reproduce frontier orbital energy, where the space distribution of the frontier orbital was not considered. The activation barrier and the reaction energy little depend on the coefficient value; see Appendix Table A1. From these results, we decided to employ -3 for the coefficient C and numerically optimized the ζ value for this coefficient value.

Now, let's start to discuss the FOC-QCP for PR_3. The model system is represented as $\mathrm{PC}^{\#(\mathrm{R})}{}_3$, where $\mathrm{C}^{\#(\mathrm{R})}$ means the pseudo-carbon atom parameterized for the R group; for example, $\mathrm{C}^{\#(\mathrm{Me})}$ is a model of the Me group. The lone pair orbital of PR_3, which is HOMO, is frontier orbital because PR_3 coordinates to the metal with its

Scheme 2

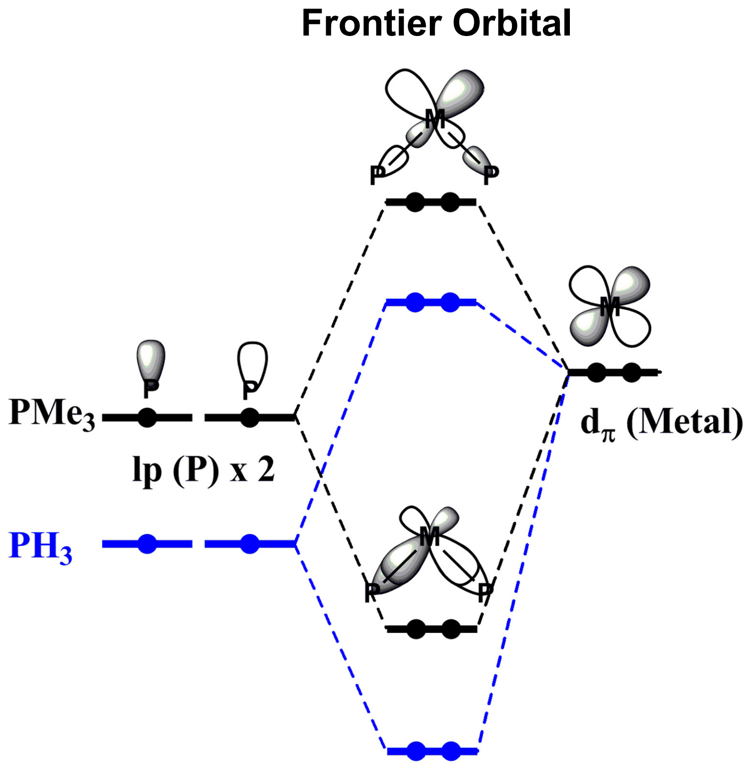

lone pair orbital. This lone pair orbital interacts with the d orbital of the metal to significantly influence the energy level and the expansion of the d orbital of the metal, as shown in Scheme 2. The d orbital further interacts with the substrates and/or the other ligand which are at the position *trans* to PR_3. It is likely that the electronic effects of PR_3 can be reproduced well if the lone pair orbital energy of PR_3 is reproduced by the FOC-QCP method. Thus, we numerically optimized the exponent ζ value, as described above.

The combination of basis set and ECP are also important. In the QCP and MC-VEEP methods, even-tempered $(5s5p1d)/[5s5p1d]$ basis set[33] was employed. This basis set is, however, expensive. Here, the $(4s4p)/[1s1p]$ basis set was employed for carbon atom with the corresponding ECP by Christiansen et al.,[34] which are usual valence basis set and ECP named as CRENBL,[34] because the basis set size is reasonable. The combination of this basis set and the FOC-QCP reproduces well the lone pair orbital energy of PR_3, as will be discussed below.

Also, there are several candidates for computational methods to be employed to optimize the parameters. In the QCP and the MC-VEEP methods, the HF method was employed. In the pseudobond approach, the hybrid density functional method (B3LYP) was employed. Here, we employed both of the computational methods, the HF and the hybrid density functional method (B3PW91),[35] for parameterization, and examined which is better.

4.3. Computational Details

The geometry of PR_3 was optimized by the DFT[B3PW91] method with 6-31G basis sets,[36,37] where a d-polarization function was added to P. In each geometry, the vibration frequencies were calculated to confirm that it was equilibrium structure. The orbital energies were calculated with the HF and the DFT[B3PW91] methods, where the cc-pVDZ basis sets were employed for all atoms.[38]

Geometries of transition metal complexes were optimized with the DFT[B3PW91] method, where core electrons of Ni (up to 2p), Pd and Rh (up to 3d), and Pt (up to 4f) were replaced with the effective core potentials (ECPs) of Stuttgart-Dresden-Bonn (SDB) group[39,40] and their valence electrons were represented by (311111/22111/411/1) basis set[39] for Ni and (311111/22111/411) basis sets[40] for Pd, Pt, and Rh. For the PR_3, 6-31G basis sets[36,37] were employed, where a d-polarization function was added to P. For the other atoms, 6-31G(d,p)[36] basis sets were employed, where one diffuse function was added to Cl.[41] This basis set system is called hereafter BS-1. Vibrational frequencies were calculated with the DFT[B3PW91]/BS-1 method in all the stationary points to check if they were either equilibrium structure or transition state. The energies were evaluated with the

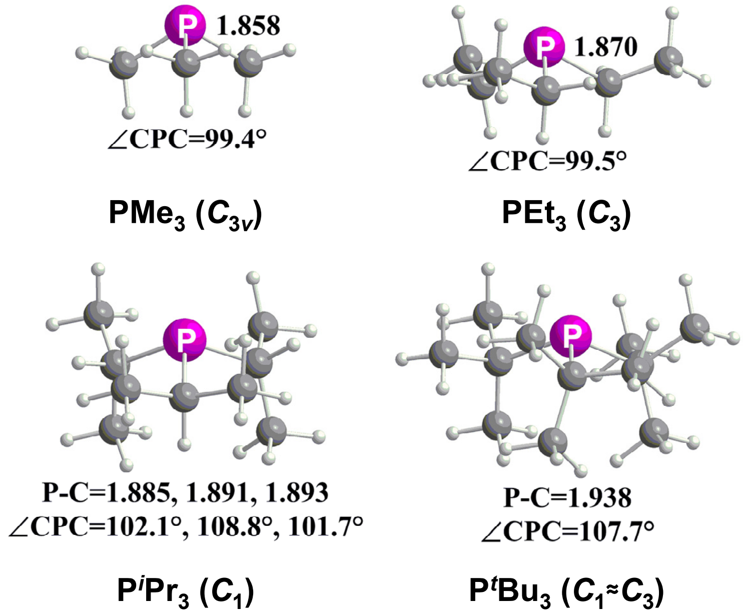

Figure 1. Geometries of PMe$_3$, PEt$_3$, P^{i}Pr$_3$, and P^{t}Bu$_3$ optimized with the DFT[B3PW91]/BS-1 method. Bond lengths are in angstrom and bond angles are in degree. In parentheses are point group.

CCSD(T), MP4(SDQ), and DFT[B3PW91] methods by using the DFT[B3PW91]-optimized geometries. In the energy evaluation, the better basis set system (BS-2) was employed as follows. For Pd, Pt, and Rh, two f polarization functions[42] were added to the above described basis sets with the same ECPs. For Ni, cc-pVTZ basis set[43] was employed because the cc-pVTZ basis set or better one should be used for Ni to present reliable energy change with the CCSD(T) method,[4] while a g polarization function was removed. For H_2 molecule and chlorine atom, aug-cc-pVDZ basis sets were used, while for the other atoms, cc-pVDZ basis sets were employed. Solvent effects were also considered with the PCM method using the integral equation formalism,[44] where the temperature was taken to be 303.15 K.

All the calculations were performed with Gaussian03 program package.[45] To optimize the parameter of the FOC-QCP, the STEPIT ver. 7.7 program[46] was employed in combination with Gaussian03.

Table 1. The HOMO energies (eV) calculated with the DFT(B3PW91) and RHF methods of PH_3, PMe_3, PEt_3, P^iPr_3, and P^tBu_3.

	PH_3	PMe_3	PEt_3	P^iPr_3	P^tBu_3
B3PW91	−7.56	−6.06	−5.98	−5.74	−5.55
RHF	−10.53	−8.90	−8.78	−8.49	−8.22

Table 2. The parameters of additional effective potential for $C^{\#(R)}$ optimized with RHF and DFT[B3PW91] methods.

PR_3	n	C	ζ(RHF)	ζ(B3PW91)
PMe_3	1	−3.0	1.46997334	1.58297547
PEt_3	1	−3.0	1.49525346	1.60203115
P^iPr_3	1	−3.0	1.48708431	1.59434019
P^tBu_3	1	−3.0	1.49195717	1.59406618

4.4. Results and Discussion

4.4.1. Frontier Orbital Consistent Quantum Capping Potential (FOC-QCP) for PR_3.

Geometries and important geometrical parameters of PH_3, PMe_3, PEt_3, P^iPr_3, and P^tBu_3 are shown in Figure 1. Their HOMO (lone pair orbital) energies were calculated with the RHF and DFT[B3PW91] methods, as shown in Table 1. The HOMO energy of PH_3 is considerably lower than that of PMe_3 by about 1.5 eV and the HOMO energy becomes higher upon going from PMe_3 to P^tBu_3. This means that in the bulky phosphine such as P^tBu_3, we should carefully consider not only the steric effect but also the electronic effect.

Table 2 lists the parameters of the additional effective potentials for each PR_3 group optimized by the RHF and DFT[B3PW91] methods. In the parameterization of $C^{\#(i\mathrm{Pr})}$, three carbon atoms bound with phosphorus atom were treated equivalently, whereas they are not equivalent, strictly speaking (see Figure 1). This procedure is

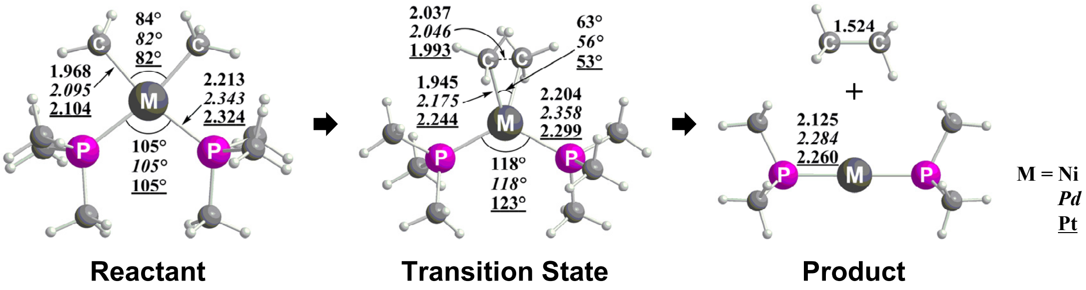

Figure 2. Geometry changes by the reductive elimination of ethane from $M(Me)_2(PMe_3)_2$ (M = Ni, Pd, Pt) optimized with the DFT[B3PW91]/BS-1 method. Bond lengths are in angstrom and bond angles are in degree. Upper: M = Ni, Middle: M = Pd, Bottom: M = Pt.

reasonable because the difference among these three carbon atoms is small and the rotation of phosphine would occur around the M−P bond. The RHF-optimized ζ values are somewhat smaller than the DFT[B3PW91]-optimized ones. The reason is not clear. It is noted that no clear relation between the ζ value and the lone pair orbital energy is observed; for example, the lone pair orbital energy of PMe_3 is lower than that of PEt_3 and the ζ value of $C^{\#(Me)}$ is smaller than that of $C^{\#(Et)}$. On the other hand, the lone pair orbital energy of PEt_3 is lower than that of P^iPr_3 but the ζ value of $C^{\#(Et)}$ is slightly larger than that of $C^{\#(i\mathrm{Pr})}$. These results suggest that neither extrapolation nor interpolation can be applied to optimization of the ζ value; in other words, the ζ value must be optimized independently for each PR_3.

4.4.2. Application of the FOC-QCP Method to the Reductive Elimination Reaction of Ethane from $M(Me)_2(PR_3)_2$ [M = Ni, Pd, or Pt; R = H or Me].

This reaction was investigated with the CCSD(T), MP4(SDQ), and DFT[B3PW91] methods, where DFT[B3PW91]-optimized geometries were employed; see Figure 2 and Figure A1 for the geometry changes by the reductive elimination from

$M(Me)_2(PMe_3)_2$ and $M(Me)_2(PH_3)_2$, respectively.

A. Reliability of Computational Methods.

Before starting to examine the performance of the FOC-QCP method, we wish to investigate the reliability of the computational methods such as RHF, MP2 to MP4(SDQ), CCSD, CCSD(T), and DFT[B3PW91] methods. Here, we employed PH_3 to reduce the size of the complex. For the nickel complex, the MP2 to MP4(SDQ) methods present unreasonable results, as shown in Table 3. The reason was previously discussed in terms of very large electron correlation effects in the nickel complex.[3,4] Although the electron correlation effects are expected to be small in the 4d metal such as palladium, the MP4(SDQ) method presents considerably different results from those of the CCSD(T) method. Moreover, the activation barrier is considerably different among the MP4(D), MP4(DQ), and MP4(SDQ) methods. This significantly large difference suggests that the MP4(SDQ) method does not present reliable energy changes in the reductive elimination of the palladium complex. In the platinum complex, on the other hand, the MP4(SDQ) method presents similar results to the CCSD(T) method and the activation barrier is little different among the MP4(D), MP4(DQ), and MP4(SDQ) methods. It is also noted that the large activation barriers calculated with these methods are consistent with the experimental result that the reductive elimination reaction does not occur in the platinum complex.[47] The reason was clearly discussed by Low and Goddard.[48] From these results it should be concluded that the MP4(SDQ) method presents reasonable results in the reductive elimination of the platinum complex but does not in the palladium and nickel complexes.

The DFT[B3PW91] method presents somewhat smaller activation barriers and somewhat larger exothermicities than does the CCSD(T) method in all cases. Although it is not clear which of the CCSD(T) and DFT[B3PW91] methods is more

Table 3. The activation barriers (E_a) and the reaction energies (ΔE) of the reductive elimination reaction of C_2H_6 from $M(Me)_2(PH_3)_2$.

	Ni		Pd		Pt	
Method	E_a	ΔE	E_a	ΔE	E_a	ΔE
RHF	61.7	−0.8	34.1	−48.5	61.7	−23.3
MP2	−64.1	−82.3	21.9	−17.6	44.4	−0.8
MP3	67.5	28.1	33.4	−23.9	56.0	−7.7
MP4(D)	−55.9	−77.6	26.1	−22.5	50.0	−5.0
MP4(DQ)	−72.0	−97.5	24.7	−25.6	50.5	−6.0
MP4(SDQ)	−86.2	−110.8	18.7	−27.0	49.5	−4.9
CCSD	27.2	−2.9	30.9	−22.1	54.4	−5.2
CCSD(T)	18.7	−6.5	29.5	−18.0	52.0	−2.0
DFT[B3PW91]	17.7	−13.8	26.0	−26.8	48.1	−9.0

reliable, at this moment, we will discuss in Sec. 4.4 that the CCSD(T)-calculated results are much better than the DFT[B3PW91]-calculated ones.

Among these computational methods, the CCSD(T) method is the most reliable. The computational cost of the CCSD(T) method is, however, too large to be applied to the real system with R = Me. The best way to present the reliable results for the reductive elimination is to employ the CCSD(T) method with the FOC-QCP method, as will be discussed below.

B. Energy Changes Calculated with the FOC-QCP Method.

Here, we wish to discuss the performance of the FOC-QCP method. The activation barriers and reaction energies calculated with the FOC-QCP method are listed in Table 4, where the R = $C^{\#(Me)}$ represents that the methyl groups of PMe_3 are substituted for $C^{\#(Me)}$, and the ζ(RHF) and ζ(B3PW91) represent the ζ values determined by RHF and DFT[B3PW91] methods, respectively. As shown in Table 4, the DFT[B3PW91]-calculated activation barrier of the R = $C^{\#(Me)}$ system agrees well with the activation barrier of the real system, where the error is 0.2, 1.4, and 0.3 kcal/mol for Ni, Pd, and Pt complexes, respectively.. These results indicate the FOC-QCP can reproduce well the electronic effect of PMe_3 in the DFT[B3PW91] calculation. In the PH_3 model system, on the other hand, the DFT[B3PW91] method presents somewhat smaller activation barriers than those for the real systems; the error is 2.7, 4.7, and 3.5 kcal/mol for Ni, Pd, and Pt complexes, respectively. These errors are not different very much between PH_3 and $PC^{\#(Me)}{}_3$ systems but not negligibly small. The DFT[B3PW91]-calculated exothermicities of the R = $C^{\#(Me)}$ system are also moderately smaller than those of the real system. This discrepancy becomes considerably small by making steric repulsion correction, which will be discussed below.

The MP4(SDQ)-calculated energy changes of the R = $C^{\#(Me)}$ system are compared with those of the real system in the platinum complex, because the MP4(SDQ) method presents reliable energy change in the reductive elimination of the platinum complex but not at all in the reductive elimination of the nickel complex. The MP4(SDQ)-calculated activation barrier and reaction energy of the R = $C^{\#(Me)}$ system agree well with those of the real system (R = Me), when the ζ(B3PW91) value is employed. On the other hand, the use of the ζ(RHF) value leads to moderate underestimation of the activation barrier. The similar results are observed in the Pd complexes with $C^{\#(Me)}$. From these results, it is concluded that the ζ(B3PW91) value should be used in the post HF calculation.

The activation barriers calculated with the CCSD(T) method are always larger than those of the DFT[B3PW91] and MP4(SDQ) methods; for example, in the platinum complex with PH_3, the activation barrier is calculated to be 48.1, 49.6, and 52.0 kcal/mol by the DFT[B3PW91], MP4(SDQ), and CCSD(T) methods, respectively. The system with R = $C^{\#(Me)}$ reproduces well this trend. The similar results are

Table 4. The activation barriers (E_a) and the reaction energies (ΔE) (kcal/mol) of the reductive elimination reaction of C_2H_6 from $M(Me)_2(PR_3)_2$.

	B3PW91		MP4(SDQ)		CCSD(T)	
R	E_a	ΔE	E_a	ΔE	E_a	ΔE
M = Ni						
Me	20.4	−14.0	−83.6	−109.9	N/A	N/A
H	17.7	−13.8	−86.2	−110.8	18.7	−6.5
$C^{\#(Me)}$ ζ(RHF)	–	–	−94.5	−125.9	20.3	−4.9
$C^{\#(Me)}$ ζ(B3PW91)	20.2	−13.5	−83.5	−114.7	21.8	−5.2
M = Pd						
Me	30.7	−26.4	22.8	−24.9	N/A	N/A
H	26.0	−26.8	18.7	−27.0	29.5	−18.0
$C^{\#(Me)}$ ζ(RHF)	–	–	18.7	−25.9	31.8	−14.8
$C^{\#(Me)}$ ζ(B3PW91)	29.3	−24.9	19.8	−26.4	32.8	−15.1
M = Pt						
Me	51.6	−11.7	53.3	−5.0	N/A	N/A
H	48.1	−9.0	49.6	−4.9	52.0	−2.0
$C^{\#(Me)}$ ζ(RHF)	–	–	50.8	−4.7	54.5	−0.3
$C^{\#(Me)}$ ζ(B3PW91)	51.9	−9.6	52.2	−5.6	56.0	−1.2
$C^{\#(Me)}$ + SRC ζ(RHF)	–	–	52.1	−5.7	54.5	−1.1
$C^{\#(Me)}$ + SRC ζ(B3PW91)	51.2	−11.9	52.2	−6.5	56.0	−2.0

observed in the nickel and palladium complexes with PH_3; for instance, the activation barrier is calculated to be 17.7 and 26.0 kcal/mol for the nickel and palladium complexes, respectively, with the DFT[B3PW91] method and 18.7 and 29.5 kcal/mol, respectively, with the CCSD(T) method. The DFT[B3PW91]-calculated exothermicities are always larger than the CCSD(T)-calculated values in both PH_3 and $PC^{\#(Me)}{}_3$ systems. For instance, the DFT[B3PW91] method overestimates the exothermicity by 7 to 9 kcal/mol for the PH_3 complex and by 8 to 10 kcal/mol for the $PC^{\#(Me)}{}_3$ complexes, compared to those of the CCSD(T) method. The MP4(SDQ) method similarly overestimates the exothermicity, compared to the CCSD(T) method in both PH_3 and $PC^{\#(Me)}{}_3$ complexes. From these results, it is concluded that the

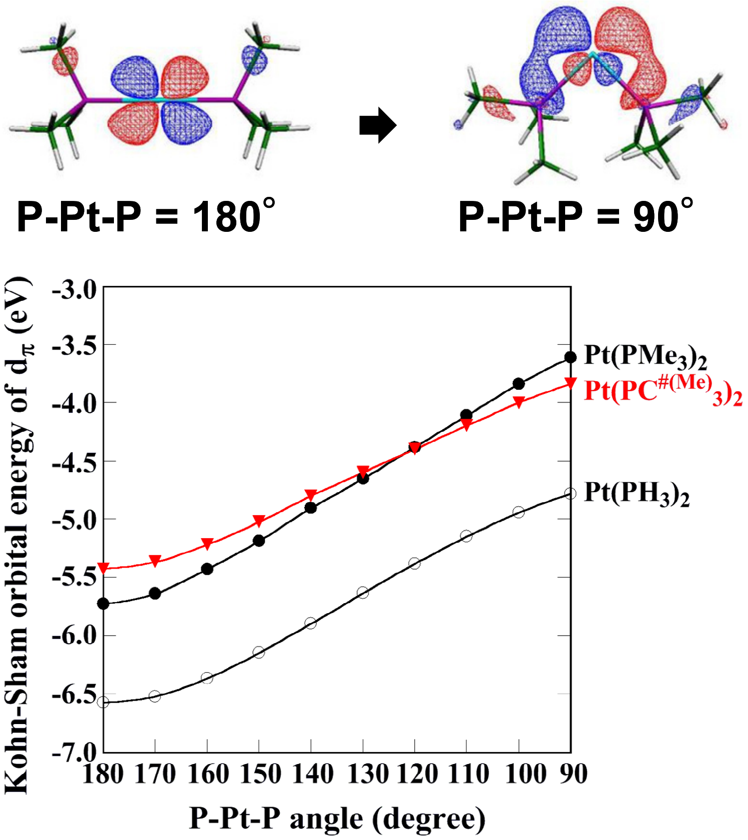

Figure 3. The molecular orbital[a)] energy changes of HOMO of $Pt(PR_3)_2$ (R = Me, H, and $C^{\#(Me)}$) vs. the P-Pt-P angle.
a) Kohn-Sham orbital. The DFT[B3PW91]/BS-2 method.

FOC-QCP method can reproduce well the energy changes of the real system and that the CCSD(T) method with the FOC-QCP presents better results of this type of reductive elimination reaction than the DFT[B3PW91] and MP4(SDQ) methods.

C. Electronic Effect of $PC^{\#(Me)}_3$

We also examined if electronic effect is reproduced well by the FOC-QCP method. Figure 3 shows the frontier orbital energy of $Pt(PR_3)_2$ (R = Me, H, or $C^{\#(Me)}$) as a function of the P−Pt−P angle from 180° to 90°, where Kohn-Sham orbital energy is given. The frontier orbital energy of $Pt(PH_3)_2$ is considerably different from that of $Pt(PMe_3)_2$ due to the difference in the lone pair orbital energy between PH_3 and PMe_3.

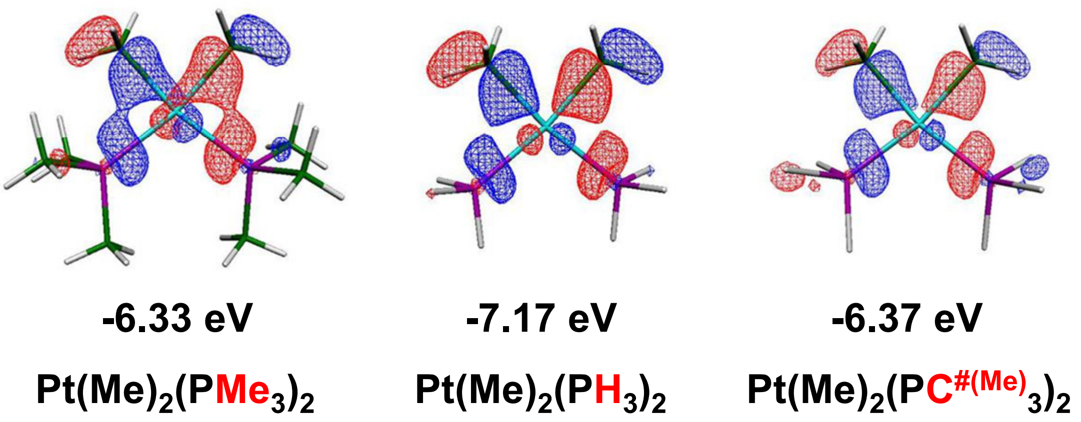

Figure 4. Bonding orbitals and orbital energy[a] of Pt(Me)$_2$(PR$_3$)$_2$. Surface value is 0.05 a.u.
a) Kohn-Sham orbital. The DFT[B3PW91]/BS-2 method.

However, the orbital energy of Pt(PC$^{\#(Me)}$$_3$)$_2$ as well as its dependence on the P−Pt−P angle agrees well with those of Pt(PMe$_3$)$_2$. In Pt(Me)$_2$(PR$_3$)$_2$ (R = Me, H, or C$^{\#(Me)}$), the FOC-QCP method also reproduces well the energy of Pt−Me bonding orbital, as shown in Figure 4, while the orbital energy of the simple model Pt(Me)$_2$(PH$_3$)$_2$ is considerably different from that of the real complex. Because this Pt−Me bonding orbital mainly participates in the reductive elimination, necessary is to reproduce correctly the energy level and the shape of this molecular orbital. This is the reason why the activation barrier of the simple model is different from that of the real system but the FOC-QCP method can reproduce well the activation barrier and the reaction energy of the real system.

4.4.3 Energy Change of Reductive Elimination of Ethane from Pt(R^1)$_2$(PR^2$_3$)$_2$ [R^1 = Me, R^2 = Et, ^{i}Pr, and R^1 = H, R^2 = ^{t}Bu] with Steric Repulsion Correction (SRC)

The steric effects of two PMe$_3$ groups are not included in the above calculation with the FOC-QCP, because the steric effect is not large in PMe$_3$. However, the

Scheme 3

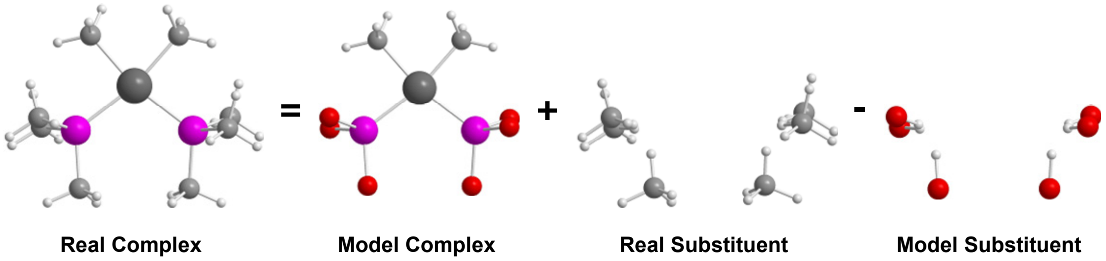

steric repulsion must be taken into consideration for bulky *tert*-phosphine. We wish to propose here a new procedure for the steric repulsion correction (SRC), as shown in Scheme 3. In this procedure, total energy is represented by eq. 6,

$$E = E_{\mathrm{MC}} + E_{\mathrm{RS}} - E_{\mathrm{MS}}\,, \tag{6}$$

where the subscripts MC, RS, and MS represent model complex, real substituent, and model substituent, respectively. The difference of latter two terms of Scheme 3 and eq. 6 corresponds to the steric repulsion correction. This evaluation is similar to but not the same as the ONIOM method, because the latter two terms of Scheme 3 and eq. 6 do not include the active region in this procedure. This is also similar to the G2 method[49] to some extent; remember that the G2 method incorporate the basis set effects as the difference between MP2 calculation with basis sets of high quality and those with basis sets of low quality.

In the platinum complex $\mathrm{Pt(Me)_2(PMe_3)_2}$, the SRC is calculated with the various computational methods (Table 5). All the SRCs are negligibly small except for the reaction energy (ΔE) calculated with the RHF and the DFT[B3PW91] methods. It is noted that the reaction energy calculated with the DFT[B3PW91] method is considerably improved with this SRC; for instance, the error of the DFT[B3PW91]-calculated reaction energy is 2.1 kcal/mol without the SRC but decreases to 0.3 kcal/mol after the SRC, as shown in Table 4, which agrees well with the reaction energy of the real system. Interestingly, the SRC is almost the same in

Table 5. The steric repulsion correction of the activation barrier (E_a) and the reaction energy (ΔE) (kcal/mol) in the reductive elimination reaction of C_2H_6 from $Pt(Me)_2(PMe_3)_2$.

	$C^{\#(Me)}$ ζ(RHF)		$C^{\#(Me)}$ ζ(B3PW91)	
Method	E_a	ΔE	E_a	ΔE
B3PW91	–	–	−0.7	−2.3
RHF	−0.6	−2.2	−0.5	−2.0
MP2	0.1	−0.7	0.1	−0.6
MP3	0.0	−0.9	0.0	−0.8
MP4(D)	0.0	−1.0	0.0	−0.9
MP4(DQ)	−0.1	−1.1	0.0	−0.9
MP4(SDQ)	−0.1	−1.0	0.0	−0.9
CCSD	−0.1	−1.1	0.0	−0.9
CCSD(T)	0.0	−0.9	0.0	−0.8

the MP2 to MP4(SDQ), CCSD, and CCSD(T) methods because the systems calculated in the SRC do not include the transition metal element. This means that the MP2 method is useful enough to evaluate the SRC.

The reason why the SRCs are large in the RHF and DFT[B3PW91] calculations is easily understood in terms of the weak point of these methods; these methods cannot incorporate well dispersion interaction, indicating that the steric repulsion is overestimated. The ζ(B3PW91) value provides better activation barrier and the reaction energy than does the ζ(RHF) value after the steric repulsion correction, too.

In more bulky ligands such as PEt_3, P^iPr_3, or P^tBu_3, the SRC becomes crucially important, as expected. We calculated the activation barrier and reaction energy of the reductive elimination of C_2H_6 from $Pt(Me)_2(PEt_3)_2$ and $Pt(Me)_2(P^iPr_3)_2$ and the reductive elimination of H_2 from $Pt(H)_2(P^tBu_3)_2$ (see Figure 5) with the DFT[B3PW91], MP4(SDQ), and CCSD(T) methods. As shown in Table 6, when the SRC is not included, the activation barrier and the reaction energy of the model $C^{\#(Et)}$ are considerably larger than those of the real complex by 4.8 and 7.8 kcal/mol,

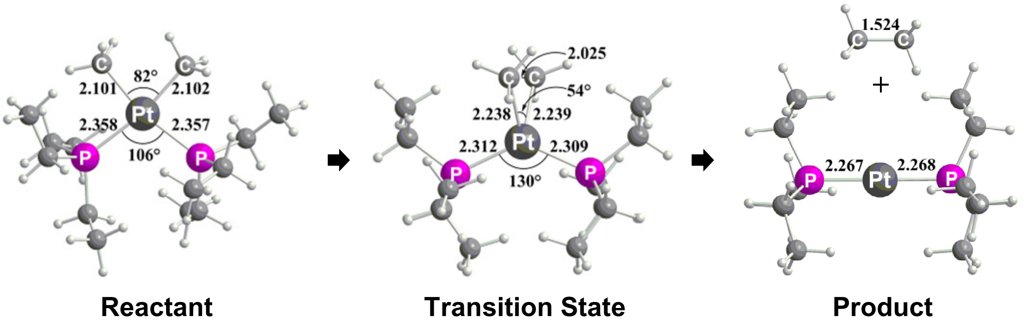

(A) $Pt(Me)_2(PEt_3)_2$

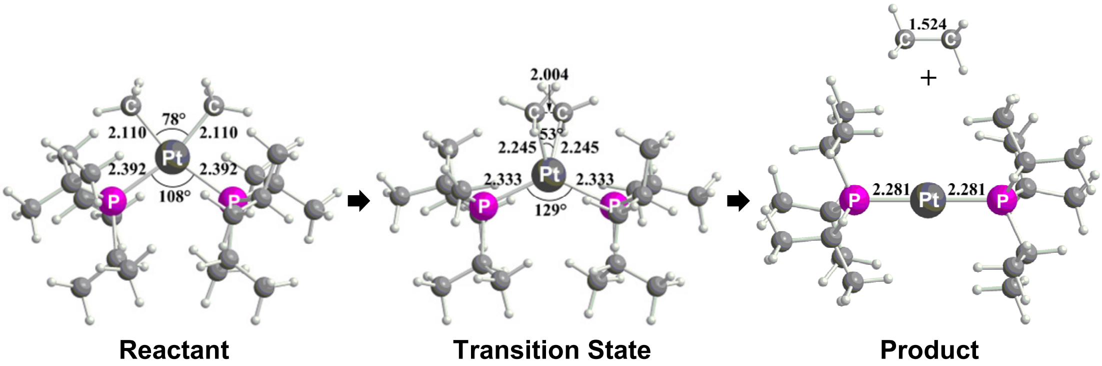

(B) $Pt(Me)_2(P^iPr_3)_2$

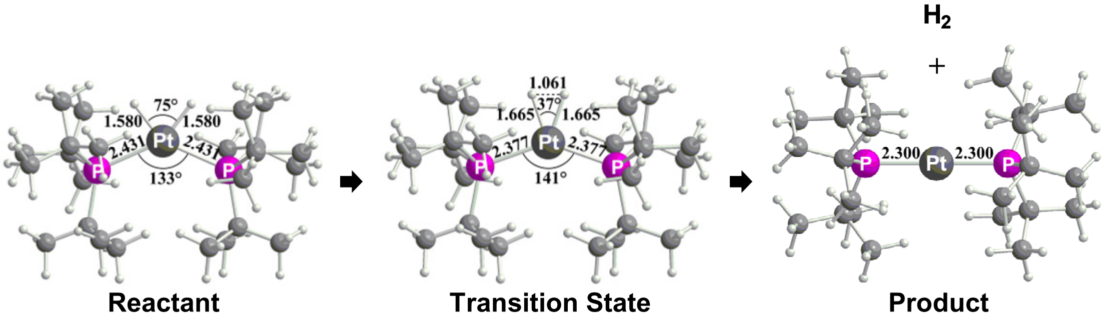

(C) $Pt(H)_2(P^tBu_3)_2$

Figure 5. DFT[B3PW91]/BS-1-optimized geometry changes by the reductive elimination reaction of C_2H_6 from $Pt(Me)_2(PEt_3)_2$ and $Pt(Me)_2(P^iPr_3)_2$ and that of H_2 from $Pt(Me)_2(P^tBu_3)_2$. Bond lengths are in angstrom and bond angles are in degree.

Table 6. The activation barriers (E_a) and the reaction energies (ΔE) (kcal/mol) of the reductive elimination reaction of C_2H_6 from $Pt(Me)_2(PEt_3)_2$ and $Pt(Me)_2(P^iPr_3)_2$ and H_2 from $Pt(Me)_2(P^tBu_3)_2$, where the SRCs are calculated with the MP2 method.

	B3PW91		MP4(SDQ)		CCSD(T)	
R	E_a	ΔE	E_a	ΔE	E_a	ΔE
Et	43.1	−22.3	44.1	−12.9	N/A	N/A
$C^{\#(Et)}$	47.9	−14.5	47.9	−10.7	51.8	−5.9
$C^{\#(Et)}$ + SRC	43.6	−22.5	46.3	−13.6	50.2	−8.8
^{i}Pr	43.3	−25.0	N/A	N/A	N/A	N/A
$C^{\#(iPr)}$	48.3	−16.5	48.4	−12.9	52.5	−7.8
$C^{\#(iPr)}$ + SRC	45.2	−24.2	48.7	−14.8	52.9	−9.7
^{t}Bu	6.7	−6.3	N/A	N/A	N/A	N/A
$C^{\#(tBu)}$	9.6	−1.0	9.3	0.4	12.1	4.3
$C^{\#(tBu)}$ + SRC	7.2	−9.0	7.2	−6.2	10.0	−2.4

respectively, in the DFT[B3PW91] calculations. However, the activation barrier and the reaction energy with the SRC (see the column of $C^{\#(Et)}$ + SRC) agree well with those of the real system, where the SRC was evaluated with the DFT[B3PW91] method. Also, the MP4(SDQ)-calculated activation barriers and reaction energies with SRC agree well with those of the real system (Table 6) in the PEt_3 complex, where the SRCs are evaluated with the MP2 method. Also in the P^iPr_3 and P^tBu_3 complexes, the SRC significantly improves the activation barriers and reaction energies in the DFT[B3PW91] calculation. For the P^tBu_3 complex, Morokuma and his co-workers previously reported the energy change of the oxidative addition of H_2 to $Pt(P^tBu_3)_2$, which is the reverse reaction of reductive elimination investigated here, by using ONIOM2(MP2:MM3)[50] and ONIOM3(CCSD(T):MP2:MM3) methods.[51] In those works, the activation barrier and the reaction energy was calculated to be 8.5 and −6.0 kcal/mol, respectively, by the ONIOM2(MP2:MM3) method, and 10.1 and −4.1

kcal/mol, respectively, by ONIOM3(CCSD(T):MP2:MM3) method. Interestingly, the CCSD(T) method with the FOC-QCP + SRC presents almost the same activation barrier as and the similar reaction energy to those of the ONIOM3(CCSD(T):MP2:MM3) method.

At the end of this section, we wish to mention that the computational cost is considerably reduced by using this FOC-QCP method. The MP4(SDQ) calculation of the real complex (R = Et) needs about 30 hours with 2 cpus of Itanium 2 (1.60 GHz), while that of the model complex (R = $C^{\#(Et)}$) needs less than 10 minutes with the same machine. To evaluate the SRC, we need to perform the MP2 calculations of six ethane molecules and six $C^{\#(Et)}$–H systems, which require 17 minutes and 2 seconds, respectively.[52]

By employing the FOC-QCP method with the SRC, the steric effects of the bulky substituent groups can be effectively considered at the MP2 level and the electronic effects of the real ligands can be incorporated well in the calculation at the CCSD(T) level.

4.4.4. CCSD(T)-Calculated Monomerization Energy of $[RhCl(P^{i}Pr_3)_2]_2$ and Coordination Energies of CO, H_2, N_2, and C_2H_4 to $[RhCl(P^{i}Pr_3)_2]_2$

It is worthy making comparison between the theoretical energy change calculated by the FOC-QCP and the experimental value. The monomerization energy of $[RhCl(P^{i}Pr_3)_2]_2$ **1** to $RhCl(P^{i}Pr_3)_2$ **2** and the coordination energies of CO, H_2, N_2, and C_2H_4 with $[RhCl(P^{i}Pr_3)_2]_2$ were experimentally reported previously.[32] We evaluated these energies by the DFT[B3PW91] and CCSD(T) methods with the FOC-QCP, where their geometries were optimized with the DFT method, as shown in Figure 6, and the SRC was calculated with the MP2 method (see Table 7). We wish to mention

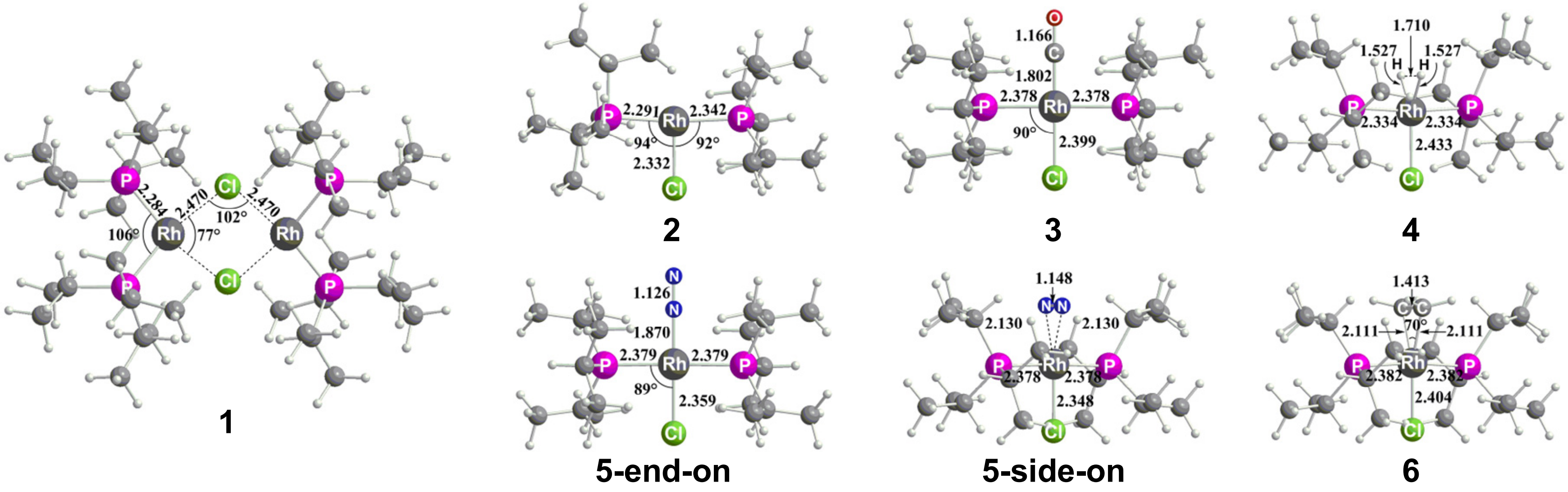

1 **2** **3** **4** **5-end-on** **5-side-on** **6**

Figure 6. Geometries of [RhCl(P^{i}Pr$_3$)$_2$]$_2$ **1**, RhCl(P^{i}Pr$_3$)$_2$ **2**, RhCl(P^{i}Pr$_3$)$_2$(CO) **3**, RhCl(P^{i}Pr$_3$)$_2$(H)$_2$ **4**, RhCl(P^{i}Pr$_3$)$_2$(N$_2$) **5-end-on** and **5-side-on**, and RhCl(P^{i}Pr$_3$)$_2$(C$_2$H$_4$) **6** optimized with the DFT[B3PW91]/BS-1 method. Bond lengths are in angstrom and bond angles are in degree.

Table 7. The monomerization energy of $[RhCl(P^iPr_3)_2]_2$ **1** and the coordination energies of CO, H_2, N_2, and C_2H_4 to **1** calculated with the DFT[B3PW91] (in vacuo), DFT[B3PW91] (in toluene), DFT[B3PW91]/$C^{\#(i\mathrm{Pr})}$ + SRC, and CCSD(T)/$C^{\#(i\mathrm{Pr})}$ + SRC methods (kcal/mol).

	B3PW91 real (in vacuo)	B3PW91 real (in benzene)	B3PW91 $C^{\#(i\mathrm{Pr})}$ + SRC (in vacuo)	CCSD(T) $C^{\#(i\mathrm{Pr})}$ + SRC (in vacuo)	expl t.[a]
$[RhCl(P^iPr_3)_2]_2$ **1** $\rightarrow$ $2RhCl(P^iPr_3)_2$ **2**	12.5	12.7	13.6	33.0	> 17.8[c,d]
$1/2[RhCl(P^iPr_3)_2]_{2(soln)} + CO_{(g)}$ $\rightarrow$ **3** $_{(soln)}$	−49.6	−47.9[b]	−52.1	−37.9	−39.3±0.7[d]
$1/2[RhCl(P^iPr_3)_2]_{2(soln)} + H_{2(g)}$ $\rightarrow$ **4** $_{(soln)}$	−23.4	−22.2[b]	−25.0	−20.3	−23.6±0.6[d]
$1/2[RhCl(P^iPr_3)_2]_{2(soln)} + N_{2(soln)}$ $\rightarrow$ **5-end-on** $_{(soln)}$	−18.4	−18.5	−23.6	−9.2	−7.6±0.7[e]
$1/2[RhCl(P^iPr_3)_2]_{2(soln)} + N_{2(soln)}$ $\rightarrow$ **5-side-on** $_{(soln)}$	−1.9	−2.8	−6.3	+6.1	
$1/2[RhCl(P^iPr_3)_2]_{2(soln)} + C_2H_{4(soln)}$ $\rightarrow$ **6** $_{(soln)}$	−18.4	−21.0	−20.0	−18.7	−15.9±0.6[e]

a) ΔH values (kcal/mol) determined by calorimetrical method and/or by equilibrium method.

b) The energies of CO and H_2 molecule are calculated in vacuo.

c) This value is lower limit determined by spectroscopic observation (see Ref. 53).

d) Ref [53a]

e) Ref [53b]

here that the solvation effect is very small in these reactions because the solvent is non-polar benzene, indicating that the CCSD(T)-calculated value in vacuo can be compared with the experimental results.

The endothermicity of the monomerization was experimentally estimated to be larger than 17.8 kcal/mol in benzene at 303.15 K.[32a] The DFT[B3PW91] method, however, presents much smaller destabilization energy by the monomerization of **1** in both vacuo and benzene than the experimental lower limit. This DFT[B3PW91]-calculated result seems incorrect, as follows: The DFT[B3PW91] method overestimates the steric repulsion by bulky ligands between two monomers because the dispersion interaction cannot be taken into consideration well by the DFT[B3PW91] method. This means that the DFT[B3PW91] method underestimates the stability of dimer **1**, which leads to underestimation of the destabilization energy by the monomerization of **1**. On the other hand, the CCSD(T) method with the FOC-QCP and SRC presents much larger monomerization energy, which agrees well with the experimental value.

In $RhCl(P^iPr_3)_2(H_2)$ and $RhCl(P^iPr_3)_2(C_2H_4)$, the DFT[B3PW91]-calculated coordination energies agree well with the experimental results. However, it is likely that this agreement is fortunate accident as follows: The dimer **1** was taken to be the standard of the coordination energy and the DFT[B3PW91] method underestimates the destabilization energy by the monomerization of **1**, as discussed above. These results indicate that the DFT[B3PW91] method underestimates the interaction energy of small molecule such as H_2 and C_2H_4 with a monomer $RhCl(P^iPr_3)_2$. In other words, the DFT[B3PW91] method underestimates the destabilization energy by the monomerization of **1** and the stabilization energy by the coordination of small molecule with $RhCl(P^iPr_3)_2$, which leads to the fortunate agreement of the DFT[B3PW91]-calculated binding energy with the experimental value.

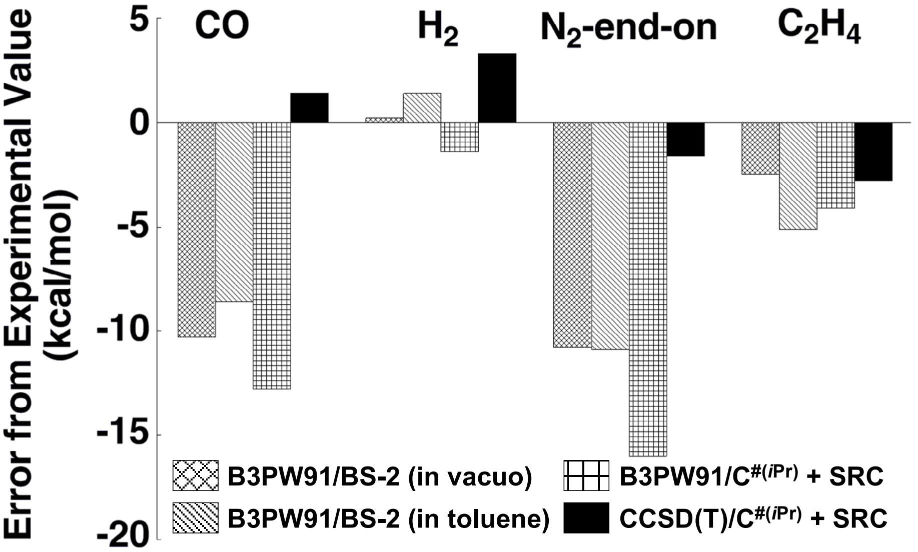

Figure 7. The error of the coordination energies (kcal/mol) of CO, H_2, N_2-end-on, and C_2H_4 to $[RhCl(P^iPr_3)_2]_2$ from the experimental values.

In $RhCl(P^iPr_3)_2(N_2)$, two coordination modes, end-on and side-on, were experimentally reported by X-ray diffraction experiments,[53] while the theoretical investigation at the HF level indicated that the end-on coordination mode was more stable than the side-on mode.[54] Also, the DFT[B3PW91]-calculated coordination energies are −18.4 and −1.9 kcal/mol for end-on and side-on coordination modes, respectively, which clearly shows that the end-on coordination mode is much more stable than the side-on mode. However, both values do not agree with the experimental result (−7.6±0.7 kcal/mol). On the other hand, the CCSD(T)-calculated coordination energy of the end-on mode agrees well with the experimental value.

It should be noted that the CCSD(T)-calculated coordination energies of CO, H_2, N_2, and C_2H_4 agree well with the experimental results within the error of about 3 kcal/mol, while the DFT[B3PW91]-calculated coordination energies considerably deviate from the experimental values, as shown in Figure 7. From these results, it is concluded that the CCSD(T)-method should be applied to these complexes and that the

FOC-QCP method with the SRC can present reliable coordination energies of such molecules as CO, H_2, N_2, and C_2H_4 with $[RhCl(P^iPr_3)_2]_2$.

4.5. Conclusions

Chemically reasonable models of PR_3 (R = Me, Et, ^{i}Pr, and ^{t}Bu) were constructed to perform the highly sophisticated post-Hartee-Fock calculations of the large transition metal complexes. The important role of PR_3 as a ligand is the σ-donation to the metal center with its lone pair orbital (HOMO). Because the strength of σ-donation, which relates to the strength of *trans* effect, is determined by the lone pair orbital energy, we optimized the effective potential on model atom ($C^{\#(R)}$) so as to reproduce the lone pair orbital energy of PR_3 (R = Me, Et, ^{i}Pr, ^{t}Bu) with the RHF and DFT[B3PW91] methods. We called this potential the frontier orbital consistent quantum capping potential (FOC-QCP).

First, we investigated the reductive elimination of ethane from model complexes $M(Me)_2(PH_3)_2$ (M = Ni, Pd, or Pt) with the DFT[B3PW91], MP2 to MP4(SDQ), CCSD, and CCSD(T) methods. Comparing to the CCSD(T) method, the DFT[B3PW91] method tends to underestimate the activation barrier and overestimate the exothermicity of the reaction. The MP4(SDQ) method cannot be applied to the reductive elimination reaction of the nickel and palladium complexes. In the reaction of the platinum complex, the MP4(SDQ) method slightly underestimates the activation barrier compared to the CCSD(T) method. These results indicate that we must apply the CCSD(T) method to this reductive elimination. However, the CCSD(T) method cannot be applied to the real reaction systems, $M(Me)_2(PR_3)_2$, because of their large sizes. This is the reason why we need the FOC-QCP method.

To examine the performance of this FOC-QCP, we calculated the activation barriers and the reaction energies of the reductive elimination reactions of C_2H_6 and H_2

from $M(R^1)_2(PR^2_3)_2$ (M = Ni, Pd, or Pt; R^1 = Me for R^2 = Me, Et, or ^{i}Pr; R^1 = H for R^2 = ^{t}Bu) with the DFT[B3PW91], MP4(SDQ), and CCSD(T) methods.

In the reductive elimination reaction of ethane from $M(Me)_2(PMe_3)_2$, the model ligand $PC^{\#(Me)}_3$ reproduces well the activation barriers and the reaction energies of the real reaction system in all the computational methods employed here except for the DFT[B3PW91]-calculated reaction energy of the $PC^{\#(Me)}_3$ system which somewhat deviates from that of the real system. However, the steric repulsion correction (SRC) leads to good agreement of this DFT[B3PW91]-calculated reaction energy with that of the $PC^{\#(Me)}_3$ and real system.

In more bulky substituent such as Et, ^{i}Pr, and ^{t}Bu, the steric repulsion becomes crucially important to present correct energy changes. The correction of steric repulsion is carried out by calculating the substituent only, to which the MP2 method is successfully applied because the substituent systems do not include the transition metal element.

By using the FOC-QCP method combined with the SRC, the monomerization energy of $[RhCl(P^iPr_3)_2]_2$ and coordination energies of CO, H_2, N_2, and C_2H_4 with the $[RhCl(P^iPr_3)_2]_2$ were calculated with the DFT[B3PW91] and CCSD(T) methods. The CCSD(T)-calculated monomerization energy and coordination energies agree well with the experimental value; the RMS error is 2.4 kcal/mol, which is much smaller than the RMS error (7.6 kcal/mol) of the DFT[B3PW91]-calculated coordination energies.

From all these results, we believe that the CCSD(T) method with the FOC-QCP + SRC is useful to theoretically investigate the large transition metal complexes including *tert*-phosphine. However, the gradient has not been implemented at this moment and the SRC is not consistent with the geometry optimization. Also, the FOC-QCP parameters are not presented for various *tert*-phosphines such as PCy_3 (Cy

= cyclohexyl), PPh_3, $POMe_3$, PF_3, and chelate diphosphine which are often used in many transition metal complexes. It is necessary to implement the gradient and to present parameters for various *tert*-phosphines.

4.6. Appendix

Table A1. The activation barrier (E_a) and reaction energy (ΔE) of reductive elimination reaction of ethane from $Pt(Me)_2(PMe_3)_2$ calculated by the DFT[B3PW91] method with various parameters of effective potential optimized with the DFT[B3PW91] methods.

C	ζ(B3PW91)	E_a	ΔE
−2.8	1.48334288	52.0	−9.6
−2.9	1.53358358	51.9	−9.6
−3.0	1.58297547	51.9	−9.6
−3.1	1.63155300	51.8	−9.6
−3.2	1.67934821	51.8	−9.6

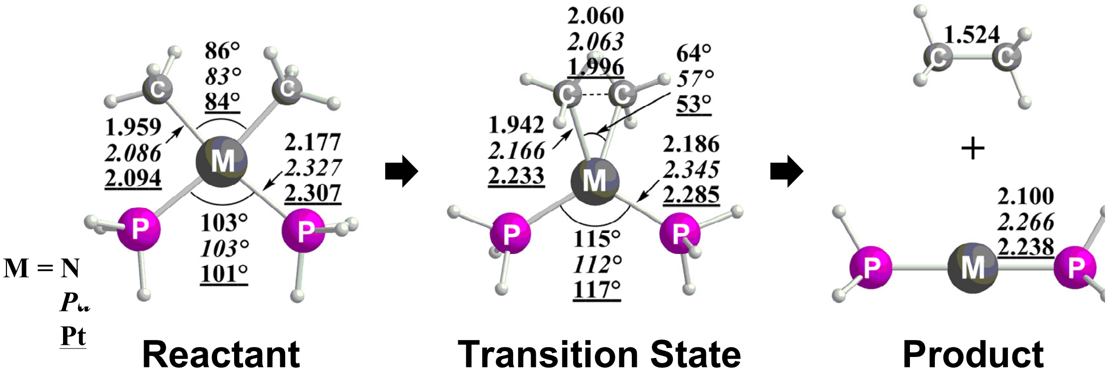

Figure A1. Geometry changes by the reductive elimination of ethane from $M(Me)_2(PH_3)_2$ (M = Ni, Pd, Pt) with DFT[B3PW91] method. Bond lengths are in angstrom and bond angles are in degree. Upper: M = Ni, Middle: M = Pd, Bottom: M = Pt.

References

(1) (a) Kameno, Y.; Ikeda, A.; Nakao, Y.; Sato, H.; Sakaki, S. *J. Phys. Chem. A* **2005**, *109*, 8055-8063. (b) Ikeda, A.; Nakao, Y.; Sato, H.; Sakaki, S. *J. Phys. Chem. A* **2007,** *111,* 7124-7132.

(2) (a) Kristyan, S.; Pulay, P. *Chem. Phys. Lett.* **1994**, *229*, 175-180. (b) Perez-Jorda, J. M.; Becke, A. D. *Chem. Phys. Lett.* **1995**, *233*, 134-137. (c) Zhang, Y.; Pan, W.; Yang, W. *J. Chem. Phys*. **1997**, *107*, 7921-7925. (d) Tsuzuki, S.; Lüthi, H. P. *J. Chem. Phys*. **2001**, *114*, 3949-3957. (e) Wu, Q.; Yang, W. *J. Chem. Phys.* **2002**, *116*, 515-524.

(3) Sakaki, S.; Ohkubo, K. *J. Phys. Chem.* **1989**, *93*, 5655-5660.

(4) Ohnishi, Y.; Nakao, Y.; Sato, H.; Sakaki, S. *J. Phys. Chem. A* **2007**, *111*, 7915-7924.

(5) Brynda, M.; Gagliardi, L.; Widmark. P.–O.; Power, P. P.; Roos, B. O. *Angew. Chem. Int. Ed.* **2006**, *45*, 3804-3807.

(6) (a) Warshel, A.; *Computer Modeling of Chemical Reactions in Enzymes and in Solutions*; Wiley: New York, 1991. (b) Monard, G.; Merz, K. M. Jr. *Acc. Chem. Res.* **1999**, *32*, 904-911.

(7) Warshel, A.; Levitt, M. *J. Mol. Biol.* **1976**, *103*, 227-249.

(8) Singh, U. C.; Kollman, P. A. *J. Comput. Chem.* **1986**, *7*, 718-730.

(9) Field, M. L.; Bash, P. A.; Karplus, M. *J. Comput. Chem.* **1990**, *11*, 700-733.

(10) (a) McCammon, J. A.; Gelin, B. R.; Karplus, M. *Nature* **1977**, *267*, 585-590. (b) Karplus, M.; McCammon, J. A. *Nat. Struct. Biol.* **2002**, *9*, 646-652 and references therein.

(11) Sauer, J.; Sierka, M. *J. Comput. Chem.* **2000**, *21*, 1470-1493.

(12) Woo, T. K.; Margl, P. M.; Deng, L.; Cavallo, L.; Ziegler, T. *Catal. Today* **1999**, *50*, 479-500.

(13) (a) Maseras, F.; Morokuma, K. *J. Comput. Chem.* **1995**, *16*, 1170-1179. (b) Maseras, F. *Chem. Commun.* **2000**, 1821-1827. (c) Ujaque, G.; Maseras, F. *Struct. Bond.* **2004**, *112*, 117-150.

(14) Bakowies, D.; Thiel, W. *J. Phys. Chem.* **1996,** *100,* 10580-10594.

(15) Lyne, P. D.; Hadoscek, M; Karplus, M. *J. Phys. Chem. A* **1999**, *103*, 3462-3471.

(16) Antes, I.; Thiel, W. *J. Phys. Chem. A* **1999**, *103*, 9290-9295.

(17) Eichinger, M.; Tavan, P.; Hutter, J.; Parrinello, M. *J. Chem. Phys.* **1999**, *110*, 10452-10467.

(18) Amara, P.; Field, M. J. *Theor. Chem. Acc.* **2003**, *109*, 43-52.

(19) Eurenius, K. P.; Chatfield, D. C.; Brooks, B. R.; Hodoscek, M. *Int. J. Quant. Chem.* **1996**, *60*, 1189-1200.

(20) Reuter, N.; Dejaegere, A.; Maigret, B.; Karplus, M. *J. Phys. Chem. A* **2000**, *104*, 1720-1735.

(21) Ferré, N.; Olivucci, M. *J. Mol. Struct. THEOCHEM* **2003**, 632*,* 71-82.

(22) (a) Théry, V.; Rinaldi, D.; Rivail, J.−L.; Maigret, B.; Ferenczy, G. G. *J. Comput. Chem.* **1994**, *15*, 269-282. (b) Assfeld, X.; Rivail, J.−L. *Chem. Phys. Lett.* **1996**, *263*, 100-106. (c) Monard, G.; Loos, M.; Théry V.; Baka, K.; Rivail, J.−L. *Int. J. Quant. Chem.* **1996**, *58*, 153-159. (d) Ferré, N.; Assfeld, X.; Rivail, J.−L. *J. Comput. Chem.* **2002**, *23*, 610-624.

(23) (a) Gao, J.; Amara, P.; Alhambra, C.; Field, M. J. *J. Phys. Chem. A* **1998**, *102*, 4714-4721. (b) Amara, P.; Field, M. J.; Alhambra, C.; Gao, J. *Theor. Chem. Acc.* **2000**, *104*, 336-343. (c) Garcia-Viloca, M.; Gao, J. *Theor. Chem. Acc.* **2004**, *111*, 280-286. (d) Pu, J.; Gao, J.; Truhlar, D. G. *J. Phys. Chem. A* **2004**, *108*, 632-650. (e) Pu, J.; Gao, J.; Truhlar, D. G. *J. Phys. Chem. A* **2004**, *108*, 5454-5463. (f) Pu, J.; Gao, J.; Truhlar, D. G. *ChemPhysChem*

2005, *6*, 1853-1865.

(24) (a) Alhambra, C.; Corchado, J. C.; Sanchez, M. L.; Gao, J.; Truhlar, D. G. *J. Am. Chem. Soc.* **2000**, *122*, 8197-8203. (b) Alhambra, C.; Corchado, J. Sanchez, M. L.; Garcia-Viloca, M.; Gao, J.; Truhlar, D. G. *J. Phys. Chem. B* **2001**, *105*, 11326-11340. (c) Devi-Kesavan, L. S.; Gao, J. *J. Am. Chem. Soc.* **2003**, *125*, 1532-1540.

(25) (a) Humbel, S.; Siebar, S.; Morokuma, K. *J. Chem. Phys.* **1996**, *105*, 1959-1967. (b) Svenson, M.; Humbel, S.; Morokuma, K. *J. Chem. Phys.* **1996**, *105*, 3654-3661. (c) Svenson, M.; Humbel, S.; Froese, R. D. J.; Matsubara, T.; Siebar, S.; Morokuma, K. *J. Phys. Chem.* **1996**, *100*, 19357-19363. (d) Dapprich, S.; Komaromi, I.; Byun, K. S.; Morokuma, K.; Frisch, M. J. *J. Mol. Struct. THEOCHEM* **1999**, *461−462*, 1-21. (e) Vreven, T.; Morokuma, K. *J. Comput. Chem.* **2000**, *21*, 1419-1432.

(26) (a) Zhang, Y.; Lee, T.–S.; Yang, W. *J. Chem. Phys.* **1999**, *110*, 46-54. (b) Zhang, Y. *J. Chem. Phys.* **2005**, *122*, 024114.

(27) (a) DiLabio, G. A.; Hurley, M. M.; Christiansen, P. A. *J. Chem. Phys.* **2002**, *116*, 9578-9584 (b) Moon, S.; Christiansen, P. A.; DiLabio, G. A. *J. Chem. Phys.* **2004**, *120*, 9080-9086.

(28) Yasuda, K.; Yamaki, D. *J. Chem. Phys.* **2004**, *121*, 3964-3972.

(29) Slaviček, P.; Martínez, T. J. *J. Chem. Phys.* **2006**, *124*, 084107.

(30) (a) Alary, F.; Poteau, R.; Heully, J.–L.; Barthelat, J.–C.; Daudey, J.–P. *Theor. Chem. Acc.* **2000**, *104*, 174-178. (b) Poteau, R.; Ortega, I.; Alary, F.; Solis, A. R.; Barthelat, J.–C.; Daudey, J.-P. *J. Phys. Chem. A* **2001**, *105*, 198-205. (c) Bessac, F.; Alary, F.; Carissan, Y.; Heully, J.–L.; Daudey, J.–P.; Poteau, R. *J. Mol. Struct. THEOCHEM* **2003**, *632*, 43-59.

(31) Koga, N.; Morokuma, K. *Chem. Phys. Lett.* **1990**, *172*, 243-248.

(32) (a) Wang, K.; Rosini, G. P.; Nolan, S. P.; Goldman, A. S. *J. Am. Chem. Soc.* **1995**, *117*, 5082-5088. (b) Wang, K.; Goldman, A. S.; Li, C.; Nolan, S. P. *Organometallics* **1995**, *14*, 4010-4013.

(33) A common *s*/*p* set of even-tempered functions with exponents; 0.12, 0.36, 1.08, 3.24, and 9.72. The *d* exponent is 0.626.

(34) Pacios, L. F.; Christiansen, P. A. *J. Chem. Phys.* **1985**, *82*, 2664-2671.

(35) Perdew, J. P.; Wang, Y. *Phys. Rev. B* **1992**, *45*, 13244-13249.

(36) Francl, M. M.; Petro, W. J.; Hehre, W. J.; Binkley, J. S.; Gordon, M. S.; DeFrees, D. J.; Pople, J. A. *J. Chem. Phys.* **1982**, *77*, 3654-3665.

(37) Hehre, W. J.; Ditchfield, R.; Pople, J. A. *J. Chem. Phys.* **1972**, *56*, 2257-2261.

(38) (a) Dunning, T. H., Jr. *J. Chem. Phys.* **1989**, *90*, 1007-1023. (b) Woon, D. E.; Dunning, T. H., Jr. *J. Chem. Phys.* **1993**, 98, 1358-1371.

(39) Dolg, M.; Stoll, W. H.; Preuss, H. *J. Chem. Phys.* **1987**, *86*, 866-872.

(40) Andrae, D.; Haeussermann, U.; Dolg, M.; Stoll, H.; Preuss, H. *Theor. Chim. Acta.* **1990**, *77*, 123-141.

(41) Frisch, M. J.; Pople, J. A.; Binkley, J. S. *J. Chem. Phys.* **1984**, *80*, 3265-3269.

(42) Martin, J. M. L.; Sundermann, A. *J. Chem. Phys.* **2001**, *114*, 3408-3420.

(43) Balabanov, N. B.; Peterson, K. A. *J. Chem. Phys.* **2005**, *123*, 064107.

(44) Cancés, M. T.; Mennucci, B.; Tomasi, J. *J. Chem. Phys.* **1997**, *107*, 3032-3041.

(45) Pople, J. A. et al. Gaussian03, Revision D.02 Gaussian, Inc., Wallingford CT, 2004.

(46) Chandler, J. P. Subroutine STEPIT - Finds local minima of a smooth function of several parameters., *Behavioral Science,* **1969**, *14*, 81-82.

(47) Chatt, J.; Shaw, B. L. *J. Chem. Soc.* **1959**, 705-716.

(48) Low, J. J.; Goddard, W. A., III *J. Am. Chem. Soc.* **1986**, *108*, 6115-6128.

(49) Curtiss, L. A.; Raghavachari, K.; Trucks, G. W.; Pople, J. A. *J. Chem. Phys.* **1991**, *94*, 7221-7230.

(50) Matsubara, T.; Maseras, F.; Koga, N.; Morokuma, K. *J. Phys. Chem.* **1996**, *100*, 2573-2580.

(51) Svensson, M.; Humbel, S.; Froese, R. D. J.; Matsubara, T.; Sieber, S.; Morokuma, K. *J. Phys. Chem.* **1996**, *100*, 19357-19363.

(52) Though the SRC is effective for this size of molecule, we wish to mention here that the SRC is still more time-consuming for large system such as enzyme than the QM/MM method.

(53) (a) End-on coordination was proposed in Thorn, D. L.; Tulip, T. H.; Ibers, J. A. *J. Chem. Soc. Dalton Trans.* **1979**, 2022-2025. (b) Side-on coordination was proposed in Buesetto, C.; D'Alfonso, A.; Maspero, F.; Perego, G.; Zazzetta, A. *J. Chem. Soc. Dalton Trans.* **1977**, 1828-1834.

(54) Sakaki, S.; Morokuma, K.; Ohkubo, K. *J. Am. Chem. Soc.* **1985**, *107*, 2686-2693.

Chapter 5

A Theoretical Study of Nickel(0)-Catalyzed Phenylcyanation of Alkynes.
Reaction Mechanism and Regioselectivity

5.1. Introduction

Activation of the C−CN σ-bond of nitrile by low-valent transition-metal complex is one of the challenging reactions in organometallic chemistry and catalytic chemistry because it is not easy to activate the strong C−CN σ-bond with transition-metal complexes. As a result of various attempts, several examples of stoichiometric C−CN σ-bond activation reaction by transition-metal complex have been reported, so far: The C−CN σ-bond activations of benzonitrile (PhCN),[1] fluorobenzonitrile (C_6H_4FCN),[2] and benzoyl cyanide (PhCOCN)[3] were succeeded with Pt(0),[1-3] Pd(0),[2] and Ni(0)[2] complexes very previously. Also, Burmeister and Edwards reported the C−CN σ-bond activation of 1,1,1-tricyanoethane by $Pt(PPh_3)_4$,[4] and Turco and co-workers reported the C−CN σ-bond activation of alkyl and aryl cyanides by Ni(0) complexes.[5] Blanchini et al. reported the C−CN σ-bond activation of ethyl cyanoformate ($NCCO_2Et$) with Ni and Co complexes.[6] Abla and Yamamoto succeeded the C−CN σ-bond activation of *o*- and *p*-$C_6H_4(CN)_2$ by Ni(bpy).[7] Churchill et al. reported the C−CN σ-bond activation of acetonitrile with Mo(0) complexes.[8] Recently, Jones and his collaborators experimentally[9a-d,f] and theoretically[9e,f] investigated the C−CN σ-bond activations of MeCN and PhCN by Ni(0) complexes. They found that η^2-nitrile and η^2-arene complexes were formed before the C−CN σ-bond activation at −60 °C.[9f] We also theoretically investigated the C−CN σ-bond activation of MeCN.[10] Besides these

Scheme 1

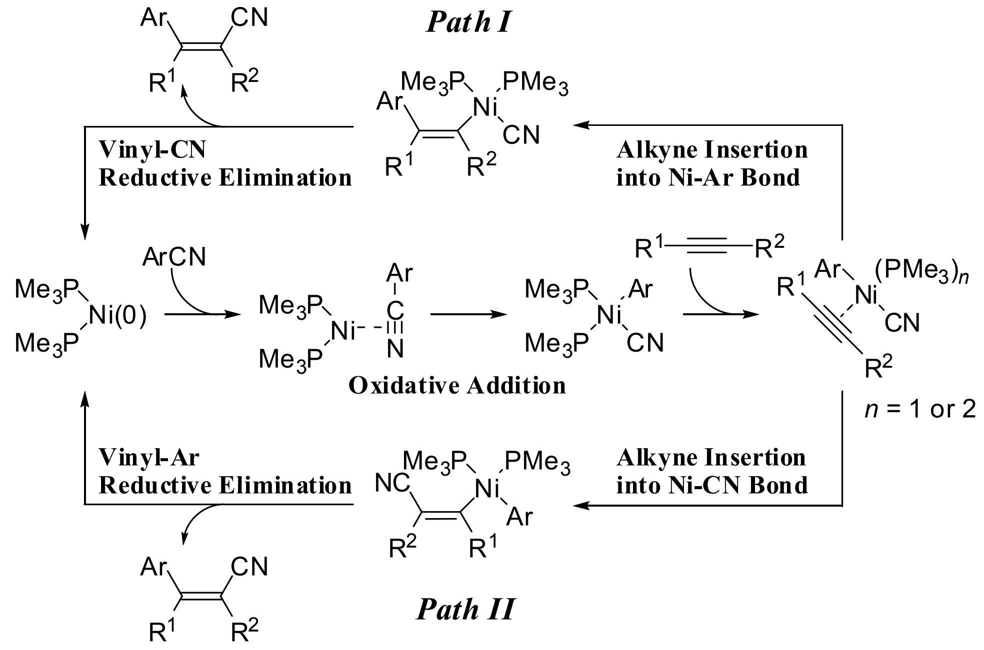

C−CN σ-bond activation reactions by the oxidative addition, another type of C−CN σ-bond activation was performed with help of silyl group in Rh(III)[11] and Fe(II) complexes.[12]

This C−CN σ-bond activation can be utilized for organic synthesis of various organic nitriles. For instance, the interesting catalytic syntheses including the C−CN σ-bond activation have been reported, as follows: Miller reported Ni-catalyzed cross coupling reaction to give biaryls,[13] where $NiCl_2(PMe_3)_2$ was employed as catalyst. Recently, Nakao, Hiyama, and co-workers reported efficient Ni(0)-catalyzed arylcyanation of alkyne.[14] This catalytic reaction is of considerable interest from the viewpoint of applied chemistry because various acrylonitrile derivatives can be synthesized by this reaction. Also, this reaction is very interesting from the viewpoint of reaction mechanism and catalysis of transition metal complex, as follows: The oxidative addition of Ar−CN to Ni(0) center occurs first, as shown in Scheme 1, which

Scheme 2

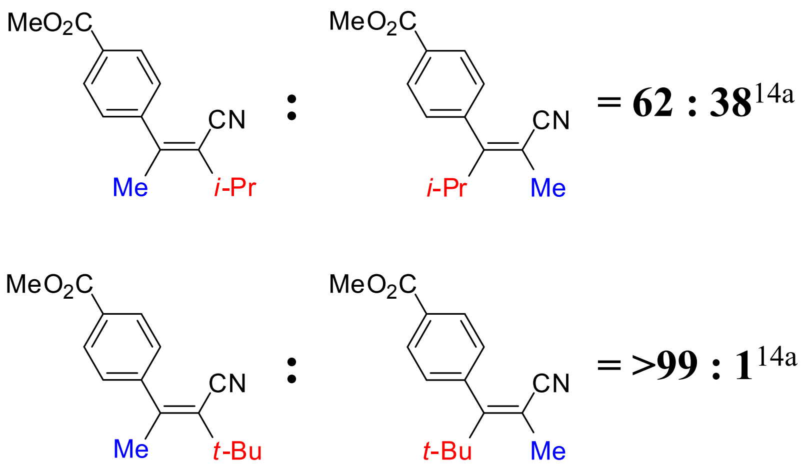

is believed to be difficult. After that, two reaction courses are possible; in one course (Path I), alkyne is inserted into the Ni−Ar bond followed by reductive elimination of vinyl and CN groups. In the other (Path II), alkyne is inserted into the Ni−CN bond followed by reductive elimination of vinyl and Ar groups. The alkyne insertion into the metal−Ar bond is often reported, while the alkyne insertion into the metal−CN bond has not been reported to our knowledge, probably because the metal−CN bond is strong. The reductive elimination of the Ph and vinyl groups is reported, while the reductive elimination of the vinyl and CN groups is considered to be difficult because of the strong metal−CN bond. Thus, both reaction courses involve difficult process. It is worth investigating theoretically the reaction mechanism of this interesting catalytic reaction. Also, significantly large regioselectivity was observed in this reaction, as shown in Scheme 2; when ^{i}PrC≡CMe was employed as alkyne, CN was introduced on the C atom bearing ^{i}Pr group in the major product and the ratio of the major product to the minor one was almost 3 to 2.[14a] This regioselectivity is strange because not small CN but bulky Ph is introduced on the C atom bearing bulky ^{i}Pr group. When ^{t}BuC≡CMe was employed, only the major product was produced but the minor product was not.[14a] The reason for such interesting regioselectivity is not clear. Thus, the theoretical investigation of the regioselectivity is also necessary.

In this paper, we theoretically investigated this Ni-catalyzed phenylcyanation of alkyne mainly with the DFT method and in part with the CCSD(T) method, where PhCN and such alkynes as HC≡CH, MeC≡CH, ^{i}PrC≡CMe, and ^{t}BuC≡CMe were employed as reactants. Our purpose here is to elucidate the reaction mechanism, the rate-determining step, the regioselectivity of the reaction, and the determining factors of the reaction mechanism and the regioselectivity. Also, we examined the formation process of the active species because it has not been theoretically examined yet, to our knowledge.

5.2. Computational Method

Geometries were optimized with the DFT method, where the B3PW91 hybrid functional[15] was used for exchange-correlation term. We ascertained that each intermediate did not exhibit imaginary frequency and each transition state exhibited one imaginary frequency. Also, we checked that geometry changes induced by the imaginary frequency were consistent with the reaction course.[16] Energy and population changes were calculated with the DFT(B3PW91) method. Energy change by the oxidative addition of PhCN to $Ni(PMe_3)_2$ was investigated by both of the DFT and CCSD(T) methods coupled with our FOC-QCP method[17] because the energy changes by the oxidative addition of MeCN to $Ni(PH_3)_2$ are somewhat different between the DFT and CCSD(T) methods.[10]

Two kinds of basis set systems were used. In geometry optimization, the following basis set system (BS-I) was employed: The (311111/22111/411/1) basis set[18] was used for valence electrons of Ni and energy-consistent effective core potentials (ECPs) of the Stuttgart-Dresden-Bonn group were used to replace its core electrons (up to 2p). For P, PhCN, and alkynes, 6-31G(d) basis sets[19] were employed. One p-polarization function was added to the H atom of small alkynes, HC≡CH and MeC≡CH, because the H atom is directly bound with the C atom, while it was not for large alkynes ^{i}PrC≡CMe and ^{t}BuC≡CMe. For the other atoms, 6-31G basis sets[20] were employed. Energy changes were calculated with better basis set system (BS-II), using the DFT(B3PW91)/BS-I-optimized geometries. In BS-II, cc-pVTZ basis set[21] was employed for Ni, where g polarization function was removed to save CPU time. In our previous work, we found that the cc-pVTZ should be employed for Ni to present the reliable energy change.[10] For the other atoms, the cc-pVDZ basis sets[22] were employed.

In this paper, we will present potential energy in vacuo, $E_{\mathrm{gas}}^{\mathrm{ev_0}}$, including zero-point vibrational energy:

$$E_{\mathrm{gas}}^{\mathrm{ev_0}} = E_{\mathrm{gas}}^{\mathrm{e}} + E_{\mathrm{gas}}^{\mathrm{v_0}} \tag{1}$$

where $E_{\mathrm{gas}}^{\mathrm{e}}$ and $E_{\mathrm{gas}}^{\mathrm{v_0}}$ represent electronic energy and zero-point vibrational energy, respectively. Also, we will present three kinds of free energies in solution defined as follows:

$$F_{\mathrm{sol}}^{\mathrm{ev}} = F_{\mathrm{sol}}^{\mathrm{e}} + E_{\mathrm{gas}}^{\mathrm{v}} - TS_{\mathrm{gas}}^{\mathrm{v}} \tag{2}$$

$$F_{\mathrm{sol}}^{\mathrm{evr}} = F_{\mathrm{sol}}^{\mathrm{e}} + E_{\mathrm{gas}}^{\mathrm{v}} + E_{\mathrm{gas}}^{\mathrm{r}} - T\left(S_{\mathrm{gas}}^{\mathrm{v}} + S_{\mathrm{gas}}^{\mathrm{r}}\right) \tag{3}$$

$$F_{\mathrm{sol}}^{\mathrm{evrt}} = F_{\mathrm{sol}}^{\mathrm{e}} + E_{\mathrm{gas}}^{\mathrm{v}} + E_{\mathrm{gas}}^{\mathrm{r}} + E_{\mathrm{gas}}^{\mathrm{t}} - T\left(S_{\mathrm{gas}}^{\mathrm{v}} + S_{\mathrm{gas}}^{\mathrm{r}} + S_{\mathrm{gas}}^{\mathrm{t}}\right) \tag{4}$$

where T is absolute temperature. $F_{\mathrm{sol}}^{\mathrm{e}}$ is electronic energy of solute in solution, where electrostatic and non-electrostatic contributions of solvent (toluene) are calculated with the IEF-PCM method[23] at 373.15 K. $E_{\mathrm{gas}}^{\mathrm{v}}$, $E_{\mathrm{gas}}^{\mathrm{r}}$, and $E_{\mathrm{gas}}^{\mathrm{t}}$ are vibrational, rotational, and translational internal energies, respectively, and $S_{\mathrm{gas}}^{\mathrm{v}}$, $S_{\mathrm{gas}}^{\mathrm{r}}$, and $S_{\mathrm{gas}}^{\mathrm{t}}$ are vibrational, rotational, and translational entropies, respectively. All these quantities are calculated in vacuo at 373.15 K. Thus, $F_{\mathrm{sol}}^{\mathrm{ev}}$ represents the free energy in solution which includes internal energy and entropy arising from vibrational motions. In the similar way, $F_{\mathrm{sol}}^{\mathrm{evr}}$ represents free energy in solution which includes internal energy and

Table 1. The reaction energy (kcal/mol) in the formation of Ni(cod)(X)(Y)[a] (X, Y = PMe_3, PhCN, or HC≡CH) from $Ni(cod)_2$ **1**.

X	Y	ΔE^{ev_0}	ΔF^{ev}	ΔF^{evr}	ΔF^{evrt}
PMe_3	–	+11.2	+10.6	+8.5	+8.2
PhC$\underline{\mathrm{N}}$(η^1)[b]	–	+13.4	+11.5	+10.4	+10.3
Ph$\underline{\mathrm{CN}}$(η^2)[b]	–	+2.5	+1.6	+0.7	+0.6
HC≡CH	–	−8.8	−7.7	−13.5	−14.7
PMe_3	PMe_3	−9.7	−17.5	−12.5	−0.8
PMe_3	PhC$\underline{\mathrm{N}}$(η^1)[b]	−5.7	−11.5	−5.3	−8.2
PMe_3	HC≡CH	−8.4	−14.7	−13.6	−1.3
PhC$\underline{\mathrm{N}}$(η^1)[b]	PhC$\underline{\mathrm{N}}$(η^1)[b]	0.0	+6.8	+0.6	+14.3
HC≡CH	HC≡CH	0.1	−4.2	−6.3	−5.0

a) Geometries are shown in Appendix Figure A1.

b) Underline represents the atom or group coordination with the Ni center.

entropy arising from vibrational and rotational motions. In addition to these terms, $F_{\mathrm{sol}}^{\mathrm{evrt}}$ involves internal energy and entropy arising from translational motions. For unimolecular process, we will present discussion based on the $F_{\mathrm{sol}}^{\mathrm{ev}}$ value because rotational and translational contributions to energy are little change in the process. In bimolecular processes such as coordinations of PhCN and alkyne, we will present discussion based on $F_{\mathrm{sol}}^{\mathrm{ev}}$ and $F_{\mathrm{sol}}^{\mathrm{evr}}$ because it is likely that the translational motion is suppressed in solution.[24] We omit subscript “sol” and “gas” hereafter for brevity.

Gaussian 03 program package[25] was used for these calculations. Population analysis was carried out with the method of Weinhold et al.[26]

5.3. Results and Discussion

As mentioned in introduction, we will investigate here two reaction mechanisms shown in Scheme 1. First, we will discuss the reaction mechanism (Path I) including the alkyne insertion into the Ni−Ph bond followed by the reductive elimination of the vinyl and CN groups. Then, we will present results and discussion of the other reaction mechanism (Path II) via the alkyne insertion into the Ni−CN bond followed by the reductive elimination of the vinyl and Ph groups. Finally, we will discuss the regioselectivity.

5.3.1. Geometry and Energy Changes of Path I

A. Coordination and Oxidative Addition of PhCN to $Ni(PMe_3)_2$

Initial nickel complex is $Ni(cod)_2$ **1** (cod = cycloocta-1,5-diene). Considering that two equivalent of PMe_3 and excess of substrates (PhCN and alkyne) are added to the reaction solution, it is likely that precursor complex is Ni(cod)(X)(Y) (X, Y = PMe_3, PhCN, alkyne). Because $Ni(cod)(PMe_3)_2$ **2** is the most stable among these species, as clearly indicated by ΔF^{ev} value shown in Table 1, we examined reaction mechanism starting from **2**, as shown in Figure 1.[27] Because of the steric hindrance, only nitrogen atom of PhCN can approach first the Ni center to form $Ni(cod)(PMe_3)_2(\underline{N}CPh)$ **3** through transition state $\mathbf{TS_{2\text{-}3}}$,[28] where the underline represents the atom or group coordinating with the Ni center, hereafter. In **3**, one of the π-bonds of cod interacts with the Ni center but the other is free (for side view of these geometrical changes, see Appendix Figure A2). Because **2** and **3** are Ni(0) complexes with four ligands, they take tetrahedral-like geometry. Then, cod dissociates from the Ni center to form a η^1-N end-on coordinate complex $Ni(PMe_3)_2(\eta^1\text{-}\underline{N}CPh)$ **4** through transition state $\mathbf{TS_{3\text{-}4}}$. From **4**, a stable η^2-NC side-on coordinate species $Ni(PMe_3)_2(\eta^2\text{-}\underline{NC}Ph)$ **5** is formed via transition state $\mathbf{TS_{4\text{-}5}}$. In this $\mathbf{TS_{4\text{-}5}}$, the CN bond is rotating clockwise so as to increase the Ni−N distance and decrease the Ni−C distance. Geometrical features and bonding natures of **4** and **5** are essentially the same as those of the similar complexes $Ni(PH_3)_2(\eta^1\text{-}\underline{N}CMe)$ and $Ni(PH_3)_2(\eta^2\text{-}\underline{NC}Me)$, respectively, which were previously discussed in detail.[10] However, several differences in geometry are observed between

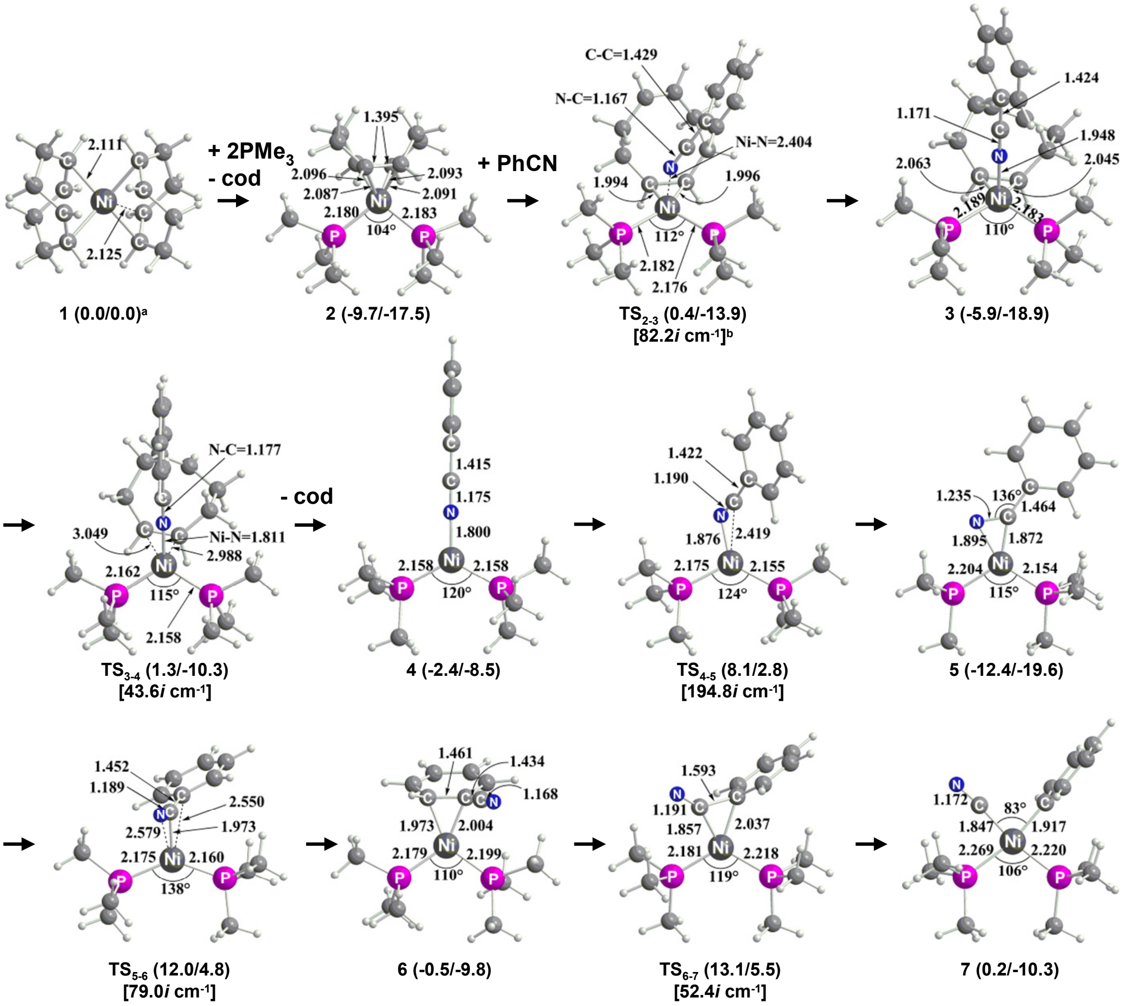

Figure 1. Geometry and energy changes (kcal/mol) in substitution of cod for PhCN, isomerization of Ni(PMe$_3$)$_2$(PhCN), and oxidative addition of PhCN to Ni(0) center. Bond lengths are in angstrom and bond angles are in degree. a) In parenthesis, E^{ev_0} and F^{ev} (kcal/mol) values relative to **1** are shown before and after the slash, respectively. b) In square brackets is the eigenvalue of imaginary frequency in transition state.

Ni(0) bisphosphine complexes of PhCN and MeCN, as follows: The η^1-N end-on and η^2-CN side-on coordinate structures are optimized in both of Ni(0) bisphosphine complexes of MeCN and PhCN. In addition to them, the η^2-C=C coordinate structure $\mathrm{Ni(PMe_3)_2}(\eta^2$-PhCN) **6** is optimized in the PhCN complex. The η^1-C interacting structure is not optimized in the PhCN complex, while it was reported in the MeCN complex.[10] In **6**, Ph coordinates with the Ni center through the interaction between the π^* orbital of Ph and the d_π orbital of Ni, which is the back donation from Ni to Ph. The similar η^2-arene complex was observed by Jones et al. in the Ph–CN σ-bond activation by Ni(dmpe).[9f] Also, such coordination structure was theoretically reported as a precursor complex of oxidative addition and in Heck reaction catalyzed by Ni and Pd complexes.[29] Starting from **6**, the PhCN rotates and slides above the Ni center so as to approach the C−CN bond to the Ni center (Figure 1). In $\mathbf{TS_{6\text{-}7}}$, the CN and Ph groups are changing their directions toward the Ni center and the Ph−CN bond cleavage is in progress.[30] The product is *cis*-$\mathrm{Ni(CN)(Ph)(PMe_3)_2}$ **7**. Because **7** is a Ni(II) complex bearing strong ligands, the complex takes square planner geometry. This step is the typical oxidative addition of PhCN to $\mathrm{Ni(PMe_3)_2}$. Though we examined *cis-trans* isomerization after the oxidative addition, we found that it does not occur in this experimental condition.[31]

The energy changes relative to **1** are also shown in Figure 1, where the values before and after slash represent E^{ev_0} and F^{ev}, respectively. PhCN coordinates with the Ni center of **2** with the activation barrier of 10.1/3.6 kcal/mol and the reaction energy of +3.8/−1.4 kcal/mol, to afford $\mathrm{Ni(cod)(PMe_3)_2}$(NCPh) **3**. In **3**, cod dissociates from the Ni center with destabilization energy of 3.5/10.4 kcal/mol, to afford $\mathrm{Ni(PMe_3)_2}(\eta^1$-NCPh) **4**. Complex **4** is less stable than **2** and **3**. The isomerization of **4** occurs with activation barrier of 10.5/11.3 kcal/mol, to form the very stable intermediate **5**. The isomerization of **5** to **6** requires large activation barrier of

Table 2. The activation barrier (E_a) and reaction energy (ΔE) (kcal/mol) in the isomerization of $Ni(PMe_3)_2(PhCN)$ (**4** → **5** and **5** → **6**) and the oxidative addition (**6** → **7**) calculated with the DFT(B3PW91) and CCSD(T) + MP2 with FOC-QCP + SRC methods.

	DFT(B3PW91) Real	DFT(B3PW91) FOC-QCP+SRC	CCSD(T)+MP2 FOC-QCP+SRC
E_a (**4** → **5**)	11.2	11.6	10.1
ΔE (**4** → **5**)	−10.6	−8.2	−16.0
E_a (**5** → **6**)	25.8	24.4	25.0
ΔE (**5** → **6**)	+12.6	+10.5	+6.2
E_a (**6** → **7**)	14.4	15.0	17.7
ΔE (**6** → **7**)	+0.3	+3.6	+1.5

24.4/24.4 kcal/mol. This activation free energy in this system is slightly lower than that (30.2 kcal/mol) in the Ni(dmpe) system reported by Jones et al;[9f] since the complex with two PMe_3 ligands is more flexible than the complex with a bidentate dmpe ligand, the activation barrier of isomerization is lower in our work than in their work, though the perfect comparison can not be made because solvent and basis sets are different between their work and ours. The η^2-C=C coordination species **6** is not stable very much. Starting from **6**, the oxidative addition occurs with moderate activation barrier of 13.6/15.3 kcal/mol. This activation free energy is moderately smaller than that (17.1 kcal/mol) in the Ni(dmpe) system reported by Jones et al.[9f] Though the Ni(II) species **7** is less stable than **6** in vacuo, **7** is slightly more stable than **6** in toluene. This solvation effect is interpreted in terms of polarity of the species, as follows: Because the Ni(II) species **7** is more polar (dipole moment = 10.65 D) than the Ni(0) species **6** (7.39 D), toluene (dielectric constant = 2.379) moderately stabilizes **7** compared to **6**.

Because the DFT and CCSD(T) methods presented somewhat different energy changes in the oxidative addition to Ni(0) complex,[10] we performed the CCSD(T) calculation combined with the FOC-QCP to evaluate the potential energy (E^c) change

Scheme 3

(A) Dissociative substitution mechanism (via 3-coordinate intermediate)

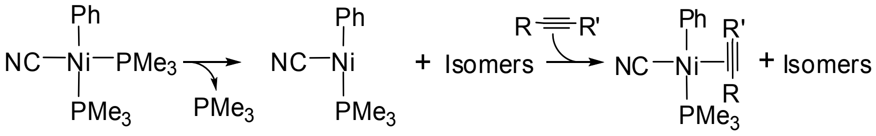

(B) Associative substitution mechanism (via 5-coordinate intermediate)

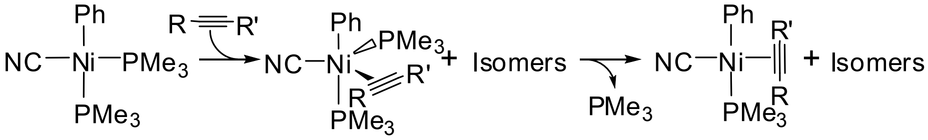

from **4** to **7**, where the MP2 method was applied to evaluate the steric repulsion correction (SRC). This computation method presents reliable energy changes in the oxidative addition reaction to $Ni(PMe_3)_2$.[17] Table 2 lists the activation barrier and the reaction energy calculated with the DFT(B3PW91) and CCSD(T) methods without ZPE correction. The DFT(B3PW91) calculation combined with the FOC-QCP + SRC presents almost the same results as the DFT(B3PW91) calculation of the real complex, indicating the FOC-QCP + SRC works well here. The CCSD(T)-calculated activation barriers of isomerization from **4** to **5** and that from **5** to **6** are similar to the DFT(B3PW91)-calculated values. On the other hand, the CCSD(T)-calculated activation barrier of the oxidative addition (**6** → **7**) is somewhat larger than the DFT(B3PW91)-calculated one. However, the CCSD(T)-calculated activation barrier of the isomerization from **4** to **5** is still larger than that of the oxidative addition like the DFT(B3PW91)-calculated results. From these results, it is concluded that the DFT(B3PW91) method leads to correct conclusion about reaction mechanism here.

B. Substitution of PMe_3 for HC≡CH in $Ni(CN)(Ph)(PMe_3)_2$

In the next step, alkyne must coordinate with the Ni center of **7**, as shown in Scheme 3.[32] One possible coordination way is dissociative substitution in which PMe_3

dissociates from the Ni center to form a three-coordinate species Ni(CN)(Ph)(PMe_3) **14A** or **14C** and then HC≡CH coordinates with the Ni center, as shown in Figure 2(A). Another possible reaction course is associative substitution in which HC≡CH first coordinates with **7** to form a five-coordinate species Ni(CN)(Ph)$(PMe_3)_2$(HC≡CH) **8A** and then PMe_3 dissociates from the Ni center to form a four-coordinate species Ni(CN)(Ph)(PMe_3)(HC≡CH) **9A**, as shown in Figure 2(B).

In the dissociative substitution, the first step is PMe_3 dissociation from the Ni center to form a three-coordinate Ni complex Ni(CN)(Ph)(PMe_3) **14A** or **14C**, where the empty coordination site is at the position *trans* to Ph in **14A** and at the position *trans* to CN in **14C**. In the associative substitution, the five-coordinate intermediate **8A** is formed first. Then, either equatorial or axial PMe_3 dissociates from the Ni center. The dissociation of the equatorial PMe_3 occurs through transition state $\mathbf{TS_{8A\text{-}9B}}$ leading to the formation of *cis*-Ni(CN)(Ph)(PMe_3)(HC≡CH) **9B**, in which CN and Ph take the positions *cis* to each other and HC≡CH takes the position *trans* to CN, as shown in the bottom of Figure 2(B). Another transition state $\mathbf{TS_{8A\text{-}9A}}$ is also optimized, as shown in the top of Figure 2(B), which is similar to the Berry pseudo-rotation. In the transition state $\mathbf{TS_{8A\text{-}9A}}$, Ph leans toward the empty coordination site at the position *trans* to CN, and simultaneously, the axial PMe_3 dissociates from the Ni center. Thus, the dissociation of axial PMe_3 leads to the formation of *trans*-Ni(CN)(Ph)(PMe_3)(HC≡CH) **9A**, in which Ph and CN take the positions *trans* to each other.

Entropy effect should be carefully considered to make comparison between the dissociative and associative substitutions. As shown in Table 3, ΔF^{e}, ΔF^{ev}, and ΔF^{evr} values relative to **7** indicate that **14A** and **14C** are much less stable than the transition state $\mathbf{TS_{8A\text{-}9A}}$ and $\mathbf{TS_{8A\text{-}9B}}$, where **14A** + PMe_3 and **14C** + PMe_3 are compared with **7** and $\mathbf{TS_{8A\text{-}9A}}$ – HC≡CH and $\mathbf{TS_{8A\text{-}9B}}$ – HC≡CH are compared with **7**. We employ ΔF^{ev} and ΔF^{evr} values in this paper, as mentioned in computational details. Because these values

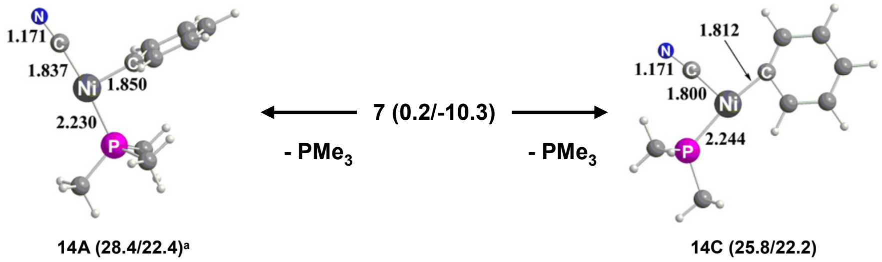

(A) Dissociative substitution from **7**[c]

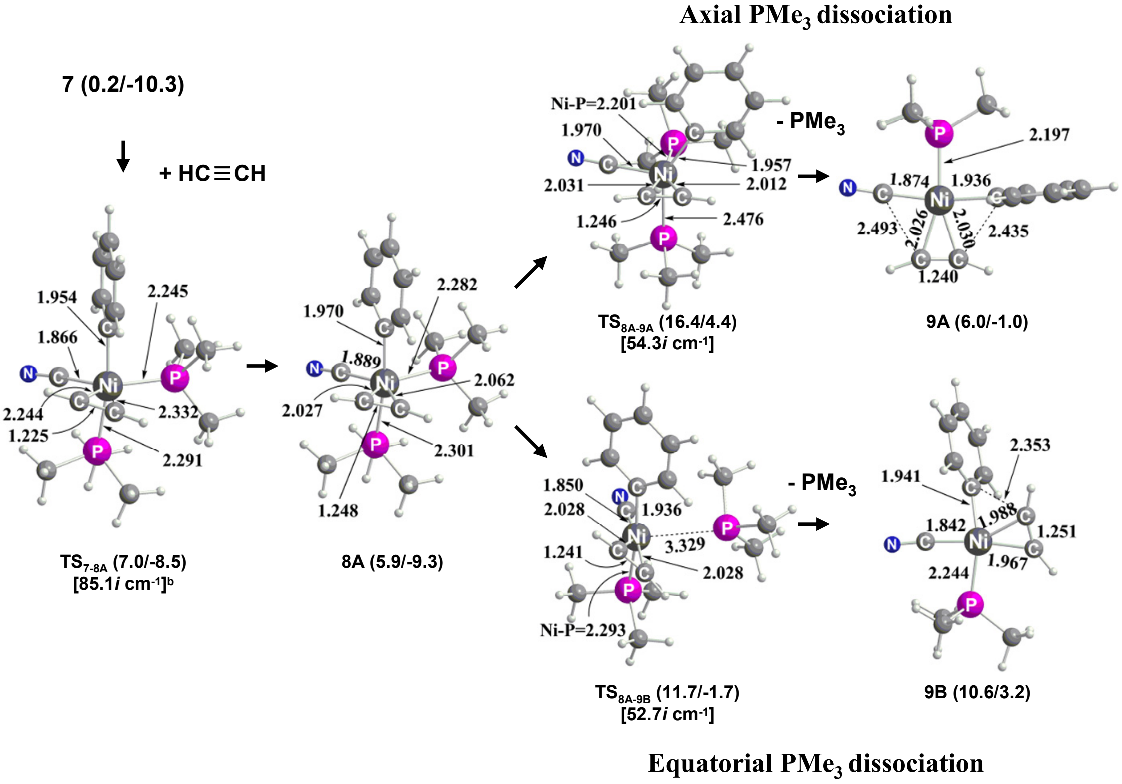

(B) Associative substitution from **7**

Figure 2. Geometry and energy changes (kcal/mol) in substitution of PMe_3 for HC≡CH through (A) dissociative mechanism and (B) associative mechanism. Bond lengths are in angstrom. a) In parenthesis, E^{ev_0} and F^{ev} (kcal/mol) values relative to **1** are shown before and after the slash, respectively. b) In square brackets is the eigenvalue of imaginary frequency in transition state. c) The other geometries in dissociative mechanism are shown in Supporting Information Figure S4.

Table 3. Free energy changes (ΔF^{e}, ΔF^{ev}, ΔF^{evr}, and ΔF^{evrt}) (kcal/mol) in dissociative and associative substitution of HC≡CH with PMe_3.

	ΔF^{e}	ΔF^{ev}	ΔF^{evr}	ΔF^{evrt}
Dissociative[a]				
14A	30.9	32.7	25.5	12.0
14C	30.5	32.5	25.3	11.7
Associative[b]				
8A	0.2	1.0	4.4	16.9
$\mathbf{TS_{8A\text{-}9A}}$	12.2	14.7	18.1	30.6
9A	6.0	9.3	5.4	4.4
$\mathbf{TS_{8A\text{-}9B}}$	11.8	8.6	11.8	24.3
9B	10.6	13.5	9.6	8.5

a) Relative values to **7** – PMe_3

b) Relative values to **7** + HC≡CH

are smaller in the associative substitution than in the dissociative one, it is likely considered that the associative substitution is more favorable than the dissociative one. Energy changes in the associative substitution are shown in Figure 2(B). The HC≡CH coordination with the Ni center occurs with the activation barrier of 6.8/1.8 kcal/mol and the reaction energy of +5.7/−8.2 kcal/mol.

It is important for the next step which of the axial and equatorial PMe_3 dissociations occurs easily. The axial PMe_3 dissociates from the Ni center with the activation barrier of 16.2/14.7 kcal/mol and the endothermicity of 5.8/9.3 kcal/mol relative to **7** + HC≡CH. The equatorial PMe_3 dissociates from the Ni center with the activation barrier of 11.5/8.6 kcal/mol and the endothermicity of 10.4/13.5 kcal/mol relative to **7** + HC≡CH. Although it can not be concluded at this moment which PMe_3 more easily dissociates, we will show the axial PMe_3 dissociation leading to the formation of **9A** is more favorable than the equatorial PMe_3 dissociation, in Sec. 3.3.

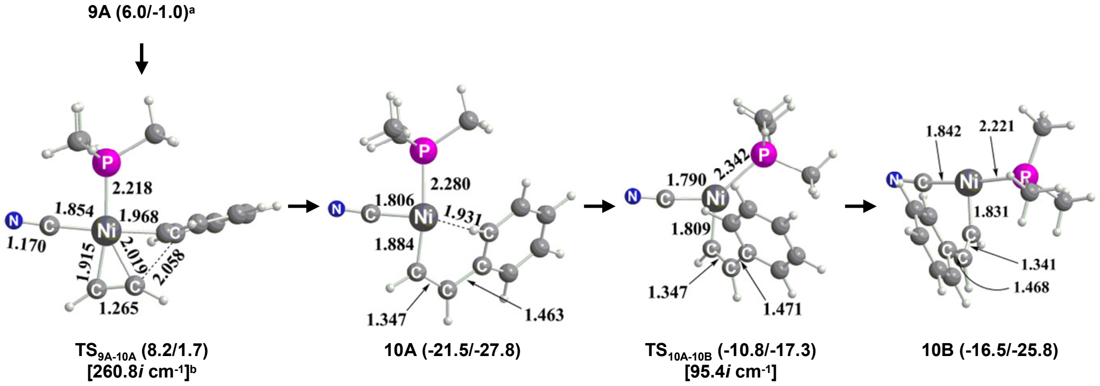

$TS_{9A\text{-}10A}$ (8.2/1.7) [260.8*i* cm^{-1}]^b

10A (-21.5/-27.8)

$TS_{10A\text{-}10B}$ (-10.8/-17.3) [95.4*i* cm^{-1}]

10B (-16.5/-25.8)

Figure 3. Geometry and energy changes (kcal/mol) in HC≡CH insertion into the Ni−Ph bond. Bond lengths are in angstrom. a) In parenthesis, E^{ev_0} and F^{ev} (kcal/mol) values relative to **1** are shown before and after the slash, respectively. b) In square brackets is the eigenvalue of imaginary frequency in transition state.

C. Insertion of HC≡CH into the Ni−Ph bond

Starting from **9A**, HC≡CH is inserted into either the Ni−Ph or Ni−CN bond. First, we will examine the HC≡CH insertion into the Ni−Ph bond, because this insertion is involved in the catalytic cycle, as will be described below. The HC≡CH insertion into the Ni−Ph bond occurs through transition state $\mathbf{TS_{9A\text{-}10A}}$ to form a *β*-phenyl-substituted vinyl complex *cis*-Ni(CH=CH(Ph))(CN)(PMe_3) **10A**, as shown in the top of Figure 3, in which *cis* means that the *β*-phenyl-substituted vinyl moiety is at the position *cis* to CN. In $\mathbf{TS_{9A\text{-}10A}}$, Ph is moderately changing its direction toward the C atom of HC≡CH and simultaneously the HC≡CH moderately shifts toward the Ph. These moderate geometry changes indicate that this is reactant-like transition state. Because **10A** involves the agostic interaction between the Ni center and the C−H bond of Ph, this intermediate does not take complete three-coordinate structure. When PMe_3 migrates to the position *trans* to CN, the agostic interaction is broken and a complete three-coordinated species *cis*-Ni(CH=CH(Ph))(CN)(PMe_3) **10B** is formed; see Figure 3 for the geometry. Two carbon atoms of vinyl group are located on the P−Ni−CN plane in **10A**, while in **10B** the vinyl group is perpendicular to the P−Ni−CN plane. This is because the steric repulsion between CH=CH(Ph) and the other moiety is larger in **10B** than in **10A**. The insertion reaction starting from **9B** does not contribute to whole catalytic cycle because **9A** is produced much more than **9A**, as will describe in Sec. 3.3. See Appendix Figure A5 and Section A1 for geometry and energy change changes for the insertion reaction starting from **9B**.

Energy changes of these processes are shown in Figure 3. In the insertion of HC≡CH into the Ni−Ph bond, the activation barrier (2.2/2.7 kcal/mol) is very small and the exothermicity (−27.5/−26.8 kcal/mol) is very large, which are consistent with the reactant-like transition state mentioned above. Thus, it is concluded that the insertion reaction rapidly occurs and the reverse reaction is very difficult. The isomerization of **10A** to **10B** requires somewhat large activation barrier of 10.7/10.5 kcal/mol and **10B** is slightly less stable than **10A** due to the lack of the agostic interaction.

D. Reductive Elimination of PhCH=CH(CN) from Ni(CN)(CH=CH(Ph))(PMe_3)$_n$ (n=1 or 2)

The final step of catalytic cycle is the reductive elimination of PhCH=CH(CN) from Ni(CN)(CH=CHPh)(PMe_3)$_n$ (n = 1 or 2), as shown in Figures 4(A) and 4(B). Since **10A** and **10B** possess a vacant site at the position *trans* to the vinyl, another ligand can coordinate to the Ni center. In the reaction solution, three species such as PMe_3, PhCN, and HC≡CH exist as candidate for such ligand. We examined the coordination of all these species to **10A** and **10B**. The coordination of HC≡CH yields smaller stabilization energy than those of PMe_3 and PhCN, as shown in Appendix Figure A7. Because the reaction course and energy changes are almost the same in both of PMe_3 and PhCN coordinations, we will discuss here the coordination of PMe_3; see Appendix Figure A8 for the geometry and energy changes in the case of PhCN coordination.

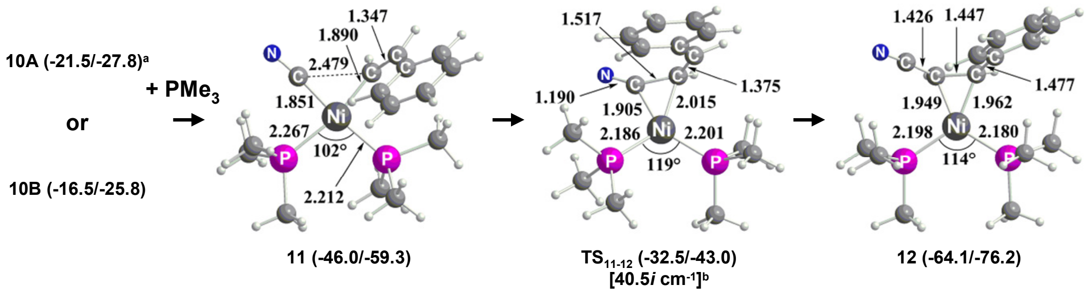

(A) Bisphosphine intetermediate

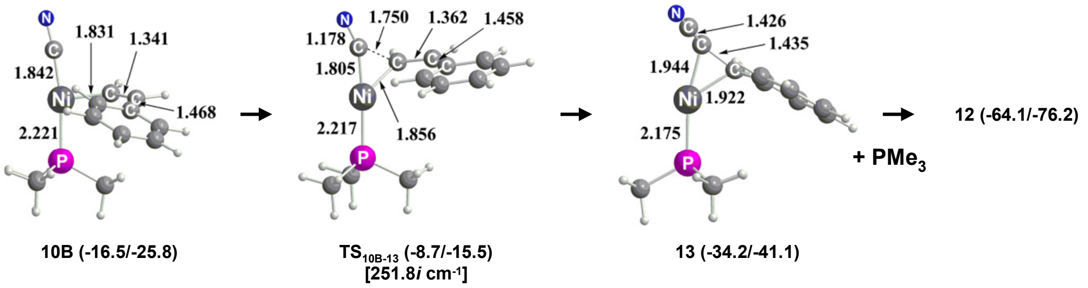

(B) Monophosphne intermediate

Figure 4. Geometry and energy changes (kcal/mol) in the reductive elimination of PhCN=CH(CN) from (A) bisphosphine intermediate Ni(CN)(CH=CH(Ph))(PMe$_3$)$_2$ **11** and (B) monophosphine intermediate Ni(CN)(CH=CH(Ph))(PMe$_3$) **10B**. Bond lengths are in angstrom and bond angles are in degree. a) In parenthesis, E^{ev_0} and F^{ev} (kcal/mol) values relative to **1** are shown before and after the slash, respectively. b) In square brackets is the eigenvalue of imaginary frequency in transition state.

PMe$_3$ coordinates with the Ni center of **10A** and **10B**, to form the same intermediate *cis*-Ni(CH=CH(Ph))(CN)(PMe$_3$)$_2$ **11** with considerably large stabilization energies of 24.5/31.5 and 29.5/33.5 kcal/mol, respectively, as shown in Figure 4(A). Starting from **11**, the reductive elimination of PhCH=CH(CN) occurs with activation barrier of 13.5/16.3 kcal/mol, to yield Ni(PMe$_3$)$_2$(η^2-Ph$\underline{\mathrm{CH{=}CH}}$(CN)) **12** through transition state **TS$_{11-12}$**. In **12**, PhCH=CH(CN) coordinates to the Ni center through the C=C bond. The activation barrier of the reductive elimination of the CN and vinyl groups is considerably lower than that (E_a = 21.2 kcal/mol in vacuo) of the CN and methyl groups.[10]

Starting from the monophosphine intermediate **10B**, the reductive elimination of PhCH=CH(CN) occurs without coordination of another species, to yield Ni(PMe_3)(PhCH=CH(CN)) **13** through transition state $\mathbf{TS_{10B\text{-}13}}$, as shown in Figure 4(B). When the concentration of coordinating species is low, three-coordinate intermediate such as **10B** can exist and the reductive elimination occurs from such species, as Driver and Hartwig reported.[33] Because **10A** is more stable than **10B** and the transition state $\mathbf{TS_{10B\text{-}13}}$ is more unstable than $\mathbf{TS_{10A\text{-}10B}}$ of the **10A → 10B** isomerization, the energy difference between $\mathbf{TS_{10B\text{-}13}}$ and **10A** is the activation barrier to complete the reductive elimination starting from **10A**. This value is calculated to be 12.8/12.3 kcal/mol, which is moderately lower than that of the reductive elimination starting from the bisphosphine intermediate **11**. The reductive elimination reaction of the monophosphine intermediate **10B** is as exothermic (−17.7/−15.3 kcal/mol) as that of the bisphosphine intermediate **11**. These results indicate the reductive elimination occurs starting from both **10B** and **11**.

E. Summary of the Catalytic Cycle

At the end of this section we summarize the catalytic cycle: (1) The first step is substitution of cod for PhCN. (2) The next is the isomerization of Ni(PMe_3)$_2$(PhCN) followed by the oxidative addition of the Ph−CN to the Ni center. (3) Alkyne coordinates with the Ni center through the associative substitution mechanism in which the axial PMe_3 dissociates from the Ni center to yield Ni(CN)(Ph)(PMe_3)(alkyne). (4) Alkyne is easier inserted into the Ni−Ph bond than into the Ni−CN bond. And, (5) the final step is the reductive elimination of the CN and CH=CH(Ph) groups from either mono or bisphosphine intermediate.

The energy change of the most favorable reaction course is shown in Figure 5. The rate determining step is the oxidative addition reaction via $\mathbf{TS_{6\text{-}7}}$. Its activation

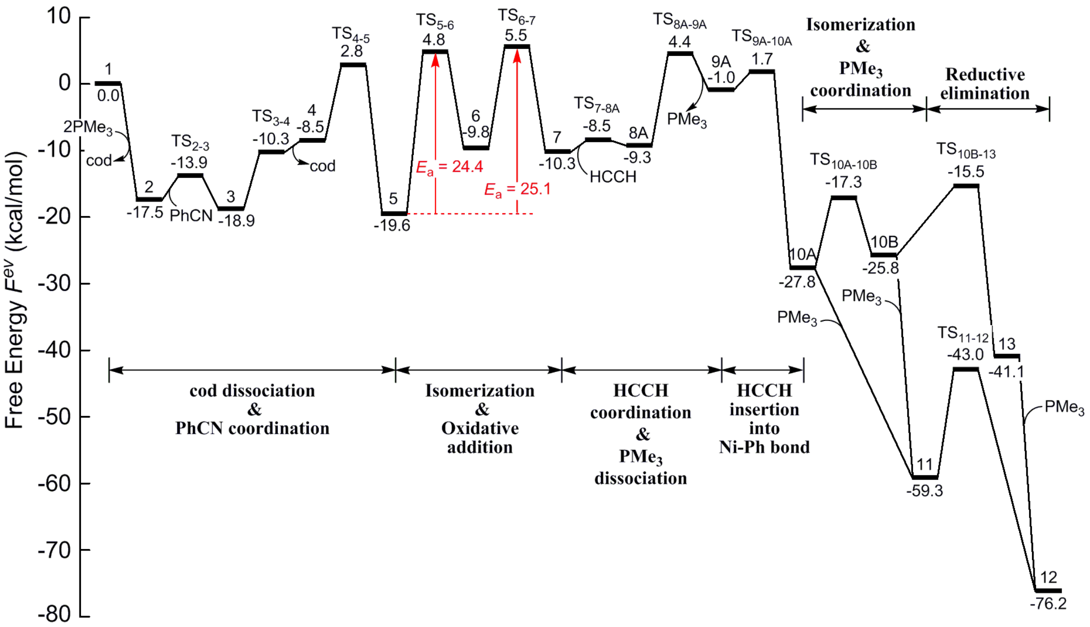

Figure 5. F^{ev} changes (kcal/mol) in the phenylcyanation of HC≡CH by Ni(PMe$_3$)$_2$.

free energy F^{ev} is calculated to be 25.1 kcal/mol, which is the energy difference between **TS$_{6-7}$** and the most stable intermediate **5** before the oxidative addition. The rate constant k evaluated with the Eyring equation (eq.5) is 1.6×10^{-2} s^{-1} = 5.8×10^{1} hour^{-1} at 373.15 K, where F^{ev} is employed as the Gibbs activation free energy change ($\Delta G^{o\ddagger}$).

$$k = \left(\frac{k_B T}{h}\right) \exp\left(-\frac{\Delta G^{\circ\ddagger}}{RT}\right) \tag{5}$$

The turnover frequency is evaluated to be 58 hour^{-1} with this k value. Considering that the k value is very sensitive to $\Delta G^{o\ddagger}$, the turnover frequency evaluated here is considered not to be different very much from the experimental results; in typical reactions, the experimental turnover frequency per catalyst and per hour is about 0.1-0.4 hour^{-1} at 100 °C, where the results of Table 2 in Ref. 14 were employed. This difference of turnover frequency between the experimental and calculated values corresponds to the small difference in $\Delta G^{o\ddagger}$ by 3 kcal/mol, which is not significantly

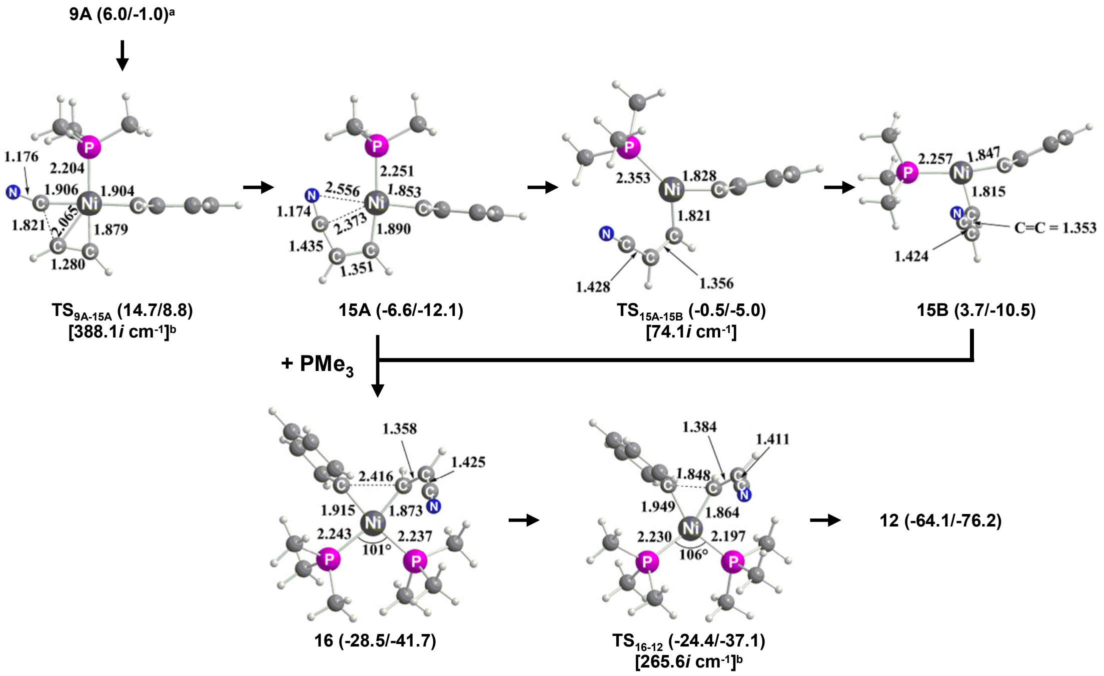

Figure 6. Geometry and energy changes (kcal/mol) in HC≡CH insertion into the Ni−CN bond and the reductive elimination of PhCN=CH(CN) from Ni(Ph)(CH=CH(CN))(PMe$_3$)$_2$ **19**. Bond lengths are in angstrom and bond angles are in degree. a) In parenthesis, E^{ev_0} and F^{ev} (kcal/mol) values relative to **7** are shown before and after the slash, respectively. b) In square brackets is the eigenvalue of imaginary frequency in transition state.

large.

5.3.2. HC≡CH Insertion into the Ni−CN Bond and the Reductive Elimination of PhCH=CH(CN) from Ni(Ph)(CH=CH(CN))(PMe$_3$)$_n$ (n = 1 or 2) (Path II)

Here, we will discuss the other reaction course (Path II) starting from **9A**, which proceeds via the HC≡CH insertion into the Ni−CN bond followed by the reductive elimination of PhCN=CH(CN) from Ni(Ph)(CH=CH(CN))(PMe$_3$)$_n$ (n = 1 or 2). As shown in Figure 6, the HC≡CH is inserted into the Ni−CN bond to yield three-coordinate species Ni(Ph)(CH=CH(CN))(PMe_3) **15A**, in which the CN weakly interacts with the Ni center. PMe_3 of **15A** migrates to the position *trans* to Ph, to form **15B** which is the isomer of **15A**. The activation barrier of this insertion is calculated to be 8.7/9.8 kcal/mol, which is much higher than that (2.3/2.7 kcal/mol) of the insertion into the Ni−Ph bond. This insertion is considerably exothermic, indicating that the reverse reaction does not occur. Therefore, the concentration ratio of **10A** to **15A** is kinetically determined by the reaction rate of the insertion. This ratio is approximately represented by eq. 6.

$$\frac{[\mathbf{10A}]}{[\mathbf{15A}]} = \frac{k_{\mathbf{9A}\to\mathbf{10A}}}{k_{\mathbf{9A}\to\mathbf{15A}}} \cong \exp\left[-\frac{\Delta G^{\circ\ddagger}(\mathbf{9A}\to\mathbf{10A}) - \Delta G^{\circ\ddagger}(\mathbf{9A}\to\mathbf{15A})}{RT}\right] \cong 1.4\times10^{4} \qquad (6)$$

where the pre-exponential factor is assumed to be the same in both reactions and F^{ev} is employed as the Gibbs activation free energy change. From this value, it should be concluded that the alkyne insertion into the Ni−CN bond little occurs. The reason is easily understood in terms of the much stronger Ni−CN bond than the Ni−Ph bond.[34]

Though the intermediates **15A** and **15B** are little formed, we will discuss briefly the reductive elimination of the β-cyano substituted vinyl and phenyl groups. PMe_3 coordinates with the Ni center in **15A** and **15B**, to afford four-coordinate intermediate Ni(Ph)(CH=CH(CN))$(PMe_3)_2$ **16**. Starting from **16**, the reductive elimination occurs through $\mathbf{TS_{16\text{-}12}}$ to form the product **12**, as shown in Figure 6, where **12** is shown in Figure 4. The activation barrier of this reductive elimination (4.1/4.6 kcal/mol) is much lower than that (13.5/16.3 kcal/mol) of the vinyl−CN reductive elimination (**11** → **12**). Because the stronger Ni−CN bond is broken in the vinyl−CN reductive elimination reaction but the weaker Ni−Ph bond is broken in the vinyl−Ph reductive elimination,[34] the former reductive elimination needs larger activation energy than the latter. Starting from the monophosphine intermediate **15B**, the reductive elimination occurs with smaller activation barrier (1.9/3.4 kcal/mol) than that starting from the

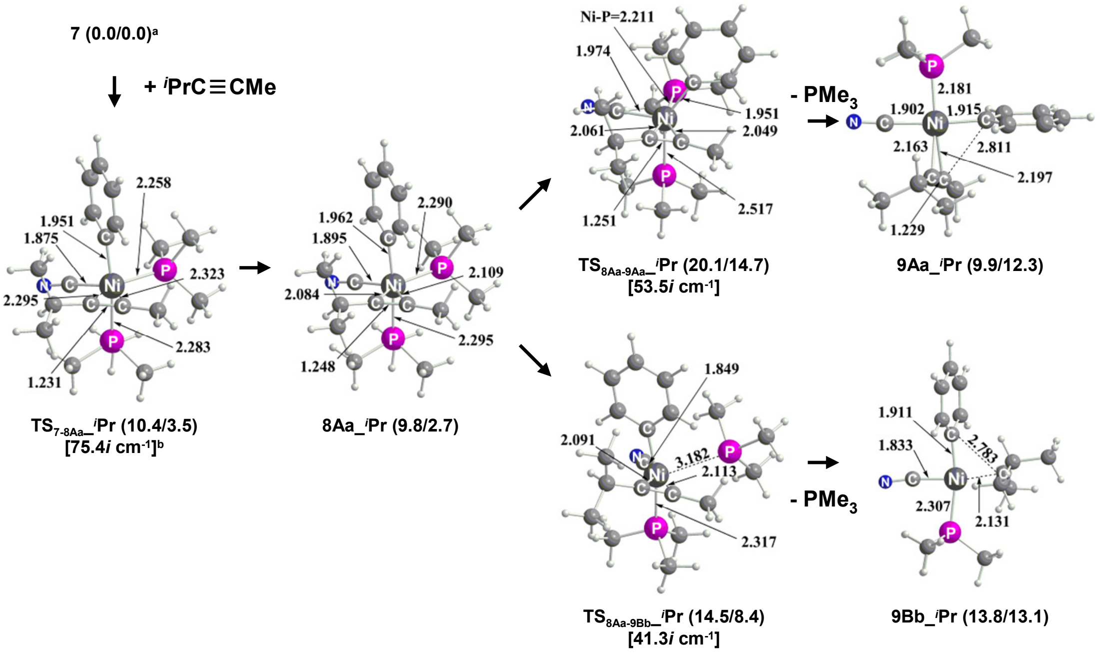

Figure 7. Geometry and energy changes (kcal/mol) in PMe_3 substitution with ^{i}PrC≡CMe through the associative mechanism. Bond lengths are in angstrom. a) In parenthesis, E^{ev_0} and F^{ev} (kcal/mol) values relative to **7** are shown before and after the slash, respectively. b) In square brackets is the eigenvalue of imaginary frequency in transition state.

bisphosphine intermediate **19**; see Appendix Figure A9 for the geometry change. The activation barrier of the vinyl−Ph reductive elimination is smaller than that of the vinyl−CN reductive elimination in the monophosphine intermediate, too.

5.3.3. Regioselectivity of the Product

Because the insertion reaction of alkyne is very exothermic and the reverse reaction is very difficult, as discussed in Sec. 3.1C, the regioselectivity of the product is determined in the alkyne coordination followed by the insertion reaction.

^{i}PrC≡CMe approaches the Ni center to form **8Aa_^{i}Pr** through **TS$_{7\text{-}8A}$_^{i}Pr**, as shown in Figure 7. We carried out the geometry optimization of substitution starting from the most stable five-coordinate geometry.[35] After the formation of **8Aa_^{i}Pr**, either axial PMe_3 or equatorial one dissociates from the Ni center, to form

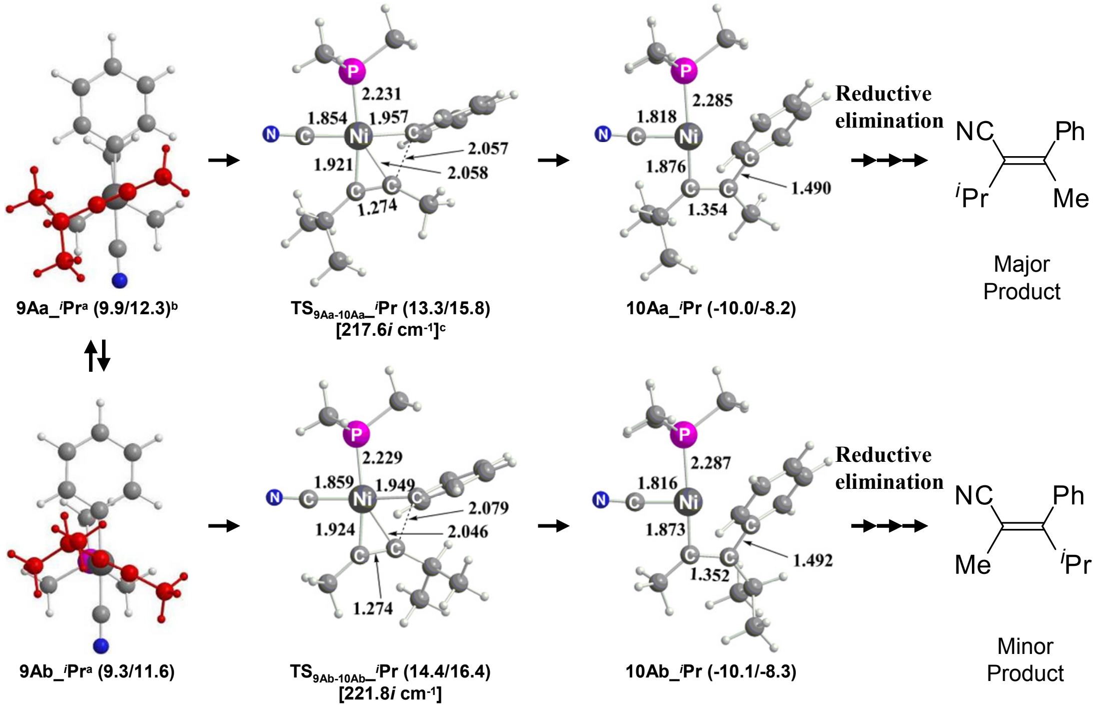

Figure 8. Geometry and energy changes (kcal/mol) in ^{i}PrC≡CMe insertion into the Ni−Ph bond after the axial PMe$_3$ dissociation. Bond lengths are in angstrom. a) Bottom view. b) In parenthesis, E^{ev_0} and F^{ev} (kcal/mol) values relative to **7** are shown before and after the slash, respectively. c) In square brackets is the eigenvalue of imaginary frequency in transition state.

Ni(CN)(Ph)(PMe$_3$)(^{i}PrC≡CMe) **9Aa_^{i}Pr** or **9Bb_^{i}Pr**, as was discussed for Ni(CN)(Ph)(PMe$_3$)$_2$(HC≡CH) in Sec. 3.1B. The dissociation of the axial PMe$_3$ occurs through transition state **TS$_{8Aa\text{-}9Aa}$_^{i}Pr** with activation barrier of 10.3/12.0 kcal/mol, as shown in Figure 7. In **9Aa_^{i}Pr**, the Me of ^{i}PrC≡CMe takes the position close to Ph; see Figure 8 for the bottom view. In **9Ab_^{i}Pr** which is isomer of **9Aa_^{i}Pr**, ^{i}Pr takes the position close to Ph. These two isomers are in almost the same energy and the interconversion between them easily occurs with nearly no barrier. The dissociation of the equatorial PMe$_3$ leads to formation of **9Bb_^{i}Pr** with activation barrier of 4.7/5.7 kcal/mol, as shown in Figure 7. **9Bb_^{i}Pr** is slightly more stable than **9Ba_^{i}Pr**, in which the orientation of alkyne is slightly different from that in **9Bb_^{i}Pr**, as shown in Figure 9. This is because the steric repulsion between PMe$_3$ and the ^{i}Pr of ^{i}PrC≡CMe

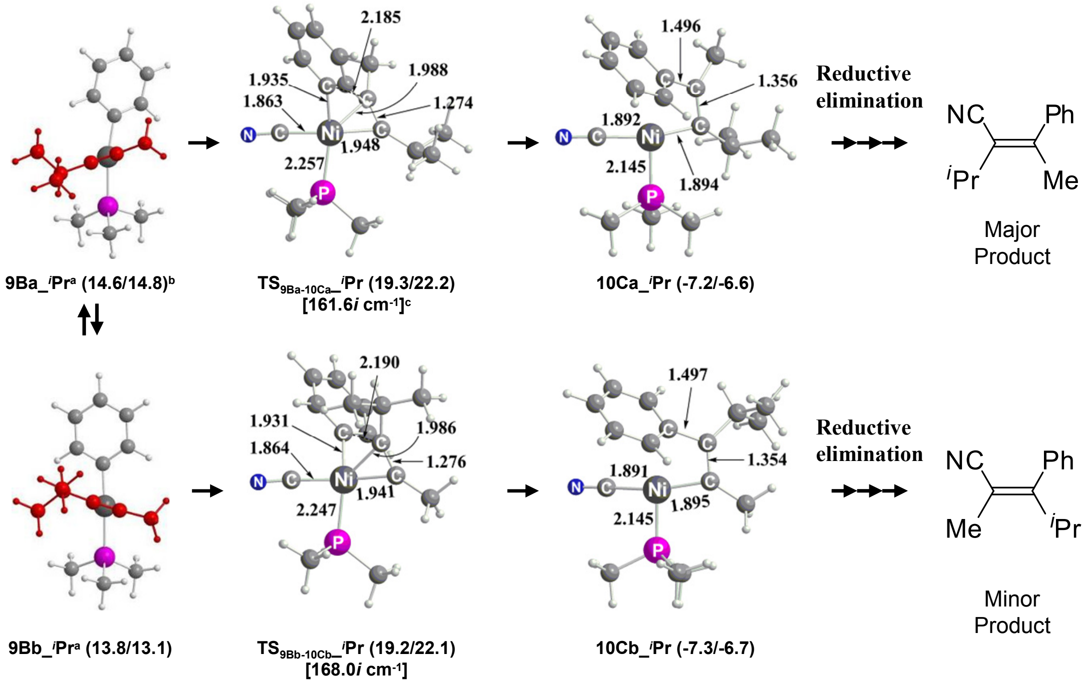

Figure 9. Geometry and energy changes (kcal/mol) in ^{i}PrC≡CMe insertion into the Ni−Ph bond after the equatorial PMe$_3$ dissociation. Bond lengths are in angstrom. a) Side view. b) In parenthesis, E^{ev_0} and F^{ev} (kcal/mol) values relative to **7** are shown before and after the slash, respectively. c) In square brackets is the eigenvalue of imaginary frequency in transition state.

is larger than that between PMe$_3$ and the Me of ^{i}PrC≡CMe.

The alkyne insertion occurs from all these intermediates, as shown in Figures 8 and 9. However, as concluded in Sec. 3.2, only the alkyne insertion into the Ni−Ph bond starting from **9Aa_^{i}Pr** and **9Ab_^{i}Pr** is involved in the catalytic cycle. Because the Me of ^{i}PrC≡CMe takes the position close to Ph in **9Aa_^{i}Pr**, the Ph approaches the carbon atom bearing Me, to form an intermediate Ni(CN)(C(^{i}Pr)=C(Me)(Ph))(PMe$_3$) **10Aa_^{i}Pr**, as shown in the top of Figure 8. The reductive elimination starting from **10Aa_^{i}Pr** leads to formation of the major product in which the CN is bound with the carbon atom bearing ^{i}Pr. In **9Ab_^{i}Pr**, on the other hand, the ^{i}Pr of ^{i}PrC≡CMe takes the position close to the Ph. Thus, the alkyne insertion into the Ni−Ph bond in **9Ab_^{i}Pr** leads to formation of **10Ab_^{i}Pr**. The reductive elimination starting from **10Ab_^{i}Pr** produces the minor product, as shown in the bottom of Figure 8. Unexpectedly, the activation barrier (5.1/4.8 kcal/mol) of the insertion reaction in **9Ab_^{i}Pr** is not different very much from that (3.4/3.4 kcal/mol) in **9Aa_^{i}Pr**. Similarly, alkyne insertion into the Ni−Ph bond of **9Ba_^{i}Pr** yields the major product but that into the Ni−Ph bond of **9Bb_^{i}Pr** yields the minor product, as shown in Figure 9.

Because the alkyne coordination is endothermic, as shown in Figure 10, the real activation barrier to complete the alkyne coordination followed by the insertion is the energy difference between **7** + ^{i}PrC≡CMe and the transition state which is at the highest energy. In both of the axial and equatorial PMe$_3$ dissociations from the Ni center, the transition state of the alkyne insertion is at the highest energy. The energy diagram clearly shows that the axial PMe$_3$ dissociation (solid line) is more favorable than the equatorial one. Thus, the reaction via **TS$_{\mathbf{8Aa\text{-}9Aa}}$_^{i}Pr** occurs easier than that via **TS$_{\mathbf{9Ba\text{-}10Ca}}$_^{i}Pr**. This trend is the same in ^{t}BuC≡CMe, as shown in Figure 11, in which the activation free energies are 24.5 and 18.5 kcal/mol for the equatorial and axial PMe$_3$ dissociations, respectively. Also, these energy diagrams clearly indicate that the activation barriers of the insertion producing the minor product (blue line) are somewhat larger than that of the insertion producing the major product (black line). This is understood in terms of the large steric repulsion between Ph and ^{t}Bu in the transition state; see Appendix Figure A11 to A13 for the geometry change in the reaction of ^{t}BuC≡CMe.

Because the reverse reactions from **10Aa_R** and **10Ab_R** (R = ^{i}Pr or ^{t}Bu) do not occur at all due to the very large exothermicity of the insertion reaction, the ratio of the major to minor products is determined by the population ratio of **10Aa_R** to **10Ab_R**, [**10Aa_R**]/[**10Ab_R**] (R = ^{i}Pr or ^{t}Bu). The ratio [**10Aa_R**]/[**10Ab_R**] is represented by the product of the concentration ratio [**9Aa_R**]/[**9Ab_R**] and the ratio of rate constant of the alkyne insertion starting from **9Aa_R** and **9Ab_R**, $k_{\mathbf{9Aa\rightarrow10Aa}}/k_{\mathbf{9Ab\rightarrow10Ab}}$.[36]

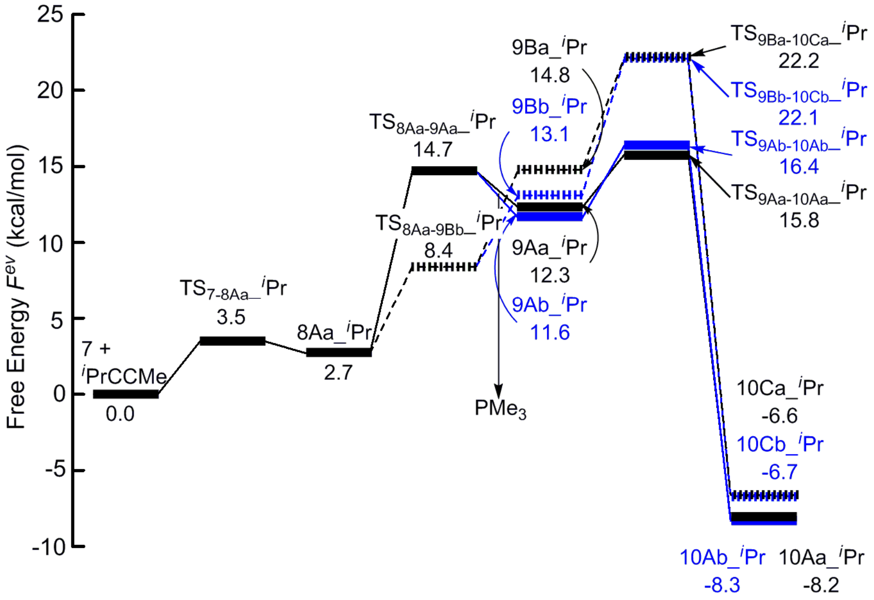

Figure 10. F^{ev} changes (kcal/mol) in the ^{i}PrC≡CMe coordination with $\mathrm{Ni(CN)(Ph)(PMe_3)_2}$ **7**, $\mathrm{PMe_3}$ dissociation, and ^{i}PrC≡CMe insertion into the Ni−Ph bond. Solid and dashed lines represent the axial and equatorial $\mathrm{PMe_3}$ dissociation, respectively. Black and blue lines represent the ^{i}PrC≡CMe insertions which lead to formation of major and minor products, respectively.

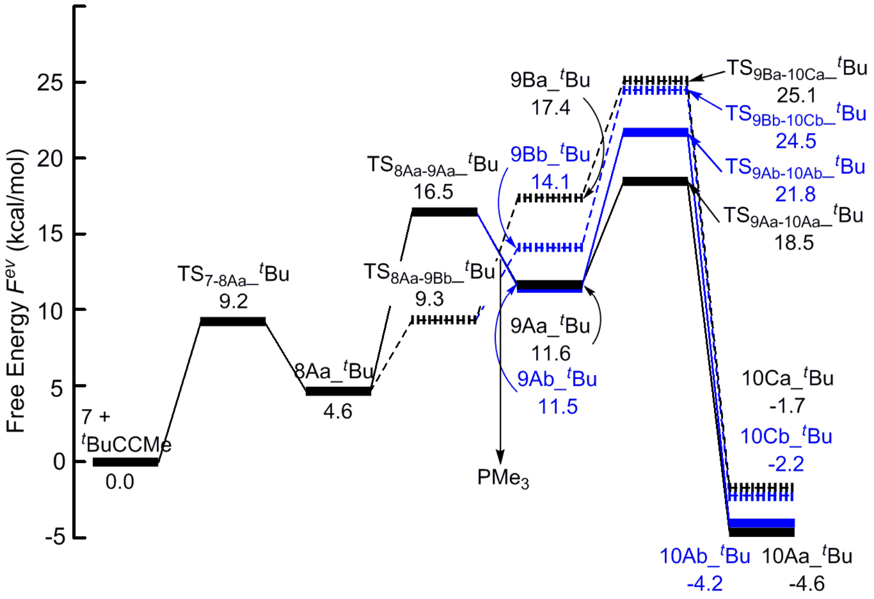

Figure 11. F^{ev} changes (kcal/mol) in the ^{t}BuC≡CMe coordination with $\mathrm{Ni(CN)(Ph)(PMe_3)_2}$ **7**, $\mathrm{PMe_3}$ dissociation, and ^{t}BuC≡CMe insertion into the Ni−Ph bond. Solid and dashed lines represent the axial and equatorial $\mathrm{PMe_3}$ dissociation, respectively. Black and blue lines represent the ^{t}BuC≡CMe insertions which lead to formation of major and minor products, respectively.

The ratio [**9Aa_R**]/[**9Ab_R**] is determined by the Boltzmann distribution law and the ratio $k_{\mathbf{9Aa}\rightarrow\mathbf{10Aa}}/k_{\mathbf{9Ab}\rightarrow\mathbf{10Ab}}$ is determined by the Eyring equation. Thus, the ratio [**10Aa_R**]/[**10Ab_R**] is represented, as follows,

$$
\begin{aligned}
\frac{\text{Major product}}{\text{Minor product}} &= \frac{[\mathbf{10Aa\_R}]}{[\mathbf{10Ab\_R}]} = \frac{[\mathbf{9Aa\_R}]}{[\mathbf{9Ab\_R}]} \times \frac{k_{\mathbf{9Aa}\rightarrow\mathbf{10Aa}}}{k_{\mathbf{9Ab}\rightarrow\mathbf{10Ab}}} \\
&\cong \exp\left[-\frac{G^{\circ}(\mathbf{9Aa}) - G^{\circ}(\mathbf{9Ab})}{\mathrm{RT}}\right] \times \exp\left[-\frac{\mathit{\Delta} G^{\circ\ddagger}(\mathbf{9Aa} \rightarrow \mathbf{10Aa}) - \mathit{\Delta} G^{\circ\ddagger}(\mathbf{9Ab} \rightarrow \mathbf{10Ab})}{\mathrm{RT}}\right]
\end{aligned}
\tag{7}
$$

where the pre-exponential factor is assumed to be the same in $k_{\mathbf{9Aa}\rightarrow\mathbf{10Aa}}$ and $k_{\mathbf{9Ab}\rightarrow\mathbf{10Ab}}$. The ratio of major to minor products is calculated to be 2.2 and 86 for ^{i}PrC≡CMe and ^{t}BuC≡CMe, respectively, at 373.15 K, where ΔF^{ev} is employed as the Gibbs free energy change. These values are similar to the experimental results that the selectivity is 1.63 and >99 for ^{i}PrC≡CMe and ^{t}BuC≡CMe, respectively.[14]

5.4. Conclusions

$\mathrm{Ni(PMe_3)_2}$-catalyzed phenylcyanation reaction of alkyne was theoretically investigated mainly with the DFT(B3PW91) method and in part with the CCSD(T) method to elucidate the reaction mechanism including the formation process of the active species, the rate-determining step, the regioselectivity of products, and the determining factors of the reaction mechanism and the regioselectivity. The reaction occurs through the following elementary steps; (1) cod of $\mathrm{Ni(cod)_2}$ is first substituted for PhCN and $\mathrm{PMe_3}$ to form $\mathrm{Ni(PhCN)(PMe_3)_2}$. (2) The isomerization of $\mathrm{Ni(PhCN)(PMe_3)_2}$ occurs followed by the oxidative addition of Ph−CN to the Ni center. Then, (3) the coordination of alkyne occurs through the associative mechanism and the axial $\mathrm{PMe_3}$ dissociates to yield $\mathrm{Ni(CN)(Ph)(PMe_3)(alkyne)}$. (4) Alkyne is inserted into the Ni−Ph bond rather than the Ni−CN bond. And, (5) the reductive elimination of the CN and CH=CH(Ph) groups occurs from either the mono or bisphosphine intermediate. The rate determining step is the oxidative addition of Ph−CN to $\mathrm{Ni(PMe_3)_2}$. Another possible reaction mechanism investigated here is the alkyne insertion into the Ni−CN bond followed by the reductive elimination of the Ph and vinyl groups. Though the reductive elimination of the Ph and vinyl groups occurs easier than that of the CN and vinyl groups, alkyne insertion into the Ni−CN bond occurs with much more difficulty than that into the Ni−Ph bond. As a result, this mechanism is less favorable than the former one. The regioselectivity of this reaction is determined by the steric repulsion between the Ph and the bulky substituent of alkyne in the step of the alkyne insertion into the Ni−Ph bond. The ratio of the major product to the minor one is theoretically evaluated well.

5.5. Appendix

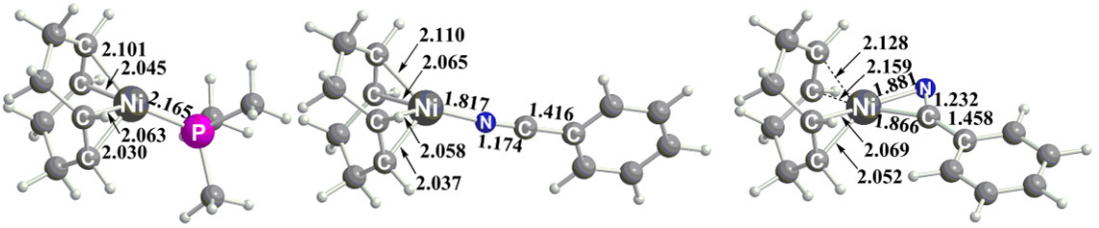

$\mathrm{Ni(cod)(PMe_3)}$ $\mathrm{Ni(cod)(\eta^1\text{-}\underline{N}CPh)}$ $\mathrm{Ni(cod)(\eta^2\text{-}\underline{NC}Ph)}$

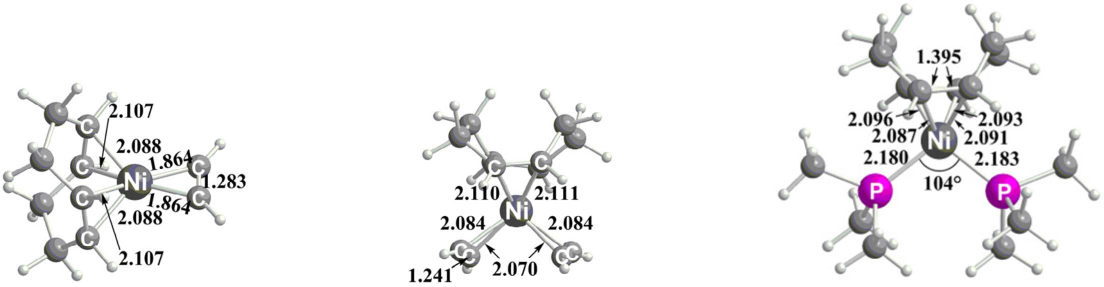

$\mathrm{Ni(cod)(HC{\equiv}CH)}$ $\mathrm{Ni(cod)(HC{\equiv}CH)_2}$ $\mathrm{Ni(cod)(PMe_3)_2}$

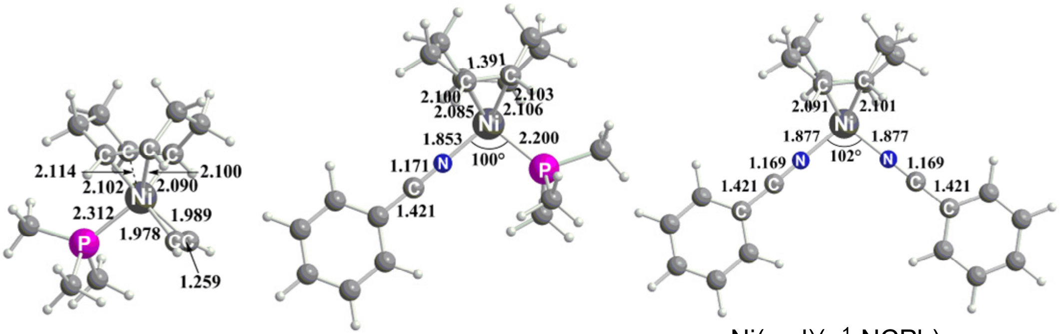

$\mathrm{Ni(cod)(PMe_3)(HC{\equiv}CH)}$ $\mathrm{Ni(cod)(PMe_3)(\eta^1\text{-}\underline{N}CPh)}$ $\mathrm{Ni(cod)(\eta^1\text{-}NCPh)_2}$

Figure A1. Geometries of Ni(cod)(X)(Y) (X, Y = $\mathrm{PMe_3}$, PhCN, HCCH). Bond lengths are in angstrom and bond angles are in degree.

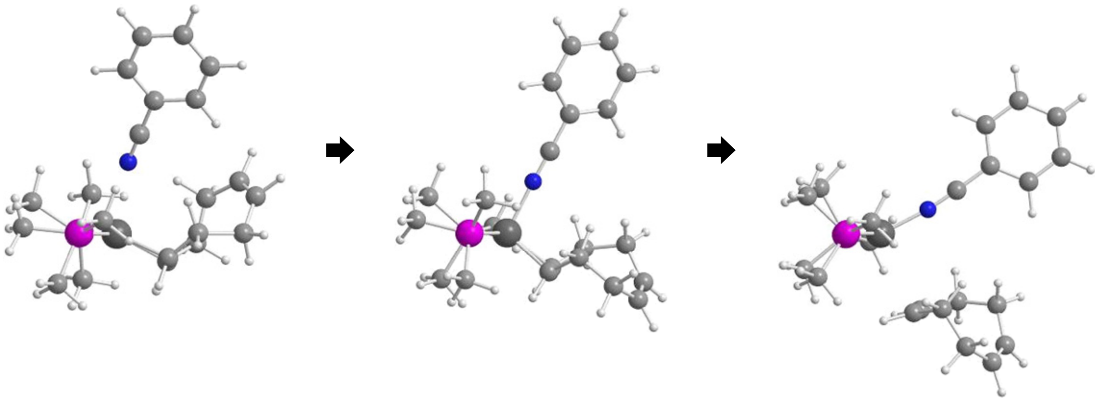

TS$_{2\text{-}3}$
0.4/-13.9[a]
(82.2*i* cm^{-1})[b]

3
-5.9/-18.9

TS$_{3\text{-}4}$
1.3/-10.3
(43.6*i* cm^{-1})

Figure A2. Sideview of geometry change in cod dissociation. a) E^{ev_0} and F^{ev} (kcal/mol) are shown before and after the slash, respectively. b) In parenthesis is the eigenvalue of imaginary frequency in transition state.

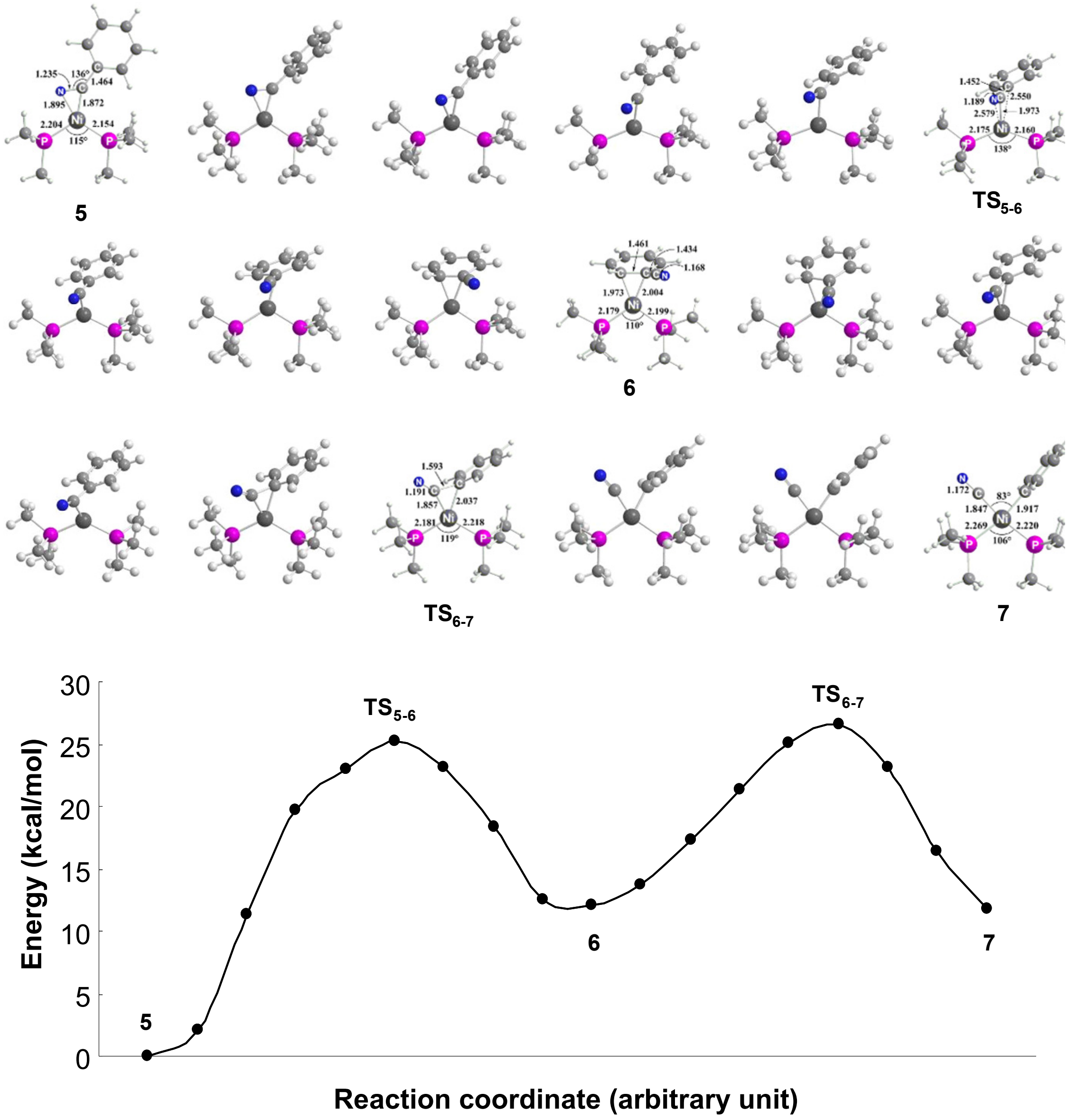

Figure A3. Geometries and energy changes (BS-1) from **5** to **7** calculated by means of steepest descent method.

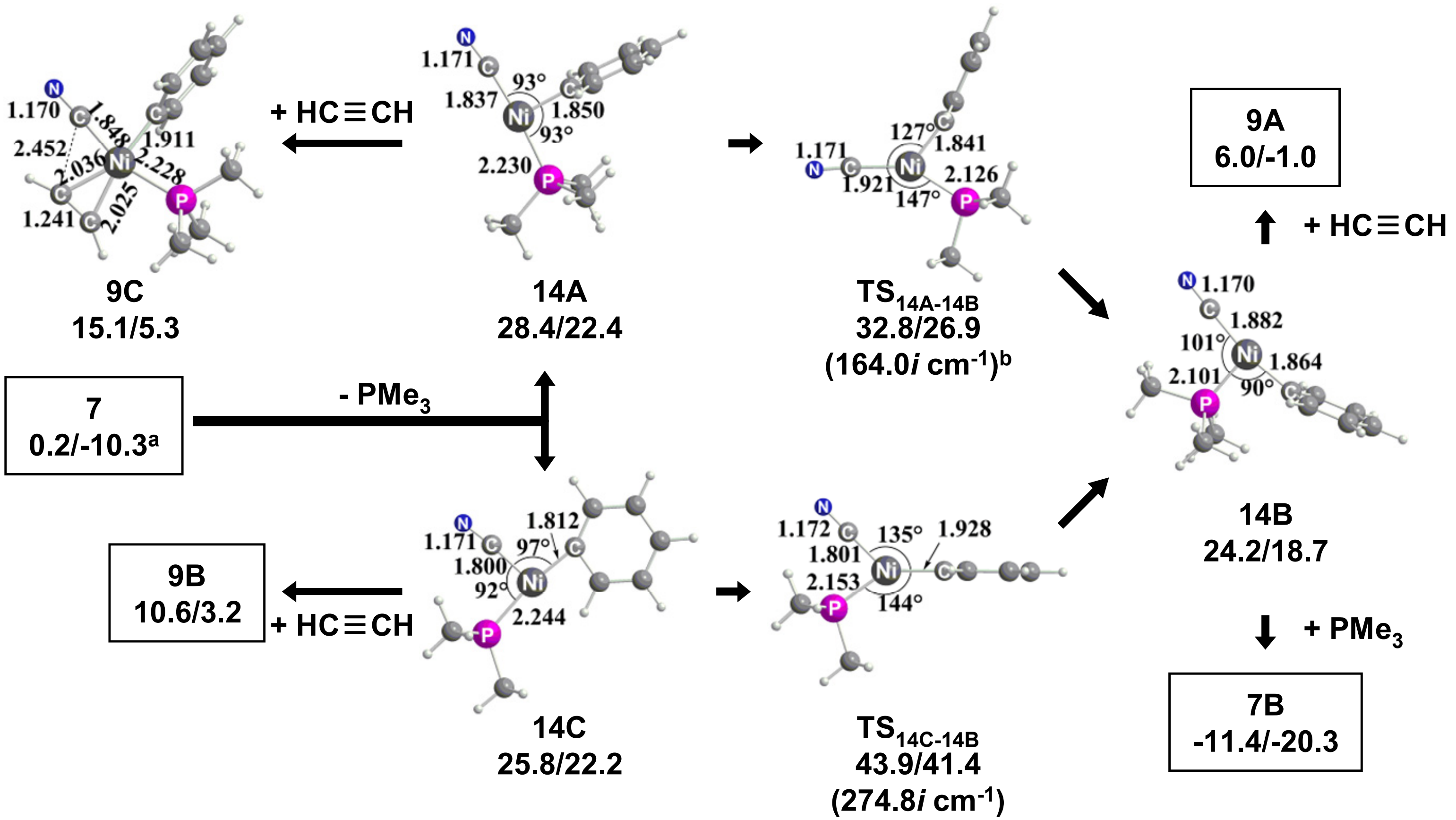

Figure A4. Geometry and energy changes (kcal/mol) in substitution of PMe_3 for HC≡CH through dissociative mechanism. Bond lengths are in angstrom and bond angles are in degree. a) E^{ev_0} and F^{ev} (kcal/mol) are shown before and after the slash, respectively. b) In parenthesis is the eigenvalue of imaginary frequency in transition state.

A1. HC≡CH insertion into the Ni-Ph bond from 9B

Because **9B** is less stable than **9A**, as discussed in the section 3.2 B, the insertion reaction starting from **9B** is less important than that starting from **9A**. However, we discuss the insertion reaction starting from **9B** as a side reaction. Because HC≡CH is located at the position *trans* to CN, the HC≡CH can be inserted only into the Ni−Ph bond through $\mathbf{TS_{9B\text{-}10C}}$, to afford *trans*-Ni(CN)(CH=CH(Ph))(PMe$_3$) **10C** with nearly no barrier and considerably large exothermicity, as shown in the bottom of Figure A5. Because the *β*-phenyl substituted vinyl moiety is located at the position *trans* to CN in **10C**, the isomerization reaction must occur to induce the reductive elimination reaction. When the vinyl moiety migrates to the position *cis* to CN, **10A** is formed from **10C** through transition state $\mathbf{TS_{10C\text{-}10A}}$ with the considerably large activation barrier (23.1/24.5 kcal/mol). This means the isomerization of **10A** to **10C** through $\mathbf{TS_{10C\text{-}10A}}$ is very difficult. As shown in Figure A5, when the CN migrates to the position *cis* to the vinyl moiety, **10B** is formed from **10C** through transition state $\mathbf{TS_{10C\text{-}10B}}$ with activation barrier of 13.0/10.6 kcal/mol. This activation barrier is similar to that of the isomerization of **10A** to **10B**. However, it should be noted that **9B** is less stable than **9A** and **10C** is not easily formed from **10A**. These results indicate that the isomerization of **9B** to **10C** and that of **10C** to **10B** are not important in whole catalytic cycle. Though **10C** can be formed from **10A**, the barrier is much higher than that of the isomerization of **10A** to **10B**. Thus, **10C** is not important in the whole catalytic cycle. These results indicate that the isomerization of **10C** to **10B** occurs with more difficulty than that of **10A** to **10B**.

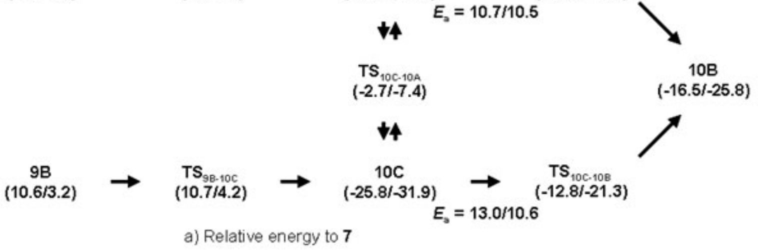

a) Relative energy to **7**

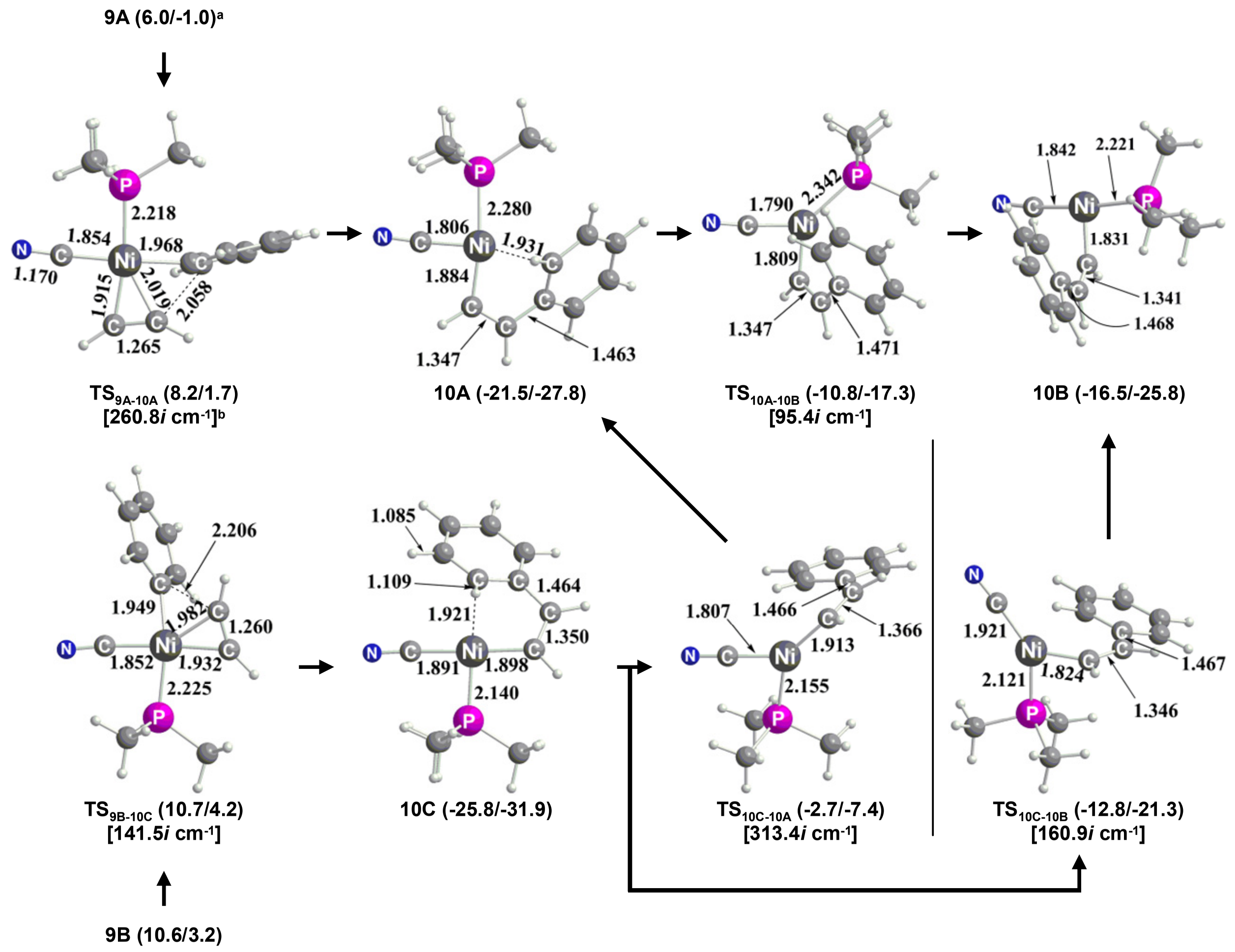

Figure A5. Geometry and energy changes (kcal/mol) in HC≡CH insertion into the Ni−Ph bond from **9A** and **9B**. Bond lengths are in angstrom. a) In parenthesis, E^{ev_0} and F^{ev} (kcal/mol) values relative to **1** are shown before and after the slash, respectively. b) In square brackets is the eigenvalue of imaginary frequency in transition state.

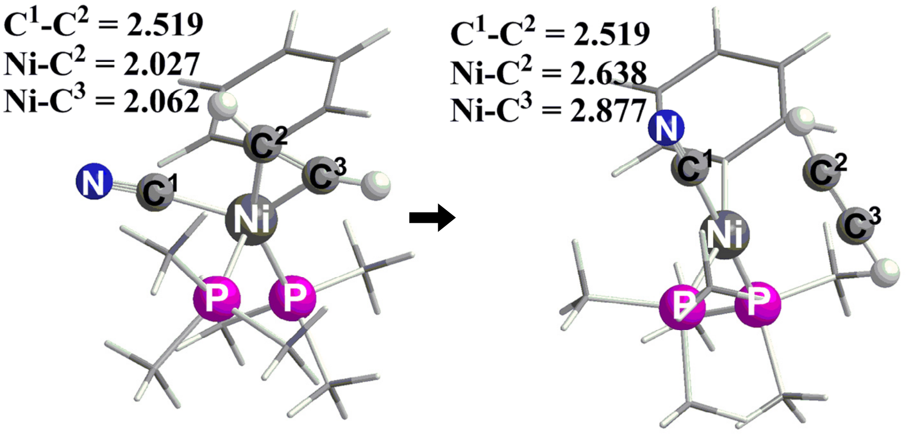

Initial geometry After 20 opt cycle

(A) R(C^1–C^2) = 2.519 Å

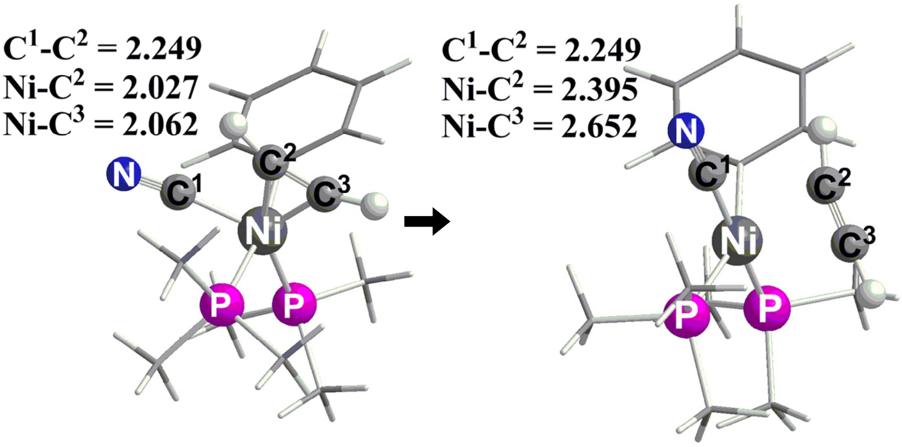

Initial geometry After 20 opt cycle

(B) R(C^1–C^2) = 2.249 Å

Figure A6. Initial geometry for the optimization of alkyne insertion into the Ni–CN bond in **8A** and the geometry after 20 optimization cycle, where the C of CN and C of alkyne distance is fixed to (A) 2.519 Å and (B) 2.249 Å.

Both in the case, the alkyne was not inserted into the Ni–CN bond but it dissociated from the Ni center. This indicates that it is impossible that the alkyne insertion into the Ni–CN bond in the five-coordinate complex.

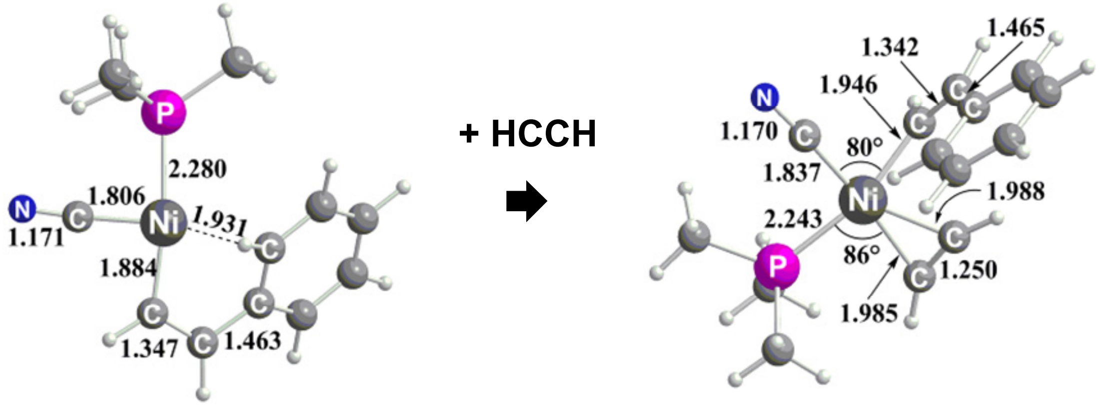

10A
-21.5/-27.8[a]

Ni(CN)(CH=CH(Ph))(HCCH)
-32.8/-45.8

Figure A7. Geometry and energy change in the coordination of HCCH with cis-Ni(CN)(CH=CH(Ph))(PMe$_3$) **10A**. a) E^{ev_0} and F^{ev} (kcal/mol) are shown before and after the slash, respectively.

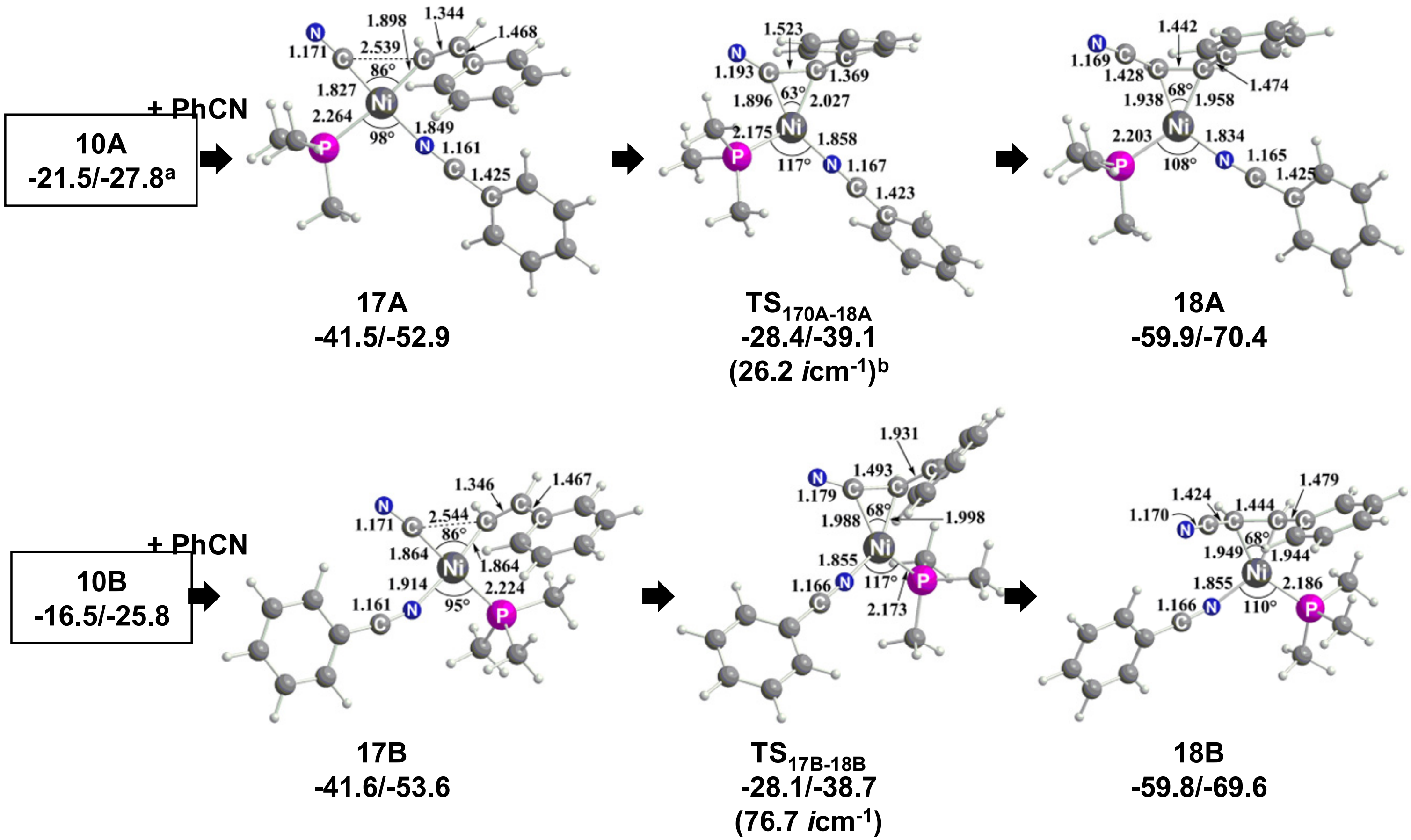

Figure A8. Geometry and energy change in the coordination of PhCN with *cis*-Ni(CN)(CH=CH(Ph))(PMe$_3$) **10A** and reductive elimination of PhCH=CH(CN). a) E^{ev_0} and F^{ev} (kcal/mol) are shown before and after the slash, respectively. b) In parenthesis is the eigenvalue of imaginary frequency in transition state.

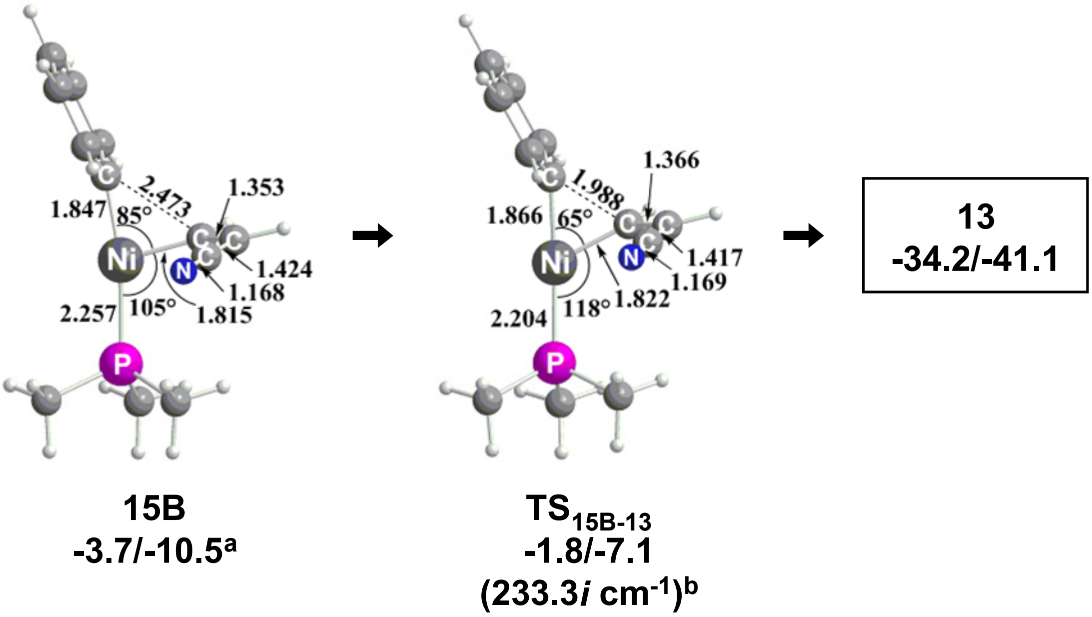

Figure A9. Geometry and energy changes (kcal/mol) in the reductive elimination of PhCN=CH(CN) from Ni(Ph)(CH=CH(CN))(PMe_3) **15B**. Bond lengths are in angstrom and bond angles are in degree. a) E^{ev_0} and F^{ev} (kcal/mol) are shown before and after the slash, respectively. b) In parenthesis is the eigenvalue of imaginary frequency in transition state.

A2. *cis-trans* Isomerization of Ni(CN)(Ph)(PMe$_3$)$_2$

Several experimental results show the *cis-trans* isomerization of d^8 four-coordinate transition metal complex occurs after the oxidative addition. We examined whether **7** isomerizes *trans*-Ni(CN)(Ph)(PMe$_3$)$_2$ **7B** occurs or not, because the reaction mechanism would become different if this isomerization easily occurs. In the isomerization mechanism, there are two possible mechanisms: one is associative and the other is dissociative.

In the associative mechanism, PMe$_3$, PhCN, and alkyne are candidates for additional coordinating species. When additional PMe$_3$ coordinates to the Ni center in **7**, a five-coordinate intermediate Ni(CN)(Ph)(PMe$_3$)$_3$ **19A** is formed through transition state **TS$_{7\text{-}19A}$** with very small activation barrier, as shown in Figure A10. From **19A**, the isomerization occurs through Berry pseudo-rotation-like transition state **TS$_{19A\text{-}19B}$** with the activation barrier of 21.0/25.7 kcal/mol, to yield **19B** in which the CN and Ph take the axial positions. One of the equatorial PMe$_3$ dissociates from the Ni center in **19B**, through transition state **TS$_{19B\text{-}7B}$** with the small activation barrier (E_a = 0.8/3.7), to yield *trans*-Ni(CN)(Ph)(PMe$_3$)$_2$ **7B**. Complex **7B** is more stable than the *cis* form **7** by 11.6/10.0 kcal/mol. The energy change described above indicates that the associative substitution is possible if free PMe$_3$ exists in the reaction solution. However, almost all PMe$_3$ molecules coordinate with the Ni center under the usual experimental conditions, because two equivalents of PMe$_3$ to Ni(cod)$_2$ are usually added to the solution. Though we examined PhCN coordination instead of PMe$_3$ coordination, we could not obtain the stable intermediate. The other candidate for additional ligand is alkyne. We have discussed above this *cis-trans* isomerization concomitant with substitution of PMe$_3$ for alkyne (**7** to **9A**) in Sec. 3.1B.

In the dissociative mechanism, one of the PMe$_3$ ligands dissociates from the Ni center, to form a monophosphine intermediate Ni(CN)(Ph)(PMe$_3$) **14A** or **14C**, as mentioned in Sec. 3.1B and shown in Figure 2(A). From **14A** and **14C**, *cis*-*trans* isomerization reaction occurs through migrations of CN and Ph with activation barriers of 4.4/4.5 or 18.1/19.2 kcal/mol, respectively, to form **14B**. Although the activation barriers are not very large, the three-coordinate species **14A** and **14B** are much more unstable than **7**, as described in Sec. 3.1B.

Summarizing these results, it is concluded that the *cis*-*trans* isomerization reaction of **7** to **7B** is ruled out except for the *cis*-*trans* isomerization concomitant with substitution of PMe_3 for alkyne.

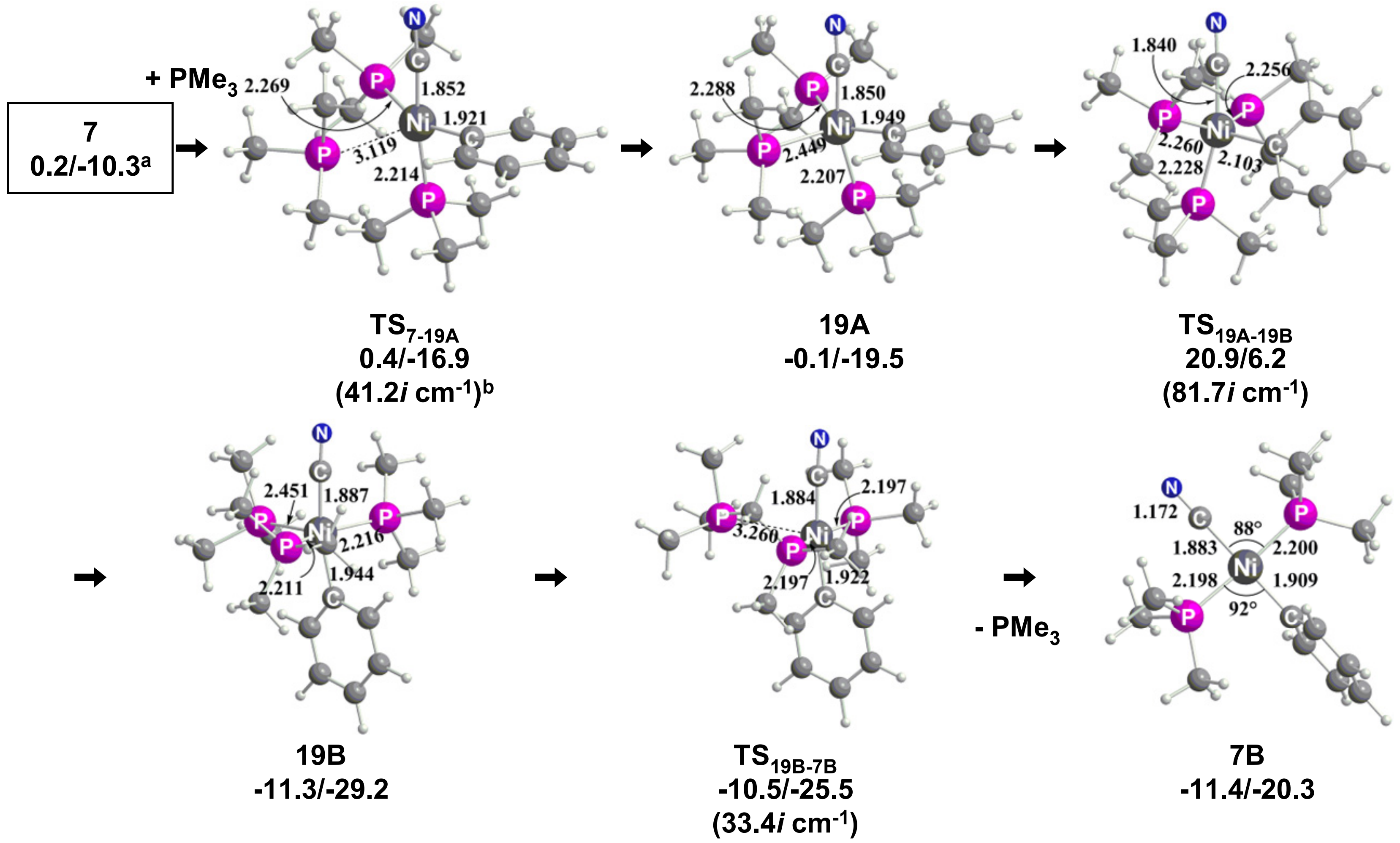

Figure A10. Geometry and energy changes (kcal/mol) in cis-trans isomerization of Ni(CN)(Ph)$(PMe_3)_2$ through the associative mechanism. Bond lengths are in angstrom and bond angles are in degree. a) E^{ev_0} and F^{ev} (kcal/mol) are shown before and after the slash, respectively. b) In parenthesis is the eigenvalue of imaginary frequency in transition state.

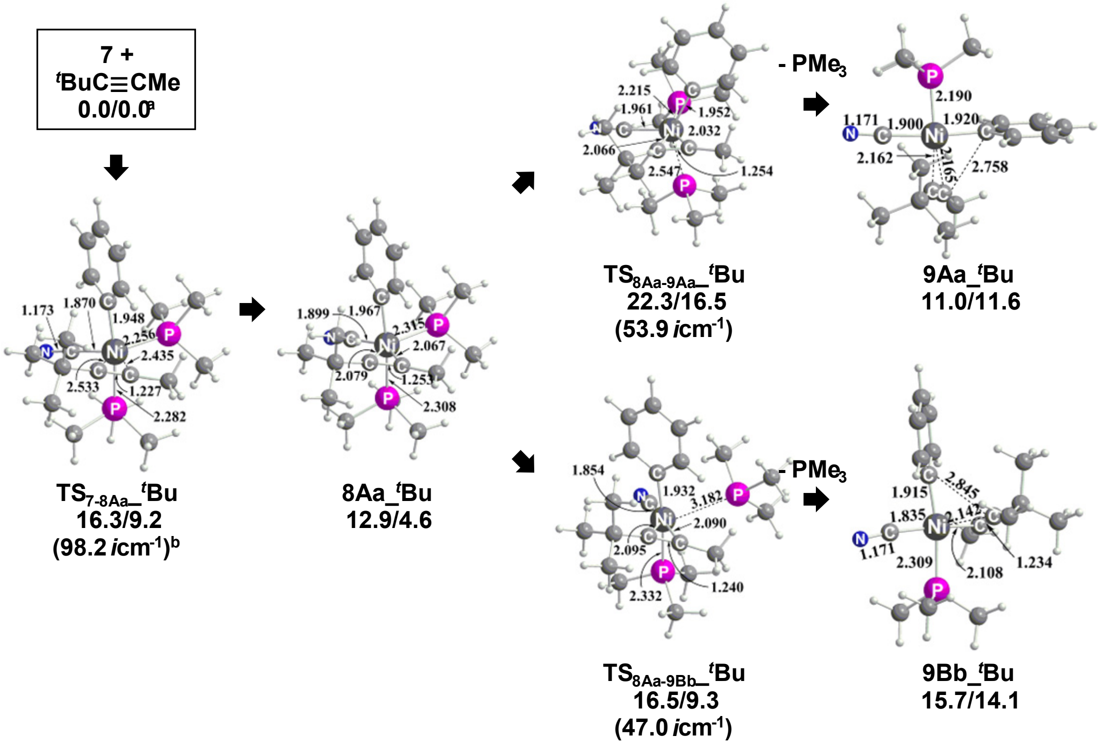

Figure A11. Geometry and energy changes (kcal/mol) in PMe$_3$ substitution with ^{t}BuC≡CMe through the associative mechanism. Bond lengths are in angstrom and bond angles are in degree. a) E^{ev_0} and F^{ev} (kcal/mol) are shown before and after the slash, respectively. b) In parenthesis is the eigenvalue of imaginary frequency in transition state.

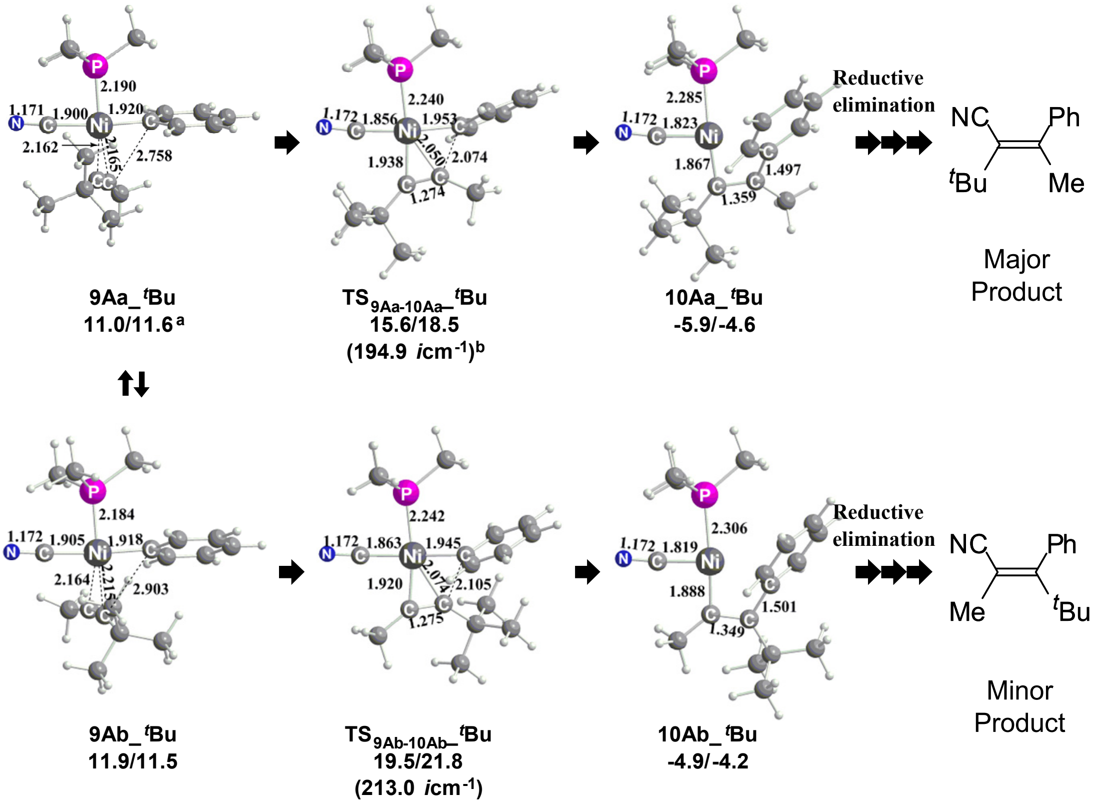

Figure A12. Geometry and energy changes (kcal/mol) in ^{t}BuC≡CMe insertion into the Ni−Ph bond after the axial PMe$_3$ dissociation. Bond lengths are in angstrom and bond angles are in degree. a) E^{ev_0} and F^{ev} (kcal/mol) are shown before and after the slash, respectively. b) In parenthesis is the eigenvalue of imaginary frequency in transition state.

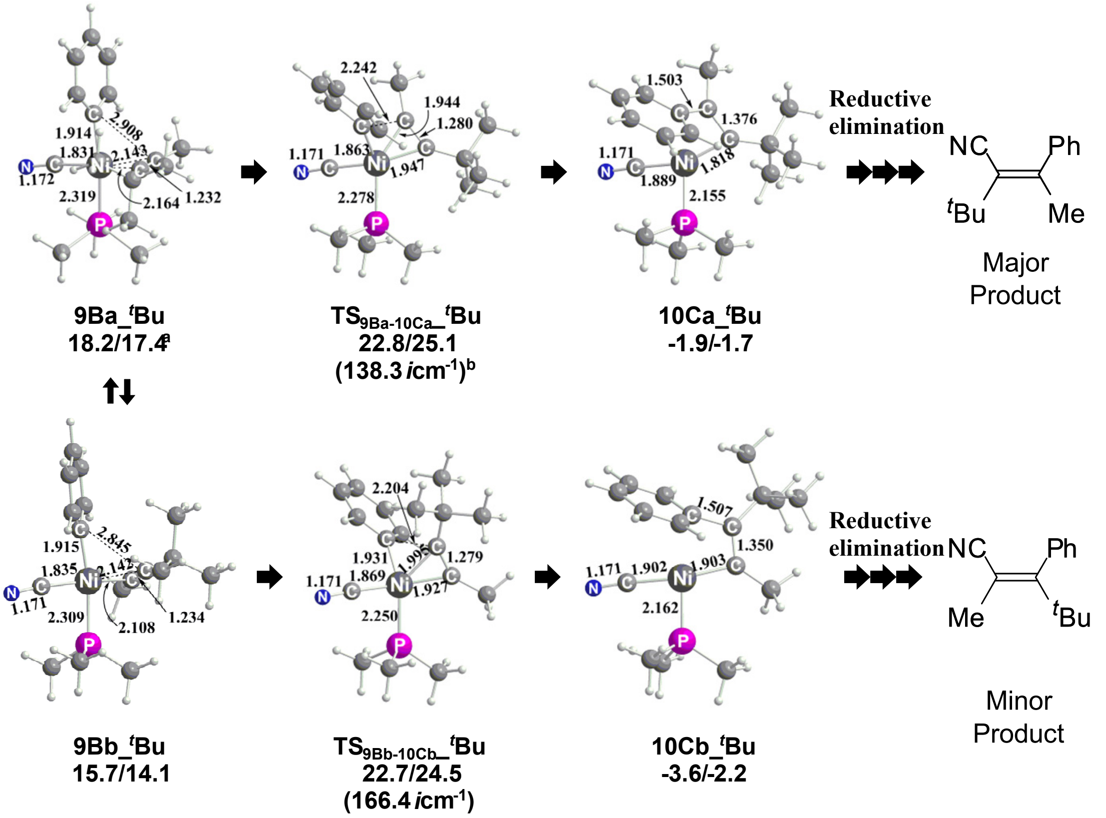

Figure A13. Geometry and energy changes (kcal/mol) in ^{t}BuC≡CMe insertion into the Ni−Ph bond after the equatorial PMe$_3$ dissociation. Bond lengths are in angstrom and bond angles are in degree. a) E^{ev_0} and F^{ev} (kcal/mol) are shown before and after the slash, respectively. b) In parenthesis is the eigenvalue of imaginary frequency in transition state.

A3. Ni−Ph and Ni−CN Bond Energies

The Ni−Ph and Ni−CN bond strengths in **9A** are evaluated, as follow: Since the metal−ligand bond is formed by the mixing of covalent and ionic interactions, we should consider both the covalent and ionic bond energies. The covalent bond energy (CBE) is evaluated on the basis of the equations below, where the energies are calculated in vacuo with ZPE correction.

$$\mathrm{Ni(CN)(Ph)(PMe_3)(HC{\equiv}CH)} \rightarrow \cdot\mathrm{Ni(Ph)(PMe_3)(HC{\equiv}CH)} + \cdot\mathrm{CN} \qquad [\mathrm{A1}]$$

CBE = 88.2 kcal/mol

$$\mathrm{Ni(CN)(Ph)(PMe_3)(HC{\equiv}CH)} \rightarrow \cdot\mathrm{Ni(CN)(PMe_3)(HC{\equiv}CH)} + \cdot\mathrm{Ph} \qquad [\mathrm{A2}]$$

CBE = 41.9 kcal/mol

On the other hand, the ionic bond energy (IBE) is evaluated on the basis of the equations below.

$$\mathrm{Ni(CN)(Ph)(PMe_3)(HC{\equiv}CH)} \rightarrow [\mathrm{Ni(Ph)(PMe_3)(HC{\equiv}CH)}]^{+} + \mathrm{CN}^{-} \qquad [\mathrm{A3}]$$

IBE = 148.6 kcal/mol

$$\mathrm{Ni(CN)(Ph)(PMe_3)(HC{\equiv}CH)} \rightarrow [\mathrm{Ni(CN)(PMe_3)(HC{\equiv}CH)}]^{+} + \mathrm{Ph}^{-} \qquad [\mathrm{A4}]$$

IBE = 189.3 kcal/mol

Because the natural charges of CN and Ph are −0.557e and −0.388e, respectively, in **9A**, we evaluated the Ni−CN and Ni−Ph bond strengths in **9A**, as follows:

$$\mathrm{BE(Ni{-}CN)} = 88.2 \times (1-0.557) + 148.6 \times 0.557 = 121.8\ \mathrm{kcal/mol} \qquad [\mathrm{A5}]$$

$$\mathrm{BE(Ni{-}Ph)} = 41.9 \times (1-0.388) + 189.3 \times 0.388 = 99.1\ \mathrm{kcal/mol} \qquad [\mathrm{A6}]$$

From these values, it is concluded that the Ni−CN bond is much stronger than the Ni−Ph bond. This is the reason of the results that the insertion into the Ni−CN bond occurs with more difficulty than that into the Ni−Ph bond, and that the vinyl−CN reductive elimination occurs with more difficulty than the vinyl−Ph one.

A4. Most favorable way of coordination of asymmetric alkynes

Scheme A1

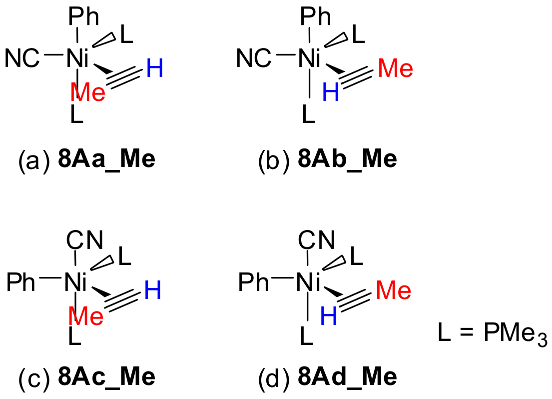

(a) **8Aa_Me** (b) **8Ab_Me**

(c) **8Ac_Me** (d) **8Ad_Me**

When alkyne is asymmetric such as MeC≡CH, there are four possible coordination structures, as shown in Scheme A1. In these four isomers, **8Ac_Me** and **8Ad_Me** could not be optimized because of the large steric repulsion between Ph and Me of MeC≡CH; in these complexes, alkyne dissociates from the Ni center during the optimization. Also, **8Ab_Me** was calculated to be slightly less stable than **8Aa_Me** by 2.6 kcal/mol because the steric repulsion between PMe_3 and the Me of MeC≡CH is larger in **8Ab_Me** than in **8Aa_Me**. Thus, the isomer **8Aa_Me** is important in the reaction. In the cases of ^{i}PrC≡CMe and ^{t}BuC≡CMe, we examined **8Aa_^{i}Pr** and **8Aa_^{t}Bu**, geometries of which are similar to that of **8Aa_Me**.

References

(1) Gerlach, D. H.; Kane, A. R.; Parshall, G. W.; Jesson, J. P.; Muetterties, E. L. *J. Am. Chem. Soc.* **1971**, *93*, 3543-3544.

(2) Parshall, G. W. *J. Am. Chem. Soc.* **1974**, *96*, 2360-2366.

(3) Clark, D. A.; Hunt, M. M.; Kemmitt, R. D. W. *J. Organomet. Chem.* **1979**, *175*, 303-313.

(4) Burmeister, J. L.; Edwards, L. M. *J. Chem. Soc. A* **1971**, 1663-1666.

(5) (a) Favero, G.; Frigo, A.; Turco, A. *Gazz. Chim. Ital.* **1974**, *104*, 869. (b) Favero, G.; Turco, A. *J. Organomet. Chem.* **1976**, *105*, 389-392. (c) Morvillo, A.; Turco, A. *J. Organomet. Chem.* **1981**, *208*, 103-113. (d) Favero, G.; Morvillo, A.; Turco, A. *J. Organomet. Chem.* **1983**, *241*, 251-257.

(6) Blanchini, C.; Masi, D.; Meli, A.; Sabat, M. *Organometallics* **1986**, *5*, 1670-1675.

(7) Abla, M.; Yamamoto, T. *J. Organomet. Chem.* **1997**, *532*, 267.

(8) Churchill, D.; Shin, J. H.; Hascall, T.; Hahn, J. M.; Bridgewater, B. M.; Parkin, G. *Organometallics* **1999**, *18*, 2403-2406.

(9) (a) García, J. J.; Jones, W. D. *Organometallics* **2000**, *19*, 5544-5545. (b) García, J. J.; Brunkan, N. M.; Jones, W. D. *J. Am. Chem. Soc.* **2002**, *124*, 9547-9555. (c) Brunkan, N. M.; Brestensky, D. M.; Jones, W. D. *J. Am. Chem. Soc.* **2004**, *126*, 3627-3641. (d) García, J. J.; Arévalo, Brunkan, N. M.; Jones, W. D. *Organometallics* **2004,** *23,* 3997-4002. (e) Ateşin, T. A.; Li, T.; Lachaize, S.; Brennessel, W. W.; García, J. J.; Jones, W. D. *J. Am. Chem. Soc.* **2007,** *129,* 7562-7569. (f) Ateşin, T. A.; Li, T.; Lachaize, S.; Garcia, J. J.; Jones, W. D. *Organometallics* **2008**, *27*, 3811-3817.

(10) Ohnishi, Y.-y.; Nakao, Y.; Sato, H.; Sakaki, S. *J. Phys. Chem. A* **2007**, *111*, 7915-7924.

(11) (a) Taw, F. L.; White, P. S.; Bergman, R. G.; Brookhart, M. *J. Am. Chem. Soc.* **2002,** *124,* 4192. (b) Taw, F. L.; Mueller, A. H.; Bergman, R. G.; Brookhart, M. *J. Am. Chem. Soc.* **2003,** *125,* 9808.

(12) (a) Nakazawa, H.; Kawasaki, T.; Miyoshi, K.; Suresh, C. H.; Koga, N. *Organometallics* **2004,** *23,* 117. (b) Nakazawa, H.; Kamata, K.; Itazaki, M. *Chem. Commun.* **2005,** 4004. (c) Nakazawa, H.; Itazaki, M.; Kamata, K.; Ueda, K. *Chem. Asia. J.* **2007**, *2*, 882-888.

(13) Miller, J. A. *Tetrahedron Lett.* **2001**, *42*, 6991-6993.

(14) (a) Nakao, Y.; Oda, S.; Hiyama, T. *J. Am. Chem. Soc.* **2004**, *126*, 13904. (b) Nakao, Y.; Oda, S.; Yada, A.; Hiyama, T. *Tetrahedron* **2006**, *62*, 7567.

(15) (a) Becke, A. D. *Phys. Rev. A* **1988**, *38*, 3098-3100. (b) Perdew, J. P.; Wang, Y. *Phys. Rev. B* **1992**, *45*, 13244-13249.

(16) We tried to perform IRC calculation but failed it in many cases here probably because of too flat potential energy surface. We ascertained that each transition state connects reactant and product by performing steepest descent geometry optimization starting from each transition state.

(17) Ohnishi, Y.-y.; Nakao, Y.; Sato, H.; Sakaki, S. *J. Phys. Chem. A* **2008**, *112*, 1946-1955.

(18) Dolg, M.; Stoll, W. H.; Preuss, H. *J. Chem. Phys.* **1987,** *86,* 866-872.

(19) Francl, M. M.; Petro, W. J.; Hehre, W. J.; Binkley, J. S.; Gordon, M. S.; DeFrees, D. J.; Pople, J. A. *J. Chem. Phys.* **1982,** *77,* 3654-3665.

(20) Hehre, W. J.; Ditchfield, R.; Pople, J. A. *J. Chem. Phys.* **1972,** *56,* 2257-2261.

(21) Balabanov, N. B.; Peterson, K. A. *J. Chem. Phys.* **2005,** *123,* 064107.

(22) (a) Dunning, T. H., Jr. *J. Chem. Phys.* **1989,** *90,* 1007-1023. (b) Woon, D. E.; Dunning, T. H., Jr. *J. Chem. Phys.* **1993,** 98, 1358-1371.

(23) Cancés, M. T.; Mennucci, B.; Tomasi, J. *J. Chem. Phys.* **1997**, *107*, 3032-3041.

(24) Mammen, M.; Shakhnovich, E. I.; Deutch, J. M.; Whitesides, G. M. *J. Org. Chem.* **1998**, *63*, 3821-3830.

(25) Pople, J. A. et al. Gaussian03, Revision D.02 Gaussian, Inc., Wallingford CT, 2004.

(26) Reed, A. E.; Curtis, L. A.; Weinhold, F. *Chem. Rev.* **1988**, *88*, 849, and references therein.

(27) ΔF^{evr} values in Table 1 indicate that Ni(cod)(PMe_3)(HC≡CH) is slightly more stable than Ni(cod)(PMe_3)$_2$. However, this is because the HC≡CH is linear and symmetrical; in other words, because of two degrees of freedom for rotation and the symmetry number in partition function, the rotational entropy is smaller than these of the unsymmetrical alkyne and PMe_3. Thus, the entropy loss by the coordination of HC≡CH is smaller than that by PMe_3 coordination. When the alkyne is not linear and not symmetrical such as ^{i}PrC≡CMe and ^{t}BuC≡CMe, Ni(cod)(PMe_3)$_2$ becomes most stable in ΔF^{evr}.

(28) We examined the other possible reaction course in which cod first dissociates from the Ni center of **2** to form Ni(PMe_3)$_2$ and then PhCN approaches the Ni center to form Ni(PhCN)(PMe_3)$_2$. However, the dissociation of cod from **2** gives rise to significantly large energy destabilization (ΔF^{ev} and ΔF^{evr} are +32.2 kcal/mol and +23.8 kcal/mol, respectively). This energy destabilization is considerably larger than the activation barrier ($\Delta F^{\mathrm{ev}\ddagger}$ and $\Delta F^{\mathrm{evr}\ddagger}$ are 3.6 kcal/mol and 12.2 kcal/mol, respectively) in the PhCN coordination from **2** to **3**. These results suggest that the cod dissociation is difficult before PhCN approaches to the Ni center.

(29) Lin, B.-L.; Liu, L.; Fu, Y.; Luo, S.-W.; Chen, Q.; Guo, Q.-X. *Organometallics* **2004**, *23*, 2114-2123.

(30) We performed geometry optimization with steepest descent method starting

from transition states **TS$_{5\text{-}6}$** and **TS$_{6\text{-}7}$** and confirmed that **TS$_{5\text{-}6}$** connects **5** and **6** and **TS$_{6\text{-}7}$** connects **6** and **7**. The IRC calculation did not work because of the very flat potential energy surface around these transition states. See Appendix Figure A3 for the geometry and energy changes.

(31) See Appendix Section A2 for more detailed discussion.

(32) We examined the alkyne insertion into the Ni−CN bond in five-coordinate intermediate **8A** and we found that it is impossible. We did not examine the alkyne insertion into the Ni−Ph bond because it does not lead to formation of major product in the case of five-coordinate intermediate. See Appendix Figure A6 for input geometry and optimization result. Thus, we discussed here the insertion reaction in four-coordinate intermediate Ni(CN)(Ph)(PMe$_3$)(alkyne) which is formed through PMe$_3$ substitution for alkyne.

(33) Driver, M. S.; Hartwig, J. F. *J. Am. Chem. Soc.* **1997,** *119,* 8232-8245.

(34) The Ni–CN and Ni–Ph bond energies in **9A** were calculated to be 121.8 and 99.1 kcal/mol, respectively. See Appendix Section A3 for more details of these values

(35) See Appendix Section A4 for more detailed discussion.

(36) Because **9Aa_R** and **9Ab_R** easily convert to each other, the concentration ratio [**9Aa_R**]/[**9Ab_R**] should be considered to evaluate the regioselectivity.

General Conclusion

In this thesis, the author theoretically studied the organometallic reactions and transition-metal-catalyzed reactions with the electronic structure theory and also developed new method which enables us to quantitatively calculate the energy change of the reaction of the large organometallic compound. The outstandingly fruitful findings and important conclusions in this thesis are summarized, as follows.

In chapter 1, ruthenium-catalyzed hydrogenation of carbon dioxide to formic acid was theoretically investigated with DFT and MP4(SDQ) methods, where a real catalyst, *cis*-$Ru(H)_2(PMe_3)_3$, was employed in calculations and compared with a model catalyst, *cis*-$Ru(H)_2(PH_3)_3$. Significant differences between the real and model systems are observed in CO_2 insertion into the Ru(II)−H bond, isomerization of a ruthenium(II) η^1-formate intermediate, and metathesis of the ruthenium(II) η^1-formate intermediate with dihydrogen molecule. All these reactions more easily occur in the real system than in the model system. The differences are interpreted in terms that PMe_3 is more donating than PH_3 and the trans-influence effect of PMe_3 is stronger than that of PH_3. The rate-determining step is the CO_2 insertion into the Ru(II)–H bond. Its $\Delta G^{\circ\ddagger}$ value is 16.8 (6.8) kcal/mol, where the value without parenthesis is calculated with the MP4(SDQ) method and in parenthesis is calculated with the DFT method. Because this insertion is considerably endothermic, the coordination of dihydrogen molecule with the ruthenium(II)-η^1-formate intermediate must necessarily occur to suppress the de-insertion. This means that the reaction rate increases with increase in the pressure of dihydrogen molecule, which is consistent with the experimental results. Solvent effects were investigated with the DPCM method. The activation barrier and reaction energy of the CO_2 insertion reaction moderately decrease in the order gas phase > *n*-heptane > THF, while the activation barrier of the metathesis considerably increases in the order gas phase < *n*-heptane < THF. Thus, a polar solvent should be used because the insertion reaction is the rate-determining step.

In chapter 2, ruthenium-catalyzed hydrogenation of carbon dioxide to formic acid was theoretically investigated with DFT and MP4(SDQ) methods, too, to clarify the reasons why water molecules accelerate this reaction. In the presence of water molecule, the reaction proceeds, as follows: (1) Carbon dioxide forms an adduct *cis*-$Ru(H)_2(PMe_3)_3(H_2O)(CO_2)$ in which the C and O atoms of CO_2 interact with the H (hydride) ligand and the H atom of H_2O, respectively. (2) Nucleophilic attack of the H ligand to CO_2 easily takes place to afford a Ru-(η^1-formate) intermediate, $Ru(H)(PMe_3)_3(\eta^1\text{-}OCOH)(H_2O)$, with much smaller activation barrier than that of the CO_2 insertion into the Ru−H bond which is the rate-determining step in the absence of water molecule. (3) Rate-determining step is the coordination of dihydrogen molecule with the Ru-(η^2-formate) complex, $Ru(H)(PMe_3)_3(\eta^2\text{-}O_2CH)(H_2O)$, of which activation barrier is smaller than that of the CO_2 insertion into the Ru–H bond. And, (4) the metathesis of the Ru-(η^1-fomate) complex with the dihydrogen molecule easily occurs in $Ru(H)(PMe_3)_3(\eta^1\text{-}OCOH)(H_2)(H_2O)$ to afford formic acid with moderate activation barrier. Based on these results, it should be concluded that the early half of the reaction mechanism changes by water molecule, which is the reason of the acceleration by water molecule. One of the most important results is that the aqua ligand accelerates the nucleophilic attack of the H (hydride) ligand to CO_2 because the hydrogen bonding interaction between the aqua ligand and carbon dioxide decreases the activation barrier and increases the exothermicity. Theoretical calculations clearly show that the similar acceleration is induced by amine and alcohol.

In chapter 3, oxidative addition of H_2 to $Ni(PH_3)_2$ was theoretically studied as a prototype of nickel-catalyzed σ-bond activation reaction, where CASSCF, CASPT2, CCSD(T), broken symmetry (Bs) MP2 to MP4(SDTQ), and DFT methods were employed. The CASPT2 method yields reliable potential energy curve (PEC) when the active space consists of 10 electrons in 10 orbitals including five outer 3d' orbitals. The CCSD(T) method presents almost the same PEC as the CASPT2-calculated one, when either ANO or cc-pVTZ basis set is used for Ni. Bs-MP4(SDTQ)-calculated PEC is similar to those calculated by the CASPT2/ANO and CCSD(T)/cc-pVTZ methods, while the PEC is not smooth around the transition state. In the DFT calculation, ANO, cc-pVTZ, and triple-zeta quality basis sets (SDB) with Stuttgart-Dresden-Bonn effective core potentials (ECPs) must be used for Ni. The DFT-calculated reaction energy is somewhat smaller than the CASPT2- and CCSD(T)-calculated values, where B3PW91 and mPW1PW91 present moderately better energy changes than BLYP, B1LYP, and B3LYP. Oxidative addition of MeCN to $Ni(PH_3)_2$ was investigated by the DFT(B3PW91) and CCSD(T) methods. Almost the same activation barrier was calculated by these methods, when cc-pVTZ was employed for Ni. However, the DFT method somewhat underestimates the binding energy of the reactant complex and the reaction energy compared to the CCSD(T) method. Important results of this oxidative addition are summarized, as follow: The barrier height relative to infinite separation is lower and the product is more stable than those of the oxidative addition of C_2H_6. These differences are discussed in detail in terms of Ni–Me and Ni–CN bond energies and the contribution of CN π* orbital to stabilization interaction in the transition state.

In chapter 4, chemically reasonable model of tertiary phosphine (R = Me, Et, ^{i}Pr, and ^{t}Bu) was constructed to apply the post Hartree-Fock method such as CCSD(T) method to large transition metal complexes. In this model, R is replaced by the H atom including the frontier orbital consistent quantum capping potential (FOC-QCP) which reproduces the frontier orbital energy of PR_3. The steric effect is incorporated by the new procedure named steric repulsion correction (SRC). To examine the performance of this FOC-QCP method with the SRC, the activation barriers and reaction energies of the reductive elimination reactions of C_2H_6 and H_2 from $M(R^1)_2(PR^2_3)_2$ (M = Ni, Pd, or Pt; R^1 = Me for R^2 = Me, Et, or ^{i}Pr, or R^1 = H for R^2 = ^{t}Bu) were evaluated with the DFT[B3PW91], MP4(SDQ), and CCSD(T) methods. The FOC-QCP method reproduced well the DFT[B3PW91]- and MP4(SDQ)-calculated energy changes of the real complexes with PMe_3. For bulky phosphine, the SRC must be added to present correct energy change, in which the MP2 method was employed to make steric repulsion correction because the systems calculated in the SRC do not include transition metal element. The monomerization energy of $[RhCl(P^iPr_3)_2]_2$ and the coordination energies of CO, H_2, N_2, and C_2H_4 with $[RhCl(P^iPr_3)_2]_2$ were theoretically calculated by the CCSD(T) method combined with the FOC-QCP and the SRC. The CCSD(T)-calculated energies agree well with the experimental ones, indicating the excellent performance of the combination of the FOC-QCP with the SRC. On the other hand, the DFT[B3PW91]-calculated energies of the real complexes considerably deviate from the experimental values.

In chapter 5, nickel(0)-catalyzed phenylcyanation of alkyne was theoretically investigated mainly by the DFT(B3PW91) method and in part by the CCSD(T) combined with the FOC-QCP + SRC to clarify the reaction mechanism including the formation process of the active species, the rate-determining step, and the regioselectivity of the reaction, where real catalyst $Ni(PMe_3)_2$ was employed. The first step of this reaction is coordination of PhCN with the Ni center followed by isomerization of $Ni(PMe_3)_2(PhCN)$ and oxidative addition of Ph−CN to the Ni(0) center. The next step is coordination of alkyne with the Ni center to form a five-coordinate intermediate. Then, PMe_3 dissociates from the Ni(II) center to form a four-coordinate intermediate Ni(CN)(Ph)(PMe_3)(alkyne). The final step is alkyne insertion into the Ni−Ph bond followed by the reductive elimination of the CN and vinyl groups. The rate determining step is the oxidative addition. Another possible reaction mechanism investigated here is the alkyne insertion into the Ni−CN bond followed by the reductive elimination of the Ph and vinyl groups. Though the reductive elimination of the Ph and vinyl groups more easily occurs than that of the CN and vinyl groups, alkyne is much less easily inserted into the Ni−CN bond than into the Ni−Ph bond. As a result, this mechanism is less favorable than the former one. The regioselectivity of the reaction is determined by the steric repulsion between the Ph and the substituent group of alkyne in the alkyne insertion step into the Ni−Ph bond.

Though the electronic structure theory, especially the density functional theory, has become powerful to study organometallic reactions nowadays, the reliability has not been established completely. The author examined what method we should employ to obtain quantitatively correct energy change by organometallic reaction. Based on the careful examination, the author wishes to propose a new FOC-QCP method with which we can apply highly accurate post Hartree-Fock methods such as CCSD(T) to organometallic compounds without loss of electronic and steric effects of real substituent group. The author believes that the accurate evaluation of energy change becomes available owing to this FOC-QCP and thus the computational methods will become more powerful to theoretically investigate organometallic compounds and their reactions.

List of Publications

Publications included in this thesis

Chapter 1

"Ruthenium(II)-Catalyzed Hydrogenation of Carbon Dioxide to Formic Acid. Theoretical Study of Real Catalyst, Ligand Effects, and Solvation Effects"

Yu-ya Ohnishi, Tadashi Matsunaga, Yoshihide Nakao, Hirofumi Sato, Shigeyoshi Sakaki

J. Am. Chem. Soc., **2005**, *127*, 4021-4032.

Chapter 2

"Ruthenium(II)-Catalyzed Hydrogenation of Carbon Dioxide to Formic Acid. Theoretical Study of Significant Acceleration by Water Molecules"

Yu-ya Ohnishi, Yoshihide Nakao, Hirofumi Sato, Shigeyoshi Sakaki

Organometallics, **2006**, *25*, 3352-3363.

Chapter 3

"Theoretical Study of Oxidative Additions of H_2 and MeCN to a Nickel(0) Complex: Significantly Large Correlation Effects and Characteristic Features of the Reaction"

Yu-ya Ohnishi, Yoshihide Nakao, Hirofumi Sato, Shigeyoshi Sakaki

J. Phys. Chem. A, **2007**, *111*, 7915-7924.

Chapter 4

"Frontier Orbital Consistent Quantum Capping Potential (FOC-QCP) for Bulky Ligand of Transition Metal Complexes"

Yu-ya Ohnishi, Yoshihide Nakao, Hirofumi Sato, Shigeyoshi Sakaki

J. Phys. Chem. A, **2008**, *112*, 1946-1955.

Chapter 5

"A Theoretical Study of Nickel(0)-Catalyzed Phenylcyanation of Alkynes. Reaction Mechanism and Regioselectivity"

Yu-ya Ohnishi, Yoshihide Nakao, Hirofumi Sato, Yoshiaki Nakao, Tamejiro Hiyama, Shigeyoshi Sakaki

Submitted.

Other publications

1. “Why Does Fluoride Anion Accelerate Transmetalation between Vinylsilane and Palladium(II)−Vinyl Complex? Theoretical Study”
   Akihiro Sugiyama, Yu-ya Ohnishi, Mayu Nakaoka, Yoshihide Nakao, Hirofumi Sato, Shigeyoshi Sakaki, Yoshiaki Nakao, Tamejiro Hiyama
   J. Am. Chem. Soc., **2008**, *130*, 12975-12985.

2. “Heterolytic σ-Bond Activation by Transition Metal Complexes”
   Shigeyoshi Sakaki, Noriaki Ochi, Yu-ya Ohnishi
   Computational Modeling for Homogeneous and Enzymatic Catalysis. A Knowledge-Base for Designing Efficient Catalysts. Morokuma, K. and Musaev, D. G. (Eds.); Wiley: Weinheim, 2008.